

CRANFIELD UNIVERSITY

THIERRY SIBILLI

MODELLING THE AERODYNAMICS OF PROPULSIVE
SYSTEM INTEGRATION AT CRUISE AND HIGH-LIFT
CONDITIONS

SCHOOL OF ENGINEERING
DEPARTMENT OF POWER & PROPULSION

PhD

Academic Year: 2011-2012

Supervisor: Prof. Mark Savill
March 2012

CRANFIELD UNIVERSITY

SCHOOL OF ENGINEERING
DEPARTMENT OF POWER & PROPULSION

PhD

Academic Year 2011 - 2012

THIERRY SIBILLI

MODELLING THE AERODYNAMICS OF PROPULSIVE
SYSTEM INTEGRATION AT CRUISE AND HIGH-LIFT
CONDITIONS

Supervisor: Prof. Mark Savill
March 2012

© Cranfield University 2012. All rights reserved. No part of this publication may be reproduced without the written permission of the copyright owner.

ABSTRACT

Due to a trend towards Ultra High Bypass Ratio engines the corresponding engine/airframe interference is becoming a key aspect in aircraft design. The present economic situation increases the pressure on commercial aviation companies to reduce the Direct Operating Cost, and the environmental situation requires a new generation of aircraft with a lower environmental impact. Therefore detailed aerodynamic investigations are required to evaluate the real benefits of new technologies.

The presented research activity is part of a long-term project with the main objective of generating a reliable and accurate tool to predict the performance of an aircraft over the whole flight domain. In particular the aim of this research was to perform advanced CFD in order to establish a tool able to evaluate engine installation effects for different configurations and attitudes. The developed tool can be provided with correlations of the Net Propulsive Force (NPF), the force exerted by the power-plant to the aircraft, as a function of position. This can be done in principle at cruise, hold, climb, descent, take-off and landing, to model the different integration effects at different phases.

Due to the complexity of the problem it was only possible at an initial stage to determine these correlations at cruise condition. Two parametric test cases were evaluated, showing that the engine horizontal positioning can influence the mission fuel burn by up to 6.4%. According to the extensive literature review that has been done, this study can be regarded as the first open literature engine position-NPF parametric study using CFD.

Even though no correlations were extracted for other conditions; a deployed high-lift wing configuration was also studied in detail, defining the main aerodynamics effects of the engine integration at high angle of attack. A topological study of the high-lift installation vortices is presented in this work and it can be considered the first in the open literature.

It should be pointed out that extensive research is currently underway to correctly evaluate the high-lift aerodynamic using CFD. The Propulsive System Integration (PSI) in high-lift conditions is adding flow features to an already demanding problem, making it a real challenge for the numerical methods.

Nevertheless the additional effects of a nacelle chine on the maximum lift were also evaluated.

The main outcomes of this PhD research were: a coupled performance modelling tool able to handle the effects of engine-airframe integration as a function of geometry and attitude, and a topological study of the high-lift installation vortices.

During the course of the work, this research was successfully suggested as an extra activity for the European NEWAC project (New Aero Engine Core Concepts), and resulted in a new deliverable for that project.

Keywords:

Engine-Airframe Interaction, Net Propulsive Force, High-Lift CFD, High-lift Installation Vortex, Nacelle chine, Drag Extraction.

ACKNOWLEDGEMENTS

First I would like to express my gratitude to Prof. Mark Savill for his guidance and support during these years of research for my PhD degree.

Thanks to all the Cranfield University Power & Propulsion departmental staff.

Big thanks to: Uyie, Leo, Adrian, Baba, Akarsh, Ahad, Conor, Leititia, Kostas, Eric, Shaab, Olivier, Kirsty, Dr. Obama, Grant, Michele, Emanuele, Anna, Bupy, Louise, Sue, Stuart, Paul, Bobby and Pablo.

A special one to Paola (alias: Dolciosa).

Thanks to my family: Marie-France, Elodie, Fanny, Ciccio and Zippy.

I really had a good time.

Thanks to all the people that make aerospace engineering an important part of their lives. It is an honour to work with you. Together we are pushing the boundaries.

A Diego
Grazie

Puntammo
sull'alto emergere alla motagna arcana

E lassù seduti su un cerchio di pietre
sopra le valli trascendemmo le nebbie.

Diego Garnero: *La luce, l'ombra e il
crepuscolo*

TABLE OF CONTENTS

ABSTRACT	i
ACKNOWLEDGEMENTS.....	iii
LIST OF FIGURES.....	iii
LIST OF TABLES	xiv
LIST OF EQUATIONS.....	xv
LIST OF ABBREVIATIONS	xxii
THESIS STRUCTURE	xxiv
1 PROPULSION SYSTEM INTEGRATION.....	1
INTRODUCTION	1
1.1 AERODYNAMICS OF PSI	3
1.2 DEGREE OF FREEDOM.....	6
1.3 CONSTRAINTS	7
1.4 AERODYNAMIC INTERFERENCE EVALUATION.....	10
1.5 NET PROPULSIVE FORCE: THRUST AND DRAG BOOK-KEEPING..	11
2 CFD & PSI MODELLING.....	20
2.1 DLR-F6 WING-BODY-NACELLE-PYLON	31
2.1.1 GEOMETRY.....	31
2.1.2 EXPERIMENTS	32
2.1.3 NUMERICAL METHOD.....	33
2.1.4 GRID GENERATION.....	34
2.1.5 RESULTS.....	38
2.1.6 CONCLUSIONS.....	45
3 PSI MODULE	46
3.1 HERMES & TURBOMATCH.....	47
3.2 THE PSI MODULE.....	52
3.2.1 STRUCTURE	52
3.2.2 CFD MODEL	55
4 NEWAC ENGINES INTEGRATION	68
4.1 PSI MODULE CORRELATIONS.....	76
4.1.1 NUMERICAL METHOD.....	77
4.1.2 RESULTS.....	78
4.2 PSI MODULE ASSESSMENT	90
4.3 CONCLUSIONS & FUTURE WORK.....	91
5 HIGH LIFT PROPULSION SYSTEM INTEGRATION	94
5.1 INTRODUCTION	94
5.2 MULTI-ELEMENTS HIGH-LIFT AERODYNAMICS AND CFD	96
5.3 HIGHT LIFT PROPULSION SYSTEM INTEGRATION	113
6 CFD HIGH LIFT PREDICTION WORKSHOP	121
6.1 GEOMETRY AND GRID GENERATION	121
6.2 EXPERIMENTAL RESULTS.....	127

6.3 NUMERICAL METHOD AND RESULTS	128
7 CFD PSI AT HIGH-LIFT CONDITION	143
7.1 NACELLE GEOMETRY GENERATION AND INSTALLATION	143
7.2 NUMERICAL METHOD AND RESULTS	147
7.3 HIGH-LIFT ENGINE INSTALLATION VORTICES	155
7.4 NACELLE CHINE	165
7.4.1 GEOMETRY DEFINITION AND INSTALLATION	165
7.4.2 RESULTS.....	168
7.5 CONCLUSIONS & FUTURE WORK.....	175
8 MAIN CONCLUSIONS & FUTURE WORK	178
REFERENCES.....	182
APPENDICE.....	194

LIST OF FIGURES

Fig. 1.1 Installation effects on the upper surface of the wing	5
Fig. 1.2 Installation effects on the lower surface of the wing	5
Fig. 1.3 Degrees of Freedom in PSI: Engine Position and Pylon Shape. (Rivoire, 2007).....	6
Fig. 1.4 Systems allocation constraint: example of fuel, air, oil and electrical systems layout. (Rivoire, 2007).	8
Fig. 1.5 Vital system safety constraint: example of blade-off constrains. The green zones are possible blade-off paths (left) and the blue striped zones are safe zones (right). (Rivoire, 2007).....	9
Fig. 1.6 Spray ingestion from landing gear constraint: example of an engine injection test. (Rivoire, 2007).....	9
Fig. 1.7 Escape slide zone constraint: example of an engine slide collision simulation (left) and real case (right). (Rivoire, 2007).....	9
Fig. 1.8 Operational constraints: example of an engine maintainability simulation (left and centre) and access to cargo doors (right). (Rivoire, 2007).....	10
Fig. 1.9 Ground clearance constraint: example of cross wind extreme landing configuration (left) and collapse of front landing gear maintaining intact the engines (right). (Rivoire, 2007).....	10
Fig. 1.10 Schematic of the ducted body flows.....	12
Fig. 1.11 Forces on a streamtube.....	13
Fig. 1.12 Forces stations definition on an isolated nacelle.....	15
Fig. 1.13 Forces stations definition on a Turbofan.	18
Fig. 2.1 PSI design process. (Central figure: Brodersen (2002), figure at the bottom courtesy of the Boeing Company)	21
Fig. 2.2 Panel model of high-bypass-ratio engines. (Clark, 1984).....	22
Fig. 2.3 Nacelle forebody experimental (white dots) and numerical (black dots) pressure parameter (normalized to the Total Pressure P_0) function of horizontal position parameter (x/X). x axial coordinate, X forebody length. (Clark, 1984)	22
Fig. 2.4 Euler structured grid (top), exp. and numerical C_p at the wing (left) and nacelle (right). (Naik and Chen, 1992).	23
Fig. 2.5 Numerical and experimental pressure coefficient computed using different numerical approaches. (Rudnik and Rossow, 2002).	24

Fig. 2.6 Engine-airframe configurations solved using RANS methods. (Rudnik and Geyr, 2007).	25
Fig. 2.7 Engine-airframe configurations boundaries. (Rudnik and Ronzheimer, 1992).	26
Fig. 2.8 Measured and calculated drag polar for different engine positions. (Brodersen, 2002)	27
Fig. 2.9 Engine position variation. (Rudnik and Rossow, 2002).	28
Fig. 2.10 Influence of vertical engine position (configurations 1, 2 and 3 fig. 2.12) on pressure coefficient. D3 inboard section, D4 outboard section (Rudnik and Rossow, 2002).	28
Fig. 2.11 Influence of horizontal engine position (configurations 3 and 4 fig. 2.12) on pressure coefficient. D3 inboard section, D4 outboard section (Rudnik and Rossow, 2002).	29
Fig. 2.12 Influence of engine position (configurations 1, 2, 3 and 4 fig. 2.12) on spanwise lift distribution. (Rudnik and Rossow, 2002).	29
Fig. 2.13 Pressure peaks (left figure: Harris, 1995).	30
Fig. 2.14 Wing pressure coefficient peaks values near the pylon function of horizontal engine position. (Oliveira, 2003).	30
Fig. 2.15 Wing pressure coefficient peaks values near the pylon function of vertical engine position. (Oliveira, 2003).	31
Fig. 2.16 DLR-F6 geometry. (AIAA, 2012).	32
Fig. 2.17 WBNP coarse hybrid mesh generated using ICEMCFD	35
Fig. 2.18 WB fine hybrid mesh generated using ICEMCFD	35
Fig. 2.19 Detail of the hybrid mesh: fuselage layer.	36
Fig. 2.20 Detail of the hybrid mesh: nacelle structural layer.	36
Fig. 2.21 WB C_D function of mesh size.	37
Fig. 2.22 WBNP C_D function of mesh size.	37
Fig. 2.23 Numerical and experimental drag polar DLR-F6 WB configuration. (Exp. AIAA, 2012)	38
Fig. 2.24 Numerical and experimental drag polar DLR-F6 WBNP configuration. (Exp. AIAA, 2012)	39
Fig. 2.25 Installation Drag polar DLR-F6 configuration	40
Fig. 2.26 Pressure coefficient at $\eta = 0.15$ for WB configuration	40
Fig. 2.27 Pressure coefficient at $\eta = 0.239$ for WBNP configuration	41

Fig. 2.28 Streamlines on the upper surface of the wing for WBNP configuration	41
Fig. 2.29 Experimental oil-flow visualization	42
Fig. 2.30 Streamlines on the lower surface of the wing for WBNP configuration	42
Fig. 2.31 Experimental oil-flow visualization with demounted pylon.....	43
Fig. 2.32 Streamlines on the inboard side of the pylon	43
Fig. 2.33 Wall shear on the upper surface of the wing.	44
Fig. 2.34 Wall shear at the inboard side of the pylon.	44
Fig. 3.1 Hermes: geometry and configuration input file.....	47
Fig. 3.2 Hermes: mission and weight input file.....	48
Fig. 3.3 Flight phases.(Doulgeris, 2009)	49
Fig. 3.4 Hermes: mission specification input file.	50
Fig. 3.5 Hermes: cruise condition output file.	51
Fig. 3.6 Turbomatch input file.....	52
Fig. 3.7 PSI module schema.	53
Fig. 3.8 PSI module input file.	54
Fig. 3.9 PSI module output.....	55
Fig. 3.10 Stations definition on a Turbofan	56
Fig. 3.11 Engine and far-field boundary conditions	56
Fig. 3.12 Nacelle geometry input file and boat-tail cord angle and radius (VITAL, 2005).....	58
Fig. 3.13 Location of engine layout constraints (VITAL, 2005).....	58
Fig. 3.14 Nacelle components. The grey line (positioned at max nacelle diameter) indicate the boundary between forebody and afterbody.....	59
Fig. 3.15 Intake geometry (co-ordinate system as fig 3.12).	60
Fig. 3.16 Reduction of sonic regions (grey surfaces) around intake and forebody for five different nacelle intake versions.	61
Fig. 3.17 Fan duct geometry (co-ordinate system as fig 3.12).	62
Fig. 3.18 Mach number at the fan/core exit for 3 different flow path configurations.....	63
Fig. 3.19 Wing and Body Common Research Model	64

Fig. 3.20 Surface stream lines on the inboard side of the pylon.....	65
Fig. 3.21 Pylon modifications from version MkI to MkII	65
Fig. 3.22 Surface streamlines on the inboard side of the pylon.....	66
Fig. 4.1 Intercooled Core layout and its new technologies.(Wilfert, 2007).	68
Fig. 4.2 Active Core layout and its new technologies. (Wilfert, 2007).	69
Fig. 4.3 AC S/R – Location of engine layout constraints. (Longeville, 2007; Andreoletti, 2007).....	69
Fig. 4.4 IC L/R - Location of engine layout constraints. (Longeville, 2007; Andreoletti, 2007).....	70
Fig. 4.5 IC L/R Nacelle Geometry input data. (Longeville, 2007; Andreoletti, 2007).....	71
Fig. 4.6 Engine-airframe configuration for the IC L/R.....	76
Fig. 4.7 Engine-airframe configuration for the AC S/R.....	76
Fig. 4.8 Engine position parameters	77
Fig. 4.9 NPF function of horizontal position for the IC L/R and AC S/R	79
Fig. 4.10 NPF function of vertical position for the IC L/R	79
Fig. 4.11 NPF function of vertical position for the AC S/R.....	80
Fig. 4.13 Pressure Contours on IC L/R V01.....	83
Fig. 4.14 Pressure Contours on IC L/R V04.....	83
Fig. 4.15 Pressure Contours on AC S/R V01	84
Fig. 4.16 Pressure Contours on AC S/R V04.....	84
Fig. 4.16 CRM IC L/R and AC S/R pressure taps position (values of eta)	85
Fig. 4.17 C_p comparison between IC L/R V04, IC L/R V01 and WB at eta 0.1	85
Fig. 4.18 C_p comparison between IC L/R V04, IC L/R V01 and WB at eta 0.3	85
Fig. 4.19 C_p comparison between IC L/R V04, IC L/R V01 and WB at eta 0.4	86
Fig. 4.20 C_p comparison between IC L/R V04, IC L/R V01 and WB at eta 0.75	86
Fig. 4.21 C_p comparison between IC L/R V04, IC L/R V06 and WB at eta 0.1	86
Fig. 4.22 C_p comparison between IC L/R V04, IC L/R V06 and WB at eta 0.3	87
Fig. 4.23 C_p comparison between IC L/R V04, IC L/R V06 and WB at eta 0.4	87

Fig. 4.24 C_p comparison between AC S/R V04,AC S/R V01 and WB at eta 0.1	87
Fig. 4.25 C_p comparison between AC S/R V04,AC S/R V01 and WB at eta 0.3	88
Fig. 4.26 C_p comparison between AC S/R V04, AC S/R V01 and WB at eta 0.4	88
Fig. 4.27 C_p comparison between AC S/R V04,AC S/R V06 and WB at eta 0.75	88
Fig. 4.28 C_p comparison between AC S/R V04, AC S/R V06 and WB at eta 0.1	89
Fig. 4.29 C_p comparison between AC S/R V04,AC S/R V06 and WB at eta 0.3	89
Fig. 4.30 C_p comparison between AC S/R V04,AC S/R V06 and WB at eta 0.4	89
Fig. 4.29 IC L/R Fuel consumed during the cruise function of horizontal position	90
Fig. 4.30 AC S/R Fuel consumed during the cruise function of horizontal position.....	91
Fig. 5.1 Velocity distributions on an airfoil with and without vortex (to simulate the flap and slat) on LE (left) and TE (right) (Smith, 1975).....	97
Fig. 5.2 High-Lift aerodynamics features [Rumsey, 2002]	98
Fig. 5.3 EUROLIFT three levels of geometry complexity [Eliasson, 2003].....	100
Fig. 5.4 ONERA F1 swept constant chord wing (Hansen, 2004)	100
Fig. 5.5 KH3Y Airbus-D model (Hansen, 2004)	100
Fig. 5.6 KH3Y Airbus-D model configurations. (Hansen, 2004).	101
Fig. 5.7 KH3Y Airbus-D model lift polar for unstructured and structured meshes for different solvers and turbulent models. (Eliasson, 2003).....	102
Fig. 5.8 KH3Y Airbus-D model lift and drag polar evaluated with different solvers and turbulence models. (Rudnik, 2003).	103
Fig. 5.9 KH3Y Airbus-D model lift polar for different Re numbers (Rudnik and Germain, 2007)	104
Fig. 5.10 EUROLIFT II KH3Y model complexity increase. (Quix, 2007)	104
Fig. 5.11 KH3Y model lift and drag polar for different wall functions. (Eliasson, 2007).....	106

Fig. 5.12	KH3Y model lift and drag polar for different turbulence models. (Eliasson, 2007).	106
Fig. 5.13	NASA Trap Wing Langley in the 14x22 Foot Subsonic Wing Tunnel. (NASA, 2012).	108
Fig. 5.14	Gridding guidelines for the grow rate in the viscous layer.(NASA, 2012).	109
Fig. 5.15	HILPW-1 Trap Wing grids topologies. (Rumsey, 2011).	111
Fig. 5.16	CL, CD and CM grid convergence study for a structured mesh:. (Wiart, 2011).	111
Fig. 5.17	CL, CD and CM grid convergence study for three unstructured meshes generated with different software: Solar, Centaur and 1to1 (Crippa, 2011). $\alpha = 15^\circ$ top, $\alpha = 28^\circ$ bottom	112
Fig. 5.18	HILPW-1 lift and drag coefficients of the 37 datasets. (Rumsey, 2011).	113
Fig. 5.19	Experimental (LaRC 14x22 Test 513 Run 105) and numerical lift polar for the configuration with flap/slat brackets (B-SAFv3-Roe, brackets on) and without (B-SAFv3-Roe, brackets off). (Slafani, 2011).	113
Fig. 5.20	HPSI aerodynamic effects: up-wash flow	115
Fig. 5.21	HPSI aerodynamic effects: nacelle/pylon vortex	115
Fig. 5.22	Single and double nacelle strake vortices	116
Fig. 5.23	Lift and drag polar for WB (conf.1), WBNP (conf.2) and WBNPC (conf.3). (Quix, 2007).	118
Fig. 5.24	PIV (left) and infra-Red flow visualization for WBNPC. (Von Geyr, 2009).	118
Fig. 5.25	Experimental (china clay) and numerical flow visualization for WBNP configuration (Yokokawa, 2008).	119
Fig. 5.26	PIV of nacelle/nacelle-strake vortices interaction (Yokokawa, 2008).	119
Fig. 6.1	Trap Wing geometry (configuration 1).	122
Fig. 6.2	Trap Wing layout and reference parameters (NASA, 2012).	122
Fig. 6.3	ICEM-CFD prism layer parameters.	123
Fig. 6.4	Control volume at wing/slat connection.	124
Fig. 6.5	Prism boundary layer at wing /flap (left) and wing/fuse (left).	125
Fig. 6.6	Trap Wing Hybrid mesh	125

Fig. 6.7	2D cut of the volume mesh around the Trap Wing.....	126
Fig. 6.8	Slat/Wing detail	126
Fig. 6.9	Flap/Wing detail	126
Fig. 6.10	CL polar repeatability. (NASA, 2012)	128
Fig. 6.11	C_D grid convergence study.....	129
Fig. 6.12	C_L grid convergence study.	129
Fig. 6.13	Trap Wing numerical and experimental lift polar.	130
Fig. 6.14	Trap Wing numerical and experimental drag polar.....	131
Fig. 6.15	Trap Wing pressure tap rows position. (NASA, 2012).....	131
Fig. 6.16	Pressure taps around the flap trailing edge.....	132
Fig. 6.17	Slat numerical and experimental slat C_P at $\eta = 0.17$, $\alpha = 6^\circ$	132
Fig. 6.18	Wing and flap numerical and experimental C_P at $\eta = 0.17$, $\alpha = 6^\circ$	132
Fig. 6.19	Slat numerical and experimental slat C_P at $\eta = 0.50$, $\alpha = 6^\circ$	133
Fig. 6.20	Wing and flap numerical and experimental C_P at $\eta = 0.50$, $\alpha = 6^\circ$	133
Fig. 6.21	Slat numerical and experimental slat C_P at $\eta = 0.85$, $\alpha = 6^\circ$	133
Fig. 6.22	Wing and flap numerical and experimental C_P at $\eta = 0.85$, $\alpha = 6^\circ$	134
Fig. 6.23	Flap edge span numerical and experimental C_P , $\alpha = 6^\circ$	134
Fig. 6.24	Slat numerical and experimental slat C_P at $\eta = 0.17$, $\alpha = 21^\circ$	134
Fig. 6.25	Wing and flap numerical and experimental C_P at $\eta = 0.17$, $\alpha = 21^\circ$	135
Fig. 6.26	Slat numerical and experimental slat C_P at $\eta = 0.50$, $\alpha = 21^\circ$	135
Fig. 6.27	Wing and flap numerical and experimental C_P at $\eta = 0.50$, $\alpha = 21^\circ$	135
Fig. 6.28	Slat numerical and experimental slat C_P at $\eta = 0.85$, $\alpha = 21^\circ$	136
Fig. 6.29	Wing and flap numerical and experimental C_P at $\eta = 0.85$, $\alpha = 21^\circ$	136
Fig. 6.30	Flap edge span numerical and experimental C_P , $\alpha = 21^\circ$	136
Fig. 6.31	Slat numerical and experimental slat C_P at $\eta = 0.17$, $\alpha = 32^\circ$	137

Fig. 6.32 Wing and flap numerical and experimental C_P at $\eta = 0.17$, $\alpha = 32^\circ$	137
Fig. 6.33 Slat numerical and experimental slat C_P at $\eta = 0.50$, $\alpha = 32^\circ$	137
Fig. 6.34 Wing and flap numerical and experimental C_P at $\eta = 0.50$, $\alpha = 32^\circ$	138
Fig. 6.35 Slat numerical and experimental slat C_P at $\eta = 0.85$, $\alpha = 32^\circ$	138
Fig. 6.36 Wing and flap numerical and experimental C_P at $\eta = 0.85$, $\alpha = 32^\circ$	138
Fig. 6.37 Flap edge span numerical and experimental C_P , $\alpha = 32^\circ$	139
Fig. 6.38 Normalized turbulence intensity (TU) contours at $\eta = 50$, $\alpha = 21^\circ$	140
Fig. 6.39 Normalized turbulence intensity (TU) contours at $\eta = 50$, $\alpha = 21^\circ$. Note the high TU values at the transition location (Steed, 2011).	141
Fig. 6.40 Wall Shear contours and surface stream lines at $\alpha = 6^\circ$	141
Fig. 6.41 Wall Shear contours and surface stream lines at $\alpha = 28^\circ$	142
Fig. 6.42 Wall Shear contours and surface stream lines at $\alpha = 32^\circ$	142
Fig. 7.1 Definition of the parameter A_o/A_i , and values at take-off and approach. (Seddon, 1993).	144
Fig. 7.2 Non-axisymmetric input inlet geometry. (Andreoletti, 2007).....	145
Fig. 7.3 Wall shear at the nacelle keel lip. Starting geometry(left), reduced separation geometry (right).	145
Fig. 7.4 Operational engine influence on the pressure distribution of the wing (left) and flap (right). (Rohlmann, 2012)	146
Fig. 7.5 Through-Flow Nacelle geometry (right) and mesh (left). Note the slat cut.	146
Fig. 7.6 High-lift engine-airframe geometry.	147
Fig. 7.7 Wing surface mesh refinement at the wing/pylon junction.	147
Fig. 7.8 Lift polar for the WB and WBNP configurations.	148
Fig. 7.9 Drag polar for the WB and WBNP configurations.	149
Fig. 7.10 Numerical pressure tap rows position WBNP and WB (values of η).	150
Fig. 7.11 WB and WBNP configurations slat pressure coefficient at $\eta = 0.45$, $\alpha = 6^\circ$	150

Fig. 7.12 Wing and flap WB and WBNP configurations pressure coefficient at $\eta = 0.45$, $\alpha = 6^\circ$	150
Fig. 7.13 WB and WBNP configurations slat pressure coefficient at $\eta = 0.45$, $\alpha = 21^\circ$	151
Fig. 7.14 Wing and flap WB and WBNP configurations pressure coefficient at $\eta = 0.45$, $\alpha = 21^\circ$	151
Fig. 7.15 Wing and flap WB and WBNP configurations pressure coefficient at $\eta = 0.50$, $\alpha = 6^\circ$	151
Fig. 7.16 Wing and flap WB and WBNP configurations pressure coefficient at $\eta = 0.50$, $\alpha = 21^\circ$	152
Fig. 7.17 WB and WBNP configurations slat pressure coefficient at $\eta = 0.60$, $\alpha = 6^\circ$	152
Fig. 7.18 Wing and flap WB and WBNP configurations pressure coefficient at $\eta = 0.60$, $\alpha = 6^\circ$	152
Fig. 7.19 WB and WBNP configurations slat pressure coefficient at $\eta = 0.60$, $\alpha = 21^\circ$	153
Fig. 7.20 Wing and flap WB and WBNP configurations pressure coefficient at $\eta = 0.60$, $\alpha = 21^\circ$	153
Fig. 7.21 Iso-vorticity surfaces (756 s^{-1}) with underlined high lift installation vortices at an AOA of 17°	156
Fig. 7.22 Iso-vorticity surfaces (756 s^{-1}) with underlined high lift installation vortices at an AOA of 10°	157
Fig. 7.23 Iso-vorticity surfaces (756 s^{-1}) with underlined high lift installation vortices at an AOA of 17°	157
Fig. 7.24 High incidence effects on the nacelle, slat and wing flows. (3D streamlines at an AOA of 21°)	158
Fig. 7.25 Iso-vorticity surfaces (756 s^{-1}), velocity curl X contours and underlined nacelle vortex at an AOA of 10°	159
Fig. 7.26 Velocity swirling normal, velocity vortex field and underlined slat gap vortices at an AOA of 10°	159
Fig. 7.27 Velocity swirling normal, velocity vortex field and underlined pylon vortex at an AOA of 17°	160
Fig. 7.28 Velocity swirling normal, 3D streamlines and underlined leading edge vortex at an AOA of 17°	160
Fig. 7.29 Vortices size and intensity at different AOA (756 s^{-1} iso-vorticity surfaces and velocity curl X contours)	161

Fig. 7.30	WBNP wall shear and surface stream lines, $\alpha = 10^\circ$	162
Fig. 7.31	WBNP wall shear and surface stream lines, $\alpha = 21^\circ$	163
Fig. 7.32	WBNP wall shear and surface stream lines, $\alpha = 24^\circ$	163
Fig. 7.33	Installation vortices (Von Geyr, 2007).	164
Fig. 7.34	Evaluation of vortex generation. (Rohlmann, 2012).	164
Fig. 7.35	Nacelle chine profile.....	166
Fig. 7.36	Maximum lift chine positioning. ϑ and χ are the positioning parameters. (Kanazaki, 2008).....	166
Fig. 7.37	Chine longitudinal angle.....	167
Fig. 7.38	Single nacelle chine installation.	168
Fig. 7.39	Double chine installations. (Left WBNP2CS, Right WBNP2C2).....	168
Fig. 7.40	Mesh refinement on the chine wake.....	169
Fig. 7.41	Lift polar for the clean wing (WB), the engine installed (WBNP), the engine installed with one chine (WBNPC) and the two engine installed with two chines (WBNP2CS and WBNP2C2).....	170
Fig. 7.42	Single chine configuration (WBNPC) vortex path (velocity swirl normal and shear stress at 21°).	170
Fig. 7.43	Two-chines configuration (WBNP2CS) chines vortices paths (velocity swirl normal and shear stress at 22°).....	171
Fig. 7.44	Two-chines configuration (WBNP2C2) chines vortices paths (velocity swirl normal and shear stress at 22°).	171
Fig. 7.45	Two-chines configurations (WBNP2CS and WBNP2C2) installation vortices (velocity swirl normal and shear stress).	172
Fig. 7.46	Shear stress contours at 21° , 22° and 23° (streamlines/shear stress).	173
Fig. 7.47	WBNP and WBNP2C2 wing pressure coefficient at $\eta = 0.45$, $\alpha = 22^\circ$	174
Fig. 7.48	WBNP and WBNP2C2 wing pressure coefficient at $\eta = 0.6$, $\alpha = 22^\circ$	174
Fig.A.1	Shock (red) and viscous (grey) volume selection for DLR-F6 WB....	201
Fig.A.2	Shock volume selection for DLR-F6 WBNP-TF configuration	202
Fig.A.3	Mid-field results for DLR-F6 WB configuration	203
Fig.A.4	Mid-field results for DLR-F6 WBNP configuration	203

Fig.A.5	<i>Mid-field</i> installation Drag polar DLR-F6 configuration	204
Fig.A.6	Mid-field/Near-Field mesh size sensibility for DLR-F6 WB configuration	204
Fig.A.7	Mid-field/Near-Field mesh size sensibility for DLR-F6 WBNP configuration.....	204
Fig.A.8	Shock volume selection for CRM WBNP-PO configuration.	206

LIST OF TABLES

Table 1.1 Net Propulsive Force for an isolated nacelle on a one stream engine	16
Table 2.1 Grid characteristics for WBNP and WB configurations.....	35
Table 3.1 Engine Performance Data	57
Table 4.1 AC S/R – Geometric dataset (mm). (Longeville, 2007; Andreoletti, 2007).....	70
Table 4.2 IC S/R Geometric dataset. (Longeville, 2007; Andreoletti, 2007).....	71
Table 4.3 IC L/R Propulsion system geometry. (Longeville, 2007; Andreoletti, 2007).....	72
Table 4.4 AC S/R Engine performance data, part I (Longeville, 2007; Andreoletti, 2007).....	72
Table 4.5 AC S/R Engine performance data, part II. (Longeville, 2007; Andreoletti, 2007).....	73
Table 4.6 IC S/R Engine performance data, part I (Longeville, 2007; Andreoletti, 2007).....	73
Table 4.7 IC S/R Engine performance data, part II. (Longeville, 2007; Andreoletti, 2007).....	74
Table 4.8 IC L/R X and Y engine positions	77
Table 4.9 AC S/R X and Y engine positions	78
Table 5.1 AC S/R X and Y	110
Table 6.1 Hybrid grid sizes.....	127
Table A.1 <i>Mid-field/Near-Field</i> Drag CRM WB configuration	205
Table A.2 <i>Mid-field/Near-Field</i> Drag CRM WBNP-PO configuration.....	205
Table A.3 <i>Mid-field/Near-Field</i> Installation Drag CRM configuration.....	206

LIST OF EQUATIONS

(1.1).....	1
(1.2).....	1
(1.3).....	1
(1.4).....	10
(1.5).....	11
(1.6).....	11
(1.7).....	11
(1.8).....	12
(1.9).....	12
(1.10).....	13
(1.11).....	13
(1.12).....	13
(1.13).....	13
(1.14).....	13
(1.15).....	14
(1.16).....	14
(1.17).....	14
(1.18).....	14
(1.19).....	15
(1.20).....	15
(1.21).....	16
(1.22).....	16
(1.23).....	16
(1.24).....	16
(1.25).....	16
(1.26).....	16
(1.27).....	16
(1.28).....	16

(1.29).....	17
(1.31).....	17
(1.32).....	17
(1.33).....	17
(1.34).....	17
(1.34).....	17
(1.35).....	18
(1.37).....	18
(1.38).....	18
(1.39).....	18
(1.40).....	18
(1.41).....	18
(1.42).....	18
(1.43).....	19
(1.44).....	19
(2.1).....	39
(3.1).....	55
(3.2).....	56
(3.3).....	56
(3.4).....	58
(3.5).....	59
(3.6).....	61
(3.7).....	61
(6.1).....	140
(7.1).....	165
(A.1).....	196
(A.2).....	196
(A.3).....	196
(A.4).....	196

(A.5)	197
(A.6)	197
(A.7)	197
(A.8)	197
(A.9)	197
(A.10)	198
(A.11)	198
(A.12)	198
(A.13)	198
(A.14)	198
(A.15)	199
(A.16)	199
(A.17)	199
(A.18)	199
(A.19)	200
(A.20)	200

NOMENCLATURE

a	Speed of Sound
A_0	Flow Area at Upstream Position
A_H	Intake Highlight Area
A_{HL}	Nacelle Sectional Area at the Lip
A_{TH}	Nacelle Throat Area
c	Mean Aerodynamic Wing Cord
C_D	Drag Coefficient
C_{Di}	Induced Drag Coefficient
$C_{D,int\ Nac}$	Internal Nacelle Drag
$C_{D-install}$	Installation Drag Coefficient
C_{DNF}	Near-field Drag Coefficient
C_{DTOTMF}	Mid-field Total Drag Coefficient
C_{Dv}	Viscous Drag Coefficient
C_{Dw}	Shockwave Drag Coefficient
C_L	Lift Coefficient
C_{LMAX}	Maximum Lift Coefficient
C_M	Momentum Coefficient
C_{MFinst}	Mid-Field Installation Drag
C_{NFinst}	Near-field Installation Drag
C_p	Pressure Coefficient
C_{ref}	Reference Cord
C_{sp}	Spurious Drag Coefficient
d	Diameter
D	Drag
D_{AF}	Afterbody Drag
$D_{\Delta s}$	Entropy Drag
D_{FO}	Forebody Drag
$D_{FO,datum}$	Datum Forebody Drag
D_i	Induced Drag
D_{MAX}	Nacelle Maximum Diameter
$D_{nacelle}$	Nacelle Drag
D_{WB}	Drag Calculated in the WB Configuration

$D_{WBNP@TFN}$	Drag Calculated in the WBNP with TFN Configuration
$D_{WBN@PO}$	Drag Calculated in the WBNP with PO Configuration
ds	Elemental Surface Area
D_{spill}	Spillage Drag
D_{sp}	Spurious Drag
D_v	Viscous Drag
D_w	Shockwave Drag
D_9	Nacelle Diameter at the Outlet
eta	Ratio of y Position and Wing Span
F_G	Gauge Stream Force
F_{G0}	Gauge Stream Force at Pre Far-field Section
F_{G1}	Gauge Stream Force at Engine Inlet
F_{G9}	Gauge Stream Force at Engine/Fan Outlet
F_{G00}	Gauge Stream Force at Post Far-field Section
F_{G91}	Gauge Stream Force at Hot-end Outlet
F_N	Standard Net Thrust
F'_N	Overall Net Thrust
F_N^*	Corrected Net Thrust
$F_{N,int}$	Intrinsic Net Thrust
F_{shock}	Shockwave Non-dimensional Factor
F_{visc}	Viscous Non-dimensional Factor
F_∞	Far-field Non-dimensional Factor
g	Gravitational Acceleration
G_{R1}	Mesh Grow Rate in the Viscous Layer
G_{R2}	Mesh Grow Rate outside the Viscous Layer
g/c	Nominal Flap Gap Cord Parameter
h	Clearance Between Wing and Nacelle
H	Clearance Between Wing and Nacelle Parameter (Rossow, 2002)
h/c	Clearance Between Wing and Nacelle Parameter
H_G	Maximum Chine Height
K_{vsc}	Cut-off Parameter
L	Lift
L_{WB}	Lift Calculated in the WB Configuration
$L_{WBNP@PO}$	Lift Calculated in the WBNP with PO Configuration

L_{aft}	Nacelle Afterbody Length
L_G	Overall Chine Length
L_f	Nacelle Forebody Length
M	Mach Number
\mathbf{n}	Normal
N	Number of Mesh Cells
o/c	Nominal Flap Overlap Cord Parameter
p	Pressure
P_0	Total Pressure
p_∞	Far-field Pressure
p_{pot}	Pressure for a Potential Flow
p/P_0	Pressure Parameter
q	Kinetic Energy
Q	Flow Parameter
Re	Reynolds Number
R_{HL}	Radius of the Nacelle Sectional Area at the Lip
R_{TH}	Radius of the Nacelle Throat Area
S_{body}	Surface of the Body
S_{far}	Far-field Surface
T	Temperature
T_u	Normalized Turbulence Intensity
u	X Velocity Component
V_j	Jet Velocity
V_o	Flight Velocity
V	Velocity
\mathbf{V}	Velocity Vector
V_∞	Far-field Velocity
v	Y Velocity Component
w	Z Velocity Component
W	Mass Flow
x	Axial Coordinate
x/c	Along the Wing Position Parameter
x/l	Along the Wing Position Parameter II (Rudnik and Rossow 2002)
x/X	Along Forebody Position Parameter

X_F/C	Engine Position Parameter
y	Vertical Coordinate
Y	Nacelle Maximum Diameter and Throat Diameter Parameter
Y^+	Dimensionless Wall Distance
α	Angle of Attach
β_c	Nacelle Boat-tail Angle
γ	Heat Capacity Ratio
Δ_1	First Layer Distance (Mesh)
$\Delta C_{D,inst}$	Installation Drag
$\Delta C_{D,G}$	Global Powerplant Installation Drag
$\Delta C_{D,jet}$	Jet Drag
$\Delta\vartheta$	Chine Incidence Angle
η_{prop}	Propulsive Efficiency
η_{th}	Thermal Efficiency
η_{tot}	Total Efficiency
θ	Vertical Chine Positioning Parameter
θ_{TR}	Taper Ratio
ϑ	Local Surface or Streamtube Angle
μ_l	Laminar Viscosity
μ_t	Eddy Viscosity
Λ	Aspect Ration
ρ	Density
τ_W	Local Shear Stress
φ_{LE}	Leading Edge Angle
ϕ	Force Acting on a Solid or Streamtube Surface
ϕ_{AF}	Afterbofy Force
$\phi_{AF,pot}$	Potential Flow Afterbody Force
ϕ_{CB}	Centrebody Force
ϕ_{cowl}	Cowl Force
ϕ_{FO}	Forebody Force
$\phi_{FO,datum}$	Datum Forebody Force
$\phi_{FO,pot}$	Potential Flow Forebody Force
$\phi_{nacelle}$	Nacelle Force
$\phi_{nacelle,pot}$	Potential Flow Nacelle Force

ϕ_{plug}	Plug Force
ϕ_{post}	Post-exit Force
ϕ_{pot}	Potential Flow Force Acting on a Solid or Streamtube Surface
ϕ_{pre}	Pre-entry force
$\phi_{pylon-scrub}$	Jet Scrubbed Pylon Force
χ	Horizontal Chine Positioning Parameter
Ω	Flow Domain
Ω_{sp}	Spurious Volume
Ω_v	Viscous Volume
Ω_w	Shockwave Volume

LIST OF ABBREVIATIONS

AB	After Body
AC	Active Core
AC S/R	Active Core Short Range
AOA	Angle Of Attack
AST	Advanced Subsonic Technology
CAD	Computer Aided Design
CB	Centre Body
CFD	Computational Fluid Dynamic
CRM	Common Research Model
DP	Design Point
DPW	Drag Prediction Workshop
EAS	Equivalent Air Speed

HBR	High Bypass Ratio
HP	High Pressure
HPC	High Pressure Compressor
HPT	High Pressure Turbine
HPSI	High lift PSI
IC	Intercooled Core
IC L/R	Intercooled Core Long Range
IPC	Intermediate Pressure Compressor
IPT	Intermediate Pressure Turbine
IP	Intermediate Pressure
LP	Low Pressure
LPT	Low Pressure Turbine
MK	Mark
MFR	Mass Flow Ratio
NEWAC	New Aero Engine Core Concepts
NPF	Net Propulsive Force
NPR	Nozzle Pressure Ratio
OP	Off Design Point
PSI	Propulsion System Integration
PWT	Pressure Wind Tunnel
RANS	Reynolds Averaged Navier-Stokes
SST	Shear Stress Turbulence
TAS	True Air Speed
TERA2020	Techno-economic Environmental and Risk Assessment for 2020
TET	Turbine Entry Temperature
UHBR	Ultra High Bypass Ratio
VHBR	Very High Bypass Ratio
WB	Wing and Body Configuration
WBNP	Wing Body Nacelle Pylon Configuration
WBNPC	Wing Body Nacelle Pylon Chine
WBNP2CS	Wing Body Nacelle Pylon 2 Symmetric Chines
WBNP2C2	Wing Body Nacelle Pylon 2 Chines
WP	Work Package

THESIS STRUCTURE

The thesis starts with an introduction to the Propulsion System Integration (PSI). An overview of the aerodynamics involved with the engine-airframe integration is given. The main design parameters and non-aerodynamic constraints are presented to underline the multidisciplinary character of PSI. Guidelines for the aerodynamic interference estimation and thrust and drag bookkeeping are given to correctly evaluate and account for the effects related to the engine installation.

The subsequent section is about modelling the PSI at cruise condition using Computational Fluid Dynamic (CFD). It is focused on the evolution of the methodologies with examples coming from past projects, giving examples of different computational methodologies with their advantages and drawbacks. A CFD calculation example is also described, where installation effects are evaluated using the DLR-F6 geometries. The numerical results were compared with experimental data of a wing and body and wing body and nacelle

configurations. This was also meant to be a validation of the numerical code used during this project

The core of this research project is described in chapter 3. The development of a PSI module for the in-house performance codes, Hermes and Turbomatch, is discussed in detail. The applied process for generating nacelle geometries and install them on a modern air liner is also defined.

Chapter 4 presents results at cruise condition for two Very-High-Bypass-Ratio new aero engines, defined in the NEWAC project.

Moving to high lift flight condition, because of the complexity of the problem, requires a detailed description of the aerodynamic effects and modelling, involved in this important phase of the project. Chapter 6 starts with a literature review of the high angle of attack flow, and ends with the engine integration effect on flight performances. Results from recent research projects are presented, underling the importance of future research to fill the knowledge gap in this area. The NASA Trap Wing is used to validate the CFD model at high angle of attack and to understand the flow physics

A high-lift PSI application is presented in chapter 7, where a very high bypass ratio engine is installed under the NASA Trap Wing to evaluate the aerodynamic effects. A topological study of the high-lift installation vortices is presented. The effects of the nacelle chine on the maximum lift are also evaluated due to its strong influence and to set up a benchmark for future work on aerodynamic optimization.

The thesis ends with the main conclusions and future work.

1 PROPULSION SYSTEM INTEGRATION

INTRODUCTION

The present economic situation increases the pressure on commercial aviation companies to reduce the Direct Operating Cost, and the environmental legislation require a new generation of aircraft with a lower environmental impact. Therefore, engine and aircraft manufactures, research centres and universities are making great efforts to reduce the drag of the complete aircraft and thereby to achieve lower fuel consumption. For the engine, the achievement of this objective requires an increase of the total efficiency of the current power plant. The latter is defined in eq. 1.1:

$$\eta_{tot} = \eta_{prop} \times \eta_{th} \quad (1.1)$$

$$\eta_{th} = \frac{\text{Jet Kinetic Power}}{\text{Fuel Power}} = \frac{V_j^2 - V_0^2}{FAR \times FHV} \quad (1.2)$$

$$\eta_{prop} = \frac{\text{Thrust Power}}{\text{Jet Kinetic Power}} = \frac{2}{1 + \frac{V_j}{V_0}} \quad (1.3)$$

We can see that from a thermal point of view (eq. 1.2) the efficiency can be maximized by reducing the fuel-to-air ratio and the fuel heating value and increasing the jet velocity (V_j). However from eq. 1.3 it can be noted that this velocity increase negatively influences the propulsion efficiency, increasing the ratio of jet velocity over flight velocity (V_0).

These conflicting requirements can be met by employing large mass flows and modest jet velocities by increasing the bypass ratio. In a conventional configuration this means an increase of engine diameter and therefore a closer aerodynamic interaction between the propulsion system and the aircraft. As the early wing mounted installations of High Bypass Ratio (HBR) engines allowed a certain distance from the wing, avoiding excessive drag penalties, now with the increase in size, passing from HB to Very High (VHBR) or Ultra High Bypass Ratio (UHBR), it is necessary to position engines closer to the wing in order to both maintain the current ground clearance and to avoid extending the already heavy main landing gear legs. The potential fuel reduction of these engines must take in count the installation penalties, this leads to the need to study and understand the effects of wing-mounted engine installations. The dimensions of VHBR or UHBR made necessary to design installations within the typical boundary, indicated by empirical law and previous studies (Berry, 1994; Lednicer et al, 1994; Mogilka, 1994). These lead to an exploration of new domain and a movement from a “flange-to-flange” perspective to an integrated design. The fuel burn reduction for the mid-decade projects will have to be around 15-17% and up 25% by 2025, to meet the ACARE objectives. A good integration that manages the aircraft’s energy demands while minimising the weight and drag, is essential. Steve Walter, president of Nexcelle, a partnership between GE and Safran, one of the leaders on integration, said: “GE Aircraft Engines spends billions of dollars to get a point of efficiency. For pretty nominal non-recurring costs for the development of an Integrated Propulsion System, you can get multiple points of fuel efficiency”. Looking at all of these aspects suggests that the Propulsion System Integration (PSI) can be an interesting research topic and can heavily contribute to reduce the environmental impact.

During a debate in the Royal Aeronautical Society in London, Mr L F Nicholson (Nicholson, 1957), stated that “[...] the performance of the integrated engine/airframe, when operated in a designed combination, is significantly different from the sum of the individual engine and airframe performance “. “[...] the aircraft cannot be conceived first and the propulsive units can be considered afterwards“. Nicholson’s argument, which still holds today, is the basis of what

we mean by engine/airframe integration. The PSI takes in count the distinction between the uninstalled performances, given by the engine manufacturers and the installed performances, as placing the engine within the airframe inevitably induces forces on the external surfaces that increase the total drag. This substantial difference, including the nacelle drag, can be around 8% of the total performance (Pate, 1997); giving to the PSI a fundamental position in a successful design since the early stage of the project is to avoid loss in time, manpower and performance. The PSI requires a multi-disciplinary approach, including aerodynamics, propulsion, structure, noise and systems. This multi-disciplinary characteristic and the intrinsic need to work with two “systems”, airframe and engine, require a relationship between different departments of a company, and on a larger scale, a strong interaction between the normally distinct engine and airframe companies

1.1 AERODYNAMICS OF PSI

The aerodynamic jet engine integration, the main subject of this project, includes the design of elementary PSI components like inlet, fan cowl, nozzle, mixer (for mixed flow engine), plug and thrust reverser and their connection to create the nacelle, in order to install the engine on the aircraft. The first phase of the integration includes the design of the individual components necessary for the integration to achieve good aerodynamic performance of the engine during all the conditions an aircraft can encounter during its life. The second step is to integrate them in order to get a nacelle that will permit the engine to obtain its required performance. The last phase is the real integration that takes to consideration not only the design of the nacelle, allowing further modifications, but also the modification of the airframe's shape. For the conventional transport aircraft, engine wing-mounted or aft-fuselage-mounted, this phase is also characterized by the engineering of the connection element between the nacelle and the airframe: the pylon. It is important to remember that the design of an integrated propulsion system requires adjustments of the single component not only in the first phases but also in the last where the performance of the whole aircraft can be evaluated. A bad installation can increase the total drag by about

2% (Pate, 1997), which in a long range aircraft represent one thousand kilograms of pay load. A critical aspect of advanced subsonic transport aircraft design is the minimization of adverse interference in junction regions between major components of the vehicle, such as the wing/pylon and the nacelle/pylon (Gea et al, 1994). The principal flow phenomena of this adverse interference for a conventional turbofan in cruise condition can be summarized as:

1. On the upper wing surface, the presence of the engine changes the location of the stagnation point on the wing, reducing the flow incidence near the junction of the wing and the pylon, causing an upstream movement of the shock front (fig.1.1). Given that most of the flow on the upper surface of the wing is supersonic, the disturbance caused by the presence of the engine will propagate along flow characteristics (Rossow, 1992). The reduction of incidence causes also an increase of pressure level at the suction plateau (Rossow, Godard et al, 1994).
2. On the lower surface the main effect is due to the creation of a virtual channel between the inboard side of the pylon and the airframe, causing an acceleration of the flow (fig.1.2). This phenomenon can cause the coincidence of the pressure recovery on the wing lower surface and the adverse pressure gradients in the rear part of the pylon, causing flow separation (Rossow and Hoheisel, 1994). Another effect of this flow acceleration is the buffeting, a shock boundary layer interaction phenomenon that causes shock wave oscillation and subsequent oscillation of lift and pitching moment (Kumano, 2006). The buffeting, in transonic regimes, is one of the major limiting factors for the cruise speed. Further outboard, the influence of the propulsion system on the lower wing almost vanish. Given that the streamlines of a swept wing are not straight lines but curved, the propulsion system distorts the inboard streamlines compressing them and thus the flow is accelerated, on the other hand the streamlines are widening and the velocity is reduced (Rossow 1994).
3. Blowing drag or jet effect is typical of an underwing engine installation and it is due to a reduction in wing circulation as the jet induces a higher

velocity counter to the direction of the natural circulation. Additional losses are incurred if the jet-induced velocity exceeds sonic levels considerably creating strong shocks and possibly flow separation (Berry, 1994).

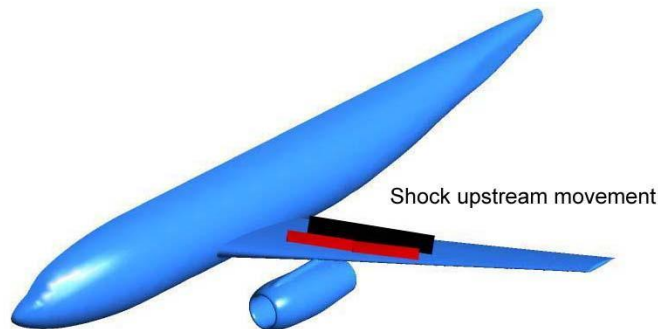


Fig. 1.1 Installation effects on the upper surface of the wing

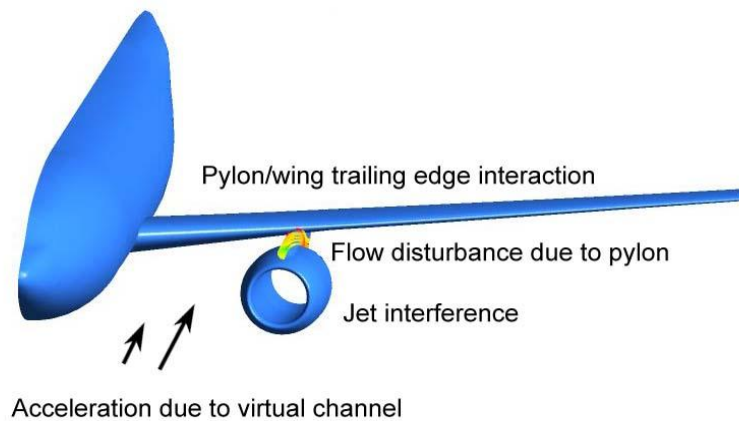


Fig. 1.2 Installation effects on the lower surface of the wing

At high angle of attack the flow is characterized by different features, and not only the intensity of these installation effects varies, but additional aerodynamic interactions take place. Due to the complexity of the problem, to understand the engine-airframe interaction at high angle of attack, it is necessary to introduce the high-lift aerodynamics. Therefore the discussion is postponed to Chapter 5, focused on the part of the project dedicated to this flight condition.

1.2 DEGREE OF FREEDOM

The main parameters that control these interference phenomena are:

1. Engine position: fore/aft, up/down, span wise positioning, pith angle, toe angle. (fig.1.3)

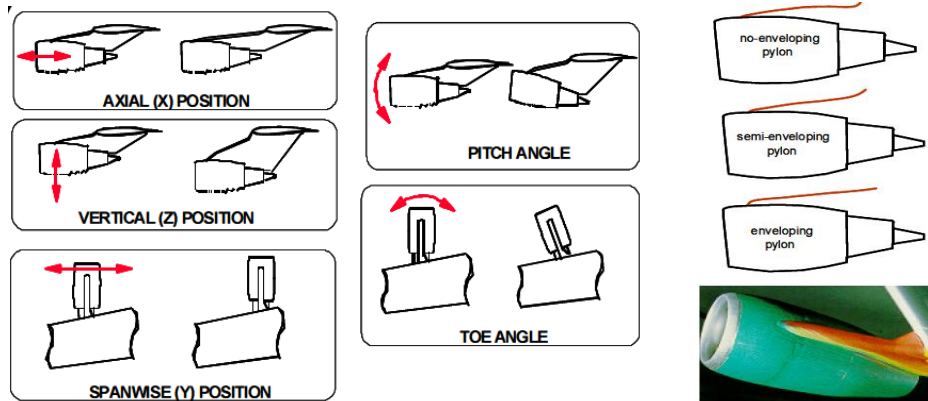


Fig. 1.3 Degrees of Freedom in PSI: Engine Position and Pylon Shape. (Rivoire, 2007)

The reduction of vertical distance leads to a more upstream shift of the shock wave on the upper wing surface (Rudnik at al, 2002). On the lower wing surface the flow is less accelerated when moving the engine closer to the wing. Concerning the lift distribution, these two effects counter-balance each other: the loss of lift due to the upstream shift of the shock is compensated by the pressure gain on the lower surface leading to a less marked deterioration of the wing aerodynamic (Rossow and Hoheisel, 1994). On the other hand the horizontal positioning strongly affects the overall wing performance, in particular moving the engine downstream influences the upper wing surface as the shock moves also downstream, with a strong loss of lift on the inboard portion of the wing. The spanwise position influences mainly the lower surface, changing the shape of the virtual channel between the inboard side of the pylon and the airframe causing a more accelerated flow in the case of an inboard position. The pitch angle influences both wing sides changing the total drag and also the lift, taking also in count that the thrust vectoring creates a thrust component in the lift direction.

The jet effect is also strongly influenced by the pitch angle as positive increase, nose up, reduces the influence on the wing (Mogilka et al, 1994; Rossow, 1992). Toe angle, like the spanwise position, changes the shape of the virtual channel influencing mainly the lower surface.

2. Pylon and nacelle shapes.

References (Rossow, 1992) and (Rudnik, 2002) show that about half of the overall lift loss can be attributed to the pylon shapes affecting the lower wing pressure distribution. This is because the pylon shape controls the acceleration on the virtual channel. Another important factor is the intersection with the fan cowl as the flow tends to stagnate on it and subsequently accelerate over the top of the structure reaching, in some cases, supersonic velocity. To mitigate this phenomenon we can operate on both nacelle and pylon shapes (Berry, 1994).

3. Wing shape

The sections of wing can be locally modified to avoid the installation suction peaks typical of the engine/airframe integration reducing the lift loss in correspondence of the pylon, in both of its sides (Oliveira, 2003).

1.3 CONSTRAINTS

It is important to remember that every potential configuration must satisfy aerodynamic criteria for take-off, cruise descent and engine-inoperative conditions. The external flow on the nacelle and pylon varies widely with the engine flow, speed and angle of attack, as the shape of the captured stream tube change with these flying conditions. The stream tube passes from a large section during take-off, with a stagnation point near the lip and therefore low external velocities on the cowl, to a reduced section in the windmill condition. As power is reduced, the stagnation streamlines moves inside the lip requiring the uncaptured flow to accelerate around the lip. The windmill condition, or engine-inoperative condition, is characterized by high velocity and gradients on the external lip that can cause flow separation.

In a twin-engine aircraft the ETOPS requirements for cruise with a failed engine at high speed for a long time, makes the engine-inoperative condition one of the more stringent.

A good PSI must also take into account non-aerodynamic constraints, which are characteristics of a multi-disciplinary design. One of most stringent and important constraint concerns the space allocation for the various systems that connect the engine and the airframe (like fuel, electricity, air and hydraulic supply – see fig 1.4). Given that we must take also in count the vital system safety, it can be seen from fig. 1.5 that the position of the engine is limited in a range to avoid a possible damage of vital systems or for safety reasons of the passengers (FAR/JAR 25.903).

Another constraint can be the spray ingestion from landing gear, given that we must avoid ingestion of great quantity of water or debris during the landing (fig. 1.6). Another safety requirement concerns the emergency evacuation, and in particular the escape slide development (fig. 1.7). Looking from an operational point of view the access of the ground service equipment and maintenance affects the engine position relative to the doors and the wing (fig. 1.8). An important and stringent constrain is the ground clearance especially in the case of a collapsed nose gear and in cross wind landing (fig.1.9).

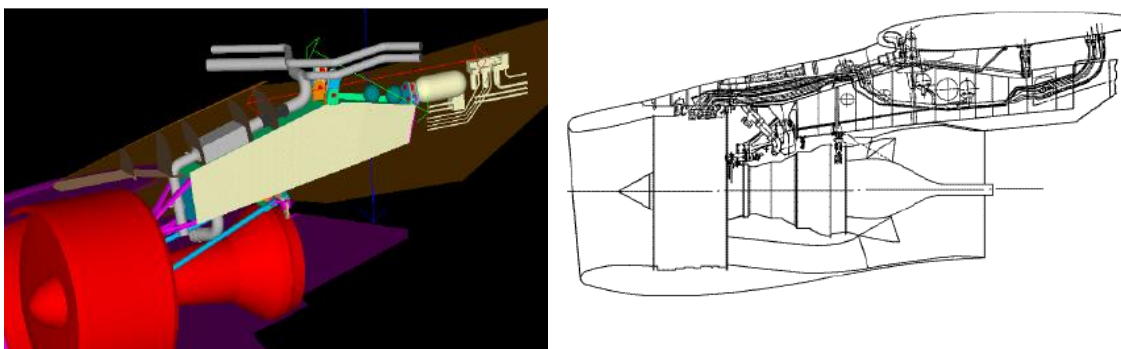


Fig. 1.4 Systems allocation constraint: example of fuel, air, oil and electrical systems layout. (Rivoire, 2007).

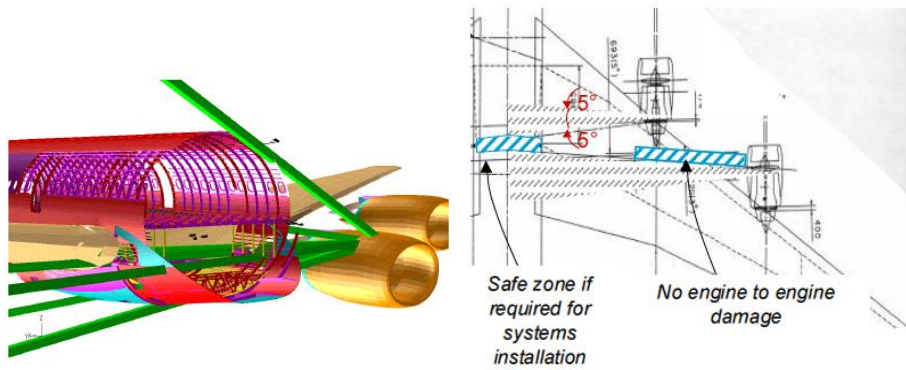


Fig. 1.5 Vital system safety constraint: example of blade-off constrains. The green zones are possible blade-off paths (left) and the blue striped zones are safe zones (right). (Rivoire, 2007).



Fig. 1.6 Spray ingestion from landing gear constraint: example of an engine injection test. (Rivoire, 2007).

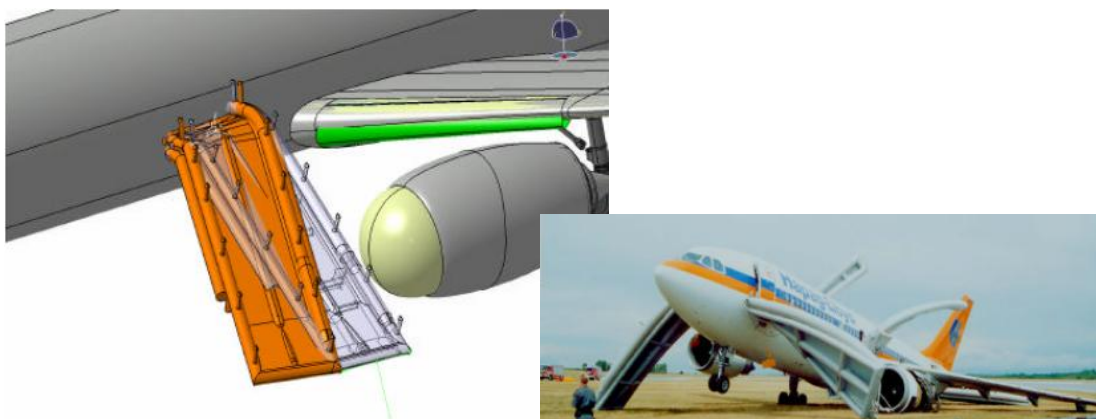


Fig. 1.7 Escape slide zone constraint: example of an engine slide collision simulation (left) and real case (right). (Rivoire, 2007).

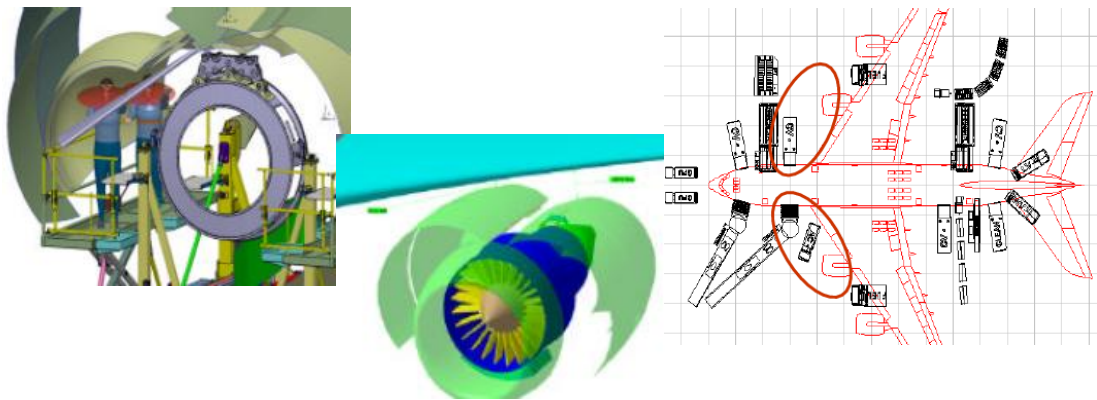


Fig. 1.8 Operational constraints: example of an engine maintainability simulation (left and centre) and access to cargo doors (right). (Rivoire, 2007).

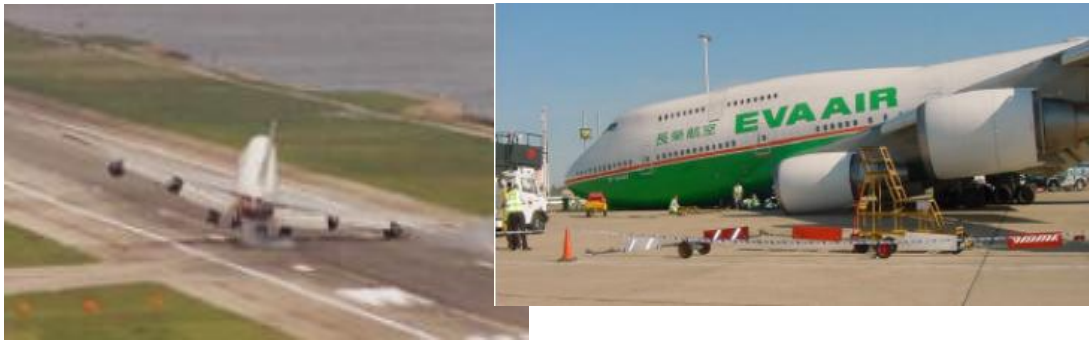


Fig. 1.9 Ground clearance constraint: example of cross wind extreme landing configuration (left) and collapse of front landing gear maintaining intact the engines (right). (Rivoire, 2007).

1.4 AERODYNAMIC INTERFERENCE EVALUATION

The aerodynamic phenomena typical of PSI can be quantified by an aerodynamic interference evaluation. This consists in an evaluation of the drag/lift losses associated to the installation of the engine, and a thrust evaluation. The global powerplant installation drag ($\Delta C_{D,G}$), can be split in two components: the installation drag ($\Delta C_{D,inst}$) and the jet drag ($\Delta C_{D,jet}$) (Tinoco, 2001):

$$\Delta C_{D,G} = \Delta C_{D,inst} + \Delta C_{D,jet} \quad (1.4)$$

The installation effect takes in to account the first two phenomena and can be evaluated by subtracting the drag calculated in the WB configuration (D_{WB}) from the drag in the WBNP with through flow nacelle ($D_{WBNP@TFN}$).

In this configuration, the engine flow is not simulated and the flow just moves along the empty nacelle: Through Flow Nacelle (TFN) (Von Geyr, 2005).

$$\text{INSTALLATION EFFECT: } D_{WBNP@TFN} - D_{WB} \quad (1.5)$$

The jet effect, or blowing drag, can be evaluated subtracting the drag calculated for the WBNP at TFN condition, from the drag calculated in the WBNP at Power-On (PO) condition ($D_{WBNP@PO}$) (Berry, 1994; Von Geyr, 2005):

$$\text{JET EFFECT: } D_{WBNP@PO} - D_{WBNP@TFN} \quad (1.6)$$

The lift loss can be quantified by subtracting the lift calculated in WBNP at PO condition ($L_{WBNP@PO}$) from the lift in WB configuration (L_{WB}):

$$\text{LIFT LOSS: } L_{WB} - L_{WBNP@PO} \quad (1.7)$$

Experimentally the drag and the lift are evaluated by investigating isolated and integrated engines driven by compressed air: Turbine Power Simulators (TPS) in a wind tunnel facility. Wind tunnel investigations are however rather complex and expensive. Therefore numerical methods are increasingly gaining attention. The evaluation of thrust needs particular attention and we must set up a correct thrust and drag book-keeping.

1.5 NET PROPULSIVE FORCE: THRUST AND DRAG BOOK-KEEPING

The simple proposition that thrust is the force applied by the propulsion system to the airframe is not helpful since a significant part of the total thrust can be distributed over the airframe surfaces external to the engine, causing a possible confusion with the drag.

Considering a ducted body, gas turbines fall in this category, we can divide the flow in internal, flow that goes through the engine, and external, flow that doesn't go through the engine (fig.1.10), both of infinite extent.

The internal flow is contained in a pre-entry streamtube extending from upstream of the body and terminating in a circular stagnation region near the nose of the intake, and a post-exit streamtube originating at the nozzle exit and extending to infinity downstream of the body (fig.1.10).

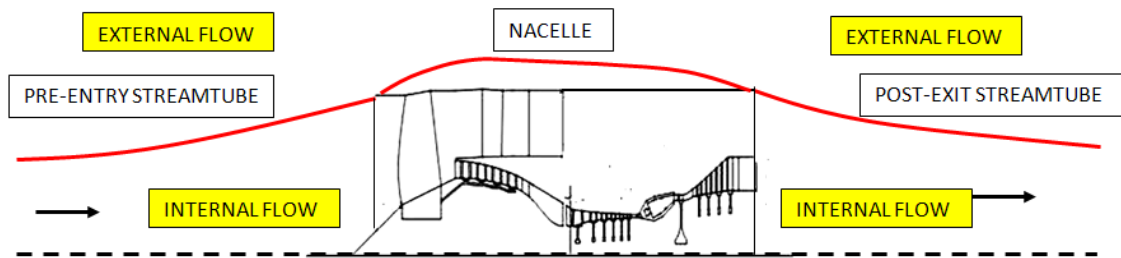


Fig. 1.10 Schematic of the ducted body flows.

We can now give a rigorous definition of thrust as the summation of the forces acting on the internal surfaces of the engine nacelle and pre-entry and post-exit streamtubes from minus to plus infinity; and the drag as the summation of the forces acting on the external surfaces of the engine nacelle and pre-entry and post-exit streamtubes from plus to minus infinity.

Referring to figure 1.11, representing a streamtube, we can define ϕ , the force acting on a solid or streamtube surface, as the sum of the integrated pressure and shear stress:

$$\phi = \int_{surface} (p - p_{\infty}) \sin\vartheta ds + \int_{surface} \tau_w \cos\vartheta ds \quad (1.8)$$

Where ϑ is the local surface or streamtube angle

ds is the elemental surface area

τ_w is the local shear stress ($\tau_w = 0$ in the absence of a solid surface: streamtube)

As the streamwise projected surface area is $dA = \sin\vartheta ds$, we can write:

$$\phi = \int_{surface} (p - p_{\infty}) dA + \int_{surface} \tau_w \cot\vartheta dA \quad (1.9)$$

Defining a potential flow as a flow with no skin friction, $\tau_w = 0$, we can write the relative potential force as:

$$\phi_{pot} = \int_{surface} (p_{pot} - p_{\infty}) dA \quad (1.10)$$

Where p_{pot} is the pressure field at a no skin friction condition.

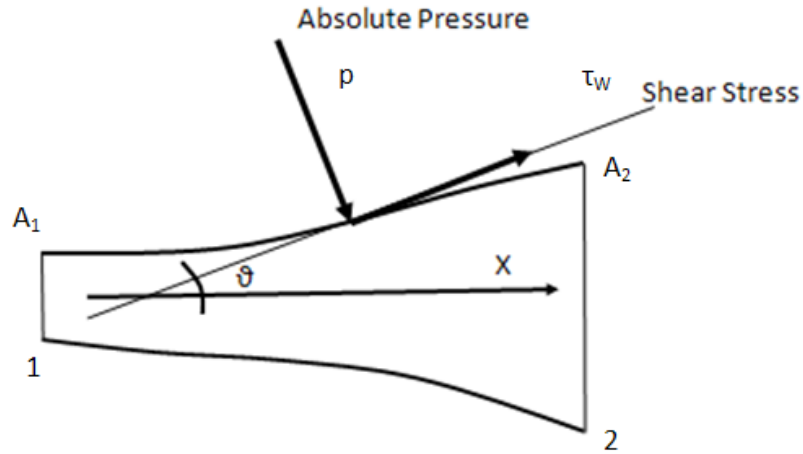


Fig. 1.11 Forces on a streamtube.

Having described the force on a streamtube, referring to figure 1.12, we can now define the drag of a ducted body as:

$$D = \phi_{pre} + \phi_{nacelle} + \phi_{post} \quad (1.11)$$

From the Prantl/d'Alembert paradox (Williams, 2009), applying eq.1.10, we obtain:

$$\phi_{pre} + \phi_{nacelle,pot} + \phi_{post} = 0 \quad (1.12)$$

Hence from eq.1.11 and 1.12:

$$D = \phi_{nacelle} - \phi_{nacelle,pot} \quad (1.13)$$

From eq.1.9 the force on the nacelle can be expressed as:

$$\phi_{nacelle} = \int_{nacelle} (p - p_{\infty}) dA + \int_{nacelle} \tau_w \cot \vartheta dA \quad (1.14)$$

Hereafter:

$$D = \int_{nacelle} (p - p_{pot})dA + \int_{nacelle} \tau_w \cot\theta dA \quad (1.15)$$

These equations provide the basic definition of drag applicable to a nacelle and show the fundamental relationship between the drag and the nacelle force. It is only in specific circumstances that these are equal; in particular this will be the case when the pre-entry and post-exit streamtubes have both constant areas (Williams, 2009).

The thrust can be determined by applying eqn. (1.9) on the internal surfaces of the nacelle duct, but the normally complex duct shape, including the interior of the engine, makes this an impossible task and it is necessary to adopt an alternative approach using Newton's second and third laws.

The force on a fluid is equal to the time rate of change of linear momentum, defining the general equation for the absolute gauge stream force F_G as:

$$F_G = WV + (p - p_\infty)A \quad (1.16)$$

From the third law, the force exerted by the walls of a streamtube can be expressed in terms of the stream forces F_1 and F_2 , at the entry and exit sections of the tube (fig.1.11). This force is called the intrinsic net thrust, and is represented by the equation:

$$F_{N,int} = F_{G2} - F_{G1} \quad (1.17)$$

Applying these equations to an isolated nacelle (fig.1.12); the nacelle intrinsic net thrust can be determined as:

$$F_{N,int} = F_{G9} - F_{G1} \quad (1.18)$$

Using different thrust interfaces, it is possible to calculate other net thrusts, in particular the standard net thrust and overall net thrust. These will be presented later.in table 1.1

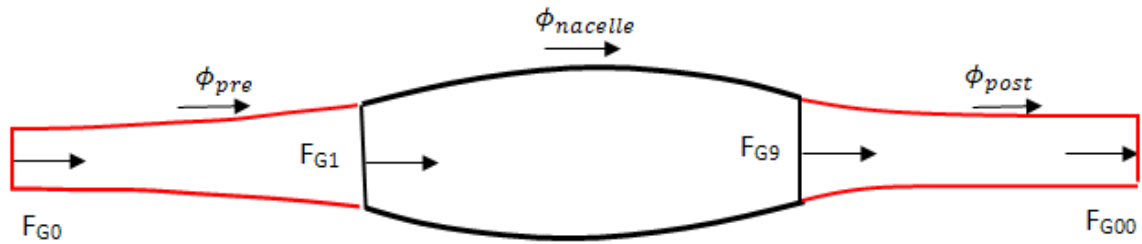


Fig. 1.12 Forces stations definition on an isolated nacelle.

Now that we have defined the thrust and the drag in order to comply with the thrust and drag book-keeping (MIDAP, 1979), it is important to define an additional force: the Net Propulsive Force (NPF). This is the force exerted by the powerplant to the airplane purged of nacelle force. This force represents the real interface between the engine and the airplane, and is different from the net thrust due to the presence of the nacelle, and pylon in the case of installed nacelle, and their interference effects. It is therefore important when assessing the engine-airframe integration effects, to evaluate this force in order to correctly capture the installation effects.

From figure 1.12 and eqn.1.18:

$$NPF = (F_{G9} - F_{G1}) - \phi_{nacelle} \quad (1.19)$$

From eqn. (1.11), (1.12), (1.13) and (1.19) we obtain:

$$NPF = (F_{G00} - F_{G0}) - D_{nacelle} \quad (1.20)$$

We can see from the last two equations the difference between the two alternative approaches; one accounting for the force and the other that considers the drag.

This demonstrates the importance of a consistence book-keeping system to avoid the overlooking or double counting of any components. A good book-keeping system must conform to the following requirements (MIDAP, 1979):

- Free from ambiguity
- So far as possible provide for the separate study of engine and airframe performance by the respective manufacturers, both in

preliminary paper projects and in any subsequent model and/or flight testing.

- Include clear definition of the interfaces where engine and airframe responsibilities meet, and facilitate a proper understanding of any zones where responsibilities overlap.

Table 1.1 show the different interface choices and the relative NPF.

Net Thrust Definition	Accounting System	Net Propulsive Force	Eq. Number
Intrinsic Net Thrust $F_{N,int} = F_{G9} - F_{G1}$	Force Drag	$F_{N,int} - \phi_{nacelle}$ $F_{N,int} + \phi_{pre} + \phi_{post} - D_{nacelle}$	(1.21)
Standard Net Thrust $F_N = F_{G9} - F_{G0}$	Force Drag	$F_N - \phi_{nacelle} - \phi_{pre}$ $F_N - \phi_{post} - D_{nacelle}$	(1.22)
Overall Net Thrust $F'_N = F_{G00} - F_{G0}$	Force Drag	$F'_N - \phi_{pre} - \phi_{post} - \phi_{nacelle}$ $F'_N - D_{nacelle}$	(1.23) (1.24)

Table 1-1 Net Propulsive Force for an isolated nacelle on a one stream engine

The pre-entry and post-exit forces introduced above are throttle-dependent as they depend on the operating flow condition.

We can express it applying the second's Newton law, obtaining:

$$\phi_{pre} = F_{G1} - F_{G0} \quad (1.25)$$

$$\phi_{post} = F_{G00} - F_{G9} \quad (1.26)$$

Considering the forebody as a semi-infinite body, we can write from Prandtl/d'Alembert :

$$\phi_{pre} + \phi_{FO,pot} = 0 \quad (1.27)$$

The forebody drag will be:

$$D_{FO} = \phi_{FO} - \phi_{FO,pot} \quad (1.28)$$

Hence:

$$D_{FO} = \phi_{pre} + \phi_{FO} \quad (1.29)$$

The forebody drag will be equal to the to the forebody force only if $\phi_{pre} = 0$, and it is the case A_0/A_I of = 1.

Where A_0 is the flow area at the upstream position, and A_I is the intake highlight area. The condition of $A_0/A_I = 1$ is called datum condition (Seddon, 1993). The datum forebody drag will be:

$$D_{FO,datum} = \phi_{FO,datum} \quad (1.30)$$

When $A_0/A_I < 1$ we can define an inlet spillage drag, or additive drag as:

$$D_{spill} = D_{FO} - D_{FO,datum} \quad (1.31)$$

The Inlet spillage can be used in NPF relations in the drag accounting form.

As we look to the afterbody we can write:

$$\phi_{post} + \phi_{AF,pot} = 0 \quad (1.32)$$

And the drag will be:

$$D_{AF} = \phi_{AF} - \phi_{AF,pot} \quad (1.33)$$

When the integral of static-pressure on the post-exit streamtube would be zero, $\phi_{post} = 0$, the afterbody drag will be equal to the afterbody force, and can be achieved only when the local static pressure in the external flow at station 9 appear to be equal to the ambient pressure. In this case the most important parameter is the Nozzle Pressure Ratio (NPR).

Looking for a more complex case of a turbofan with no mixed flow (fig.1.13), we can write the NPF as:

$$NPF = (F_{G9} + F_{G91} - F_{G1}) - \phi_{nacelle} \quad (1.34)$$

Where:

$$\phi_{nacelle} = \phi_{CB} + \phi_{cowl} + \phi_{AB} + \phi_{plug} \quad (1.35)$$

With AB = After-Body, CB = Centre-Body (Midap, 1979).

Therefore eqn. (1.34) become:

$$NPF = F_{N,int} - \phi_{plug} - \phi_{AB} - \phi_{CB} - \phi_{cowl} \quad (1.36)$$

Applying the momentum conservation in the pre-entry streamtube we obtain:

$$\phi_{pre} = (F_{G1} - F_{G0}) + \phi_{CB} \quad (1.37)$$

From the definition of Standard Net Thrust:

$$F_N = F_{N,int} + F_{G1} - F_{G0} = F_{N,int} + \phi_{pre} - \phi_{CB} \quad (1.38)$$

We can rewrite the NPF in terms of standard net thrust:

$$NPF = F_N - \phi_{plug} - \phi_{AB} - \phi_{pre} - \phi_{cowl} \quad (1.39)$$

And in a drag accounting system with a corrected net thrust:

$$F_N^* = F_N - \phi_{plug} - \phi_{AB} \quad (1.40)$$

$$NPF = F_N^* - D_{nac} - \phi_{post} \quad (1.41)$$

The equations developed are for an isolated nacelle, and when we take in to account an installed nacelle additional consideration must be made to consider the interference effect.

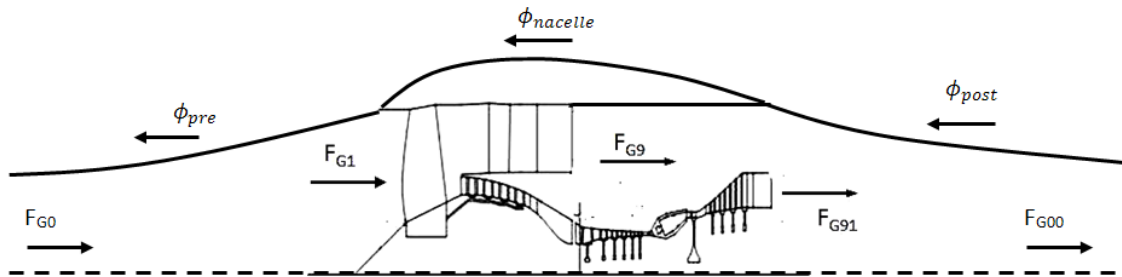


Fig. 1.13 Forces stations definition on a Turbofan.

The force acting on the part of the pylon scrubbed by the jet-exhaust must be accounted in the NPF relation, obtaining:

$$NPF = F_N - \phi_{plug} - \phi_{AB} - \phi_{pylon-scrub} - \phi_{pre} - \phi_{cowl} \quad (1.42)$$

Or for in the case of drag accounting with the same NPF equation, eq.1.40, the corrected net thrust, eq.1.41, becomes:

$$F_N^* = F_N - \phi_{plug} - \phi_{AB} - \phi_{pylon-scrub} \quad (1.43)$$

2 CFD & PSI MODELLING

The demand of high efficiency engine-airframe integration has considerably grown in the last decades. The present economic situation increases the pressure on commercial aviation companies to reduce the Direct Operating Cost, and the environmental situation require a new generation of aircraft with a lower environmental impact. On the other hand the increased complexity of these new configurations requires new, expensive and complicated design techniques. To face this problem it is necessary to look at alternative tools that reduce the necessary time and costs to perform a reliable design evaluation.

The aerodynamics beyond the PSI is one of the more complicated to model, given that it involves the simulation of the aircraft and the engine flow. The level of detail of the model should be kept as high as possible to capture all the aerodynamic features, keeping in mind the importance of reducing engineering costs.

This is one of the reasons that brought the use of CFD into the PSI project, for the fact that engine-airframe integration by wind tunnel test is particularly expensive in time and resources (Burgsmueller and Szodruch, 1985). Moreover the use of CFD also allows the exploration of unconventional designs, pushing the boundaries of PSI. However, as pointed out in reference (Gacherieu, 2000), the current level of fidelity of CFD doesn't grant a total replacement of the experimental work with the numerical techniques.

Recent improvements have considerably increased the computational capabilities, nevertheless in order to correctly evaluate the PSI effects it is essential to perform high fidelity CFD simulations of the whole aircraft, including the engines. This is a lengthy and computational expensive task. For these reasons, even if CFD is fully integrated in the design process, it's not replacing the experimental tests, like the experimental tests, don't replace flight campaigns. The present role of numerical aerodynamics is mostly to reduce the time spent in the wind tunnel and the number of tests.

Consequently the design process can be summarized as (fig.2.1):

- Aerodynamic shape definition using CAD.
- CFD analysis of the Flow and geometry optimization.
- Wind tunnel tests of the most promising configurations.
- Flight tests.

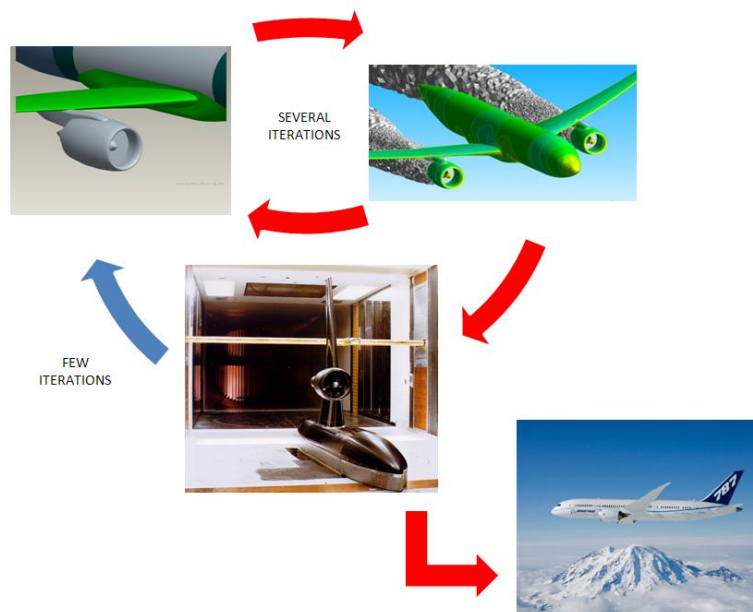


Fig. 2.1 PSI design process. (Central figure: Brodersen (2002), figure at the bottom courtesy of the Boeing Company)

The use of CFD to assist the design of engine installation began decades ago, following the development of the numerical aerodynamics. It started with the earlier linear potential methods, fully-potential and then the boundary-layer prediction methods, mostly to design isolated nacelle geometries (Lynch, 1994;

Rubbert, 1983). However, there have been several cases where these linear methods significantly under predicted supersonic flow regions, especially when applied to nacelle/pylon/wing installations (Rubbert, 1983, Maskew, 1981). Figure 2.2 shows typical panel models used to numerically represent high-bypass ratio turbofans nacelle and flow-through wind tunnel representation of turbofan (Clark, 1984).

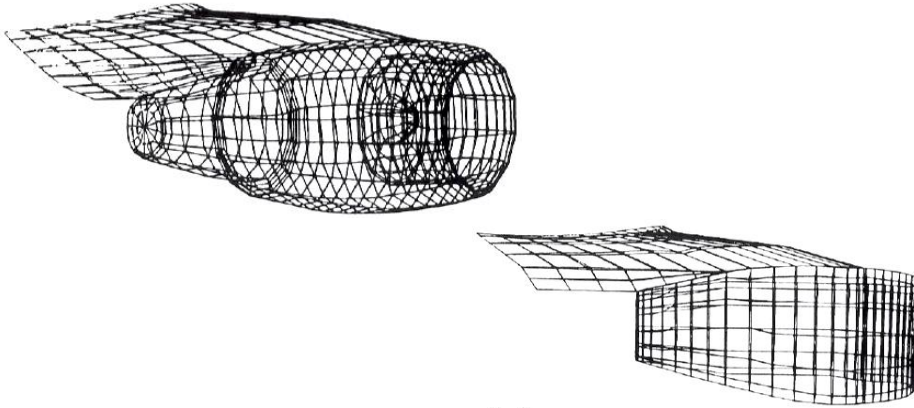


Fig. 2.2 Panel model of high-bypass-ratio engines. (Clark, 1984)

Figure 2.3 shows the difference between the experimental and numerical pressure calculated with a second order panel method (Clark, 1984). The results are extracted from the nacelle forebody at a flying Mach number of 0.6. Even if the numerical results follow the experimental trend, the peak at the nacelle forebody is underpredicted.

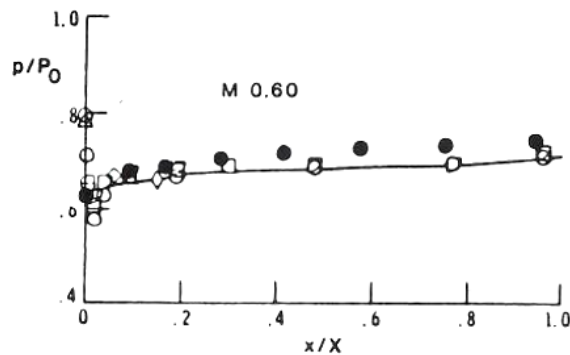


Fig. 2.3 Nacelle forebody experimental (white dots) and numerical (black dots) pressure parameter (normalized to the Total Pressure P_0) function of horizontal position parameter (x/X). x axial coordinate, X forebody length. (Clark, 1984)

Studies like the ones presented in reference (Atkins, 1991) and (Lednicer, 1994), even if they show reasonably good results, they underline the importance of solving accurately phenomena like viscous effects and shock boundary layer interactions, to properly capture the PSI aerodynamics. Figure 2.4 shows the differences between the numerical and experimental results using the Euler method presented in reference (Naik and Chen, 1992).

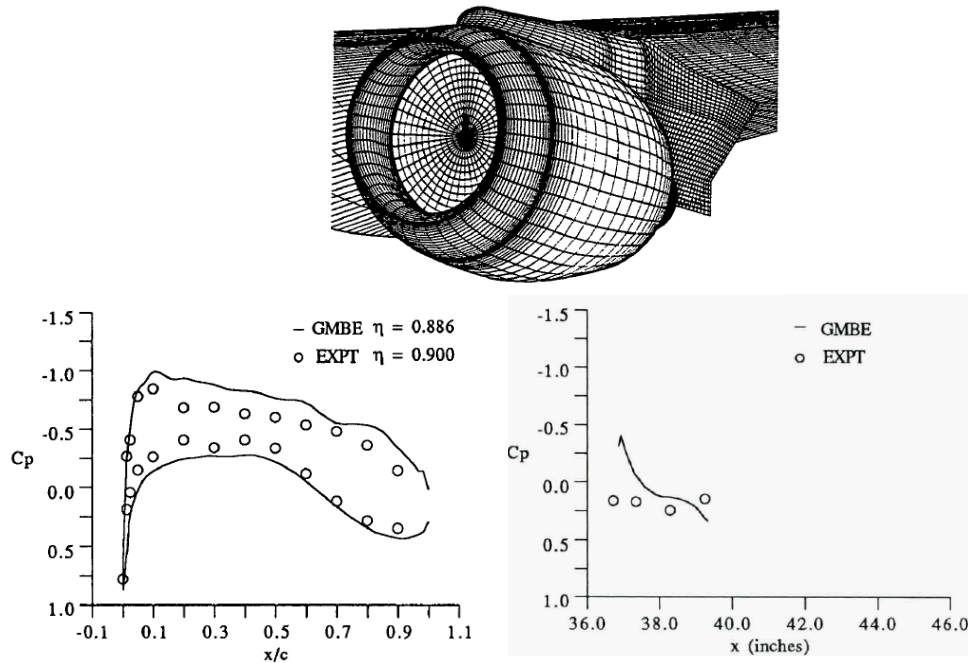


Fig. 2.4 Euler structured grid (top), exp. and numerical Cp at the wing (left) and nacelle (right). (Naik and Chen, 1992).

Therefore the next upgrade, with the advance of CFD, was the use of Navier-Stokes methods. An example of the prediction improvement using Navier-Stokes methods compared to Euler methods and Euler methods coupled with a 3D boundary layer code is represented in figure 2.5 (Rudnik and Rossow, 2002). It is possible to see that the Euler computation tends to over predict the pressure due to the missing effects of the boundary layer. The shock on the upper surface is shifted downstream compared to the numerical results, creating a bigger expansion on the second half of the wing surface. The second approach is an Euler method coupled with a 3D boundary layer code that allows calculating the displacement thickness applied to the model due to the viscous effects.

This approach improves the prediction of the shock position and reduces the over predicted expansion after the shock. However it can be seen that the pressure coefficient is better captured with the solution obtained from the RANS equations.

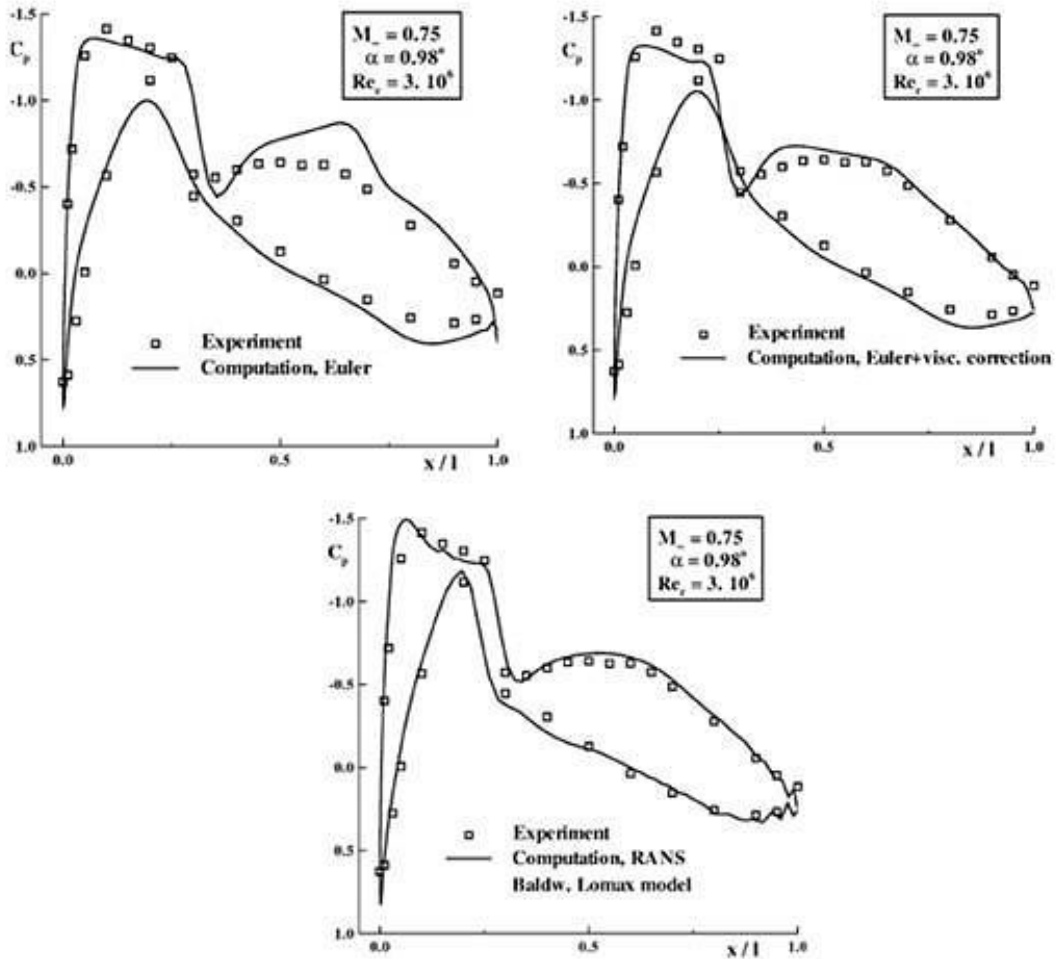


Fig. 2.5 Numerical and experimental pressure coefficient computed using different numerical approaches. (Rudnik and Rossow, 2002).

The high viscous-unviscous interaction flow characteristic of high-lift flow, it is even more sensitive to the computational method, therefore to capture the effects of PSI for high-lift configurations it is even more necessary to use the RANS equations (Van Dam, 2002). For more details see chapter 5.

Despite the improvement on the quality of the results, the computational effort increases considerably, going from a nominal value of 1 for the Euler method and 3 for the Euler-3D layer method to 10 for the Navier-Stokes.

For this reason early applications were confined to relatively simple geometries and coarse meshes. Reference (Gea, 1994) underlines the difficulties on generating an appropriate grid system for both capture the viscous effects, and allow to perform calculations in a reasonable computational time.

With the fast increase of computational resources, nowadays it is possible to perform calculations with realistic configurations in cruise and high-lift conditions, with an improved quality of results. Figure 2.6 shows examples of different engine-airframe configurations solved using RANS methods.

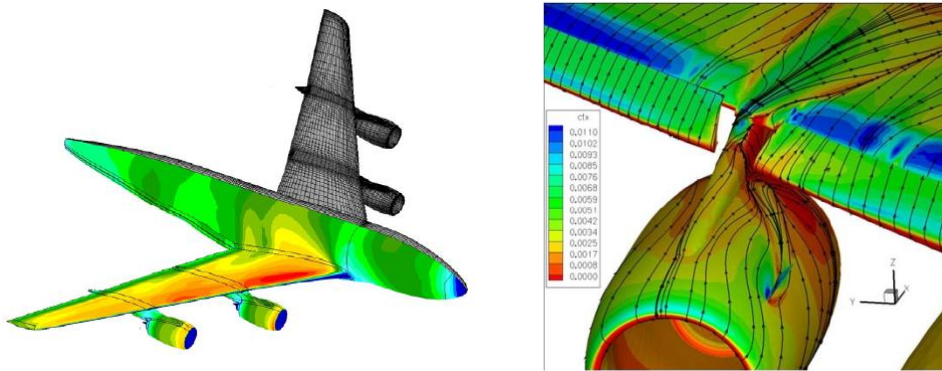


Fig. 2.6 Engine-airframe configurations solved using RANS methods. (Rudnik and Geyr, 2007).

These capabilities allows for the investigation of new engine integration design as pointed out in Lynch (1994). Due to the increase in size, passing from HB to UHBR engines, it is necessary to position engines closer to the wing in order to both maintain the current ground clearance and to avoid extending the already heavy main landing gear legs. Figure 2.7 is the classic guide to nacelle positioning, (on the x axis the horizontal position and on the y the vertical) showing the region where past designs were confined. It also possible to notice few new designs, where a more close coupled integration is allowed by a reduction of interference effects, applying CFD methodologies (Rudnik and Ronzheimer, 1992).

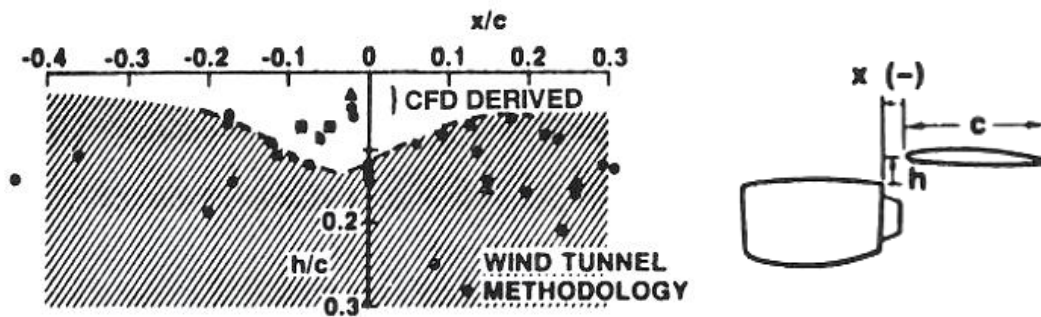


Fig. 2.7 Engine-airframe configurations boundaries. (Rudnik and Ronzheimer, 1992).

The dimensions of VHBR, or UHBR made it necessary to design installations within this typical boundary. These lead to an exploration of new domain and the use of CFD can guarantee a more efficient and vast design evaluation. It was therefore decided to apply CFD in order to evaluate the installation penalties as function of engine position. Few previous published studies present results extracted from CFD investigations, but none of them is focused on the variation of NPF in the range of BPR presented in this study. In the subsequent paragraphs an overview of these studies are presented.

Brodersen et al. (2002) performed a numerical and experimental study to investigate the engine installation drag as a function of position. The comparison of the drag polar of three different configurations is presented in figure 2.8, where it is possible to notice that the numerical results are in good agreement with the experiments.

The results show that the “best” engine position is the one far from the airframe (CFM-L-3), and the influence of the vertical position is by far less important (difference between CFM-L-2 and CFM-L-3). The paper points out that based on computational results three nacelle positions were chosen for experimental verification, reducing the design cost.

Another relevant research was performed by the German Aerospace Centre DLR, where the influence of increasing the engine size, with related engine position, was investigated (Rudnik and Rossow, 2002). In particular a VHBR engine, with a bypass ratio of 9.2, was used to perform an engine position study.

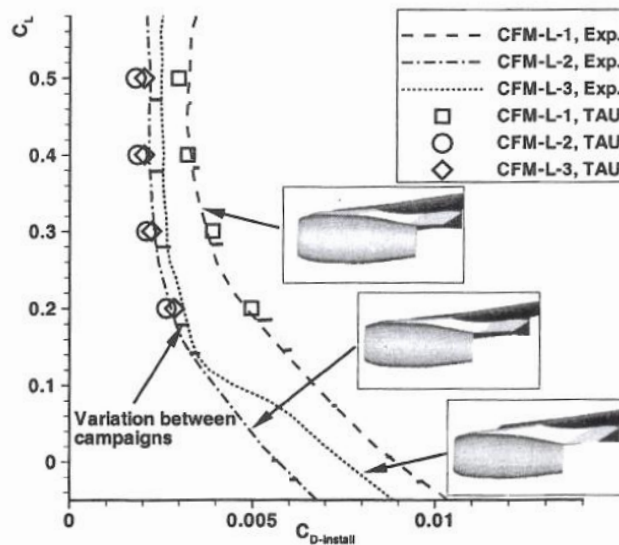


Fig. 2.8 Measured and calculated drag polar for different engine positions. (Brodersen, 2002)

The engine was moved vertically (H) and horizontally (X_F/c), within the conventional design boundary (fig. 2.9), to determine the variation of the installation drag with the engine position. H and X_F/c are the same parameters defined in figure 2.7 respectively as h/c and x/c . Figure 2.9 shows the four different configurations evaluated in terms of vertical and horizontal position. The results, computed with an Euler method coupled with a 3D boundary layer code, are shown in figure 2.10, 2.11 and 2.12.

It is possible to see that the reduction of vertical distance results in an upstream shift of the upper wing shock, with a reduction of the lift. However the reduction of vertical clearance causes a much more coupled interaction between the engine flow and the under wing aerodynamics, that results in an increase of pressure level and therefore lift, matching the reduction on the upper surface. These counter balancing effects reduce the vertical positioning influence on the lift and drag (Rudnik and Rossow, 2002). Looking at the horizontal positioning influence it can be seen that moving the engine downstream (from 3 to 4 fig. 2.9) will result on a downstream shift of the shockwave on the upper wing, that in a way is relaxing the engine influence on the wing pressure field.

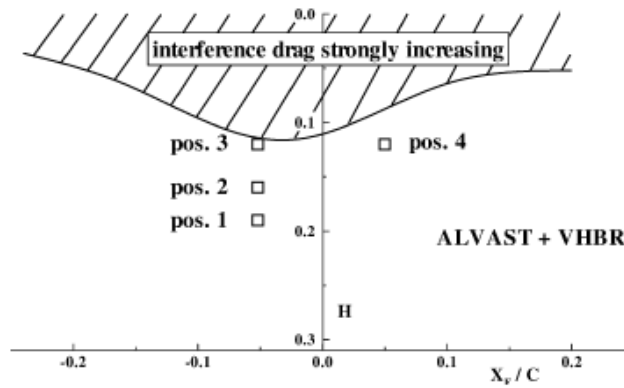


Fig. 2.9 Engine position variation. (Rudnik and Rossow, 2002).

However positioning the engine closer to the wing will strongly affect the pressure field on the wing surface. This is due to the reduction of the cross section of the channel between the engine, wing and fuselage, which will increase the flow speed in the inboard side of the pylon. This influence can be clearly seen in figure 2.11, where the pressure coefficient variation is much more pronounced compared to figure 2.10. Figure 2.12 shows the influence of the horizontal engine position on the spanwise pressure coefficient distribution. Even if almost the entire wing pressure field is affected by the engine installation positioning, it can be easily seen that the inboard side presents the widest variation of pressure coefficient between the four engine positions.

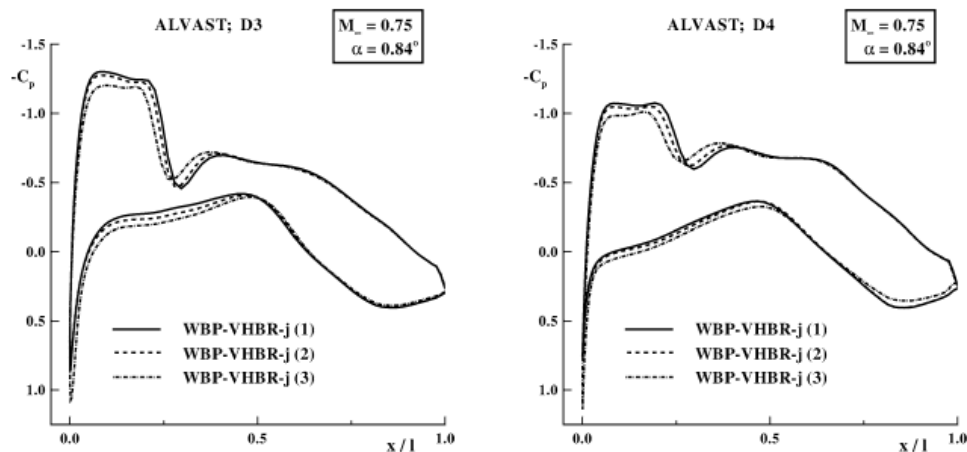


Fig. 2.10 Influence of vertical engine position (configurations 1, 2 and 3 fig. 2.12) on pressure coefficient. D3 inboard section, D4 outboard section (Rudnik and Rossow, 2002).

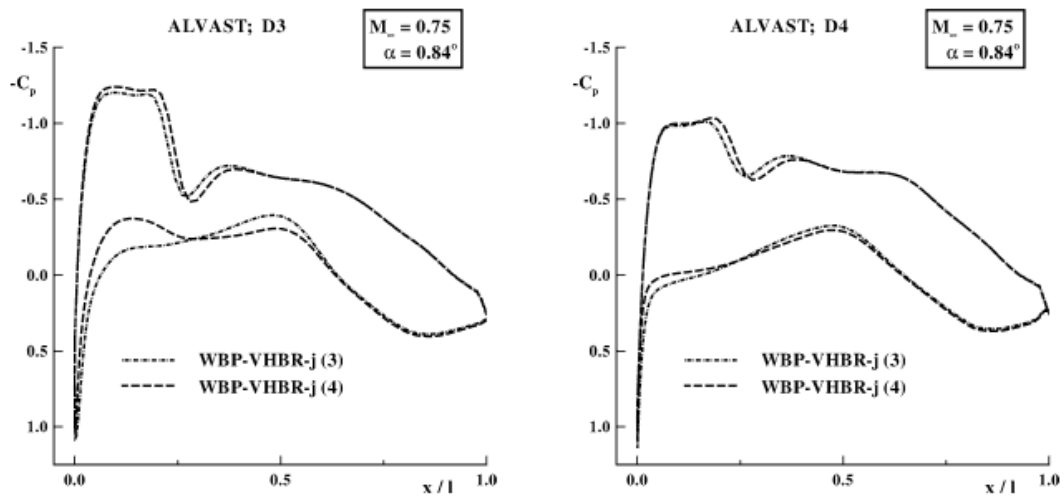


Fig. 2.11 Influence of horizontal engine position (configurations 3 and 4 fig. 2.12) on pressure coefficient. D3 inboard section, D4 outboard section (Rudnik and Rossow, 2002).

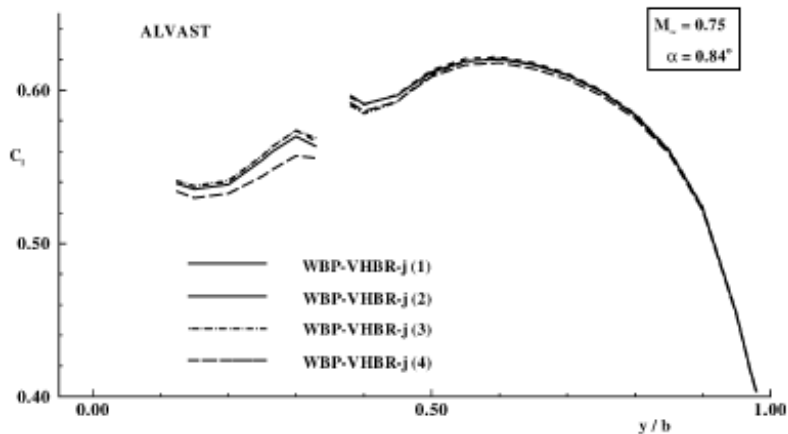


Fig. 2.12 Influence of engine position (configurations 1, 2, 3 and 4 fig. 2.12) on spanwise lift distribution. (Rudnik and Rossow, 2002).

A parametric analysis of different nacelle positions was also performed using the DLR-F6 geometry (De Souza, 2008). The results are similar to the ones presented in Brodersens' work. However given that the lift coefficient wasn't kept constant in all the calculations, the results should be considered only as a reference for future work.

Oliveira (2003) shows the results of another numerical study where the nacelle position was changed both horizontally and vertically, also mentioning the concept of suction peaks.

These peaks are due to the interaction with the jet and wing and pylon that creates pressure fluctuations on the lower wing surface (Harris et al, 1995). This is due to the high velocity of the gas expelled from the engine that affects the circulation around the wing. Figure 2.13 gives a graphical explanation of the peaks and shows the pressure coefficient of the wing next to the engine.

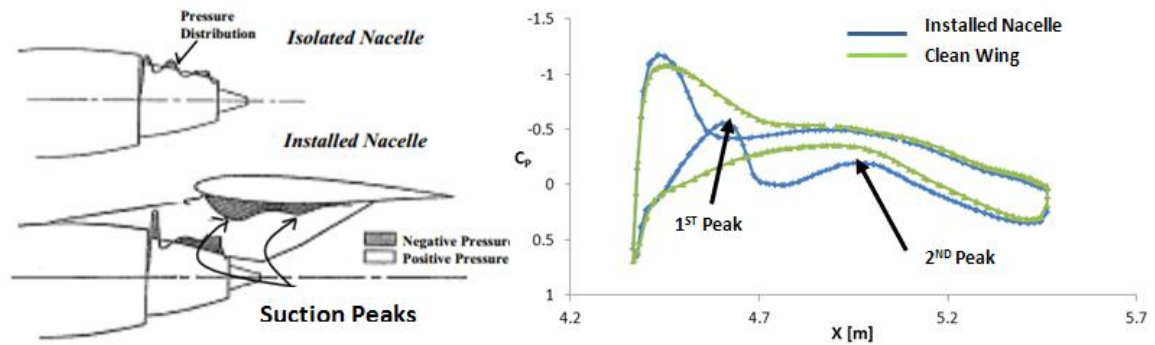


Fig. 2.13 Pressure peaks (left figure: Harris, 1995).

The pressure coefficient suction peaks as function of the engine positions are displayed in figures 2.14 and 2.15, confirming that the nacelle positioning is more sensitive to horizontal than vertical displacement.

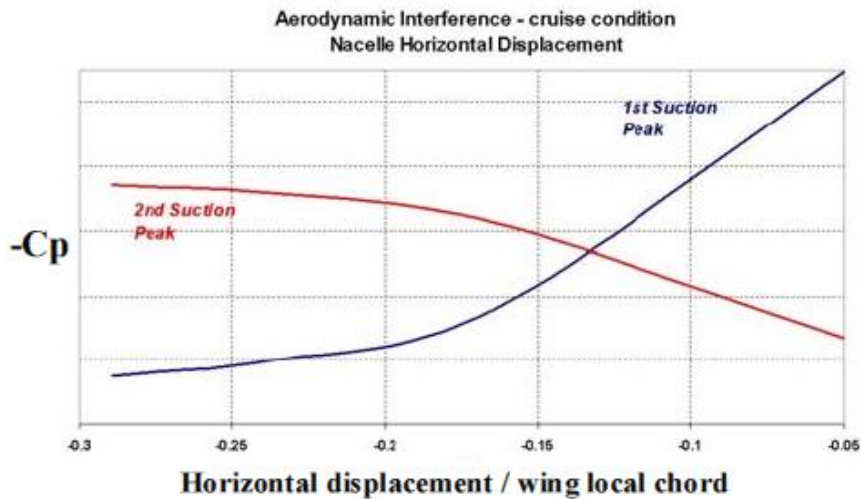


Fig. 2.14 Wing pressure coefficient peaks values near the pylon function of horizontal engine position. (Oliveira, 2003).

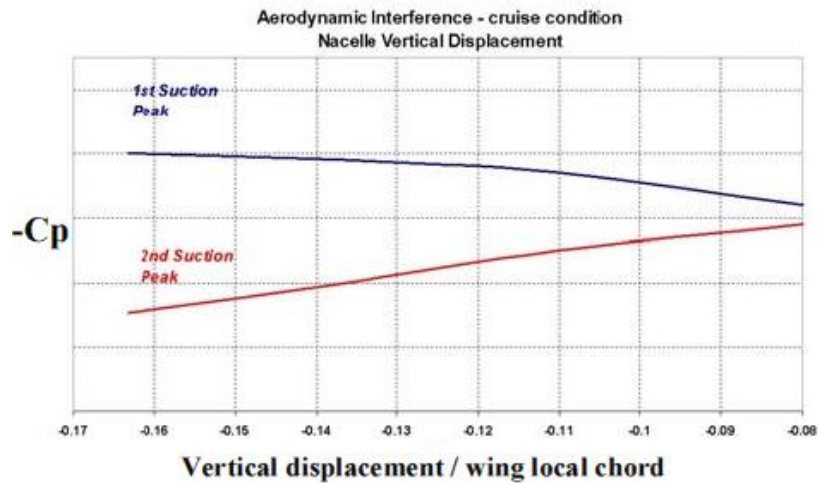


Fig. 2.15 Wing pressure coefficient peaks values near the pylon function of vertical engine position. (Oliveira, 2003).

All the mentioned references show that the engine position significantly influences the PSI effects, taking an important part in the definition of the aircraft layout. The CFD simulation is able to capture the main PSI aerodynamics, giving the opportunity to explore new design with an easier, less expensive, and wider exploration of the possible future designs.

2.1 DLR-F6 WING-BODY-NACELLE-PYLON

A preliminary calculation with CFD was done to evaluate the capability of commercial software, CFX-5™, in engine/airframe installation. The calculations were done for a WB and WBNP configurations in order to evaluate the installation effects.

2.1.1 GEOMETRY

The selected geometry is the DLR-F6 due to the availability of experimental results (AIAA, 2012) done at the ONERA S2MA facility. The DLR-F6 model represents a twin-engine low-wing wide-body aircraft of Airbus type and is derived from the earlier DLR-F4 configuration. The geometry is show in fig. 2.16. The aspect ratio is $\Lambda = 9.5$, the leading-edge angle is $\varphi_{LE} = 27.1$ deg, and the taper ratio is $\theta_{TR} = 0.3$.

The engine has a CFM56 like shape with long duct and is represented by throughflow nacelles with the real engine intake mass flow. This is to guarantee a representative flow at the inlet, avoiding shocks, recirculation, and other peculiar flow features. The nacelle has an axis-symmetrical shape. The wing and fuselage configurations are the same both WB and WBNP

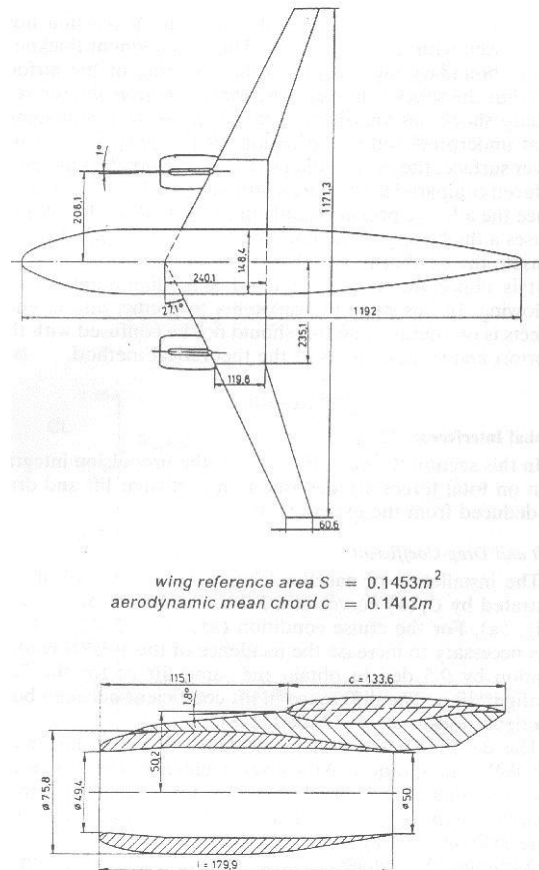


Fig. 2.16 DLR-F6 geometry. (AIAA, 2012).

2.1.2 EXPERIMENTS

The test campaigns have been performed in the ONERA S2MA pressurized wind tunnel with a ring mounted system and a 1.77x1.75 meters. transonic test section. Pressure distributions are measured by 288 taps located in 8 spanwise wing sections and 47 locations in 3 radial sections of the nacelle. The Mach number was varied between 0.6 and 0.8 and the Reynolds number was kept constant at $Re = 3 \cdot 10^6$.

The influence of the wind-tunnel walls and the model support was determined as $\Delta M = -0.002$, $\Delta\alpha = 0.023$ deg, $\Delta C_L = 5.8 \times 10^{-4}$ for the design point of $M_\infty = 0.75$ and $C_L = 0.5$. During the test standard deviations of drag coefficients between $0.3 \cdot 10^{-4}$ and $0.9 \cdot 10^{-4}$ have been measured. It has been observed that drag increased slightly from one test to another, probably due to a small deterioration of the geometry. The results used in this work include these deviations and influences. Additional information can be found in Brodersen (2002).

2.1.3 NUMERICAL METHOD

The computation of the flow has been carried out with a commercial solver named CFX-5™ (ANSYS, 2012). In this solver the Reynolds Averaged Navier-Stokes (RANS) equations are discretized using a vertex-based finite volume method. A control volume is constructed around each nodal point of the mesh, and the fluxes are computed at the integration points located at the sub-faces between two control surfaces. The discrete systems of equations are solved by the coupled algebraic multigrid method developed by Raw (1996). The Reynolds stresses in the momentum equations are computed using the Shear Stress Transport (SST) two-equation turbulence model. The two-equation turbulent model is presented in Menter (1994), showing a good agreement with the experimental results. The idea behind the SST is to retain the robust and accurate formulation of the k - ω model in the near wall region and to take advantage of the free-stream independence of the k - ϵ model by switching model in the different regions, and model the eddy viscosity taking into account the production and dissipation rates. The k - ϵ model has two main weaknesses: it over-predicts the shear stress in adverse pressure gradient flows because of too large length scale (due to too low dissipation) and it requires near-wall modification (i.e. low-Re number damping functions/terms). The k - ω model is better at predicting adverse pressure gradient flow and the model of Wilcox (1988) does not use any damping functions. However, the disadvantage of the k - ω model is that it is dependent on the free-stream value of ω (Menter, 1994).

The free-stream sensitivity has largely prevented the ω -equation from replacing the ε -equation as the standard scale-equation in turbulence modelling, despite its superior performance in the near wall region. This was one of the main motivations for the development of the zonal SST model. The SST model was selected by CFX-5™ for its contribution to the 2nd AIAA Drag Prediction Workshop (AIAA, 2012) showing good agreement with the experimental results. It was therefore decided to use the same turbulence model.

2.1.4 GRID GENERATION

The grids have been carried out with a commercial software named ICEMCFD™ (ANSYS, 2012). The grids are Hybrid type and have been done following the basic gridding guidelines proposed after the experience gained with the Drag Prediction Workshops (AIAA, 2012), regarding the grid related issues on drag prediction accuracy (Mavriplis, 2009).

Basic Gridding Guidelines for Coarse Mesh:

- Boundary Layer Region:
 - $Y^+ \leq 1$
 - $\Delta_1 \approx 0.0006 \text{ mm}$
 - $\Delta_2 = \Delta_1$ (First two layers with the same spacing)
 - Growth rate 1.25
- Farfield (domain size):
 - $\approx 100 C_{ref}$ lengths away from the geometry

Gridding guidelines were also presented for the medium and fine mesh (AIAA, 2012). Following these guidelines, three grids were created: coarse, medium and fine. The grids characteristics for both WB and WBNP are summarized in table 2.1.

The next figures, fig. 2.17 to fig. 2.20, show the coarse grid for the WBNP and the fine mesh for the WB configurations created following the gridding guidelines.

Conf.	Coarse		Medium		Fine	
	Nodes (x10 ⁶)	Elem. (x10 ⁶)	Nodes (x10 ⁶)	Elem. (x10 ⁶)	Nodes (x10 ⁶)	Elem. (x10 ⁶)
WBNP	1.1	3.1	1.75	3.5	2.2	5.6
WB	0.63	2.1	1.4	3.3	1.6	5

Table 2.1 Grid characteristics for WBNP and WB configurations

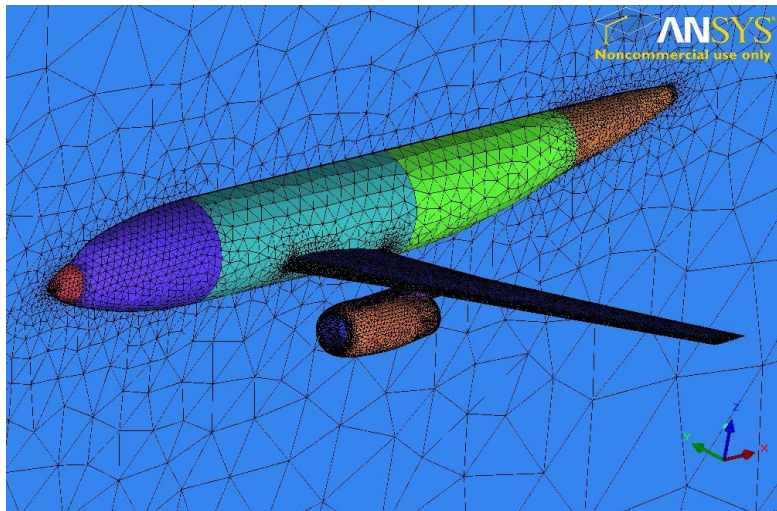


Fig. 2.17 WBNP coarse hybrid mesh generated using ICEMCFD

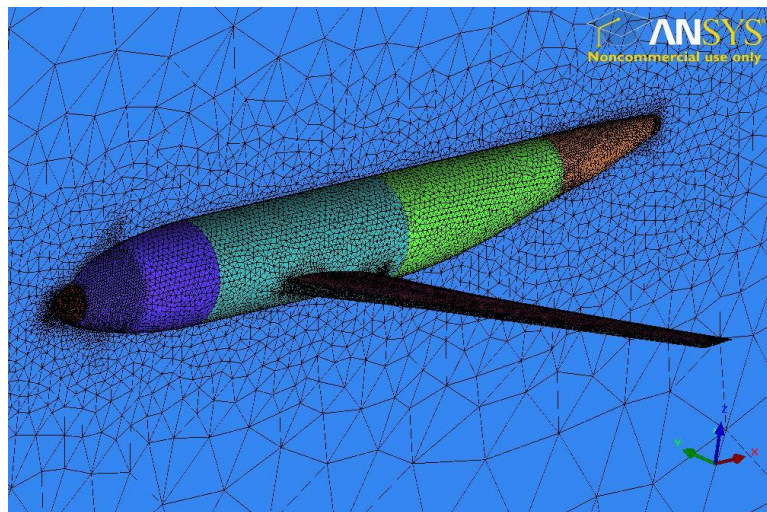


Fig. 2.18 WB fine hybrid mesh generated using ICEMCFD

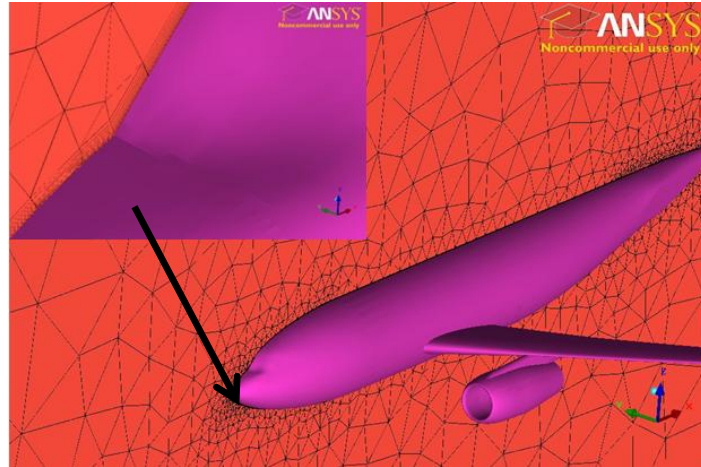


Fig. 2.19 Detail of the hybrid mesh: fuselage layer.

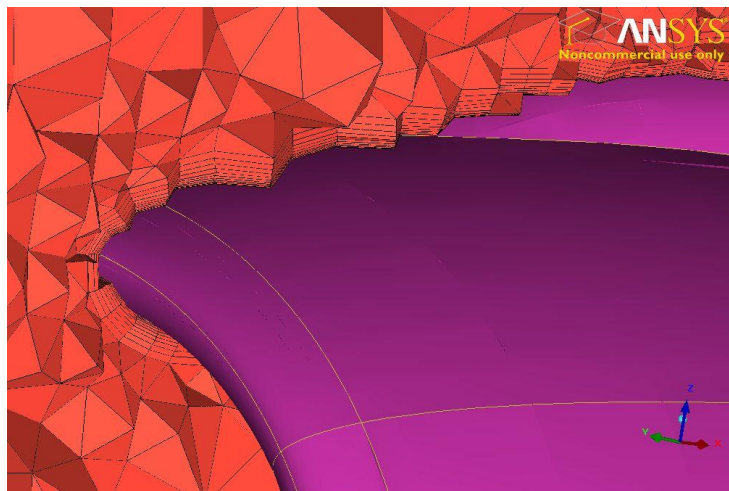


Fig. 2.20 Detail of the hybrid mesh: nacelle structural layer.

A grid dependency study was performed in order to verify the validity of the mesh guidelines presented at Drag Prediction Workshop (AIAA, 2012). Figure 2.21 and 2.22 show the variation of drag coefficient with the number of mesh elements. The WB configuration was evaluated at $\alpha = 0$ resulting on a $C_L = 0.5$ with a scatter of ± 0.008 and the WBNP configuration at $\alpha = 0.5$ resulting on a $C_L = 0.5$ with a scatter of ± 0.01 , in line with the results presented by Brodersen (2002) for the same geometry.

It is clear that increasing the number of elements, the drag prediction becomes more accurate, and in particular, it does it asymptotically. Even if the use of the fine mesh resulted in more accurate results, it was decided to use the

medium grid for the work presented in chapter 3 and 4. This is due the considerably lower computational cost and the modest increase in accuracy opting for the fine mesh

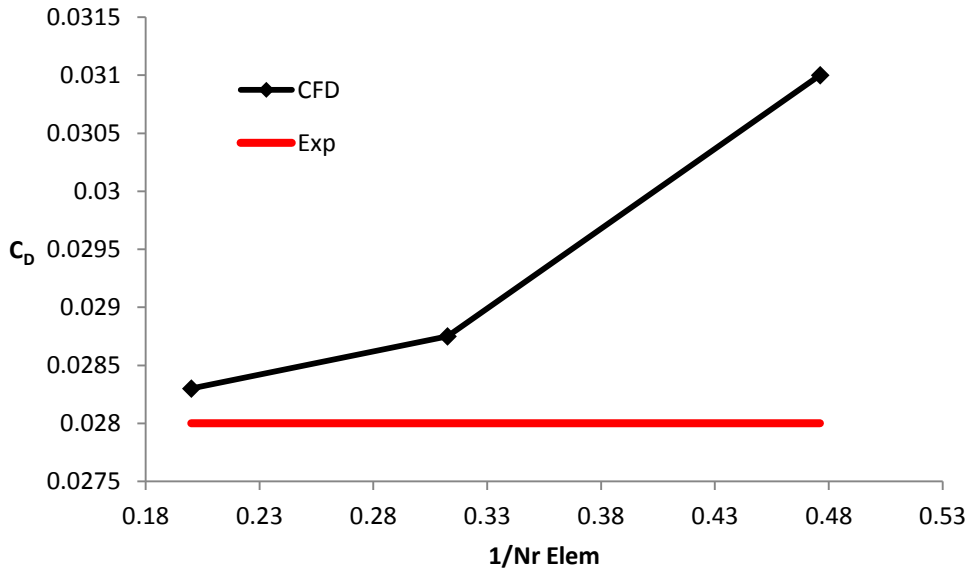


Fig. 2.21 WB C_D function of mesh size.

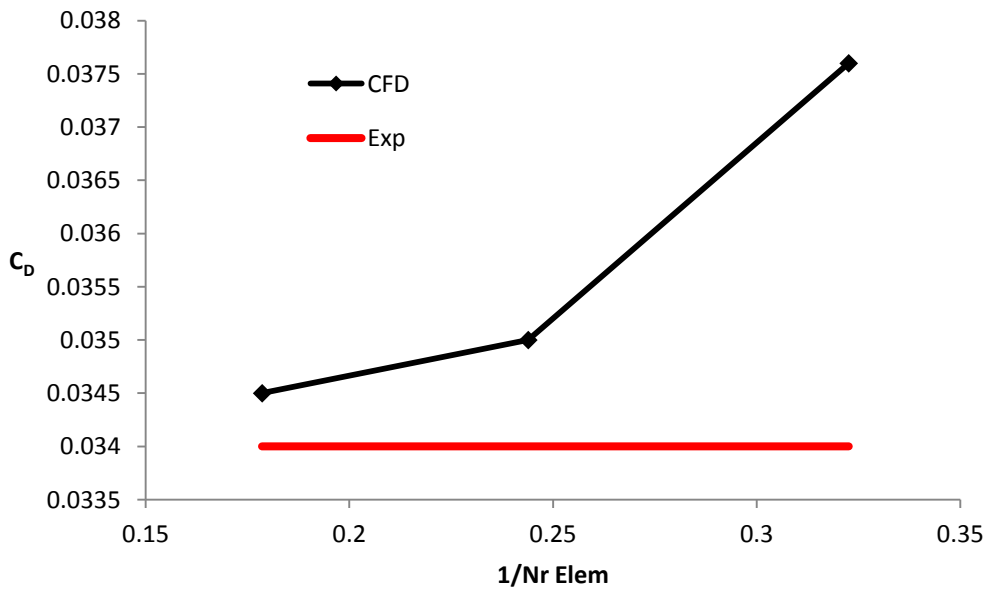


Fig. 2.22 WBNP C_D function of mesh size.

2.1.5 RESULTS

The boundary conditions were the same as the ones used in the experimental campaigns: $Re = 3 \times 10^6$ (based on $c = 141.2\text{mm}$), $M = 0.75$.

The drag polars were calculated running simulations varying the angle of attack, in particular the simulations were run at $\alpha = -1^\circ, 0^\circ$ and 1° .

The coarse and medium drag polar are presented in fig. 2.23 for the WB and fig. 2.24 for the WBNP.

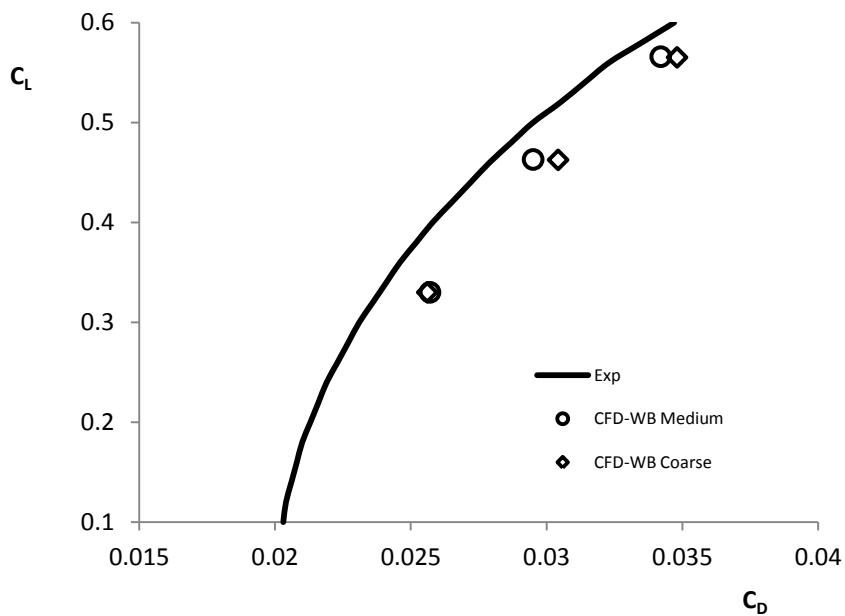


Fig. 2.23 Numerical and experimental drag polar DLR-F6 WB configuration. (Exp. AIAA, 2012)

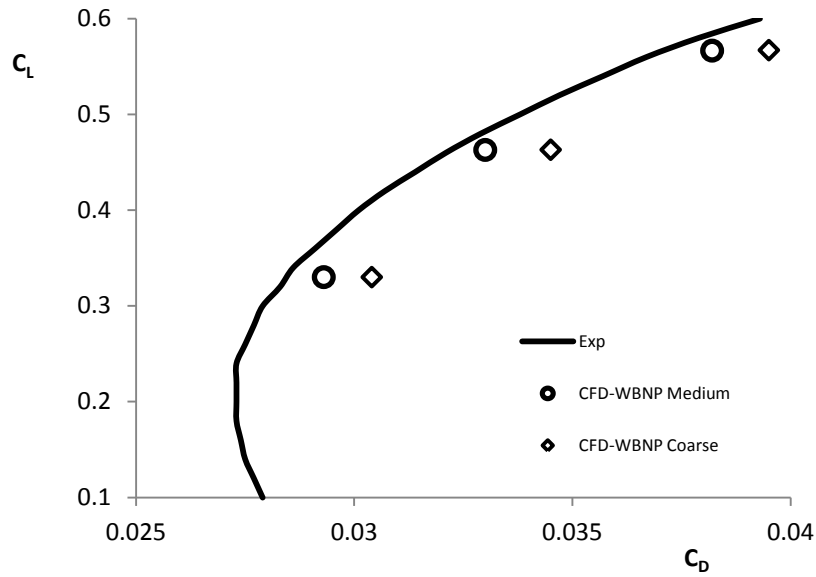


Fig. 2.24 Numerical and experimental drag polar DLR-F6 WBNP configuration. (Exp. AIAA, 2012)

It is possible to see that the WBNP presents higher discrepancy between the medium and coarse results. This is due to the more complex geometry and therefore more complicated aerodynamics. The insufficient resolution of the coarse grid results in a less realistic flow model. In order to capture the aerodynamic interaction between engine and airframe of relatively complex WBNP configuration, a correct mesh size should be applied. As mentioned previously, the results obtained with the medium mesh were considered satisfactory, also taking in to account the computational cost.

The installation drag polar, show in fig.2.22, is computed from:

$$C_{D_{inst}} = C_{D_{WBNP-TF}} - C_{D_{WB}} - C_{D_{Int\,Nac}} \quad (2.1)$$

Where $C_{D_{Int\,Nac}}$ is the internal nacelle drag, relative to the internal surface of the nacelle which was measured in calibrated tests (AIAA, 2012).

The figures 2.25 to 2.27 show the pressure coefficient on the wing near the engine at various spanwise locations, compared with the experimental results. The selected angle of attack is 0° . In general the agreement is good. However, the shock on the suction side of the wing does not appear to be quite as sharp

as in the experiment. One of the causes can be that the grids need a further refinement in the upper wing region to capture the shock correctly.

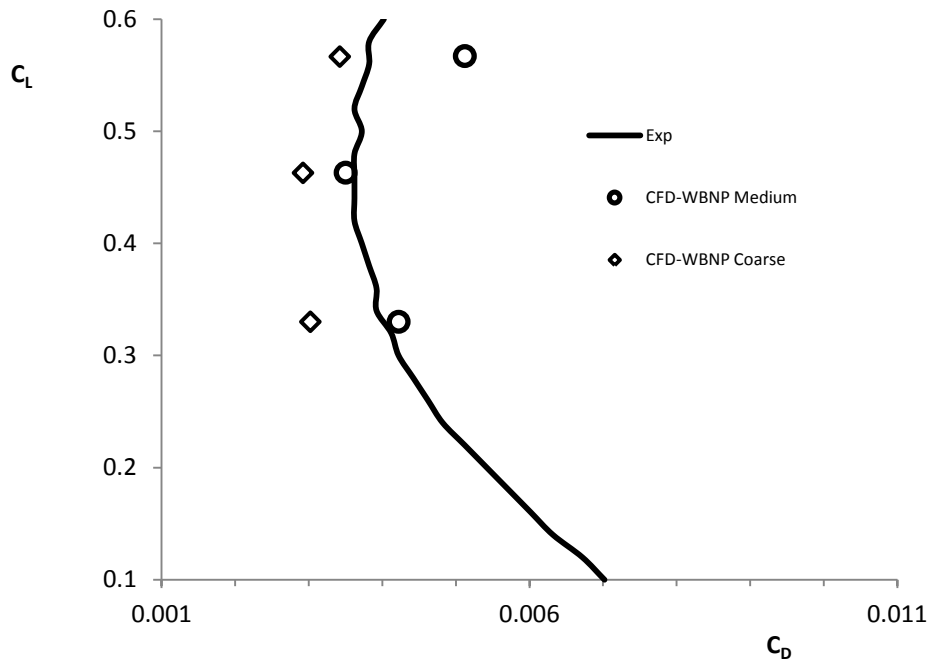


Fig. 2.25 Installation Drag polar DLR-F6 configuration

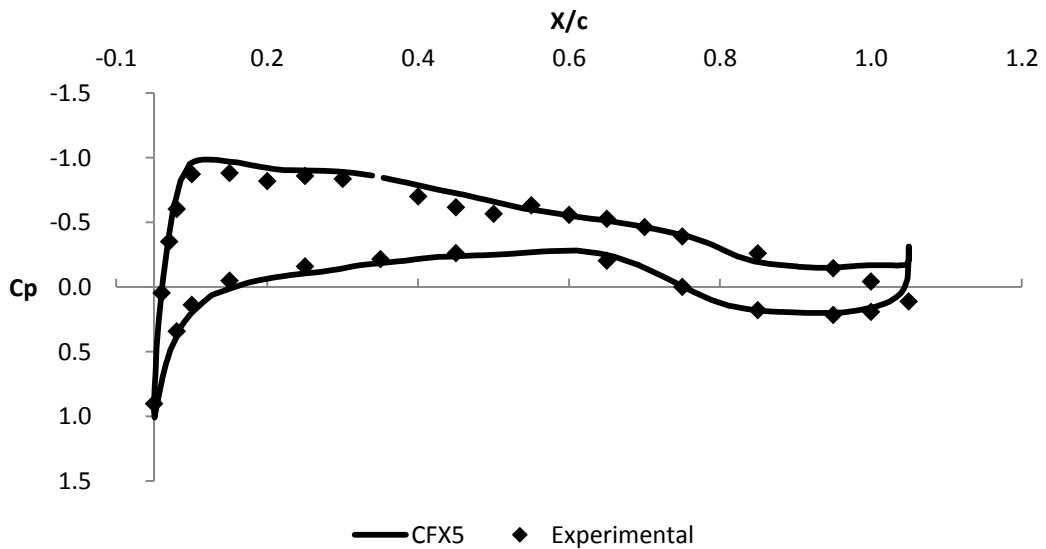


Fig. 2.26 Pressure coefficient at $\eta = 0.15$ for WB configuration

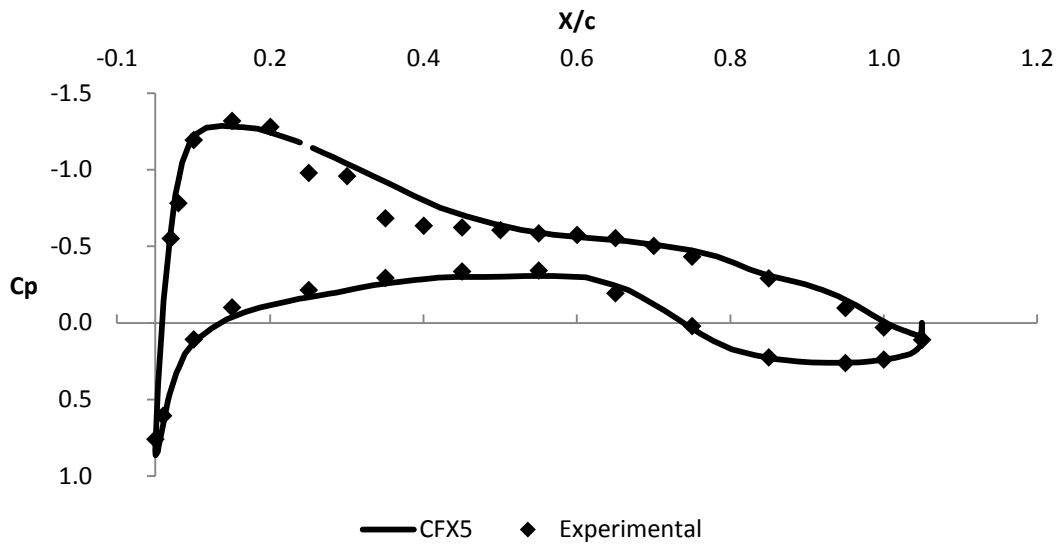


Fig. 2.27 Pressure coefficient at $\eta = 0.239$ for WBNP configuration

Figure 2.28 to 2.31 demonstrates the good agreement with the oil-flow visualization. In particular on the upper surface of the wing, the numerical code is able to predict the separation in correspondence of the wing/body junction and on the trailing edge of the wing, even if in the wing/body junction the code slightly over-predicts the size of these separation zones.

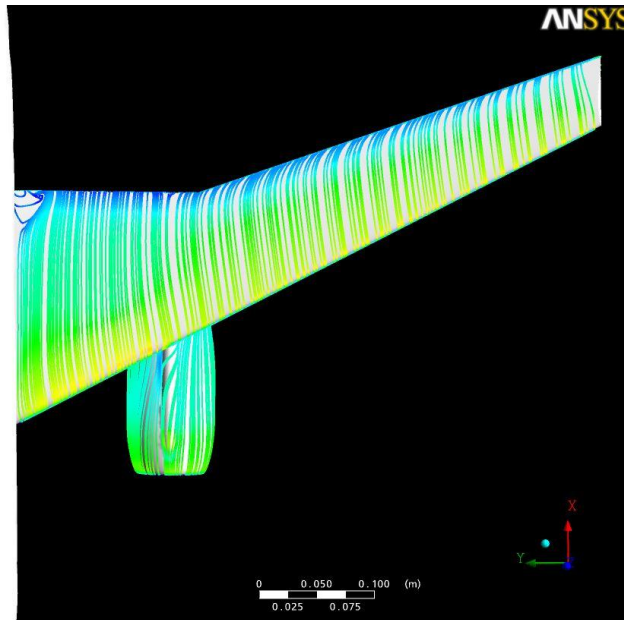


Fig. 2.28 Streamlines on the upper surface of the wing for WBNP configuration

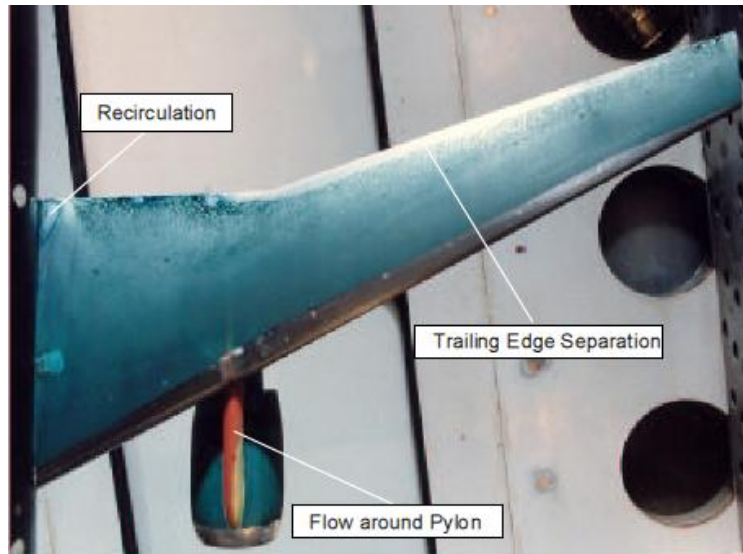


Fig. 2.29 Experimental oil-flow visualization

As it is show in chapter 1, the inboard side of the pylon is a potential separation zone when the pressure recovery on the wing lower surface, coincides with the adverse pressure gradients in the rear part of the pylon. This phenomenon is well predicted by the code, as we see in fig 2.28, 2.30 and 2.32, even if, like the wing/body junction, the code slightly over predict the size of this separation zone and is slightly down stream compared with the experiments. It is also encouraging to see the similar deformation of the streamlines.

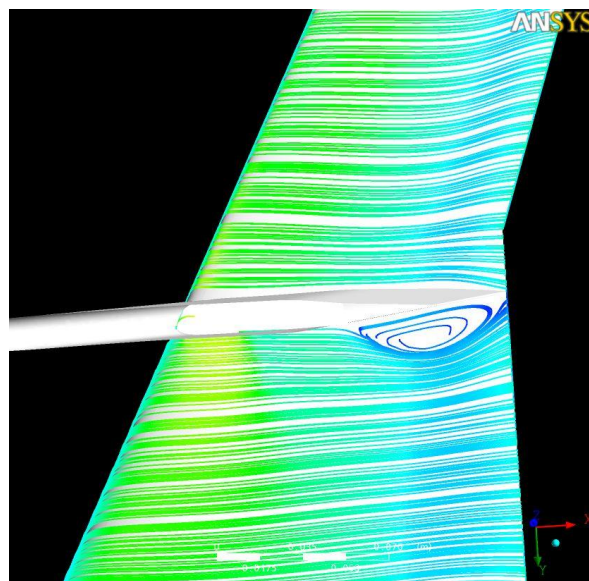


Fig. 2.30 Streamlines on the lower surface of the wing for WBNP configuration

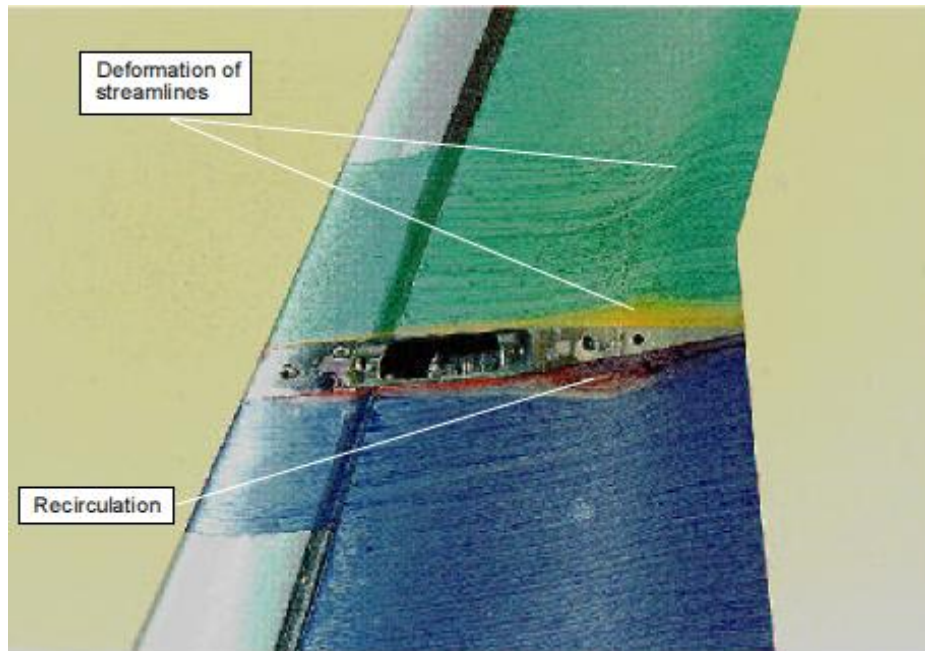


Fig. 2.31 Experimental oil-flow visualization with demounted pylon

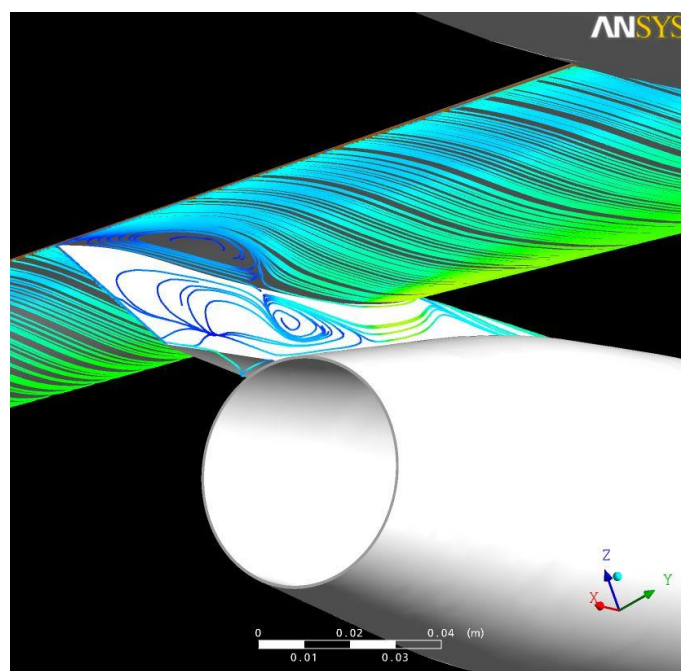


Fig. 2.32 Streamlines on the inboard side of the pylon

The separation zones are confirmed by plotting the wall shear stress on the upper wing surface (fig.2.33) and nacelle-pylon-lower wing surface interception (fig.2.34). Note that low shear stress correspond to separated flow.

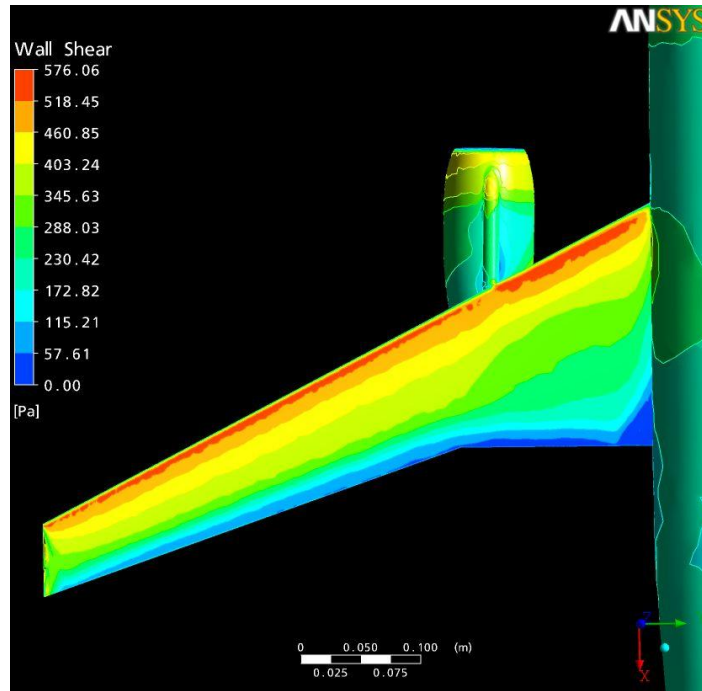


Fig. 2.33 Wall shear on the upper surface of the wing.

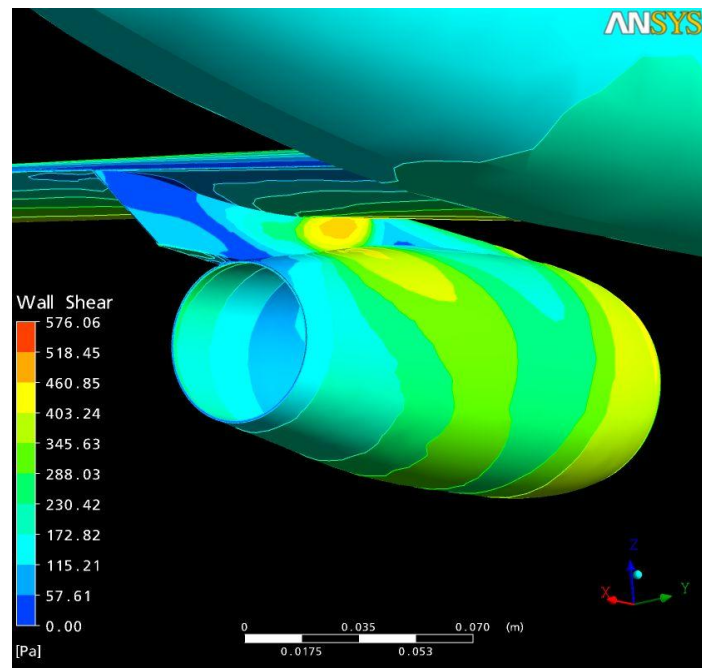


Fig. 2.34 Wall shear at the inboard side of the pylon.

2.1.6 CONCLUSIONS

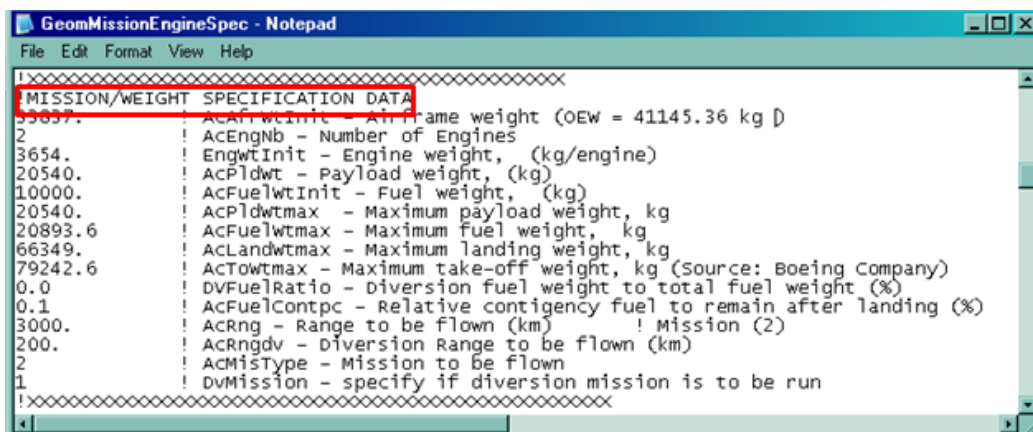
Comparisons between measured and calculated results demonstrate the capability of the commercial solver CFX-5™, to solve RANS with the SST turbulent model and correctly predict the interference effects due to propulsion integration. The predicted drag and installation drag for a WBNP are in line with experimental data, and the comparison with numerical surface streamlines, shear stress contours and experimental oil flow visualization present similar patterns. Even if there is still room for improvements, for example better evaluation of the separation zones around wing-body and pylon-wing junctions, the results are encouraging. Furthermore, despite the importance of a correct grid size, it is demonstrated that good results can be obtained with a relatively coarse mesh (3.5M elements), reducing the already demanding computational costs.

3 PSI MODULE

Modelling the effects of engine integration in aircraft-engine performance codes is not as common as other features which may be included in their capabilities. This is because the phenomenon is complex and affects both the aircraft and the propulsive system. However with the increase of engine size, the propulsive system is becoming highly coupled with the airframe. Therefore to correctly evaluate the performance of both systems, it is necessary to take into account the installation effects, “the aircraft cannot be conceived first and the propulsive units be considered afterwards”.

The main objective of this research project was to upgrade the aircraft performance codes, Hermes (Doulgeris, 2009) and Turbomatch (Cranfield, 2007), in order to account for the aerodynamic effects due to engine airframe integration. To do so a PSI module was created with the capability of evaluating the losses of thrust due to the engine installation. The PSI model was created with the flexibility of being able to use correlations coming from external models. In particular, for this project, due to the complexity of the problem, it was decided to use an high-fidelity model, CFD, to correctly model the aerodynamic effects. However the PSI module can be feed with correlations coming from other sources, like experimental tests. A brief description of the Hermes and Turbomatch is given, followed by a discussion on the PSI module and the CFD modelling necessary to instruct the computer program.

In the second part information regarding the mission and weight breakdown of the aircraft are given. It is possible not only to control the weight breakdown of the aircraft according to the aircraft and mission specifications, but also to select the way Hermes will do the mission calculation, or in other words to select the mission type. Two mission types are available. In mission type 1 the user specifies the total fuel available and the mission range is calculated by Hermes. The value given for the range is just an initial guess and doesn't affect the final solution. In mission type 2 the code works the other way around and the user specifies the range and gets as a result the total fuel. This time the value given for the total fuel is a guess and doesn't affect the final solution. In this section the user also specifies the fuel used for the diversion mission and the contingency fuel, both as percentages of the main mission fuel. The diversion mission can only be flown with the mission type 2, where the user specifies the diversion airport range and gets the calculated value of the diversion fuel needed. Obviously in this case the diversion fuel, given as a percentage before, is just an initial guess. When mission type 1 is selected, the percentage specified as diversion fuel will count towards the total fuel in exactly the same way as the contingency fuel. The aircraft will be heavier by this amount of fuel but the diversion range will not be calculated. An example of the input file is given in fig. 3.2.



```
!XXXXXXXXXXXXXXXXXXXXXXXXXXXXXXXXXXXXXXXXXXXXXXXXXXXXXXXXXXXXXXXXXXXXXXXXXXXX!  
!MISSION/WEIGHT SPECIFICATION DATA  
55037.      ! ACATWtInit - Airframe weight (OEW = 41145.36 kg )  
2          ! ACEngNb - Number of Engines  
3654.      ! EngWtInit - Engine weight, (kg/engine)  
20540.     ! ACPlDwt - Payload weight, (kg)  
10000.     ! ACFuelWtInit - Fuel weight, (kg)  
20540.     ! ACPlDwtmax - Maximum payload weight, kg  
20893.6    ! ACFuelWtmax - Maximum fuel weight, kg  
66349.     ! ACLandWtmax - Maximum landing weight, kg  
79242.6    ! ACTowTmax - Maximum take-off weight, kg (Source: Boeing Company)  
0.0        ! DVFuelRatio - Diversion fuel weight to total fuel weight (%)  
0.1        ! ACFuelContpc - Relative contingency fuel to remain after landing (%)  
3000.      ! ACRng - Range to be flown (km)           ! Mission (2)  
200.       ! ACRngdv - Diversion Range to be flown (km)  
2          ! ACMistype - Mission to be flown  
1          ! DVMission - specify if diversion mission is to be run  
!XXXXXXXXXXXXXXXXXXXXXXXXXXXXXXXXXXXXXXXXXXXXXXXXXXXXXXXXXXXXXXXXXXXXXXXXXXXX!
```

Fig. 3.2 Hermes: mission and weight input file.

The following parts are used to describe all the flight phases (fig.3.3), namely the main and diversion cruise, the hold phase, the climb, descent, take off, landing and taxi phases.

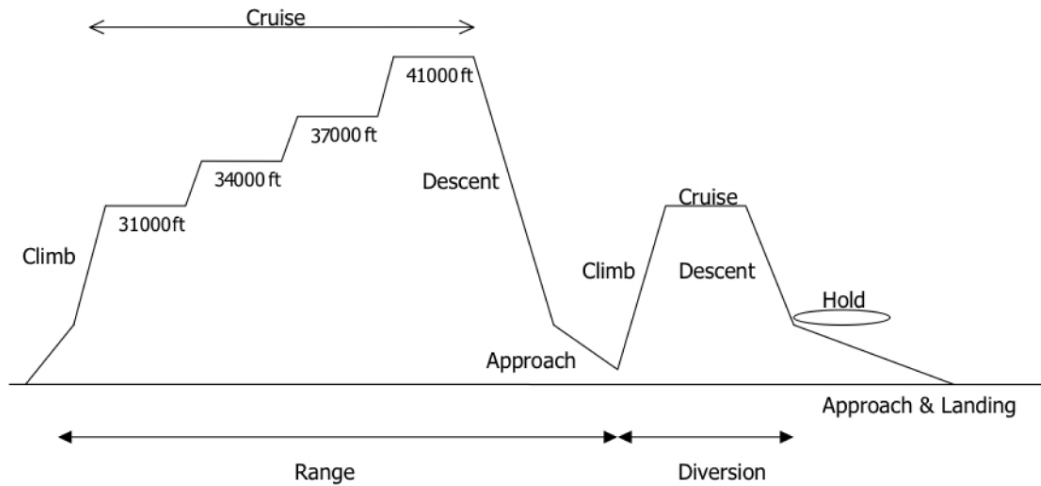


Fig. 3.3 Flight phases.(Doulgeris, 2009)

It is therefore possible to account for the PSI effects in each flight phase, and given that these are normally different for each one, differentiating each phase strongly increase the level of accuracy of the model. An example of the input file is given in fig. 3.4.

The output data are split in two files: the Engine Flight Path Performance file and the Aircraft Flight Path Performance file. The Engine Flight Path Performance file contains the performance of the engine (excluding SFC and TET) for each segment, during all the phases of the flight.

The Aircraft Flight Path Performance file contains the results regarding the aircraft/engine performance. The results refer to every segment of the flight and to the whole flight as well. The weight of the aircraft is printed after every phase of the flight (take off, climb, cruise etc.). The aerodynamic performances are calculated for each segment, including the L/D ratio, the climb and descent rates, the climb and descent gradients, and the lift and drag coefficients. The distance covered, duration and fuel consumed is printed for every segment and phase of the flight. Engine performance data, like thrust and specific fuel consumption, are also given.

```

GeomMissionEngineSpec - Notepad
File Edit Format View Help
=====
CRUISE MAIN/DIVERSION AND HOLDING DATA
! number of cruise altitudes and Mach numbers
1
! number of cruise Temperature Deviations from ISA day
1
! number of diversion cruise altitudes
5
! Cruise small segment time interval in (min).
10668.
! Cruise altitudes in [m] (WARNING: THE ALTITUDES CANNOT BE THE SAME!!!!!!!!!!)
0.785
! Cruise Mach numbers, the same number with cruise altitudes
3.
! Cruise ambient temperature deviation from ISA, in [K]
6096.
! Diversion cruise altitudes (m)
0.65
! Diversion cruise Mach numbers,
457.0
! Holding altitude (m)
30.
! Hold Time in (min)
=====
CLIMB DATA
! Climb segments Number
! Altitudes(m) | DTisa(K) | EAS(knots) | Power(0.-1.)
557.20 3. 250. 1.
900.00 3. 250. 1.
1500.00 3. 250. 1.
1981.20 3. 250. 1.
2438.40 3. 250. 1.
2743.20 3. 250. 1.
3048.00 3. 250. 1.
3048.10 3. 320. 1.
3657.60 3. 320. 1.
4267.20 3. 320. 1.
4876.80 3. 320. 1.
5486.40 3. 320. 1.
6096.00 3. 320. 1.
7620.00 3. 320. 1.
8077.20 3. 320. 1.
9144.00 3. 320. 1.
10058.00 3. 320. 1.
10668.00 3. 320. 1.
11227.00 3. 320. 1.
11887.00 3. 320. 1.
12000.00 3. 320. 1.
12496.8 3. 320. 1.
=====
DESCENT DATA
! Descent segments Number
! The altitudes are dependant on the final cruise altitude, so they are calculated inside the code.
! DTisa(K) | TAS(knots) | Power(0.-1.) ****Note: the last 3 power settings use the Approach rating
3. 233.1 1.
3. 221.5 1.
3. 202.9 1.
3. 195.0 1.
3. 183.1 1.
3. 164.7 1.
3. 150.9 1.
3. 140.0 1.
3. 135.0 1.
3. 135.0 1.
=====
LANDING DATA
! Note: do not put final landing altitude = 0.0, use a very small value instead.
135.00
! Approach speed (TAS), in [m/s]
3.00
! Deviation From standard atmosphere for Landing in [K]
6.00
! Duration of Landing phase in [min]
=====
TAXI and TAKE-OFF DATA
! ActaxiCF1 - Runway Friction Coefficient
0.02
! ActaxiCF2 - Runway Friction Coefficient,BREAKES-OFF
0.3
! ActaxiTime - Taxi time in [min] (12mins for LR, 9mins for SR)
10.0
! ActoTime - Take-off time in [min]
1.0
! ActoALT - Take-off altitude in [m]
0.00
! Take-off temperature deviation from ISA in [K]
3.00
! Takeoff Derate (Real values from 0 to 1, 0.0->100% of Maximum Thrust, 1.0->0% of Maximum Thrust)
0.0
=====

```

Fig. 3.4 Hermes: mission specification input file.

The complete flight path is included in the output in terms of altitude, Mach number, equivalent (EAS) and true (TAS) airspeed. Finally, the output file includes the total fuel consumption, distance covered and duration for the whole flight. An example of output file for the cruise condition is given in fig. 3.5.

```

AircraftFlightPathPerf - Notepad
File Edit Format View Help
A/C weight at beginning of cruise: 66814.6266891728
Cruise data
Dt of each cruise segment: 4.94 min
First and last cruise segment duration: 2.47 min
Seg No    TIME (hrs)    alt (m)    alt (th ft)    Thrust/engine (kN)
1          0.0411       10668.0000 35.0000       18.4466
2          0.1234       10668.0000 35.0000       18.4378
3          0.2057       10668.0000 35.0000       18.4202
4          0.2880       10668.0000 35.0000       18.4027
5          0.3703       10668.0000 35.0000       18.3852
6          0.4526       10668.0000 35.0000       18.3678
7          0.5349       10668.0000 35.0000       18.3504
8          0.6172       10668.0000 35.0000       18.3330
9          0.6995       10668.0000 35.0000       18.3157
10         0.7818       10668.0000 35.0000       18.2984
11         0.8641       10668.0000 35.0000       18.2812
12         0.9464       10668.0000 35.0000       18.2640
13         1.0287       10668.0000 35.0000       18.2468
14         1.1110       10668.0000 35.0000       18.2297
15         1.1933       10668.0000 35.0000       18.2126
16         1.2756       10668.0000 35.0000       18.1956
17         1.3579       10668.0000 35.0000       18.1786
18         1.4402       10668.0000 35.0000       18.1616
19         1.5225       10668.0000 35.0000       18.1447
20         1.6048       10668.0000 35.0000       18.1278
21         1.6871       10668.0000 35.0000       18.1110
22         1.7694       10668.0000 35.0000       18.0942
23         1.8517       10668.0000 35.0000       18.0774
24         1.9340       10668.0000 35.0000       18.0607
25         2.0163       10668.0000 35.0000       18.0440
26         2.0986       10668.0000 35.0000       18.0274
27         2.1809       10668.0000 35.0000       18.0107
28         2.2632       10668.0000 35.0000       17.9942
29         2.3455       10668.0000 35.0000       17.9776
30         2.4278       10668.0000 35.0000       17.9611
31         2.5101       10668.0000 35.0000       17.9447
32         2.5924       10668.0000 35.0000       17.9283
33         2.6335       10668.0000 35.0000       17.9119

cruise duration: 158.011824020682 (min)
Fuel burnt during the cruise 2942.19112514446
Aircraft weight at END of cruise (kg): 63872.4355640283
Distance flown during cruise (km): 2222.95631087253
A/C weight at beginning of cruise, check: 66814.6266891727

```

Fig. 3.5 Hermes: cruise condition output file.

For further details about input/output files and additional calculation parameters, the interested reader can find further information in the user manual (Doulgeris, 2009).

Hermes is designed to be able to interact with several engine performance models, but in this particular project it was decided to use Turbomatch to evaluate the engine. Turbomatch is an engine performance code developed at Cranfield University. It is able to perform design and off-design performance calculations for gas turbine engines (Cranfield, 2007). The code is developed by means of various subroutines, called “bricks” which evaluate the thermodynamic properties of the different components of the engine. Examples of bricks are: Intake, Compressor, Burner, Turbine etc. A typical input file (intake and fan data only) is presented in fig. 3.6. It is possible to see that in addition to the main engine parameters, it is possible to define the type of the simulation: design point (DP) or off-design (OD).

The off-design simulation output will include the effects of changing the engine parameters (like TET, altitude, compressor pressure ratio etc.). These features are essential when coupled with an aircraft performance program like Hermes.

```

00 SI KE VA FP
-1
-1
INTAKE S1,2 D1-6 R300
ARITHY D153-155
ARITHY D163-165
ARITHY D170-176
COMPRES S2,3 D7-18 R305 V7 V8
PREMAS S3,30,4 D19-22 V19
PREMAS S30,35,31 D201-204
DUCTER S31,32 D23-27 R310
DUCTER S4,5 D28-32 R315
COMPRES S5,6 D33,8,35-44 R320 V33
PREMAS S6,40,7 D45-48
PREMAS S7,41,8 D49-52
COMPRES S8,9 D53-64 R335 V53 V54
PREMAS S9,42,10 D65-68
COMPRES S10,11 D69,54,71-80 R340 V69
PREMAS S11,43,12 D81-84
COMPRES S12,13 D85,54,87-96 R345 V85
PREMAS S13,44,14 D97-100
PREMAS S14,45,15 D101-104
BURNER S15,16 D105-112 R350
MIXEES S16,44,17
TURBIN S17,18 D113-127 V114
MIXEES S18,42,19 D128-142 V129
TURBIN S19,20
MIXEES S20,41,21
MIXEES S21,40,22
NOZCON S32,33,1 D143,144 R351
NOZCON S22,23,1 D145,146 R355
PERFOR S1,0,0 D147-150,355,300,350,351,0,0,0,0,0
CODEND

BRICK DATA:///
1 10668. ! IN TAKE Altitude
2 0. ! Deviation from ISA temperature
3 0.80 ! Mach number
4 -1 ! Pressure recovery, according to USAF
5 0. ! Deviation from ISA pressure [atm]
6 0. ! Relative humidity [%]

7 0.85 ! FAN - COMPRESSOR: Z = (R-R[choke])/(R[surge]-R[choke])
8 1. ! DP Relative rotational speed PCN
9 1.8 ! DP Pressure ratio
10 0.885 ! DP isentropic efficiency
11 0. ! Error selection
12 2. ! Compressor Map Number
13 1. ! Shaft number
14 1. ! Scaling Factor of Pressure Ratio - Degradation factor
15 1. ! Scaling Factor of Non-D Mass Flow - Degradation factor
16 1. ! Scaling Factor of Isentropic Efficiency - Degradation factor
17 1.5 ! Effective component volume [m^3]
18 0. ! Stator angle (vsv) relative to DP

```

Fig. 3.6 Turbomatch input file.

3.2 THE PSI MODULE

3.2.1 STRUCTURE

The PSI module forms a new link between the aircraft performance model, Hermes, and the engine performance model, Turbomatch. The PSI module takes the requested thrust from Hermes and, by considering the PSI effects, generates the Net Propulsive Force (NPF), the real force that the engine applies to the aircraft (fig.3.7).

According to the thrust and drag book-keeping, presented in chapter 1, the NPF is the force exerted by the powerplant to the airplane purged of nacelle force (see chapter 1).

This force represents the real interface between the engine and the airplane and it is different from the gross thrust due to the presence of the nacelle and pylon and their interference effects.

Afterwards the engine performance model, in this case Turbomatch, adjusts the engine parameters, like SFC, to the requested NPF and returns them to Hermes in order to calculate the performance of the entire aircraft (Fig.1).

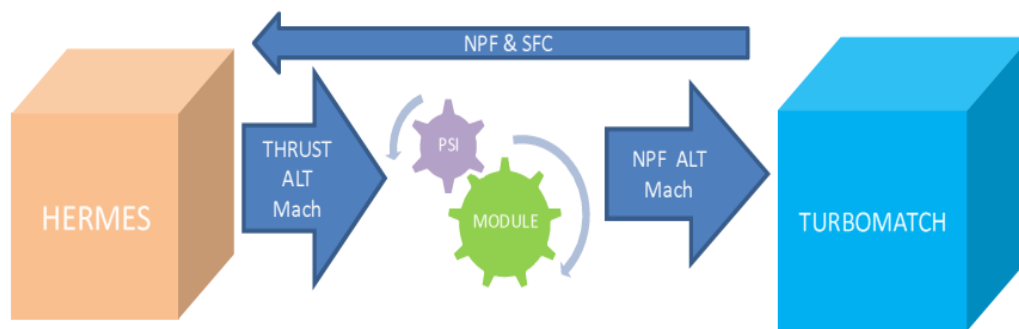


Fig. 3.7 PSI module schema.

The input file is presented in fig. 3.8. The module is able to be instructed knowing the relationship between the net thrust and net propulsive force for a single engine position or for multiple engine positions. This feature allows the engine and aircraft performances to be evaluated for different engine installation configurations or simply evaluate the performance of a particular engine installation. Given that Hermes is used in several other tools, like the TERA2020 software (Techno-economic Environmental and Risk Assessment for 2020) (Bretschneider, 2007), this capability gives a wide range of options, like aircraft configuration optimization for future applications.

```

EngineIntegrSpec - Notepad
File Edit Format View Help
!Input file for the Propulsion System Integration (PSI)
!Definition of the NPF/Fn (net propulsive force/net thrust)
!for single position or law for multiposition
1 ! Selector for single position (0) when the relation is know only for 1 position,
! or (1) for multiposition law in known
!
! Single Engine position
! Climb Costants
1 !Thrust funct
0 !Drag funct
! Cruise Costants
1 !Thrust funct
0 !Drag funct
! Descent Costants
1 !Thrust funct
0 !Drag funct
! Holding Costants
1 !Thrust funct
0 !Drag funct
! Landing Costants
1 !Thrust funct
0 !Drag funct
! Take-off Costants
1 !Thrust funct
0 !Drag funct
!
! Multiple Engine positions --> Law ax^2+bx+c
! Climb Costants
0 !AClimb
0 !BClimb
1 !CClimb
! Cruise Costants
0.3427 !ACruise
0.9077 !BCruise
0.3662 !CCruise
! Descent Costants
0 !ADescent
1 !BDescent
1 !CDescent
! Holding Costants
0 !Aholding
0 !Bholding
1 !Cholding
! Landing Costants
0 !ALanding
0 !BLanding
1 !CLanding
! Take-off Costants
0 !ATake-off
0 !BTake-off
1 !CTake-off

```

Fig. 3.8 PSI module input file.

Another interesting feature is the ability to differentiate the different phases of the flight applying appropriate correlations for each engine/airframe attitude. This characteristic is very important given that the interaction effects are strongly dependent on the flight conditions, as pointed out in chapter 1.

An example of the updated Hermes output with the PSI effects is given in figure 3.9. The Aircraft Flight Path Performance file gives both the NPF and the Net Thrust, but the real interface between the engine and the airplane is the NPF. It can be see that the NPF is lower compared to the Net Thrust. This is due to the effects of the engine installation that reduces the force applied by the engine to the airframe.

The next section will describe the CFD models used to generate the correlations that feed the PSI model.

```

AircraftFlightPathPerf - Notepad
File Edit Format View Help
A/C weight at beginning of cruise: 67128.6466883725
Cruise data
Dt of each cruise segment: 4.56 min
First and last cruise segment duration: 2.47 min
Seg No    TIME (hrs)    alt (m)    alt (th ft)    NPF/engine (kN)    NetThrust/engine(kN)
1         0.0411       10668.0000 35.0000       18.4400           19.2399
2         0.1234       10668.0000 35.0000       18.4378           19.2307
3         0.2057       10668.0000 35.0000       18.4202           19.2124
4         0.2880       10668.0000 35.0000       18.4027           19.1941
5         0.3703       10668.0000 35.0000       18.3852           19.1759
6         0.4526       10668.0000 35.0000       18.3678           19.1577
7         0.5349       10668.0000 35.0000       18.3504           19.1396
8         0.6172       10668.0000 35.0000       18.3330           19.1215
9         0.6995       10668.0000 35.0000       18.3157           19.1034
10        0.7818       10668.0000 35.0000       18.2984           19.0854
11        0.8641       10668.0000 35.0000       18.2812           19.0674
12        0.9464       10668.0000 35.0000       18.2640           19.0495
13        1.0287       10668.0000 35.0000       18.2468           19.0316
14        1.1110       10668.0000 35.0000       18.2297           19.0137
15        1.1933       10668.0000 35.0000       18.2126           18.9959
16        1.2756       10668.0000 35.0000       18.1956           18.9781
17        1.3579       10668.0000 35.0000       18.1786           18.9604
18        1.4402       10668.0000 35.0000       18.1616           18.9427
19        1.5225       10668.0000 35.0000       18.1447           18.9251
20        1.6048       10668.0000 35.0000       18.1278           18.9075
21        1.6871       10668.0000 35.0000       18.1110           18.8899
22        1.7694       10668.0000 35.0000       18.0942           18.8724
23        1.8517       10668.0000 35.0000       18.0774           18.8549
24        1.9340       10668.0000 35.0000       18.0607           18.8374
25        2.0163       10668.0000 35.0000       18.0440           18.8200
26        2.0986       10668.0000 35.0000       18.0274           18.8027
27        2.1809       10668.0000 35.0000       18.0107           18.7853
28        2.2632       10668.0000 35.0000       17.9942           18.7680
29        2.3455       10668.0000 35.0000       17.9776           18.7508
30        2.4278       10668.0000 35.0000       17.9611           18.7336
31        2.5101       10668.0000 35.0000       17.9447           18.7164
32        2.5924       10668.0000 35.0000       17.9283           18.6993
33        2.6335       10668.0000 35.0000       17.9119           18.6822

Cruise duration: 132.03524789081 (min)
Fuel burnt during the cruise: 1862.12233565976
Aircraft weight at END of cruise (kg): 62952.4122240193
Distance flown during cruise (km): 2222.83625104821

```

Fig. 3.9 PSI module output

3.2.2 CFD MODEL

The most time consuming part of this research project was the evaluation of the correlations necessary to instruct the PSI model. In order to evaluate the aerodynamic effects of PSI, it was necessary to perform high fidelity CFD simulations of the whole aircraft, including the engines. As identified in chapter 2, this is an elaborate and computational expensive task.

The NPF was extracted from high fidelity CFD calculations. In reference to chapter 1 paragraph 5, the relevant equation, suited for CFD result analysis, is:

$$NPF = F_{N,int} - \phi_{plug} - \phi_{AB} - \phi_{cowl} - \phi_{pylon-scrub} \quad (3.1)$$

Where $F_{N,int}$ (eq.3.2) is the Intrinsic Net Thrust, ϕ_{plug} , ϕ_{AB} , ϕ_{cowl} , and $\phi_{pylon-scrub}$ are the force applied respectively on the plug, after-body, nacelle cowl and the portion of pylon wetted by the engine plume. Furthermore F_{G9} and F_{G91} are the gross thrusts of the primary and secondary nacelle flows, and F_{G1} is the intake stream force (fig.3.10), calculated using eq. 3.3 already presented in chapter 1.

$$F_{N,int} = F_{G9} + F_{G91} - F_{G1} \quad (3.2)$$

$$F_G = WV + (p - p_\infty)A \quad (3.3)$$

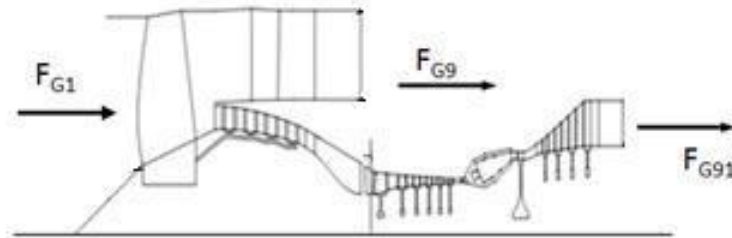


Fig. 3.10 Stations definition on a Turboprop

The engine was modelled applying boundary conditions at the inlet and outlet of the fan and core section. No rotating parts were defined considerably reducing the already high computational cost. Li (1998) and Mogilka (1994) underline the difficulties to model the fan and turbine blades and the necessity of using a simplified model. Various configurations have been validated through experimentation/computation comparisons, with encouraging results. The computational domain, with boundary conditions, is presented in fig.3.10. The boundary conditions for the fan and core inlet and outlet flows were given, specifying the mass flow rate and the total temperature. The domain inlet boundary condition was given specifying the flow velocity and direction. The far-field boundaries were modelled using an opening boundary condition defining an open pressure (ANSYS, 2012).

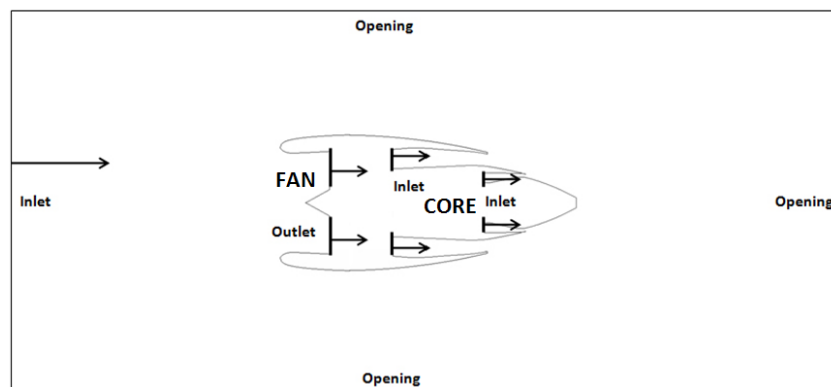


Fig. 3.11 Engine and far-field boundary conditions

3.2.2.1 NACELLE GEOMETRY GENERATION

It was necessary to create a methodology to define the nacelle geometry starting from the available data coming from the engine performance code. Table 3.1 gives an overview of the typical Turbomatch engine performance data. The engine PDE4089 Rolls & Royce Vital (VITAL, 2005) was selected as a test case due to the availability of the data. Starting from these files a procedure based on engine performance, engine/nacelle dimensions, NACA profiles (ESDU, 1994) and public domain correlations (Williams, 2009), was defined and applied in order to generate the whole nacelle and fan/core nozzles geometries. Typical input files containing engine/nacelle geometries are represented in fig.3.12 and 3.13. These data contain geometrical and installation constraints points in order to apply correlations and NACA procedures. The engine must fit in to the nacelle and therefore points 1, 2, 3, 4, 6 and 7 of fig.3.13 are fixed. The point 5, HPC flange station where the engine is attached to the pylon, wasn't considered given that doesn't directly affect the shape of the nacelle. Propulsive system, as a whole, geometric data, i.e. max nacelle diameter and length, are showed in fig.3.12. To simplify the model, the nacelle geometry was taken as being axisymmetric. This assumption does not reduce the reliability of the results given that the calculations are done at cruise condition, and the non-axisymmetric shape will mainly affect the performance at off-design conditions (take off, climb, etc.).

Parameter	Unit	Parameter	Unit
Altitude	ft	Bypass Duct T°	K
Mach	-	Core Duct T°	K
BPR	-	Bypass Duct P°	Pa
Fn	N	Core Duct P°	Pa
Fan Tip Mass Flow	Kg/s	Bypass Duct Mass Flow	Kg/s
Fan Face T°	K	Core Duct Mass Flow	Kg/s

Table 3.1 Engine Performance Data

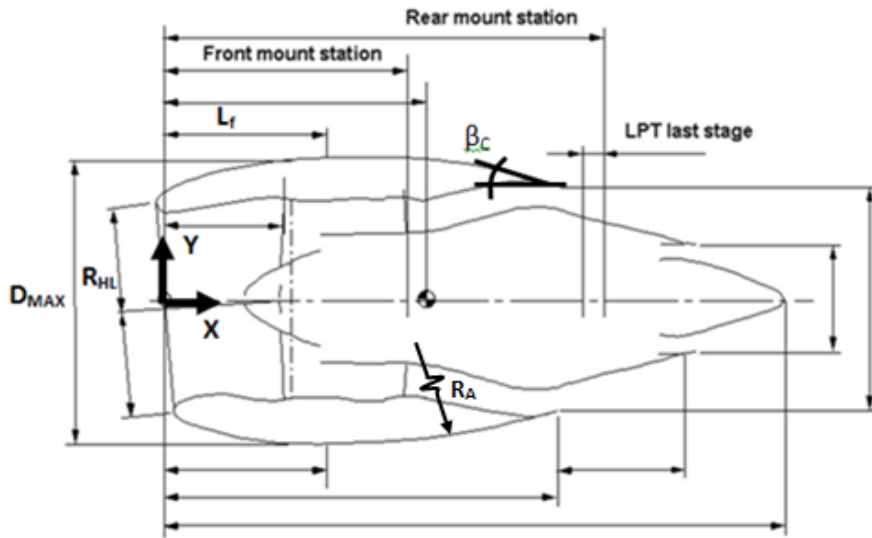


Fig. 3.12 Nacelle geometry input file and boat-tail cord angle and radius (VITAL, 2005)

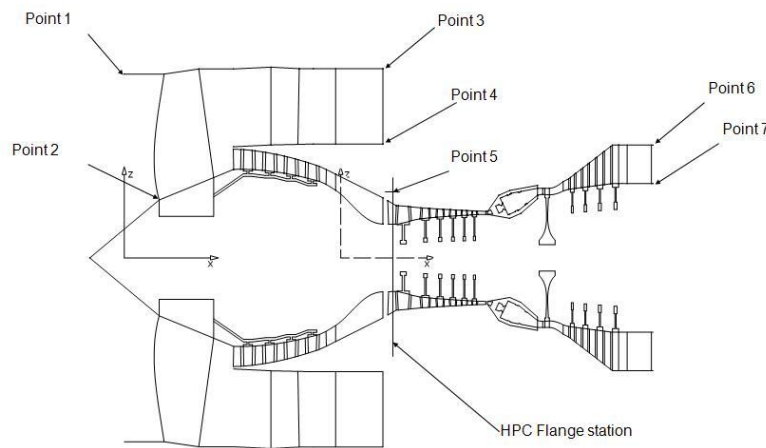


Fig. 3.13 Location of engine layout constraints (VITAL, 2005)

The nacelle can be divided into an intake, forebody, afterbody, corecowl, coreduct, fan duct and plug, as shown in fig.3.14. The boundary between the forebody and afterbody is defined by a line at the max nacelle diameter (fig.3.12).

The flow parameter Q (ESDU, 1994), defined in eq.3.4, allows to calculate the area knowing: mass flow (W), temperature (T), pressure (P) and Mach number (M).

$$Q = \frac{W\sqrt{T}}{PA} = \sqrt{\frac{\gamma}{R}} M \left[1 + \left(\frac{\gamma - 1}{2} \right) M^2 \right]^{\frac{\gamma + 1}{2(\gamma - 1)}} \quad (3.4)$$

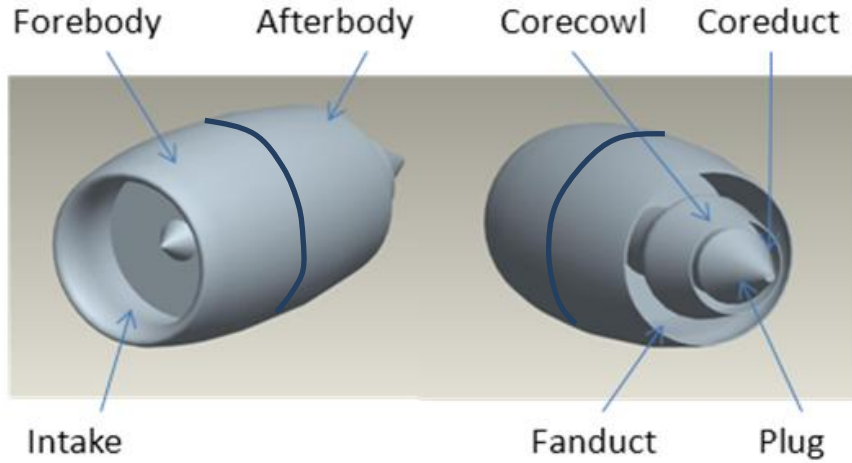


Fig. 3.14 Nacelle components. The grey line (positioned at max nacelle diameter) indicate the boundary between forebody and afterbody

The highlight area A_{HL} (nacelle sectional area at the lip, fig.3.12) was known, therefore the throat area A_{TH} was calculated using eq. 3.4 with an appropriate Mach number (around 0.75) and checking that the contraction factor A_{HL} / A_{TH} remained in a prescribed range of 1.2÷1.3 for civil aviation (Williams, 2009).

The geometry was then constructed as an ellipse, with the extreme position points as the highlight (R_{HL}) and the throat (R_{TH}) radius (fig.3.15). The connection between the throat and the fan was then defined according to the engine dimensions and to elude flow separation, the diameter variations along the axial coordinate were kept as smooth as possible. CFD calculations were performed to refine the geometry to avoid sonic flow at the throat and flow separations.

The geometry of the forebody was defined using a NACA 1-Series (ESDU, 1994) and in particular using the smoothed NACA 1-Series (eq.3.4)

$$\frac{y}{Y} = c \left(\frac{x}{X}\right)^{1/2} \left[\frac{1}{c} - \left[\left(\frac{x}{X} - 1\right) \frac{1}{2c} \right] + \left[\left(1 - \frac{1.5}{c}\right) \left(\frac{x}{X} - 1\right)^2 \right] \right] + \left[\sum_{n=0}^7 (-1)^{n+1} A_n \left(\frac{x}{X}\right)^n \right] \left[\frac{\left(\frac{x}{X}\right)^{3/2} \left(\frac{x}{X} - 1\right)^2}{\left(b + \frac{x}{X}\right)^2} \right] \quad (3.5)$$

In which

n	A_n
0	0.0094
1	0.38
2	1.71
3	7.73
4	22.79
5	40.64
6	38.05
7	14.23

$b = 0.05$, $c = 1.045$. x/X and y/Y are the cowl non-dimensional longitudinal coordinates where X is the length of the forebody (L_f fig. 3.12) and $Y = (D_{MAX} - D_{HL})/2$ with D_{MAX} as the maximum cowl diameter.

However, like the intake, the geometry was updated after preliminary CFD calculations to avoid shocks and flow separations, which can considerably affect the nacelle aerodynamics and resultant force distributions.

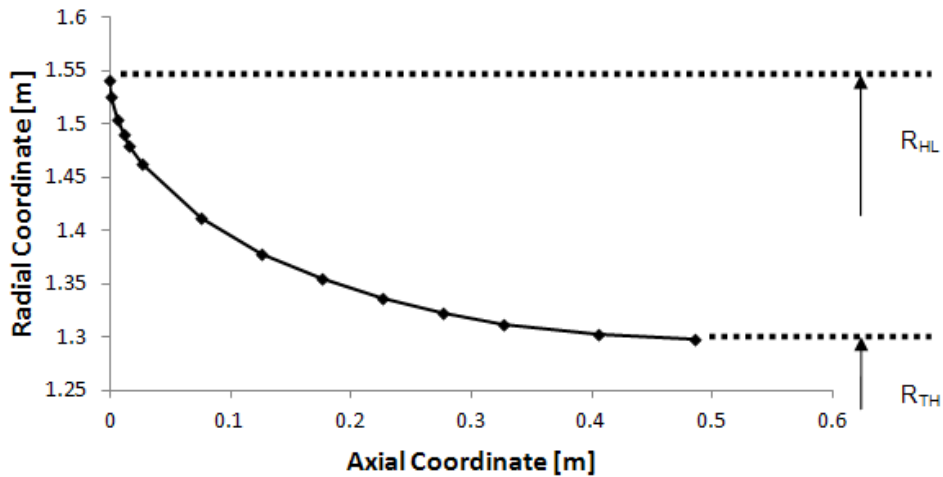


Fig. 3.15 Intake geometry (co-ordinate system as fig 3.12).

Fig.3.16 shows the different nacelle versions. The grey regions indicate sonic conditions. Notice the absence of regions of sonic flow on the last version (fig. 3.15e) compared to the early versions (fig. 3.15a-b-c-d).

Small geometry modifications, as a result of initial CFD calculations ensured that an appropriate geometry with acceptable baseline aerodynamics was used for the subsequent predictions.

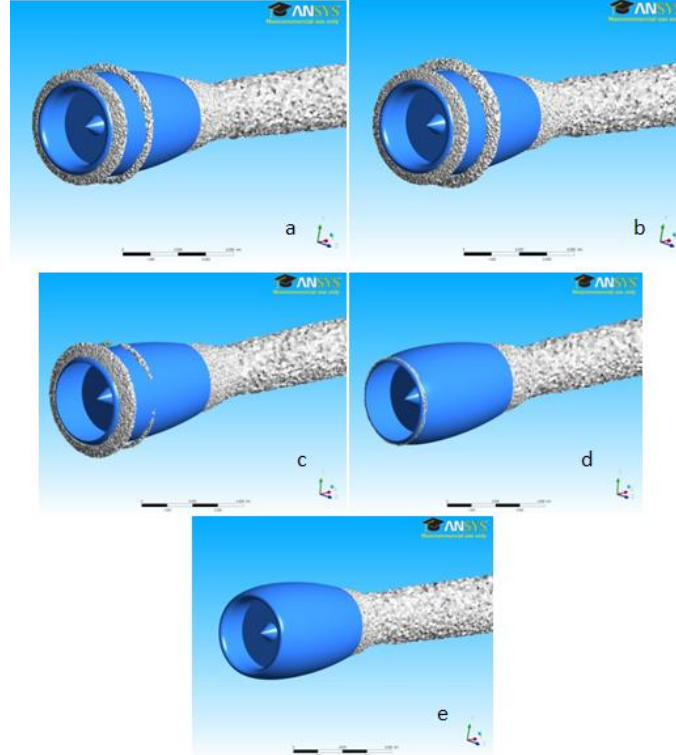


Fig. 3.16 Reduction of sonic regions (grey surfaces) around intake and forebody for five different nacelle intake versions.

The afterbody design was constrained by the dimensions of the nacelle and engine, (fig. 3.12). It was decided to represent the profile as a circular arc (Williams, 2009), calculating the boat-tail angle β_c (eq.3.6, fig.3.12), and from it deriving the boat-tail radius R_A (eq.3.7, fig.3.12). D_{max} is the maximum diameter of the nacelle, D_9 is the nacelle diameter at the bypass duct outlet, L_{aft} is the length of the afterbody and β_c is the boat-tail chord angle (Williams, 2009).

$$L_{aft} = \frac{D_{max} - D_9}{2 \tan(\beta_c)} \quad (3.6)$$

$$R_A = \frac{L_{aft}}{\sin(2 * \beta_c)} \quad (3.7)$$

The afterbody circular arc radius, also called boat-tail radius, needs to be long enough to avoid the generation of flow separations and recirculation zones in the aft part of the body. By taking a large radius, the premature drag rise in the flow suction region of the initial expansion around the shoulder of the afterbody was avoided. A smaller radius leads to excessive boundary layer growth and flow separation on the afterbody in the flow re-compression region at the rear of the boat tail. Otherwise a larger radius leads to an increase in the wetted surface area and therefore an increase in the skin friction drag (Williams, 2009).

The fan duct was generated from the geometric data of the engine-nacelle geometry input files (fig. 3.11 and .12). Using the Q function (eq. 3.4) for a choked nozzle, which occurs at cruise conditions (MIDAP, 1979; Williams, 2009), the Mach number was varied from the fan exit conditions, taken from the engine performance data, to Mach 1 at the throat. The geometry was then defined as a variation of area ratio along the duct length and the geometry constraints enabled the fan duct path geometry to be defined (fig.3.17).

The geometry was also refined by performing initial CFD calculations in a similar manner to that undertaken for the other nacelle parts. Similarly the requirement was to generate acceptable baseline aerodynamics to avoid strong shocks and to ensure that the air leaves the nacelle mainly in the axial direction.

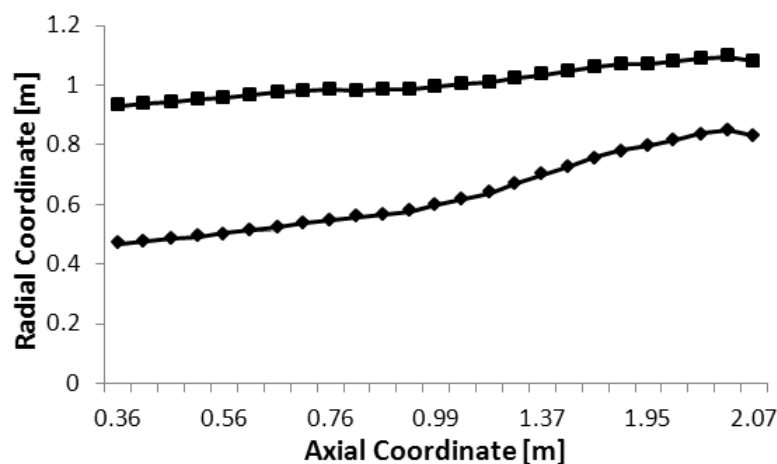


Fig. 3.17 Fan duct geometry (co-ordinate system as fig 3.12).

Fig. 3.18a, b, c illustrate the different duct/cowl geometries adopted to reduce the intensity of shocks and to align the core/fan flows to the horizontal direction. The three analyses were performed with the same boundary conditions, but changing the nozzle geometry, varying area and slope angles of both plug and corecowl. The same procedure was applied to the core duct, with a higher total temperature, except that the latter is linked to the plug that must be sized in order to avoid recirculation.

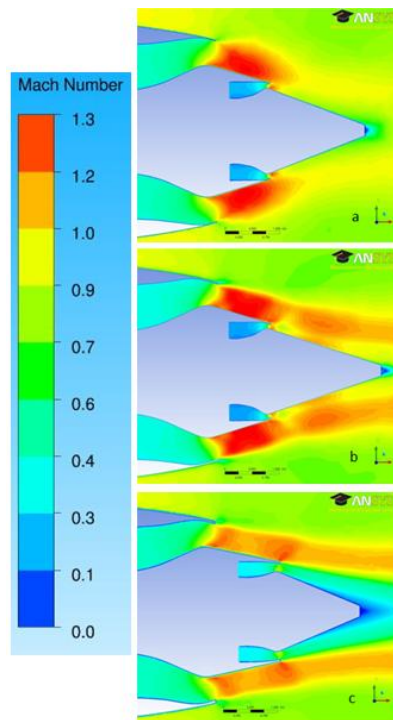


Fig. 3.18 Mach number at the fan/core exit for 3 different flow path configurations.

3.2.2.2 NACELLE GEOMETRY INSTALLATION

The final nacelle configuration was then installed on an aircraft to assess the interference effects. The Wing Body (WB) configuration selected was the Common Research Model (CRM) (Vassberg, 2008), developed by the Boeing Company, and used during the 4th Drag Prediction Workshop (AIAA, 2012). It is a wing-body aircraft with a transonic supercritical, Mach = 0.81, wing and a fairing between the wing and the body (fig.3.17). The engine was positioned following previous work (Vassberg, 2008), where an empty nacelle was installed on the CRM. The span position was the same but the engine was positioned vertically closer to the wing to increase the ground clearance.

This was to account for the larger fan diameter compared to the engine presented in the previous study.

Due to the lack of information available in the open literature, the pylon was generated using a simple symmetric profile and by applying standard shapes taken from others pylon designs (Devine, 2009; Dinesh, 1992).

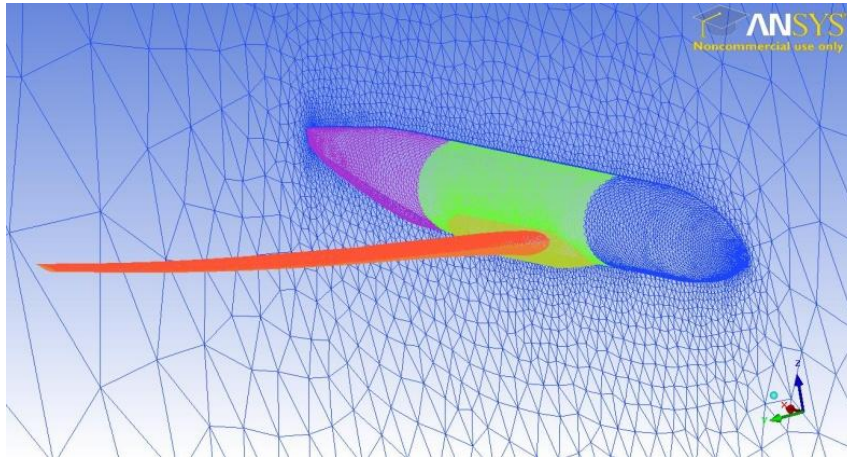


Fig. 3.19 Wing and Body Common Research Model

The CFD results, performed at cruise condition, were characterised by strong shocks on the inboard side of the pylon, on the junction between the pylon/nacelle and the pylon/wing.

Fig. 3.20 shows that this led to a flow separation, making this configuration unusable to estimate the typical PSI interference effects, given that the drag extracted will be too large compared with a “standard” installation.

To reduce or eliminate these installation issues several pylon geometry modifications were investigated. Figure 3.21 shows the engine modifications made on the early version MkI to obtain the final engine installation configuration MkII.

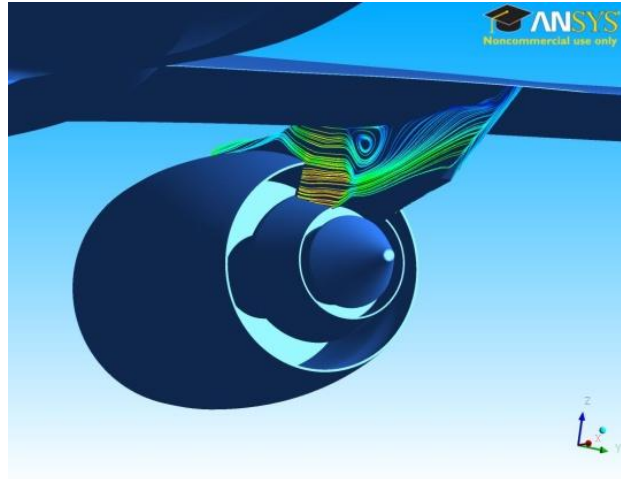


Fig. 3.20 Surface stream lines on the inboard side of the pylon.

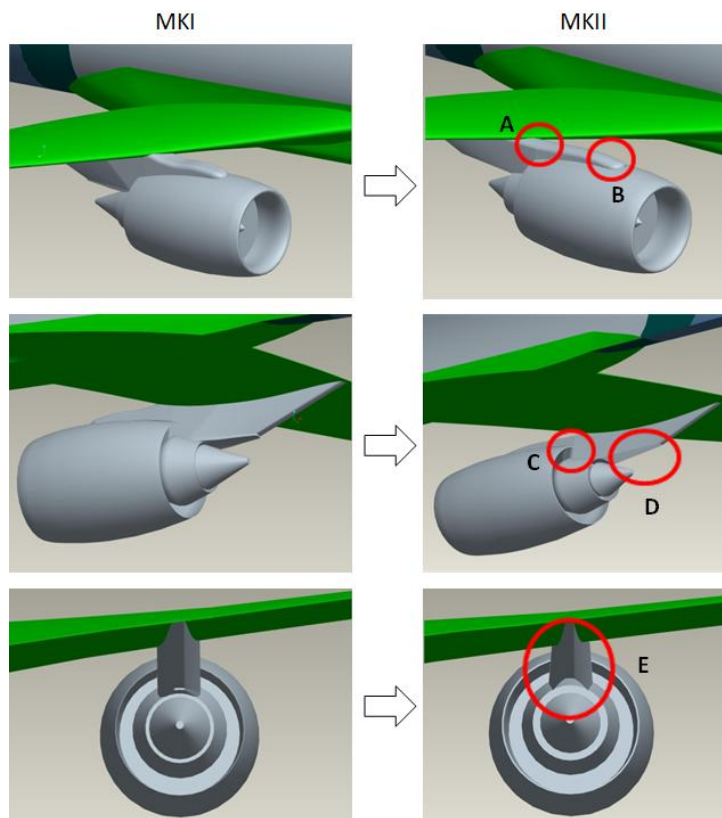


Fig. 3.21 Pylon modifications from version MkI to MkII

The profile of the MkII pylon forepart presents a smoother junction between the nacelle and the pylon (fig.3.20 detail A) and between the pylon and the wing (fig.3.20 detail B). This is to avoid fast flow acceleration/deceleration with possible flow separation and/or shocks that can decrement the aerodynamic performances.

The profile was also designed to avoid a sharp transition between the fore-pylon and the aft-pylon. In order to reduce the hot-flow Mach number, the aft-pylon presents a higher angle between its underside and the axial flow direction (fig.3.21 detail D). The pylon root section was also reduced to increase the channel between the engine and the fuselage fairing (fig.3.21 details C, E), thereby reducing the flow velocity in this region.

The modifications to the pylon geometry had improved the aerodynamics and as can be seen from fig.3.22, the flow separation on the inboard side of the pylon has disappeared.

To evaluate the performance improvement the ratio of Net Propulsive Force (NPF), as defined in chapter 1, over the Net Thrust (F_n) was evaluated for the two configurations: MkI and MkII. The MkI configuration presented a NPF/ F_n of 0.972 and the MkII a NPF/ F_n of 0.964. These values don't account for the whole drag/force variation, given that following the thrust-drag bookkeeping, only the surface scrubbed by the engine exhausts is part of the NPF, the rest is part of the aircraft drag variation. Even if out of the contest of this project, it was evaluated that the aircraft drag reduced from 0.0422 to 0.0385, going from engine installation MkI to MkII, confirming the importance of a well-integrated propulsive system.

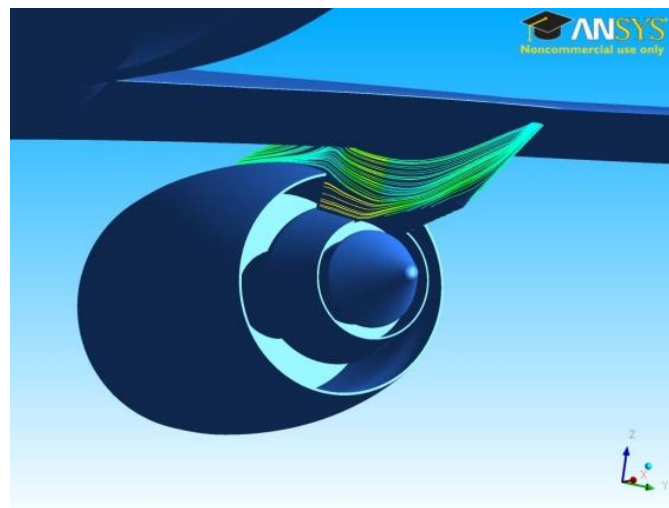


Fig. 3.22 Surface streamlines on the inboard side of the pylon

The aerodynamics of this refined configuration was considered satisfactory, and although further refinement could decrease the installation effects, it was used as the standard geometry to perform CFD calculations and to generate the correlations necessary to update the PSI module. The same procedure was applied to the two future engines as part of the NEWAC project (Wilfert, 2007), described in the next chapter.

4 NEWAC ENGINES INTEGRATION

The procedure previously described was applied to two engines developed within NEWAC (Wilfert, 2007) (New Aero engine Core Concepts, a European Sixth Framework Programme). The aim of this work was to correctly assess the engine performance, taking into account the engine-airframe integration effects. This section presents results for the: Intercooled Core Long Range (IC L/R) and the Active Core Short Range (AC S/R). These engines were selected as they are respectively the biggest and the smallest NEWAC engines.

The Intercooled Core (IC) engine is a three-shaft direct drive high bypass ratio turbofan (fig.4.1). It is mainly characterized by an intercooler that allows very high overall pressure ratios, leading to fuel burn improvements and increasing turbine expansion ratios (Wilfert, 2007).

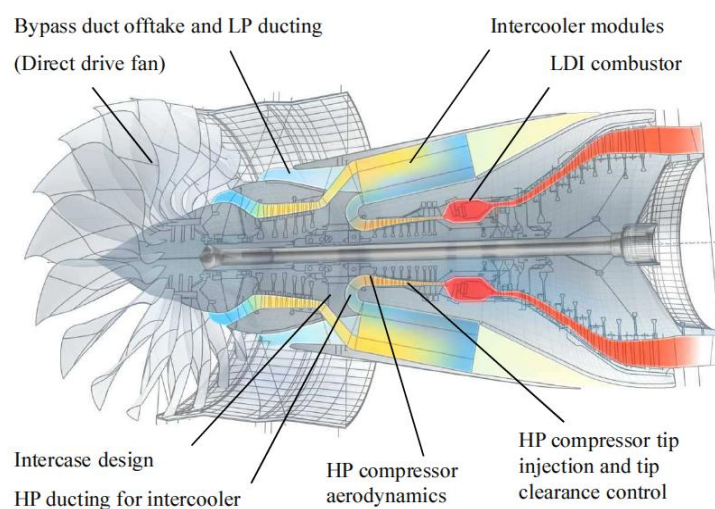


Fig. 4.1 Intercooled Core layout and its new technologies.(Wilfert, 2007).

The Active Core (AC) is a two-shaft geared high bypass turbofan (fig.4.2). The actively controlled core can be adapted to each operating condition, reducing fuel burn, and compensates the loss of efficiency due to deterioration (Wilfert, 2007).

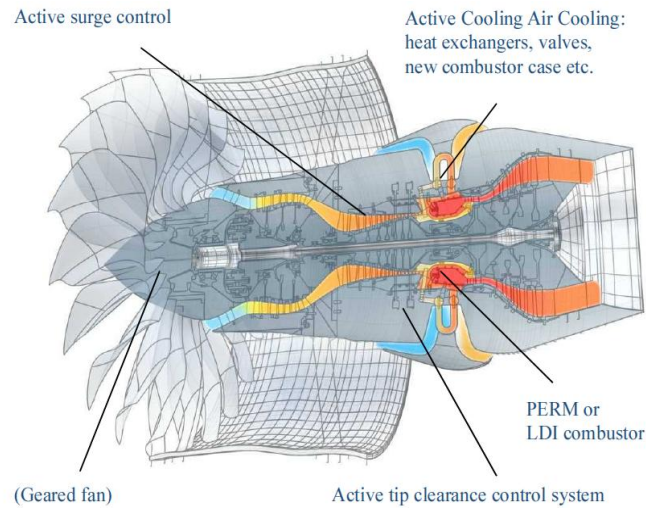


Fig. 4.2 Active Core layout and its new technologies. (Wilfert, 2007).

The input files (Longeville, 2007; Andreoletti, 2007) necessary to apply the geometry generation methodology to the AC S/R are summarized in fig.4.3 and table.4.1. No input data for the nacelle geometry was available.

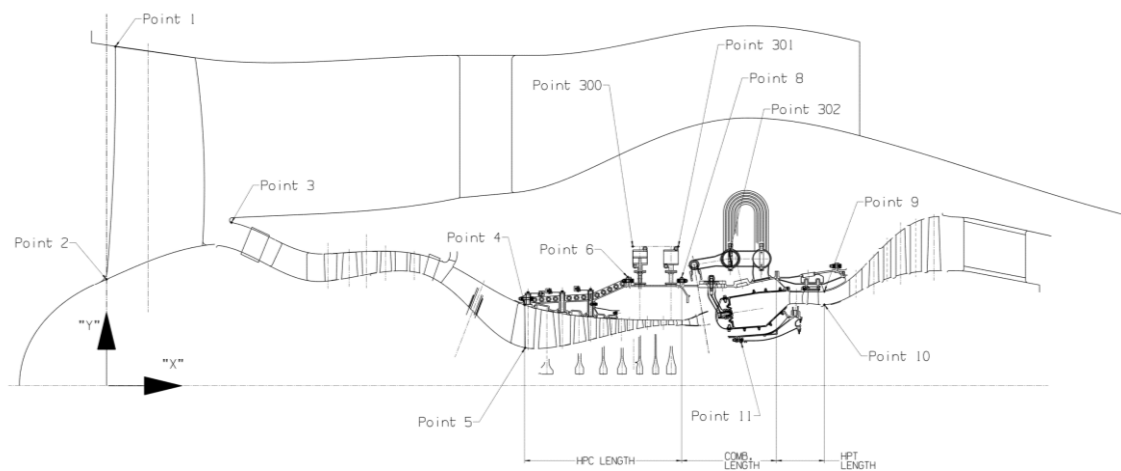


Fig. 4.3 AC S/R – Location of engine layout constraints. (Longeville, 2007; Andreoletti, 2007)

Axial datum (X=0.0) at LPC fan root					
Sub-assembly	Point	Description	X +ve: downstream -ve: upstream	Y (From engine CL)	Comments
Fan	1	LE tip	26	975	
	2	LE root	0	305	
	3	Splitter OD	360	469	
HPC	4	HPC entry OD (annulus)	1206	232	
	5	HPC entry ID (annulus)	1207	109	
	6	HPC Casing OD	1503	312	
	8	HPC Casing OD	1658	310	
HPC Active Tip Clearance Control system (ACC)	300	Forward outer point of "Keep Out Zone"	1517	400	
	301	Rearward outer point of "Keep Out Zone"	1648	400	
Heat exchanger	302	Plenum ACAC OD	1799	393	ACAC=Air cooled Air Cooler
HPT	9	HPT Exit OD	2070	271	
	10	HPT Exit ID	2070	232	
Combustion Chamber	11	Comb. Casing ID	1830	124	
HPC	NA	HPC axial length ("flange-to-flange")	Axial length = 452		
Combustion Chamber	NA	CC axial length ("flange-to-flange")	Axial length = 273		
HPT	NA	HPT axial length ("flange-to-exit")	Axial length = 138		

Table 4.1 AC S/R – Geometric dataset (mm). (Longeville, 2007; Andreoletti, 2007)

The input files necessary to apply the geometry generation methodology to the IC L/R are summarized in fig.4.4 and table 4.2.

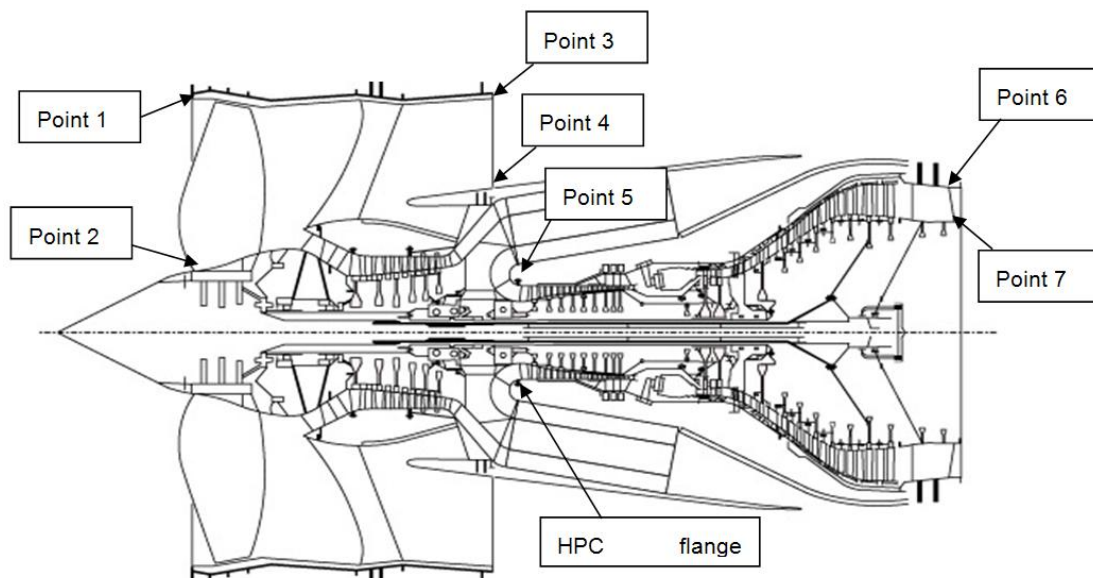


Fig. 4.4 IC L/R - Location of engine layout constraints. (Longeville, 2007; Andreoletti, 2007)

Number in Fig	Length* [m]	Radius** [m]	Description
1	1,370	1,425	Front flange.
2	1,422	0,370	Fan hub at leading edge.
3	3,124	1,510	Back of fancase outer.
4	3,124	0,911	Back of fancase inner.
5	3,264	0,295	HPC Flange Section
6	5,613	0,829	Tail bearing housing vane at trailing edge tip.
7	5,648	0,621	Tail bearing housing vane at trailing edge hub.

* Referred from intercept point: where the engine centre-line meets the line connecting the intake highlight at top and bottom dead centre position.

** Referred from the engine centre-line.

Table 4.2 IC S/R Geometric dataset [m]. (Longeville, 2007; Andreoletti, 2007).

Nacelle geometry input data was also available and are presented in fig.4.5 and tab. 4.3.

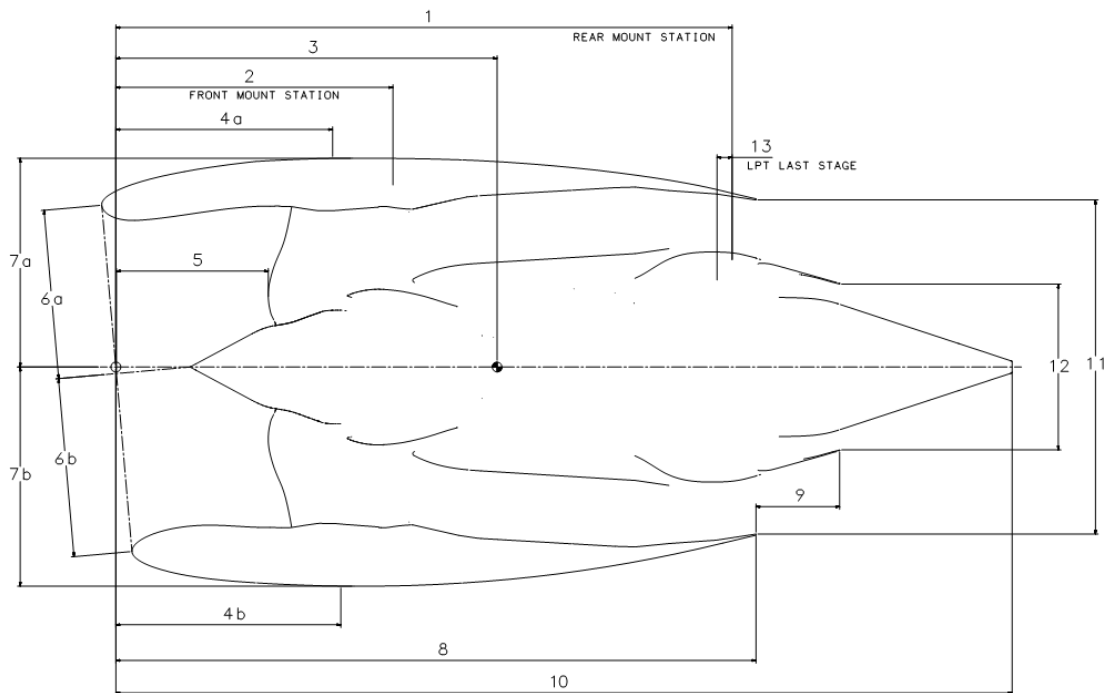


Fig. 4.5 IC L/R Nacelle Geometry input data. (Longeville, 2007; Andreoletti, 2007).

Propulsion System Geometry

Number	Length [m]	Description
1	5,485	Rear mount station centre (from intercept*).
2	2,466	Front mount station centre (from intercept).
3	TBA	Centre of gravity (from intercept).
4a	1,929	Upper forebody length.
4b	2,003	Lower forebody length.
5	1,351	Fan leading edge at bulge (from intercept).
6a	1,498	Intake upper radius (highlight to droop line).
6b	1,585	Intake lower depth (highlight to droop line).
7a	1,852	Nacelle radius.
7b	1,943	Nacelle lower depth
8	5,696	Nacelle length (from intercept).
9	0,745	Afterbody length.
10	7,976	Engine length (Intercept to plug end).
11	2,962	Cold nozzle diameter.
12	1,471	Hot nozzle diameter.
13	0,135	End of last LPT stage to centre of Rear mount station.

*Intercept - where the engine centre-line meets the line connecting the intake highlight at top and bottom dead centre position.

Table 4.3 IC L/R Propulsion system geometry. (Longeville, 2007; Andreoletti, 2007).

Performance data for both configurations was necessary to provide boundary conditions for the CFD calculations and to define the nacelle geometries. The data was extracted from the deliverable D1.1.1.A and is presented for the AC S/R in tab. 4.4 and tab 4.5, and for the IC L/R in tab. 4.6 and tab 4.7.

	Type Test	ICAO Points, ISA; SLS				Cruise	descent idle	Low idle		Altitude windmilling (1)	Altitude windmilling (2)
		100%	85%	30%	7%						
Case	16	5	6	7	8	4	12	13		14	15
DTAMB	10	0	0	0	0	0	0	0	X	0	0
Ma	0	0	0	0	0	0.82	0.82	0	X	0.67	0.86
Altitude ft	0	0	0	0	0	35000	35000	0	X	30000	30000
Thrust [lbf]	33700	31340	26640	9405	2195	5000	0	728			
WFE [lb/hr]	9217	7831	6368	1856	577.8	2402	452	661			
W30 [lb/s]**	66.8	64.70	57.10	27.63	11.07	24.87	7.43	5.79	X ***	1.1	1.6
P30 [psi]	609.8	565.6	484.7	196.4	70.63	201.2	49.9	40.29	X ***	4.8	5.8
T30 [K]	917	863	822	633	487	750	522	411	X ***	260	274
AFR	26.09	29.73	32.29	53.59	68.96	37.26	60.09	52.50			
P40 [psi]	583.2	540.3	462.7	186.7	67.28	192.1	47.64	38.94			
T40 [K]	2083	1919	1814	1294	1022	1640	1130	1085			
outer bleed *	6.19	5.98	5.29	2.56	1.02	2.30	0.69	0.54			
inner bleed *	7.01	6.79	6.00	2.90	1.16	2.61	0.78	0.61			
Overall PQ	41.6	38.6	33.1	13.4	4.82	39.0	9.30	2.75			

Table 4.4 AC S/R Engine performance data, part I (Longeville, 2007; Andreoletti, 2007)

NEWAC AC-GTF S/R

Parameter	unit	Take-off	Top of Climb	MidCruise
Altitude	ft	0	35000	35000
Mach No.	-	0.25	0.78	0.78
DTAMB	K	15	10	0
BPR	-	13.4	11.8	13.0
OPR	-	36.7	47.0	39.0
Net thrust	lbf	22680	6320	4950
SFC	lb/lbf/hr	0.3507	0.5103	0.4853
Fan dia	inch	75.1		
Fan mass flow	kg/s	522.2	216.2	207.9
Fan OD PR	-	1.461	1.585	1.485
Fan OD Tip speed actual	m/s	325	335	305
Fan ID PR	-	1.283	1.358	1.297
LPC inlet pressure	kPa	135.5	48.31	46.15
LPC inlet temperature	K	332	263	266
LPC PR	-	2.07	2.55	2.23
HPC inlet pressure	kPa	279.8	121.8	101.8
HPC inlet temperature	K	415	376	342
HPC PR	-	13.9	13.7	13.6
HPC inlet mass flow	kg/s	36.31	16.84	14.85
W HPC exit	kg/s	35.84	16.17	14.21
W CAC exit	kg/s	28.67	12.85	11.28
CAC exit pressure	kPa	3876	1673	1387
CAC exit temperature	K	895	822	750
P main BPD	kPa	153.5	56.03	52.53
T main BPD	K	344	295	277

Table 4.5 AC S/R Engine performance data, part II. (Longeville, 2007; Andreoletti, 2007).

	unit	Type Test	ICAO Points, ISA; SLS				Cruise	descent idle	Low idle
			100%	85%	30%	7%			
Case		6*	11	13	15	18	22	26	21
DTAMB		15	0	0	0	0	0	0	0
Ma		0	0	0	0	0	0.85	0.85	0
Altitude	ft	0	0	0	0	0	35000	43100	0
Thrust	lbf	81154	73130	62161	21940	5119	11500	-	2736
WFE	lb/hr	21987	18570	15251	5074	1602	5756	487	1142
W30	lb/s	163	157	139	63	27	57	10	21
P30	psi	1097	1002	863	351	136	343	39	100
T30	K	871	792	765	679	557	713	448	522
AFR		26.5	30.5	32.8	44.4	61.1	35.8	71.5	64.7
P40	psi	1058	966	832	338	131	330	38	96
T40	K	2041	1855	1768	1463	1162	1653	965	1101
outer bleed	lb/s	3.95	3.80	3.36	1.51	0.66	1.38	0.23	0.50
inner bleed	lb/s	14.45	13.89	12.28	5.53	2.40	5.06	0.86	1.82
Overall PQ		74.6	68.2	58.7	23.9	9.2	61.8	10.4	6.8

Table 4.6 IC S/R Engine performance data, part I (Longeville, 2007; Andreoletti, 2007).

NEWAC L/R IC DDTF

Parameter	unit	Take-off	Top of Climb	MidCruise
Altitude	ft	0	35000	35000
Mach No.	-	0.25	0.82	0.82
DTAMB	K	15	10	0
BPR	-	13.09	12.57	14.34
OPR	-	67.1	78.9	62.5
Net thrust	lbf	56670	15140	11500
Power offtake (IP spool)	kW	157	123	123
Customer bleed	lb/s	0	1.85	1.85
SFC	lb/lbf/hr	0.348	0.543	0.493
Fan dia	inch	112	-	-
Fan mass flow	lb/s	2684	1103	1071
Fan tip stage PR	-	1.507	1.577	1.474
Fan hub stage PR	-	1.420	1.520	1.408
IPC inlet pressure	psi	21.8	8.17	7.57
IPC inlet temperature	K	341	296	276
IPC PR	-	4.74	4.81	4.66
IPC mass flow inlet	lb/s	190.5	81.3	69.8
IPC exit temperature	K	552	496	448
HPC inlet pressure	psi	96.5	35.6	33.1
HPC inlet temperature	K	410	370	347
HPC PR	-	10.7	11.9	10.1
HPC inlet mass flow	lb/s	185.4	79.1	67.9
HPC exit temperature	K	835	787	706
HPT inlet pressure	psi	994	409	324
HPT rotor inlet temperature	K	1896	1859	1615
IPT inlet pressure	psi	335	138	109
IPT inlet temperature	K	1466	1430	1237
LPT inlet pressure	psi	176	73	57
LPT inlet temperature	K	1273	1240	1068
IC ΔT hot	K	-142	-126	-101
IC and ducts ΔP hot	%	-6.6	-9.4	-6.2
P main BPD inlet	psi	23.1	8.5	7.9
T main BPD inlet	K	348	302	280
LP speed	rpm	2611	2648	2329
IP speed	rpm	7994	7776	7088
HP speed	rpm	13592	13591	12406

Table 4.7 IC S/R Engine performance data, part II. (Longeville, 2007; Andreoletti, 2007).

It can be seen in fig.4.4 that the Intercooled Core (IC) fan duct geometry is characterised by an air split to allow part of the flow to go through the intercooler and back in the main flow (fig.1). To reduce the computational cost, and the complexity of the model, the split at the intercooler was not considered, keeping all the flow in a single duct. This didn't affect the engine integration effects given that the two flows are pre-mixed before leaving the engine. Simulating the flow in the intercooler will considerably increase the computational cost. The same principle was applied for the Active Core (AC) fan duct but in this case to the Active Cooling Air Cooling (fig.4.2).

The final geometries were obtained applying the methodology presented in chapter 3. The IC L/R was installed on the CRM given that this engine is designed to propel an aircraft with similar characteristics (Airbus A330 type). For the Active Core Short Range (AC S/R) the CRM was geometrically scaled to match the wing area of an A320 type aircraft.

Again the engine was positioned following previous work (Vassberg, 2008) where an empty nacelle was installed on the CRM. The span position was the same but the engine was positioned vertically closer to the wing to increase the ground clearance. This was to account for both the IC and AC engines having larger fan diameters than the engine presented in the previous study.

The full configurations, engine-aircraft, are presented in fig. 4.6 and fig. 4.7 for the IC L/R and AC S/R respectively. To create the correlations, the engines were moved from these starting positions and the corresponding Net Propulsive Force extracted.

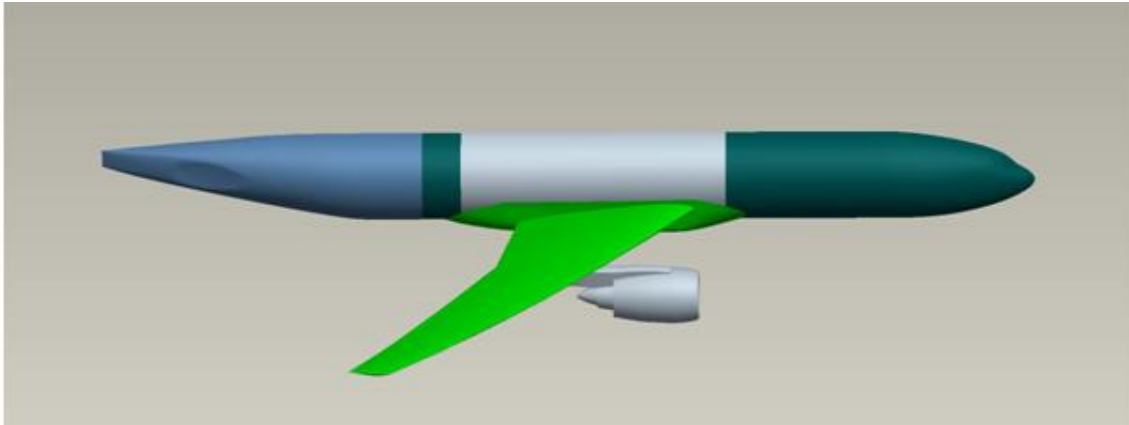


Fig. 4.6 Engine-airframe configuration for the IC L/R

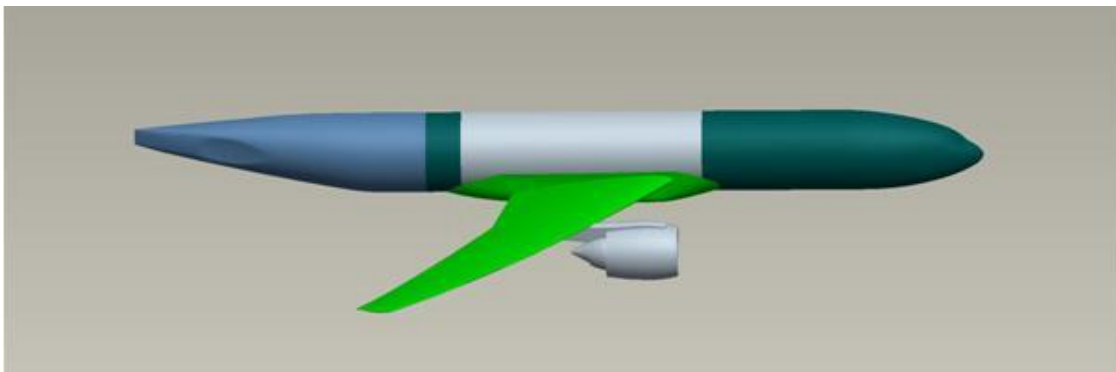


Fig. 4.7 Engine-airframe configuration for the AC S/R

4.1 PSI MODULE CORRELATIONS

To extract the Net Propulsive Force (NPF) data as a function of axial (x) and vertical (y) positions, several CFD calculations were performed which varied the engine location (fig. 4.8). Note that the span-wise position was fixed, given that a variation of this coordinate would require a substantial change to the baseline aircraft geometry (example: rudder size and position) (Oliveira, 2003).

In general the positioning of the engine on the aircraft is a multidisciplinary task, and therefore requires a detailed study. A highly detailed study is outside the scope of this project and therefore the engine position variation was defined following the major constraints presented in previous works (Berry, 1994; De Souza, 2008; Oliveira, 2003). Although aware of the other constraints in this area, the main focus of this work is on the aerodynamic aspects.

The engine position variations for the IC L/R and AC S/R engines are presented in tab. 4.8 and tab. 4.9, respectively. X is the horizontal coordinate from the cowl edge to the wing trailing edge, “ c ” is the mean aerodynamic wing cord, Y is the vertical coordinate from the leading edge to the engine axis, and D is the maximum nacelle diameter (fig. 4.8). For the IC L/R “ c ” is 7.007m and “ D ” to 3.79m. For the AC S/R “ c ” is 4.78m and “ D ” to 2.51m.

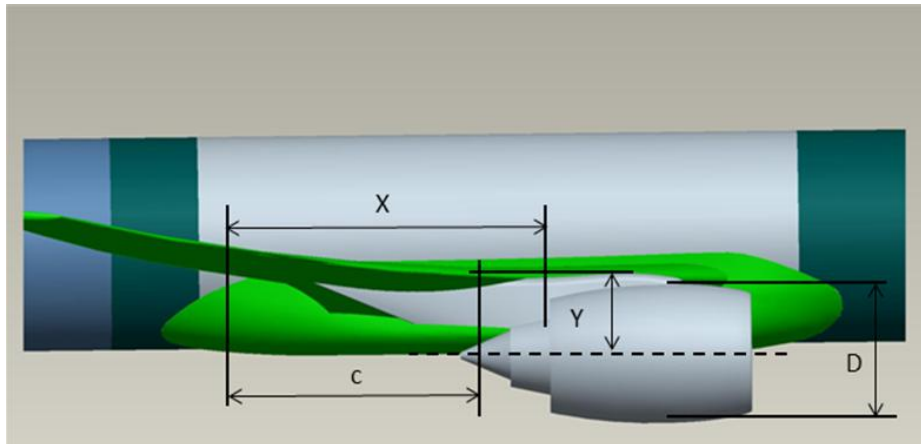


Fig. 4.8 Engine position parameters

	V01	V02	V03	V04
x/c	0.853	1	1.07	1.284
Y/D	0.593	0.593	0.593	0.593
	V05			V06
X/c	0.856			1.284
y/D	0.633			0.633

Table 4.8 IC L/R X and Y engine positions

4.1.1 NUMERICAL METHOD

The numerical method was based on the Reynolds Averaged Navier-Stokes (RANS) equations that were discretised using a vertex-based finite volume method. The Reynolds stresses in the momentum equations, were computed using the Menter’s zonal two equations SST turbulence model (Menter, 1994). Chapter 2 paragraph 2.1.3 gives a more detailed description of the model.

The grids were hybrid type and were constructed following the basic gridding guidelines proposed by Mavriplis, (2009), following the experience gained within the Drag Prediction Workshops (see chapter 2). The grids had approximately 14×10^6 elements and 5×10^6 nodes for all the configurations.

	V01	V02	V03	V04
x/c	0.856	0.958	1.062	1.167
y/D	0.557	0.557	0.557	0.557
	V05			V06
x/c	0.853			1.167
y/D	0.617			0.617

Table 4.9 AC S/R X and Y engine positions

The Reynolds number for both configurations, based on the mean aerodynamic chord, was $Re = 5 \times 10^6$, and the cruise lift coefficient was $C_L = 0.5 \pm 0.02$.

4.1.2 RESULTS

The ratio of the Net Propulsive Force (NPF) to the Net Thrust (F_n) values as a function of the axial position (x/c) for the IC L/R and AC S/R configurations are presented in fig. 4.9. Fig. 4.10 shows the same variable but as a function of the vertical position (y/D) for the IC L/R and AC S/R. The correlations coming from these results will be used as inputs for the PSI module.

The Active Core Short Range (AC S/R) presents a 7.3% of increase of the NPF/F_n , between the extreme horizontal positions, while the Intercooled Core Long Range (IC L/R) presents a 5.7% of increase. Remembering that the IC L/R is characterised by a bigger diameter compared to the AC S/R but is installed on a bigger aircraft, the differences in NPF/F_n are mainly due to the dissimilar nacelle length that allows the AC S/R to be positioned closer to the wing. In particular, the trends are similar in the range $0.96 < x/c < 1.16$.

It is possible to see that the NPF force tends to match the uninstalled value when the engine is positioned far from the aircraft, and in particular at the

maximum axial positioning. The NPF is nearly constant for the different vertical positions (fig.4.10, 4.11). This is also confirmed by previous studies (Oliveira, 2003; Rossow, 1992).

Therefore the PSI module only takes into account the horizontal positioning (x/c) dependency. Furthermore, feasible vertical positions are also limited by additional installation issues which are beyond the scope of this preliminary study. Note that the studied range of movement happened to be greater for the x dimension, predominantly due to the ground clearance constraint.

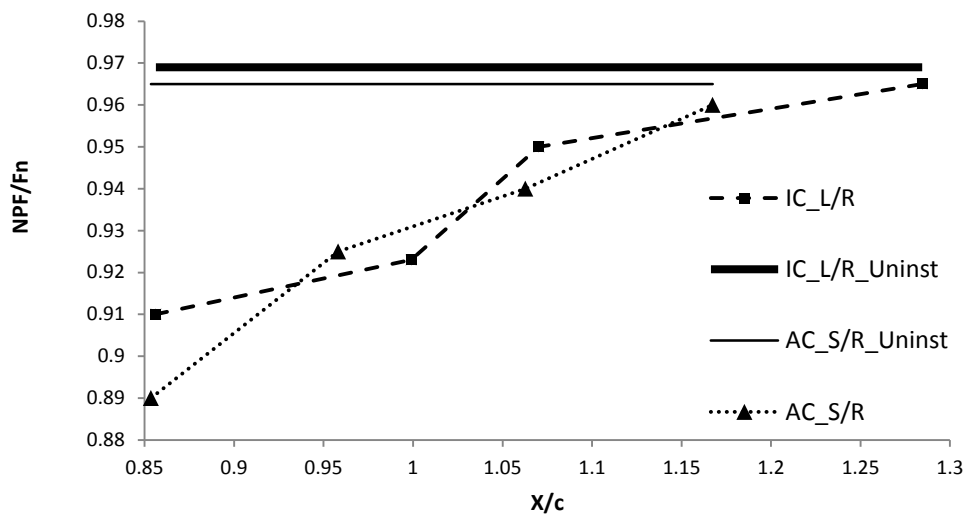


Fig. 4.9 NPF function of horizontal position for the IC L/R and AC S/R

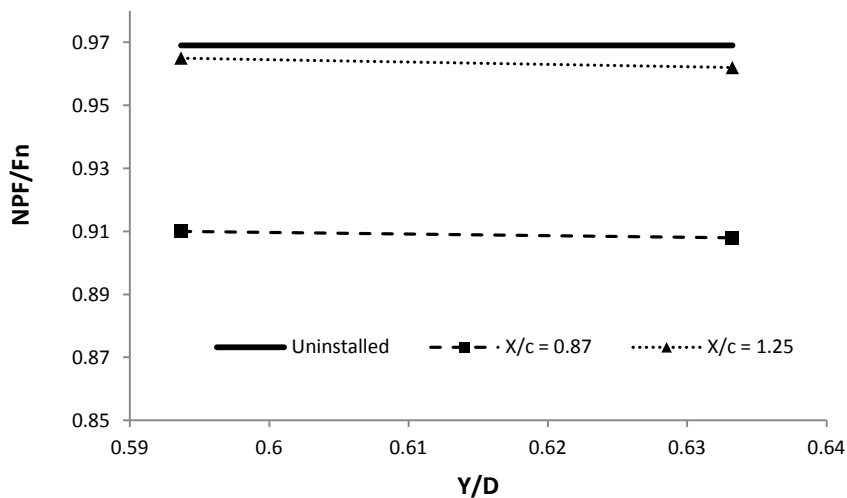


Fig. 4.10 NPF function of vertical position for the IC L/R

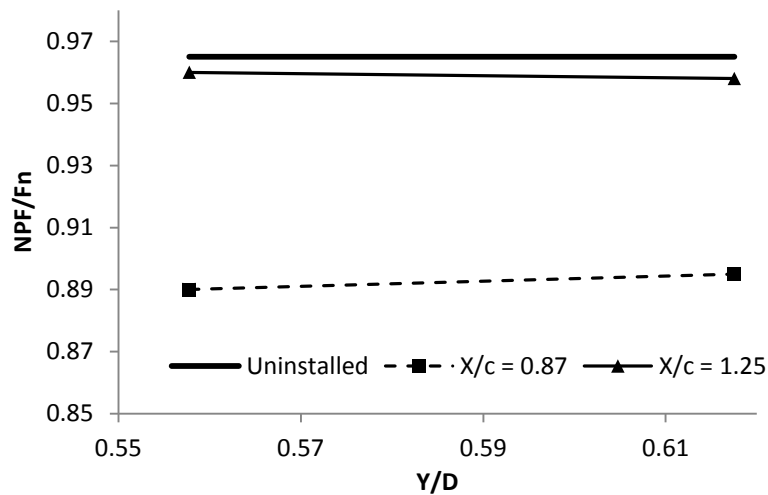


Fig. 4.11 NPF function of vertical position for the AC S/R

These performance changes are reflected on the flow results and in particular the effects of the engine positioning can be seen analysing the pressure field variations due to the installation of the engine for the different configurations.

The pressure contours for IC V01 (min x) are presented in fig.4.13, and for IC V04 (max x) in fig.4.14. The Active Core engine's pressure contours are presented in fig. 4.15 for the AC V01 (min x) and fig. 4.16 for the AC V04 (max x). It is noticeable that the closer position of the engines, versions 01, (fig. 4.13 & 4.15) induced a higher suction peak on the upper surface of the wing just above the nacelle, due to the stronger interaction between the propulsive system and the airframe.

However to provide a stronger link to the performance trends it is necessary to get a closer look plotting the pressure coefficient around selected wing span locations (fig.4.6), for the extreme vertical and horizontal positions. The sections at eta = 0.3 and 0.4 are respectively placed on the closer inboard and outboard side of the pylon, to capture the local effect of the engine installation. The sections at eta = 0.1 and 0.7 are placed relatively far from the engine to evaluate the effects moving away from the engine. Note that eta is commonly defined as the ratio of y position and wing span.

Four both IC L/R and AC S/R, version 04 is compared with version 01 to assess the horizontal influence, and version 06 is compared with version 04 for the vertical influence. As a reference all the versions are compared with the clean wing configuration (WB).

From all of the pressure coefficient plots it is clear that the presence of the engine strongly affects the pressure field and in particular around the engine and wing junction. From fig. 4.18 it can be seen that moving the engine downstream (from V04 to V01) the pressure coefficient on the upper wing presents an increased suction peak with a downstream shift of the upper wing shock wave (pressure front moves following the black arrows fig.4.18). This was also observed by Rossow (2002), as described in chapter 2. This can be seen as a reduction on the engine installation effects, given that the pressure coefficient tends to match the wing alone configuration. However looking at the lower wing surface, the closest engine installation of V01, strongly affects the pressure coefficient, resulting in a marked reduction of the pressure coefficient on the whole pressure side. This is due to the reduction of the cross section of the channel between the engine, wing and fuselage, which will increase the flow speed on the inboard side of the pylon, with a consequent impact on the aerodynamic field around engine and wing. Positioning the engine in the vicinity of to the wing, results in an overall reduction of the pressure coefficient, similarly to the decrease on NPF presented in fig.4.11.

The wing pressure coefficient on the outer side of the pylon (fig.4.19), presents similar variations due to horizontal engine positioning, but with reduced amplitude comparing the installed configurations, similarly to the results presented by Rossow (2002). However both WBNP configurations present a much lower pressure coefficient on the suction side, compared to the WB configuration. This can be reduced redesigning the wing profile around the engine.

The pressure coefficient plots at section $\eta=0.1$ and $\eta=0.75$, respectively the far inboard and outboard sections, (fig.4.17 and 4.20) show a less pronounced change on the pressure field due to the engine installation

compared to the sections near the engine. However the inboard section pressure field is still affected by the engine installation, especially on the lower wing surface, being included in the channel created between the engine and the fuselage. Looking at the far outboard section, (fig.4.20), the engine installation is almost only affecting the upper wing surface, and given that most of the flow on the upper surface of the wing is supersonic, the disturbances caused by the presence of the engine will be restricted to a Mach cone in the immediate vicinity of the installation (Rossow, 1992).

Figures 4.21 to 4.23 show the pressure coefficient comparison between V04 and V06 to assess the vertical positioning effects. It can be seen that moving the engine closer to the wing (V04) leads to an upstream shift of the shock wave on the upper wing surface. On the lower wing the pressure peaks are less pronounced for V06, resulting in a pressure coefficient more similar to the WB configuration. Similar results were obtained by Rossow (1994). Furthermore comparing fig. 4.18 with fig.4.22 it can be noticed that the pressure coefficient plots of the two horizontal positions (fig.4.18), presents a much bigger variation on both upper and lower wing surfaces, compared to the vertical positions (fig.4.22). This is reflected on the results shown in fig.4.9 and fig.4.10 where the NPF is almost constant for the varying the vertical position.

Similar conclusions can be gathered from the AC S/R configurations (fig.4.24 to 4.30). Moving the engine in closer to the wing, results in an overall reduction of the pressure coefficient, similarly to the decrease on NPF presented in fig.4.11. However on a closer look, even if V01 presents a higher suction peak, the front of the upper wing shock is located in a very similar location for both V01 and V04 (fig.4.25) and not on an downstream position moving the engine closer to the wing like the IC L/R. Moreover in fig.4.29 the shock wave on the upper wing surface moves downstream instead of upstream. Additionally from figures 4.26 and 4.30 it can be seen that both WBNP configurations present a closer lower pressure coefficient on the suction side to the WB configuration compared to the IC installations.

It is believed that these variances are due to the dissimilar nacelle dimensions and positioning, aircraft size and flow configuration, but future work should be planned to investigate.

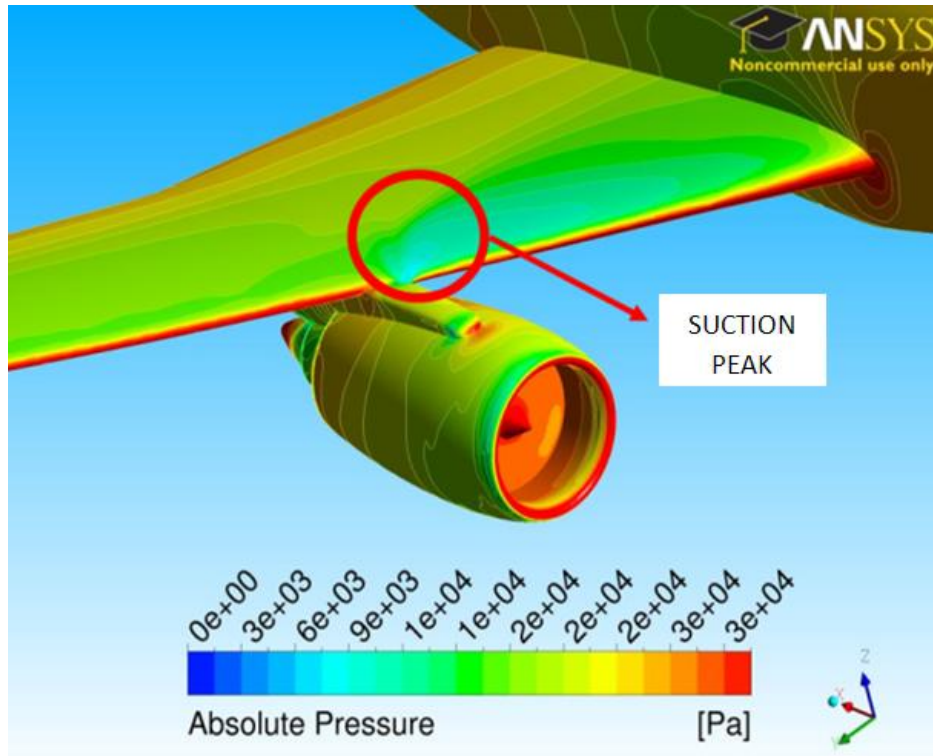


Fig. 4.12 Pressure Contours on IC L/R V01

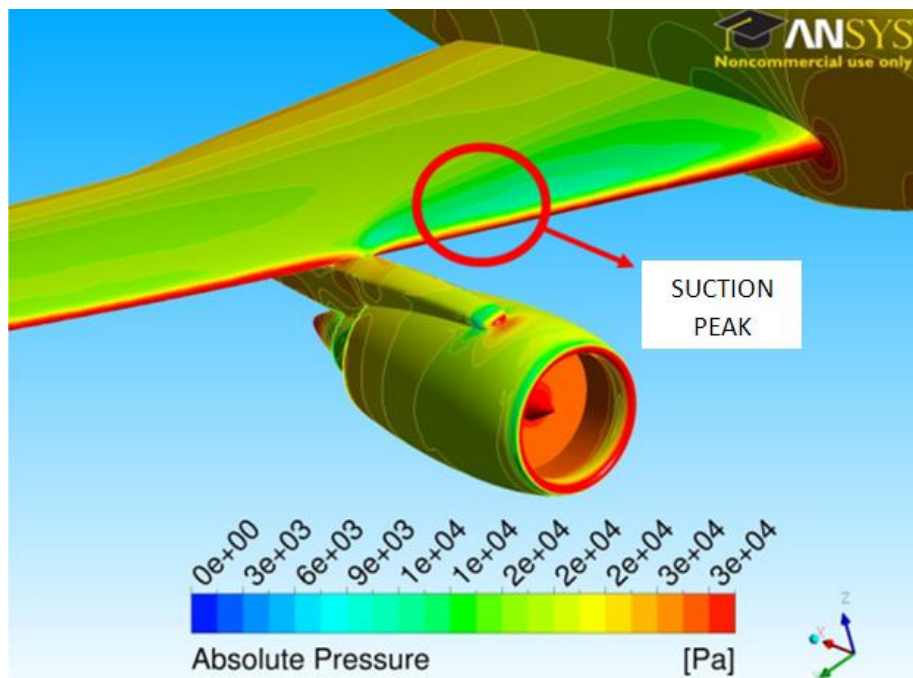


Fig. 4.13 Pressure Contours on IC L/R V04

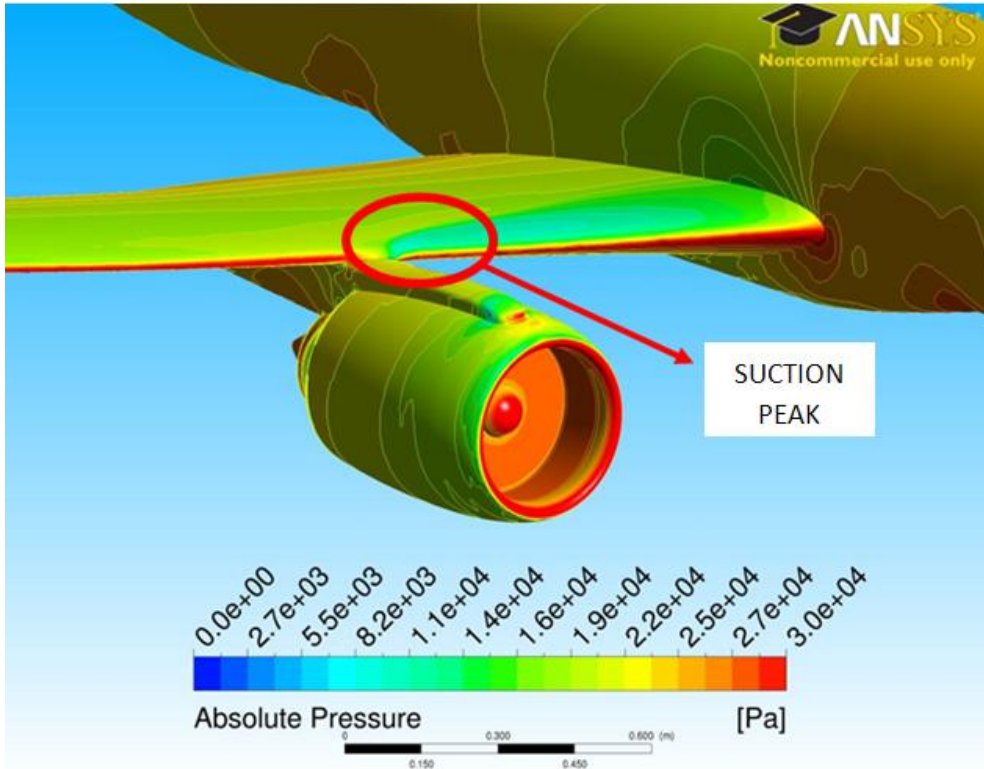


Fig. 4.14 Pressure Contours on AC S/R V01

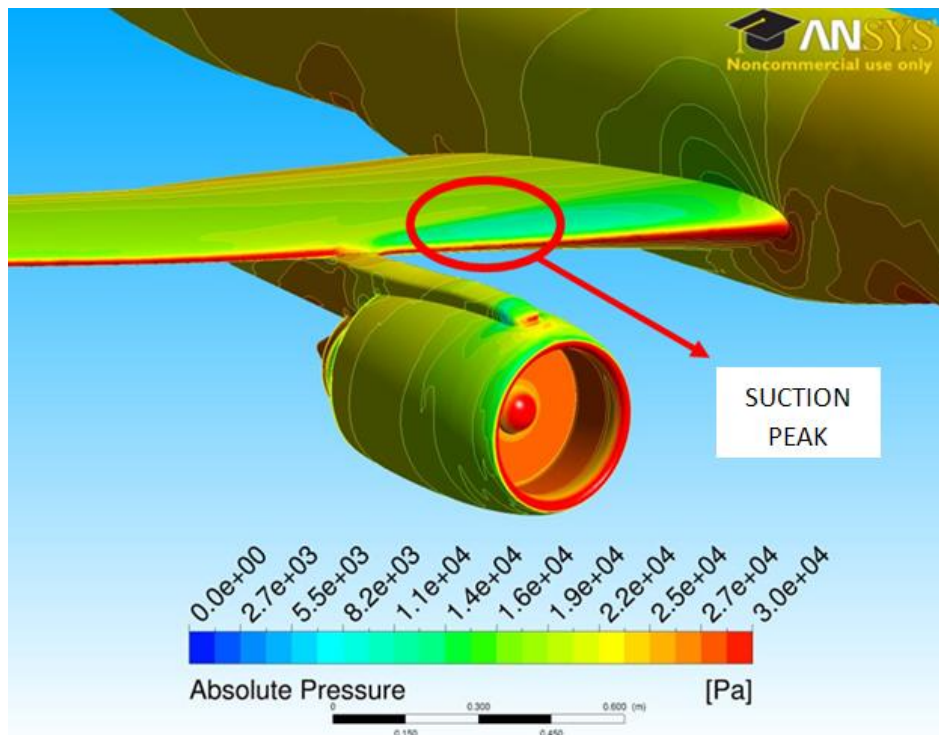


Fig. 4.15 Pressure Contours on AC S/R V04

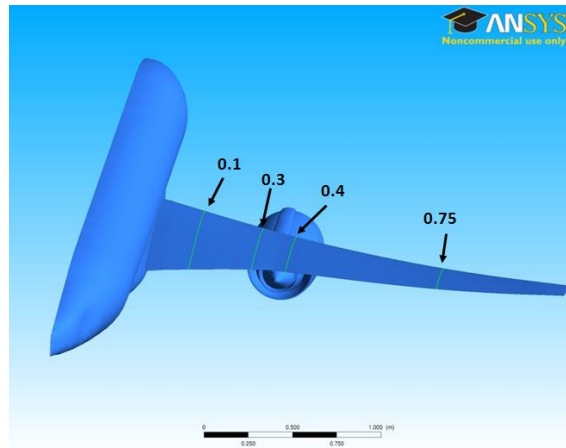


Fig. 4.16 CRM IC L/R and AC S/R pressure taps position (values of eta)

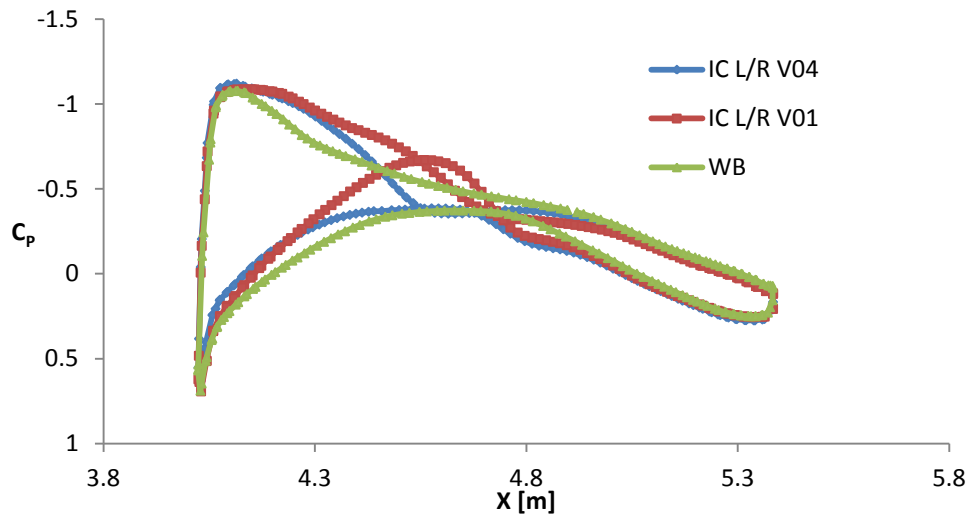


Fig. 4.17 C_p comparison between IC L/R V04, IC L/R V01 and WB at eta 0.1

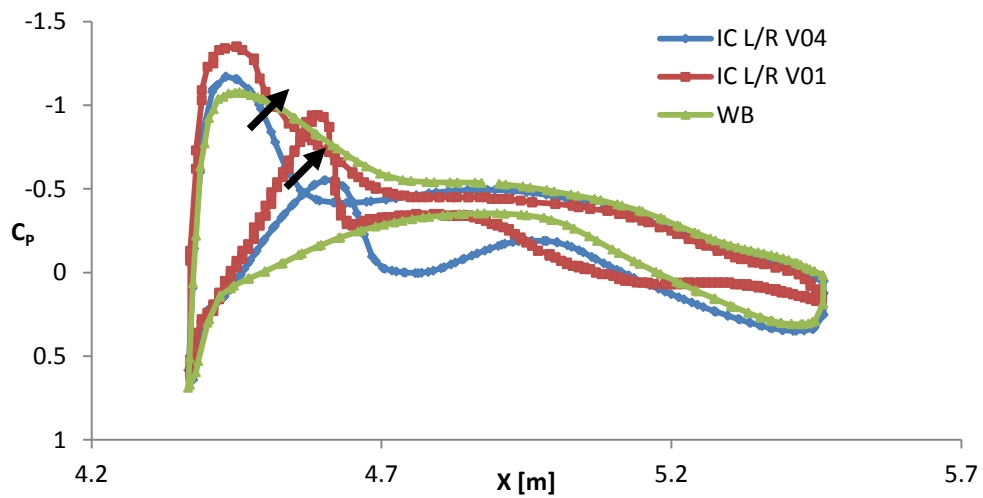


Fig. 4.18 C_p comparison between IC L/R V04, IC L/R V01 and WB at eta 0.3

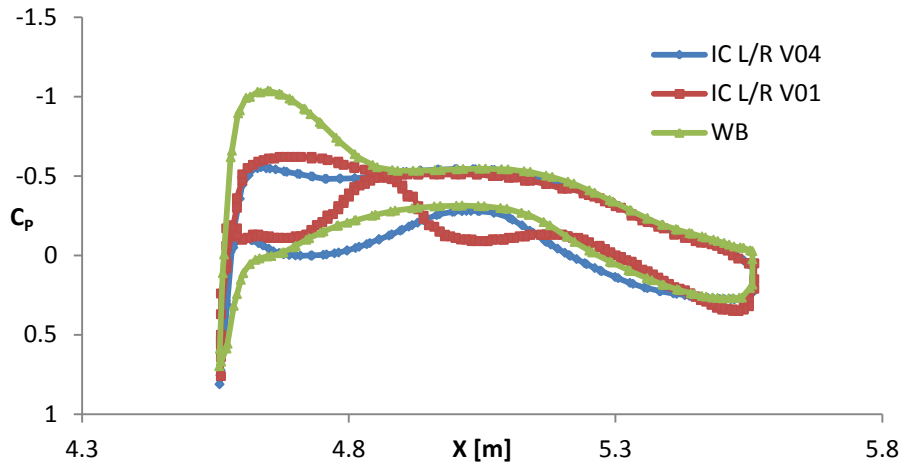


Fig. 4.19 C_p comparison between IC L/R V04, IC L/R V01 and WB at eta 0.4

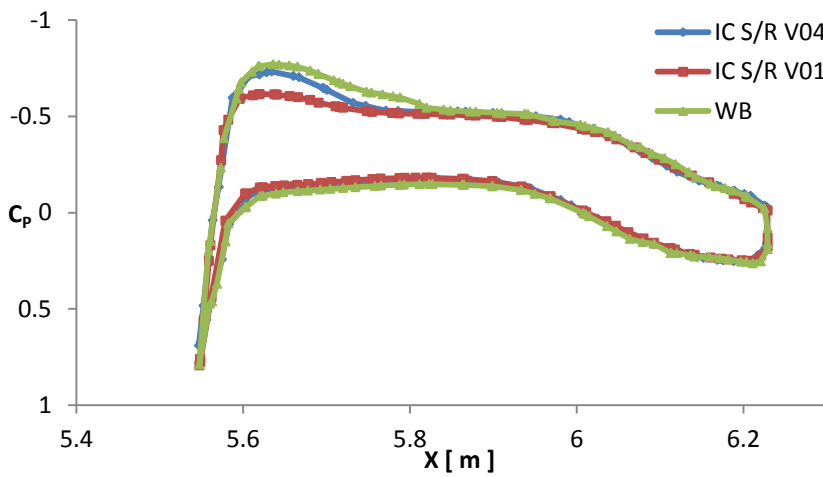


Fig. 4.20 C_p comparison between IC L/R V04, IC L/R V01 and WB at eta 0.75

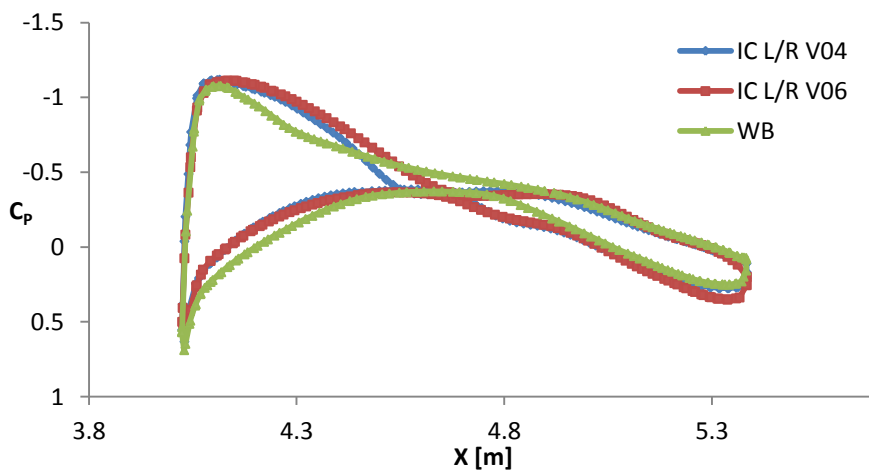


Fig. 4.21 C_p comparison between IC L/R V04, IC L/R V06 and WB at eta 0.1

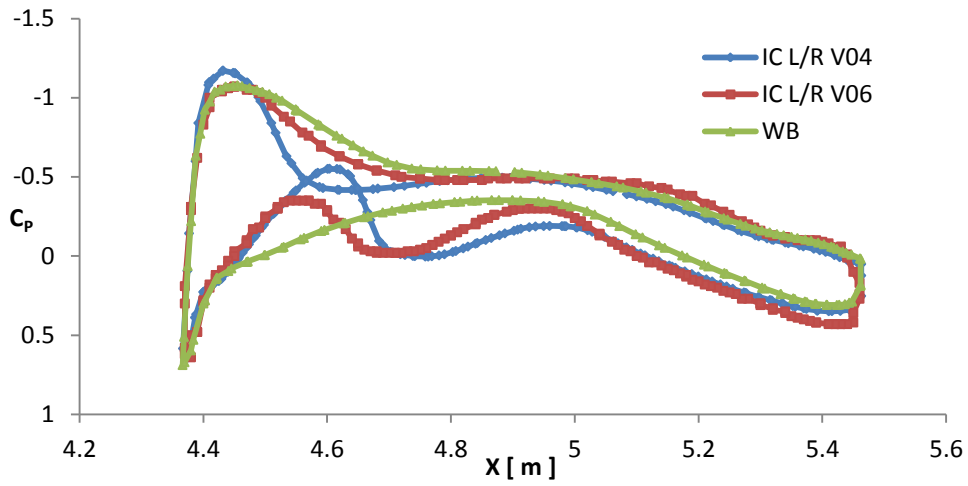


Fig. 4.22 C_p comparison between IC L/R V04, IC L/R V06 and WB at eta 0.3

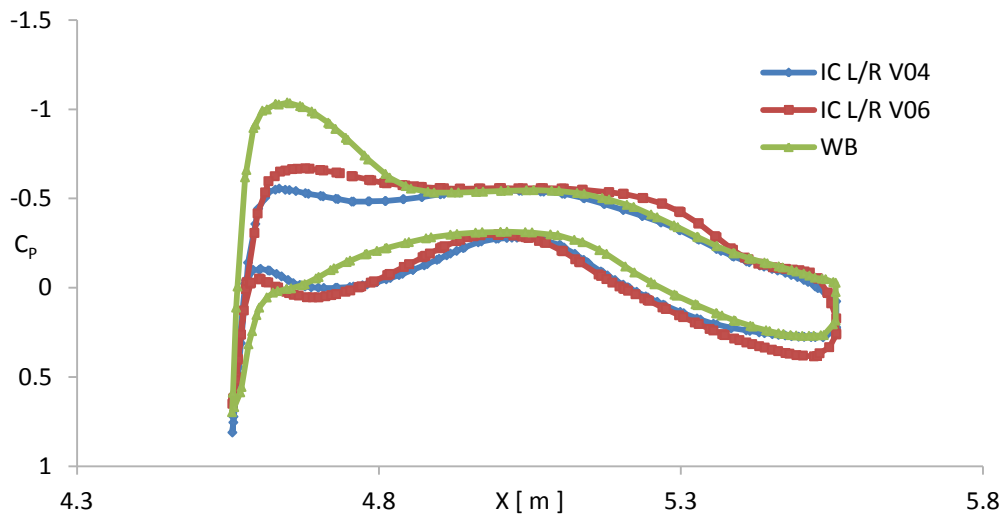


Fig. 4.23 C_p comparison between IC L/R V04, IC L/R V06 and WB at eta 0.4

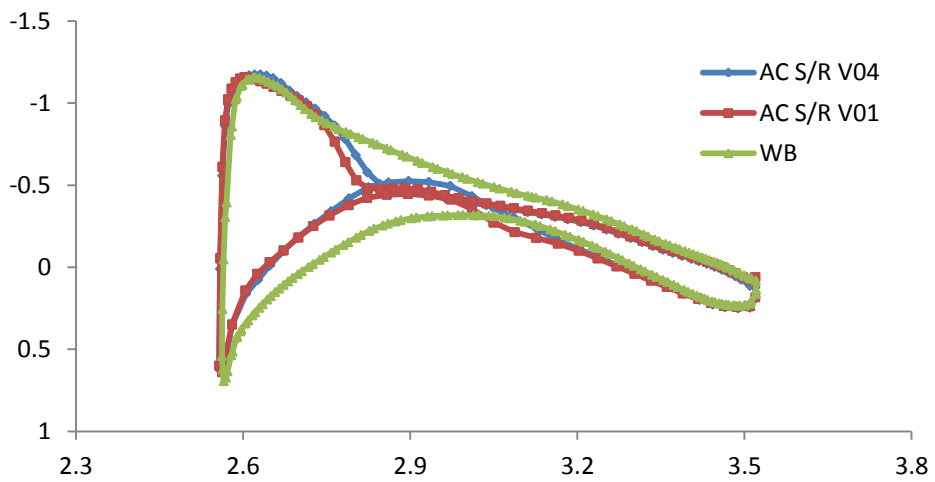


Fig. 4.24 C_p comparison between AC S/R V04, AC S/R V01 and WB at eta 0.1

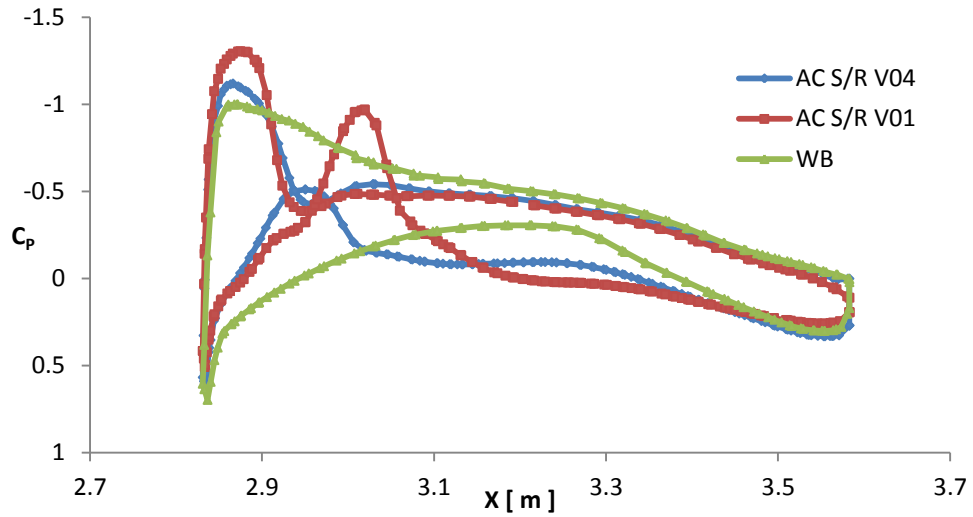


Fig. 4.25 C_p comparison between AC S/R V04, AC S/R V01 and WB at eta 0.3

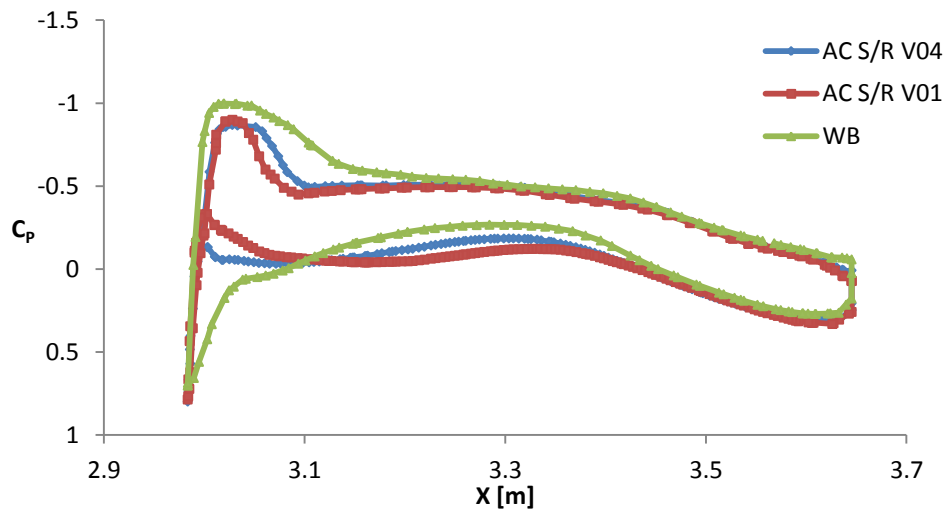


Fig. 4.26 C_p comparison between AC S/R V04, AC S/R V01 and WB at eta 0.4

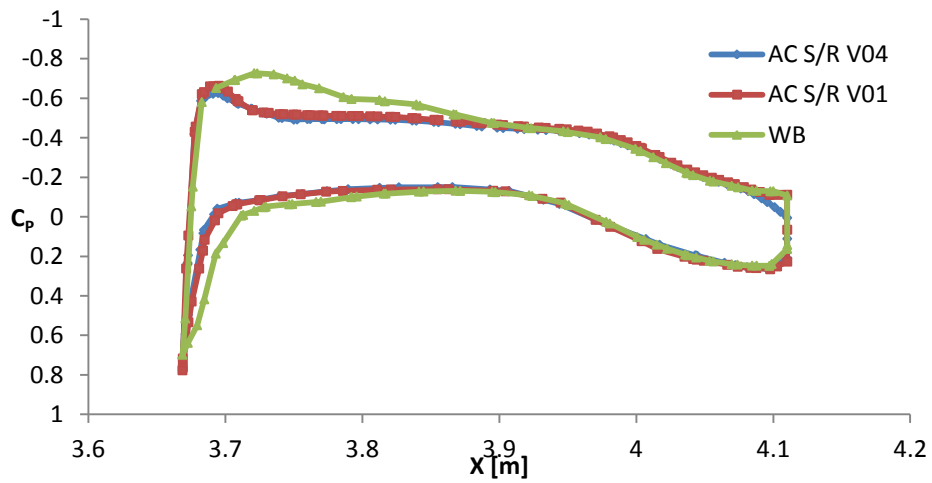


Fig. 4.27 C_p comparison between AC S/R V04, AC S/R V06 and WB at eta 0.75

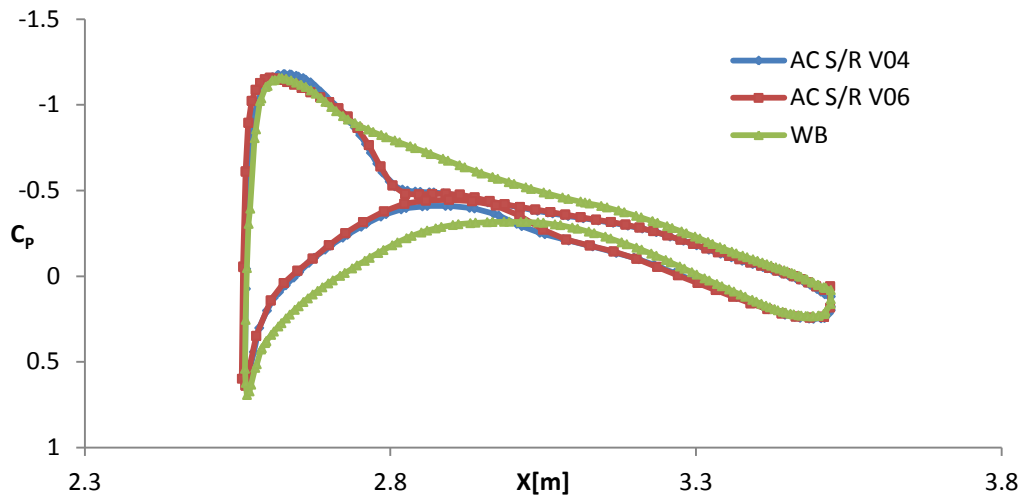


Fig. 4.28 C_p comparison between AC S/R V04, AC S/R V06 and WB at eta 0.1

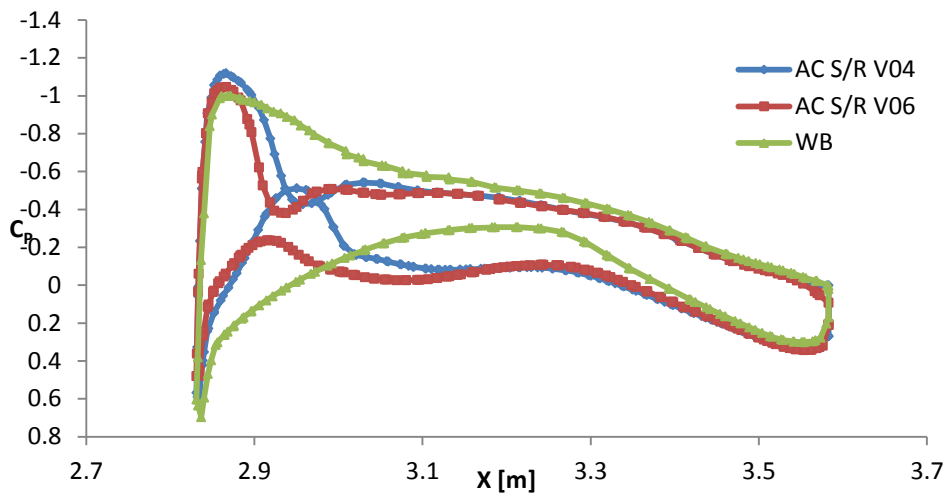


Fig. 4.29 C_p comparison between AC S/R V04, AC S/R V06 and WB at eta 0.3

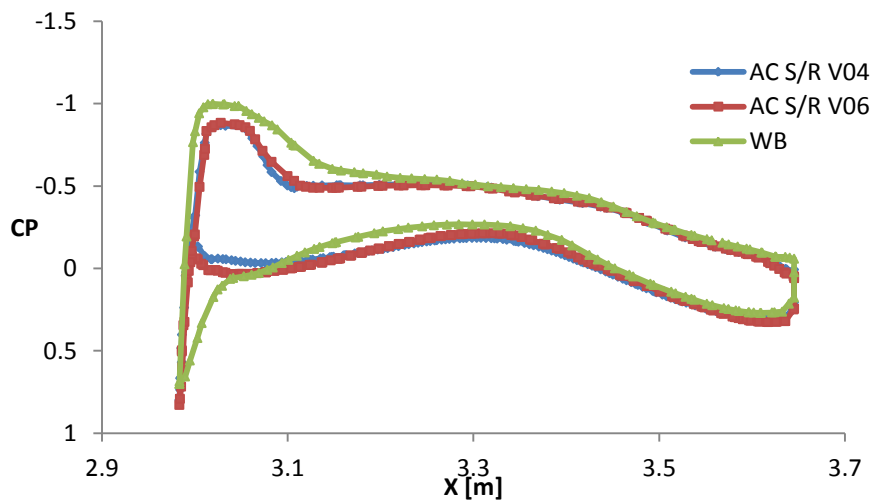


Fig. 4.30 C_p comparison between AC S/R V04, AC S/R V06 and WB at eta 0.4

4.2 PSI MODULE ASSESSMENT

The assessment of the PSI module was done by performing several simulations using the correlations coming from the CFD models, extracted from the data presented in fig.4.9, NPF function of engine position. Currently the module is only capable of taking into account the penalties during cruise; therefore, results are only presented for this part of the mission. Hermes, Turbomatch and the PSI module used the same flight boundary conditions as those applied in the CFD simulations, with a mission fixed range of 3000km for both engines.

The results, shown in fig. 4.29 for the Intercooled Core Long Range (IC L/R) and fig. 4.30 for the Active Core Short Range (AC S/R), illustrate the variation in consumed fuel during the cruise with respect to the engine position. In particular, the IC L/R configuration shows an increase in consumed fuel of 4.2% between the extreme engine positions. The AC S/R configuration shows an increase of 6.4% in consumed fuel between the two maximum horizontal engine positions. It is important to underline that due to physical constraints, the amplitude of the engine displacements were different for the two cases as explained in the previous paragraph.

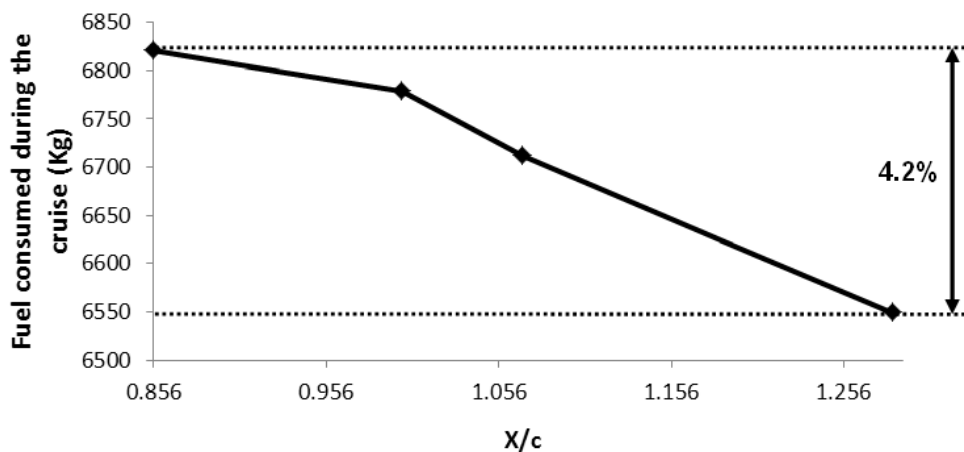


Fig. 4.31 IC L/R Fuel consumed during the cruise function of horizontal position

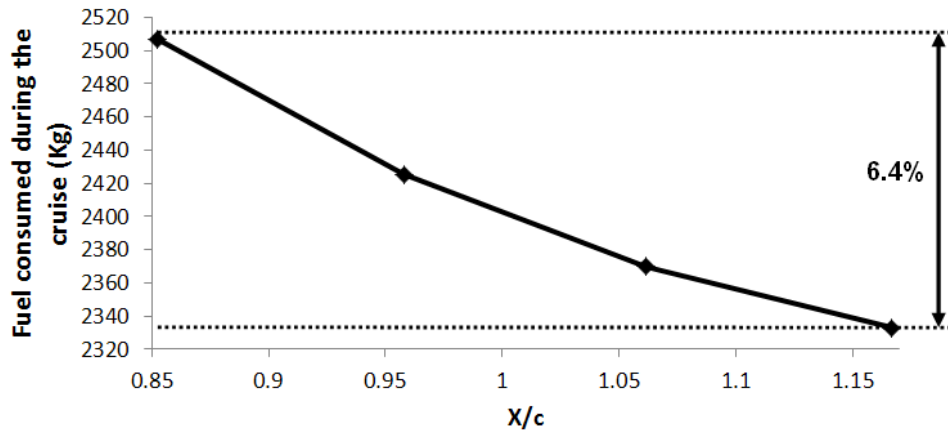


Fig. 4.32 AC S/R Fuel consumed during the cruise function of horizontal position

4.3 CONCLUSIONS & FUTURE WORK

As part of this research, the installation penalties of two novel engines, Active Core Short Range (AC S/R) and Intercooled Core Long Range (IC L/R), were studied, resulting in the development of a new tool which is able to take in to account the variation of Net Propulsive Force (NPF) as a function of engine position.

The Computational Fluid Dynamic (CFD) results, used to update the tool, show similarities with previous studies (Oliveira, 2003; Rossow, 1992), showing the horizontal engine position (x) has more influence on the NPF variance than the vertical (y) engine position.

Two mission simulations have been carried out using the new tool, resulting in increases of 4.2% and 6.4% of used fuel during the cruise with respect to the extreme horizontal positions for the IC L/R and AC S/R, respectively. This underlines the importance of taking into account the installation effects at an early stage, and therefore the need to use such a tool to correctly evaluate the performance of new aircraft-engine configurations.

However, the current study has assumed fixed wing geometry and has not allowed for any reprofiling of the wing to minimise interference effects for particular powerplant locations. It is probable that the reported installation penalties could, in practice, be reduced by detail wing design iterations.

Future work should be carried out to evaluate another engine-airframe integration effect on the aircraft performance: the reduction of lift due to the presence of the pylon and the engine. However, as pointed out, no wing reprofiling has been performed to mitigate PSI effects on the wing performance, reducing the applicability of this methodology for a real engine-airframe application. Nevertheless the present numerical results can be used as a starting point with relatively low amount of work, given that no additional CFD calculations are needed, directly post processing them evaluating the lift reduction. The pressure coefficient comparison study presented in paragraph 4.1 can be considered a starting point for this evaluation.

Due to the lack of available data to generate detailed nacelle and pylon geometry, these are still not totally representative of a “standard” configuration. Further CFD calculations could refine the geometries and improve the quality of the results. For the same reason, to simplify the model the nacelle geometry was taken as being axi-symmetric. To improve the reliability of the results a non-axi-symmetric shape should be designed. This is compulsory for off-design (take-off, landing, climb, descent and engine-off) numerical calculations. At the moment the model is only able to evaluate the NPF variation at cruise condition. Therefore, it is important to look at off-design studies, given that these conditions have a strong impact on the whole aircraft performance. Consequently the next chapter will discuss the engine airframe integration at high-lift conditions.

The pressure coefficient comparisons between the IC and AC showed that positioning the engine in the vicinity of to the wing, results in an overall reduction of the pressure coefficient, similarly to the decrease on NPF. However on a closer look few differences were noticed between the two installations. It is believed that these variances are due to the dissimilar nacelle dimensions and positioning, aircraft size and flow configuration, but future work should be planned to investigate.

According to the extensive literature review performed (see chapter 2), this study can be regarded as the first open literature engine position-NPF parametric study using CFD.

5 HIGH LIFT PROPULSION SYSTEM INTEGRATION

5.1 INTRODUCTION

The previous section was focused on PSI at cruise condition; however other parts of the flight envelope are significantly affected by the presence of the propulsive system. This performance reduction can have a detrimental effect as important as in the cruise condition, considerably reducing the payload. These flight phases are the landing and take-off and are characterized by high-lift aerodynamics.

The main objective of this part of the project is to model the aerodynamics of High lift PSI (HPSI) using CFD, to evaluate lift and drag in a Wing-Body-Nacelle-Pylon (WBNP) configuration at high-angle of attack. This will enable future CFD campaigns to instruct the PSI module. To achieve these objectives, it is essential to understand the multi-element high-lift aerodynamics and consecutively integrate the engine to determine the influence of propulsive system integration.

The design of multi-elements high-lift systems has a very serious impact on the cost and time needed to design an aircraft, characterized by complex aerodynamics, complex geometries and actuation mechanisms.

The engineering/production cost of the high-lift system can be around 10% (Rudolph, 1996) of the total cost of a typical aircraft, making this a key part of a successful project. To emphasize the importance of the project of high-lift devices, Meredith (1993) gives an example for a typical large twin engine transport: a 1% increase in maximum lift led to an increase of 22 passengers, and 1% improvement in L/D ratio allowed for an additional 14 passengers.

Keeping in mind these numbers, it is clear that it is necessary to tackle the problem trying to reduce the cost of engineering/production and at the same time, to guarantee a correct design evaluation given that even small change of the performance can lead to a large decrement of the whole aircraft performance. A possible solution to reduce costs could be the extensive use of CFD for design and analysis. To fulfil the second requirement, CFD evaluations should be carried out to assess the capabilities of this numerical tool on predicting the aerodynamics of high-lift devices.

In order to do this, in 2010 it was decided to initiate an international workshop series on CFD high-lift prediction to assess the state-of-art, and draw guidelines for a correct evaluation. The first AIAA CFD High Lift Prediction Workshop (HiLPW-1) was held in June 2010 and due to the complexity of the problem, it is still on-going (NASA, 2012).

The second part of this PhD research is related to this work; in particular the author uses geometries and experimental data given to the workshop participants, adding a HPSI study to the cases presented. The objective of this research is to model the HPSI using CFD tools in order to evaluate the performances of the aircraft as a whole system. The results obtained will be the first step to a similar CFD campaign to the one presented in chapter 4, that will populate the PSI correlations coefficients relative to landing and take-off conditions. However, compared to the cruise condition, these flight phases present different challenges, and in a way are even harder to model and understand, as it is underlined by the decision to organize AIAA workshops focused on high-lift prediction (NASA, 2012).

The subsequent chapter gives an overview of the high-lift and HPIS aerodynamics and its CFD evaluation. The presented literature review stands as an introduction to the next final two chapters, where the CFD is used to model the high-lift aerodynamic of an increasingly complicated aircraft model. This is done starting with a wing and body configuration, then adding the propulsive system and finally including the nacelle vortex generator, to realistically evaluate the effects of the presence of the engine of the whole aircraft performance.

5.2 MULTI-ELEMENTS HIGH-LIFT AERODYNAMICS AND CFD

Although high-lift aerodynamics has been studied since the early days of aeronautics, few publications addressed the topic formulating a satisfactory theory, until the early 70s, when A.M.O Smith (Smith, 1975) published his work titled "High-Lift Aerodynamics". The main outcome of this work was the definition of five primary aerodynamic effects of gaps in a multi-element airfoil flow.

- 1) *Slat Effect*: the circulation of upstream elements contra-rotate with respect to the velocities on the downstream elements, reducing the pressure peaks and giving the boundary layer the capability to better negotiate the lowered adverse gradient. Figure 5.1)
- 2) *Circulation Effect*: at the same time the velocity due to the downstream elements increases the circulation on the forward elements, considerably increasing the lift. (fig.5.1 right)
- 3) *Damping Effect*: because the velocity of the flow at the trailing edge of the upstream elements is higher than the mean stream velocity, therefore the discharge velocity of the boundary layer is higher reducing the possibilities of flow separation on the downstream elements.
- 4) *Off-the-surface pressure recovery*: the final deceleration of the boundary layer wakes coming from upstream elements takes place out of contact with the wall. This is a safer way of dumping the wake velocity, alleviating separation problems.

5) *Fresh-boundary-layer Effect*: each element has its own thin boundary layer and therefore is able to endure greater adverse pressure gradients.

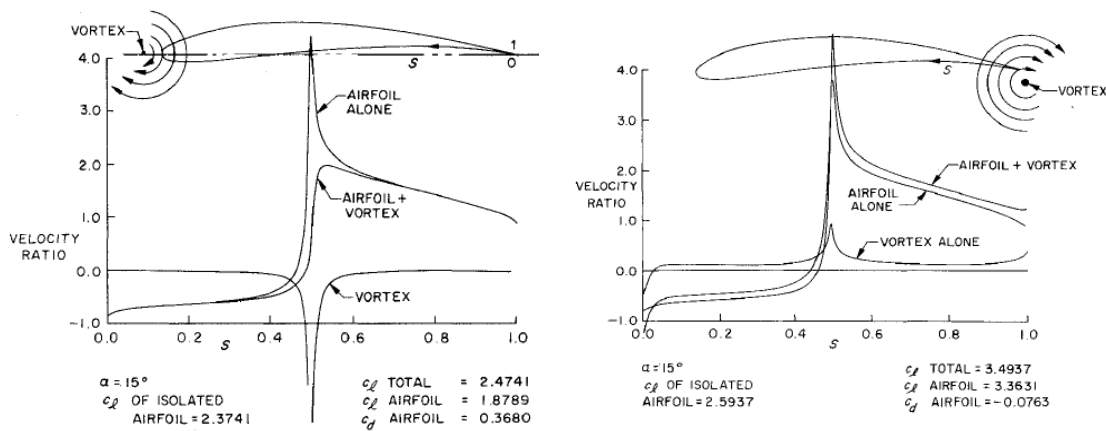


Fig. 5.1 Velocity distributions on an airfoil with and without vortex (to simulate the flap and slat) on LE (left) and TE (right) (Smith, 1975).

As part of the *GARTEUR* High Lift Research Programme (Meredith, 1993), 20 years later, Meredith focused on the viscous effects, defining the following main viscous flow features (fig 5.2):

1. Attachment line transition from laminar to turbulent
2. Relaminarization of turbulent boundary layers
3. Transition of boundary layers from laminar to turbulent
4. Shock/boundary layer interactions
5. Viscous wake interactions
6. Confluent wakes and boundary layers
7. Separated core flows

Obert (1993) underlined an important primary viscous effect: the confluent boundary layer (CBL). The boundary layers of the different elements merge creating a thicker CBL with more chances of flow separation. It is therefore important to optimize the gap between the elements looking at all the aerodynamics effects.

In order to better understand the high-lift aerodynamics, the NASA Langley Research Centre performed a full scale test with the Transport System Research Vehicle (B737-100) (Yip, 1993).

The aircraft was fully equipped with sensors to obtain detailed full scale measurements used to obtain in-flight flow characteristics at full-scale Reynolds numbers. The main objective of the project was to understand the 3-D high lift aerodynamics looking also at scale effects. The outcomes can be summarized as three multi-dimensional flow features:

1. Crossflow instability transition downstream of the attachment line;
2. Sweep effects on confluent boundary-layer development;
3. Local flow modifications: vortex generators flap side-edge-separated and tip effects, engine pylon interaction and landing gear struts.

All these features interact together making the high-lift flow extremely complicated to study. To capture the high-lift aerodynamic, the level of simulation should be as realistic as possible, simulating inviscid/viscid effects and their interaction (Van Dam, 2002).

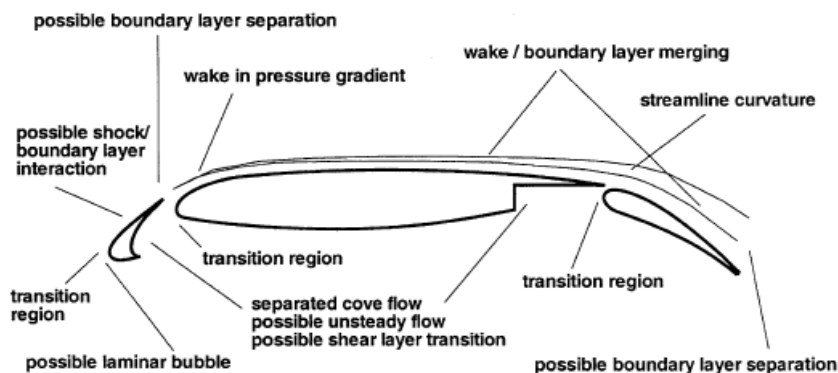


Fig. 5.2 High-Lift aerodynamics features [Rumsey, 2002]

Against this background, in the year 2000, it was decided to organize a joint European Programme within a consortium of European aircraft manufacturers and research organizations. The program was named EUROLIFT, under the coordination of Airbus-Deutschland with the aim of investigating high Reynolds 3-D high-lift aerodynamics, performing wind tunnel experiments and numerical simulations (Hansen, 2004).

The strategy of the project was to generate a database of experimental data with detailed flow field information and assess the state-of-the-art of numerical codes with the experimental database.

Special attention was given to Reynolds number effects, using a cryogenic wind tunnel in order to achieve in-flight conditions. A step by step approach was applied starting with 2-D experiments, a 3-D swept constant chord wing and a WB configuration with gradually increased high-lift geometry complexity (fig. 5.3). On this optic the project was structured with three work packages (Eliasson, 2003):

1. WP1: Validation Experiments and Flow Phenomena
2. WP2: CFD Assessment and Improvement
3. WP3: Verification and Application of High Re Testing

In WP1, task 1.1 was fulfilled using 2-D results from previous experiments, in particular from the previously mentioned *GARTEUR* High Lift Research Programme (Meredith, 1993).

The main objective was to evaluate the existing 2-D codes for the ability to capture the main aerodynamic characteristics in an industrial time frame. RE scale effects were also taken into account.

In task 1.2 a swept constant chord wing (fig 5.4) was used to understand the transition process and again the effects of different Reynolds numbers on the model. The database of results was used to assess and develop transition models for 3-D codes.

Due to the lack of experimental results for realistic aircraft configurations, task 1.3 focused on running an experimental campaign using the half Wing and Body (WB) model designed by Airbus-D (fig.5.5).

The modular construction of the model made it possible to increase the complexity of the geometry and to perform experiments at different attitudes (fig 5.6). It was used to perform experiments at take-off and landing, with a full span slat, a non-divided flap and new design flap system.

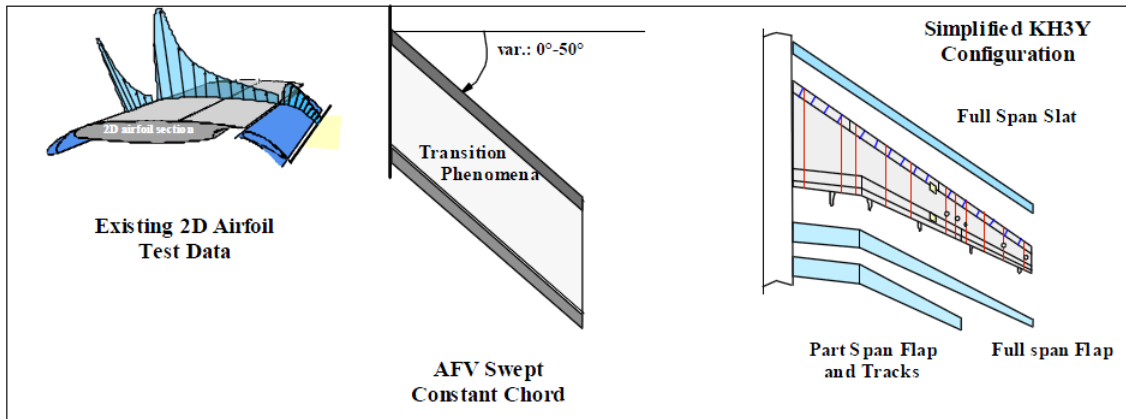


Fig. 5.3 EUROLIFT three levels of geometry complexity [Eliasson, 2003]



Fig. 5.4 ONERA F1 swept constant chord wing (Hansen, 2004)



Fig. 5.5 KH3Y Airbus-D model (Hansen, 2004)

The created database of experimental results was used in the WP2 to validate and assess CFD tools. The main parameters subjected to evaluation were: grid generation, turbulence modelling and increased geometry complexity. A summary of results is presented in references (Eliasson, 2003, Rudnik, 2003).

A major problem of CFD is the time consuming operation of generating the mesh. Therefore it is important to perform grid topology/size studies, reducing the generation time, while still guaranteeing accurate results.

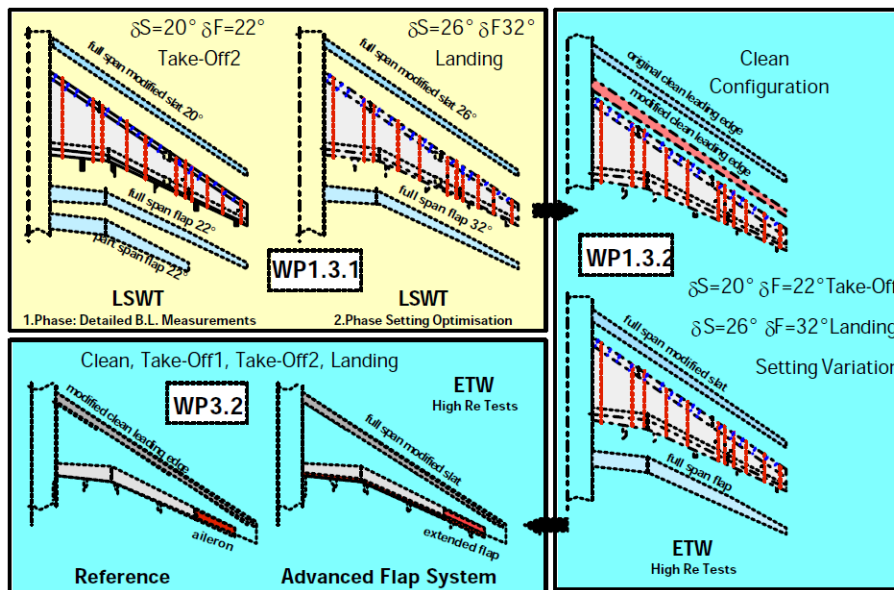


Fig. 5.6 KH3Y Airbus-D model configurations. (Hansen, 2004).

Part of the WP2 work was focused on evaluating the hybrid-unstructured mesh approach compared to the structured approach. Fig.5.7 shows a comparison of computed and calculated lift polar for the two approaches, using different solvers and turbulent models. The results are in good agreement with some deviances, especially at post stall condition. As explained by Hansen (2004), increasing the mesh nodes, for example by using a mesh adapting method, could significantly increase the quality of the results.

Rudnik (2004) stated that the hybrid unstructured mesh technique appears to be superior compared to the structured mesh technique, in terms of grid generation automation and off surface adaptation capabilities.

This is really important for complex 3D high-lift configurations, looking at the pre-processing time, the hybrid unstructured mesh should be favoured.

The turbulence modelling study was mainly focused on evaluating the nonlinear eddy viscosity EARSM model (Rudnik, 2003), pointing out that no substantial improvement were found compared with SA, $k-\epsilon$ and $k-\omega$ models (fig.5.8).

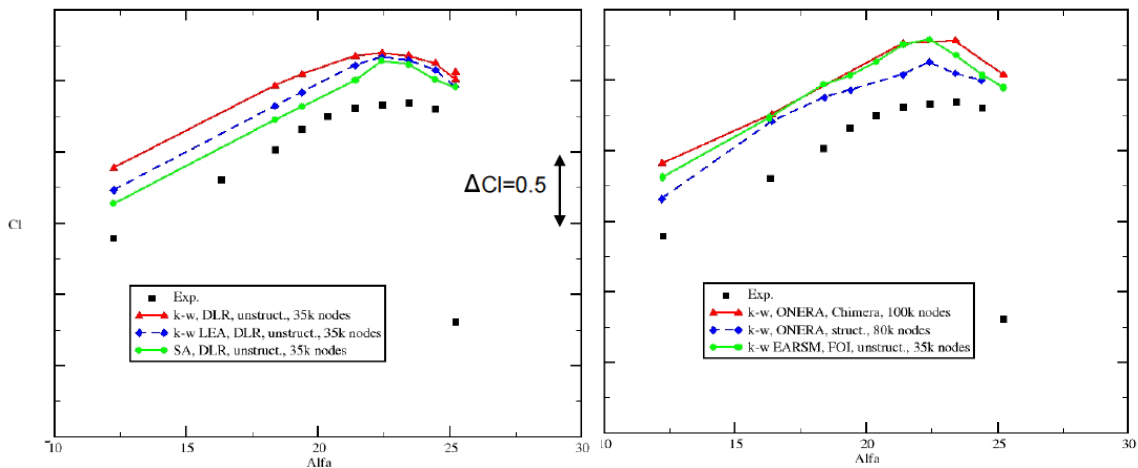


Fig. 5.7 KH3Y Airbus-D model lift polar for unstructured and structured meshes for different solvers and turbulent models. (Eliasson, 2003).

In addition to the grid topology and turbulence model studies, the complexity of the geometry was also increased to evaluate the aerodynamic behaviour and the capability of the codes to evaluate secondary effects. For this topic five flap tracks fairing were included. Hansen's (2004) results show that these geometrical details influence the results and should be taken into account. The step-by-step methodology should end with a configuration close to the real geometry to take into account the different aerodynamic effects but also the interactions between themselves. Due to the complexity of the final geometry, once again a hybrid-unstructured mesh approach is favoured, enabling fast and reliable mesh generation.

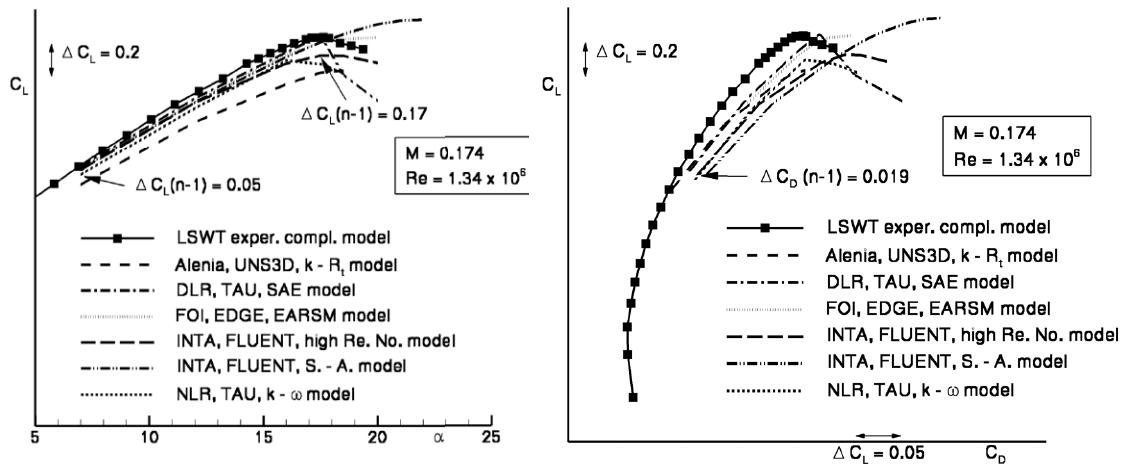


Fig. 5.8 KH3Y Airbus-D model lift and drag polar evaluated with different solvers and turbulence models. (Rudnik, 2003).

WP3 of EUROLIFT was dedicated to high Re testing, and in particular the main outcome was a Re dependency study. A summary can be found in reference (Rudnik and Germain, 2007). Figure 5.9 shows the different experimental lift polar obtained increasing the Re number from 6.5×10^6 to 25.5×10^6 . As described in reference (Haines, 1999) there are four sources of scale effects relevant for multi-element high lift wings. These are conventional scale effects related with the reduction of the boundary layer thickness with increasing Re number and the ability of the boundary layer to withstand higher pressure gradients without separating, bubble dominated scale effects which typically characterize the viscous interaction between the wake of an upstream element with the boundary layer of a downstream element, and finally transition dominated scale effects. All of these phenomena can strongly affect the high-lift aerodynamics, and therefore a Re number study is recommended to fully understand the flow behaviour at real flight conditions.

Following the work of EUROLIFT a second European High-Lift Programme, the EUROLIFT II, further studied the high-lift aerodynamics performing additional experimental and numerical evaluations over a three year project. The main objectives remained the same, but with an increase of geometry complexity, including the effects of slat cut out and engine-integration. The project was again divided in three major WPs (Rudnik and Geyr, 2007): WP1 “Improved Validation Based on EUROLIFT I Data”, WP2 “Realistic High Lift Configurations” and WP3 “Methods and Tools”.

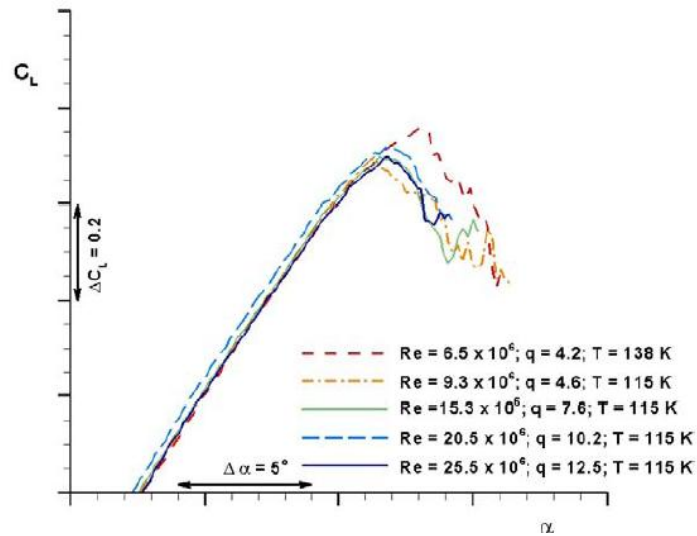


Fig. 5.9 KH3Y Airbus-D model lift polar for different Re numbers (Rudnik and Germain, 2007)

WP1 was based on numerical investigations exclusively using data from EUROLIFT I, looking at geometrical model installation and deformation effects, boundary layer and transition effects and a flap setting study.

In WP2 the geometry complexity of the KH3Y model was further increased by adding slat tracks and their fairing, cutting the slat at the fuselage junction, adding the engine and finally adding a nacelle strake (fig. 5.10). The part related to the engine installation and nacelle strake will be discussed in the subsequent paragraph dedicated to HPSI.



Fig. 5.10 EUROLIFT II KH3Y model complexity increase. (Quix, 2007)

WP3 was focused on developing numerical and experimental tools for high-lift simulations, looking at transition prediction, numerical simulation improvement and experimental techniques for transition and deformation detection.

The key objectives of the entire project were to evaluate the capabilities of CFD to capture the maximum lift, to understand the dominant effects of vortex phenomena related with the integration of the propulsive system and define the Re-number dependence. To do this, additional activities to the ones of EUROLIFT I were necessary in order to define a methodology suitable for high-lift flows, mainly focusing on turbulent modelling and grid generation.

The turbulent modelling study was focused on the evaluation of wall functions, the comparison with SA, SST turbulence models and higher order turbulence models, like the k- ω EARSM Hellsten and the Differential Reynolds Stress Model (DRSM) (Eliasson, 2007).

The wall function study involved the generation of the boundary layer mesh with a Y^+ of around 10, and the use of a scalable wall function, a universal wall function and a generalized wall function. Figure 5.11 shows an example of lift and drag polar for the different wall functions compared to the near-wall approach ($Y^+ \approx 1$). In particular FOI used a universal wall function, CIRA used a scalable wall function and INTA used a generalized wall function.

It can be seen that for all the wall functions methods, even though they have good agreement in the linear range of the lift curve, they over predict the maximum lift compared to the near-wall approach. The over prediction comes from a different skin friction distribution, that can contribute to avoiding flow separation in the wall function computation, missing the drop on the lift curve. Therefore, the wall functions are not well suited for reliable maximum lift predictions. It should be noted that no conjectures can be made about the drag, given that, as stated by reference (Eliasson, 2007), the experimental results were corrupted by the installation of the half model in the wind tunnel.

To continue the work done in EUROLIFT I, additional turbulence models were tested and compared with SA and Menter SST models. Figure 5.12 shows the comparison of the Hellsten EARSM with k- ω closure and the more traditional turbulence models. The comparison was made on an 8 million nodes grid with a near wall approach ($Y^+ \approx 1$).

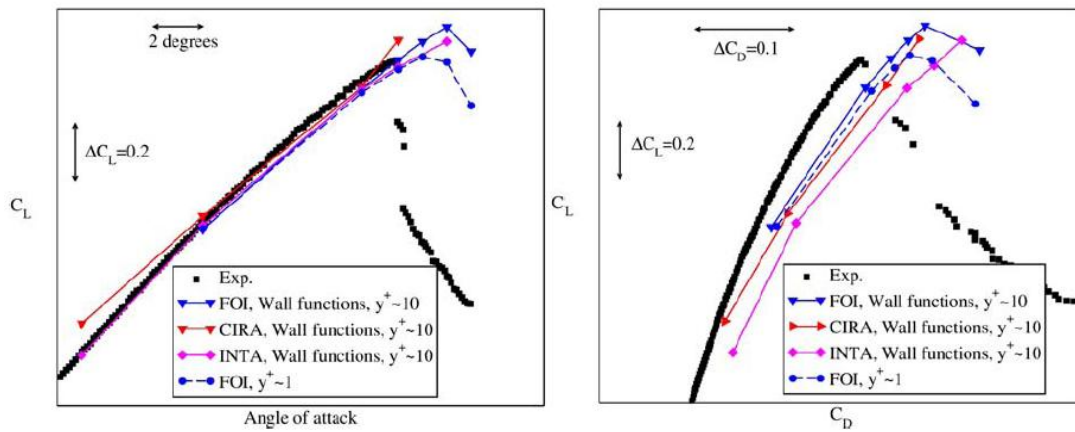


Fig. 5.11 KH3Y model lift and drag polar for different wall functions. (Eliasson, 2007).

The numerical results show good agreement with the experimental data but again, they can't be considered conclusive because of the installation of the half model in the wind tunnel (Eliasson, 2007).

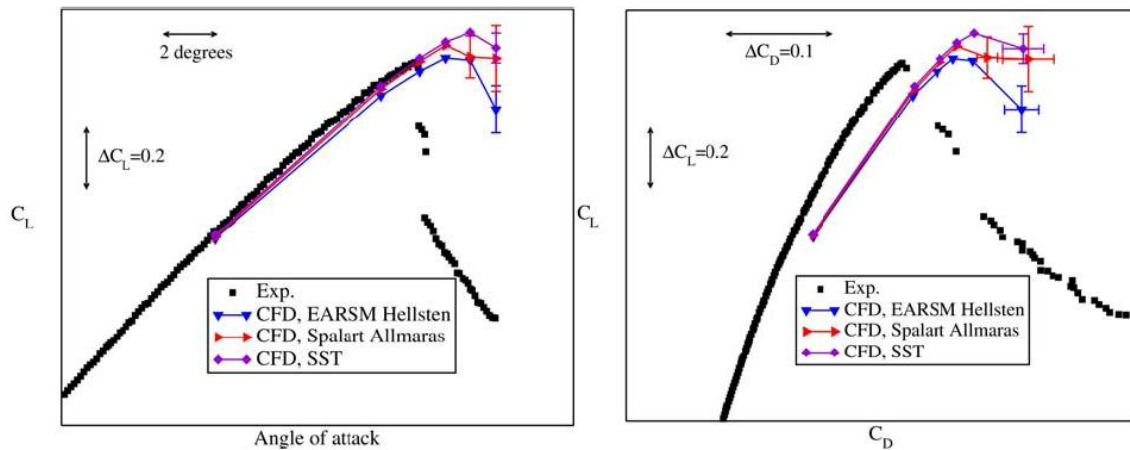


Fig. 5.12 KH3Y model lift and drag polar for different turbulence models. (Eliasson, 2007).

Similar conclusions were found using the DRSM model underlining that the experimental installation effects dominate over the turbulence model effects. Further studies were therefore suggested. The work done on grid generation, using structured/unstructured grids, hybrid grids and overlapping grids, showed that the effects of grid topology and size are often larger than the effects related to turbulence models, giving the grid generation process priority compared to the use of different turbulence models.

Another important part of the project was to assess the capability of CFD to predict the effects of geometrical changes, in particular the engine integration and the use of the nacelle strake. This part will be discussed in the next paragraph focused on HPSI.

Following the EUROLIFT projects, it was clear that further work was necessary to address the still open questions. Therefore, it was decided to hold a series of High Lift Prediction Workshops (HiLPW) (NASA, 2012) to help advance the state-of-the-art of high lift prediction. The work is still on-going but the first results were presented in June 2010 and January 2011 using a three element trapezoidal swept wing, tested at NASA (fig.5.13). The geometry and the experimental data were used in the work described in chapter 6.

The long term objectives of the HiLPW workshops are (Rumsey, 2011):

1. Assess the numerical prediction capabilities of current generation of CFD codes looking at parameters like mesh and turbulence modelling.
2. Define practical guidelines for CFD prediction of high-lift flows.
3. Advance the understanding of high-lift flow physics.
4. Identify areas that need additional research.
5. Develop a database of results.

To fulfil these objectives the first HiLPW (HiLPW-1) made available on the web (NASA, 2012) the collection of experimental data and the CAD models of the NASA Trap Wing. The experimental data come from two different test campaigns in 1998-1999 and 2002-2003, in the Langley NASA 14x22 Foot Subsonic Wind Tunnel. More details will be presented in the next chapter. Special attention was given to assure data repeatability, evaluating the uncertainty bounds for lift, drag and pitch moment.

The problem of the wind tunnel effects was also taken into account looking at the installation of the model on the wind tunnel floor and using wall corrections [NASA, 2012]. Data from an additional campaign, performed in the NASA Ames 12 Foot Pressure Wind Tunnel, were discarded due to wall effects concerns.

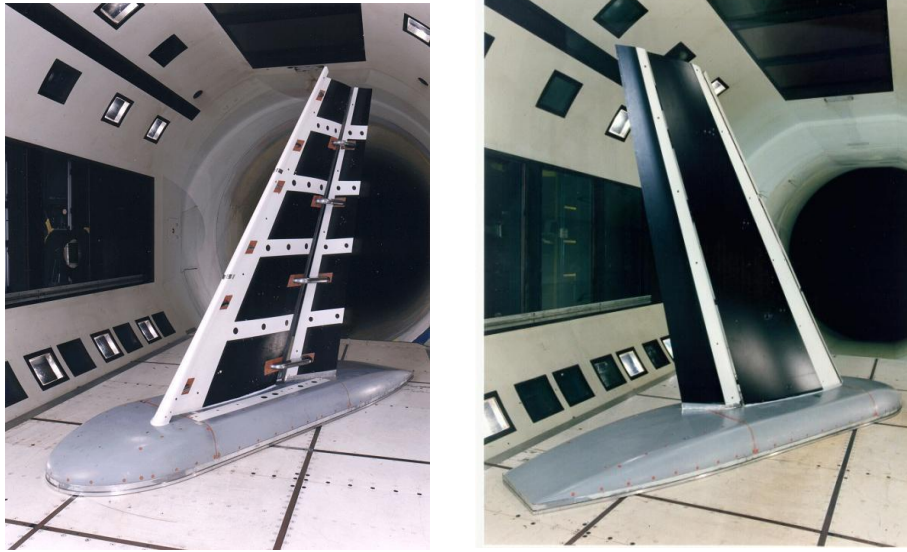


Fig. 5.13 NASA Trap Wing Langley in the 14x22 Foot Subsonic Wing Tunnel. (NASA, 2012).

The 18 organizations (34% government labs, 28% industry, 20% CFD software vendors, and 17% universities) presented 37 separate CFD datasets including a grid convergence study, a drag polar study and a slat and flap supports study. For the grid dependency study, participants were asked to run simulations for coarse, medium and fine meshes for angles of attack of 13° and 28° . A set of grids were available but it was also possible to create self-generated grids according to the following gridding guidelines:

1. Initial spacing normal to all viscous walls ($RE = 4.3 \times 10^6$ based on $C_{REF}=39.6$ in):
 - coarse: $Y^+ \approx 1.0$ $\Delta_1 = 0.00020$ in
 - medium: $Y^+ \approx 2/3$ $\Delta_1 = 0.00013$ in
 - fine: $Y^+ \approx 4/9$ $\Delta_1 = 0.00009$ in
 - extra-fine: $Y^+ \approx 8/27$ $\Delta_1 = 0.00006$ in
2. Recommend grids have at least 2 cell layers of constant spacing normal to viscous walls.
3. Total grid size to grow $\approx 3X$ between each grid level for grid convergence cases. For structured meshes, this growth is $\approx 1.5X$ in each coordinate direction.
4. Recommend variable off-body cell growth rates for wing and flap grids:

- Growth rate in the viscous layer (GR_1) should be < 1.25 for all grids (fig.1.14).
 - To capture the wake from upstream elements, the wing and flap grids should include a region where the growth rate (GR_2) is 1.0 (fig.1.14).
5. Farfield located at $\approx 100 C_{REF}$'s for all grid levels.
 6. For the Medium Grids:
 - Chordwise spacing at leading edge (LE) and trailing edge (TE) $\approx 0.1\%$ local device chord (use local slat chord for slat grid, wingbox chord for wingbox grid and flap chord for flap grid).
 - Spanwise spacing at root and tip $\approx 0.1\%$ local semispan.
 - Size near body nose and tail $\sim 2.0\% C_{REF}$.
 - For the Coarse and Fine Grids, the above values should be scaled accordingly.
 7. The TE base grid should contain:
 - A minimum of 4 cells across TE base for the coarse mesh.
 - A minimum of 6 cells across TE base for the medium mesh.
 - A minimum of 9 cells across TE base for the fine mesh.
 - A minimum of 14 cells across TE base for the extra-fine mesh.

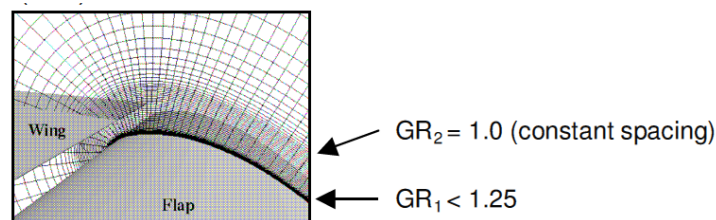


Fig. 5.14 Gridding guidelines for the grow rate in the viscous layer.(NASA, 2012).

Table 5.1 and figure 5.15 give an overview of the grid sizes, number of nodes and cells, and the grid topology generated by the HiLPW-1 committee.

An example of the HiLPW-1 grid convergence study can be found in reference (Wiert, 2011). The authors used the coarse, medium and fine multi-block structured mesh (made with ICEM-CFD™) at an angle of attack of 13° and 28° .

Figure 5.16 shows that for this level of mesh size, the coefficients variation between the different grids is very small, although bigger at $\alpha = 28^\circ$, suggesting that the convergence is almost reached already with the coarse mesh.

Similar results are shown in figure 5.17 (Crippa, 2011) but using three unstructured mesh generator (Solar, Centaur and 1to1). In this case, the differences are slightly bigger, as expected due to the intrinsic mesh dependency of the results computed with this meshing technique. The results are presented at $\alpha = 13^\circ$ and $\alpha = 28^\circ$.

The computed lift and drag for the medium grids as a function of the angle of attack are showed in figure 5.18. The results were obtained using different turbulence models: the SA, k- ω , k- ϵ and SST for a medium size grid.

Grid Generation Tool	Grid Type	Extra Coarse		Coarse		Medium		Fine	
		Nodes (x10 ⁶)	Cells (x10 ⁶)	Nodes (x10 ⁶)	Cells (x10 ⁶)	Nodes (x10 ⁶)	Cells (x10 ⁶)	Nodes (x10 ⁶)	Cells (x10 ⁶)
ICEM-CFD	Structured	7	6	23	20	52	48	171	161
ICEM-CFD	Unstructured	6	6	20	20	48	48	162	161
GridGen	Structured	4	3	11	10	29	27	85	81
CGT	Structured	11	-	25	-	83	-	282	-
VGRID	Unstructured	-	-	1	7	4	22	11	63
VGRID	Unstructured	-	-	4	21	11	64	32	190
VGRID	Unstructured	-	-	4	10	11	38	32	127
CENTAUR	Unstructured	13	37	16	44	31	79	-	-
SOLAR	Unstructured	-	-	12	17	37	49	111	141

Table 5.1 Overview of the Grids Size

A relatively large discrepancy between the different CFD datasets can be noticed, that in some cases can be as much as 50%. The reason for this noticeable difference is given to a hysteresis effect (Biber, 1993), leading to two separated steady flow solutions, one with a higher lift coefficient. To avoid the unreal solution it was suggested to initialize the runs with the previously converged solutions at lower angles of attack.

For an overview and statistical summary of the all 37 datasets it is suggested to look at reference (Rumsey, 2011).

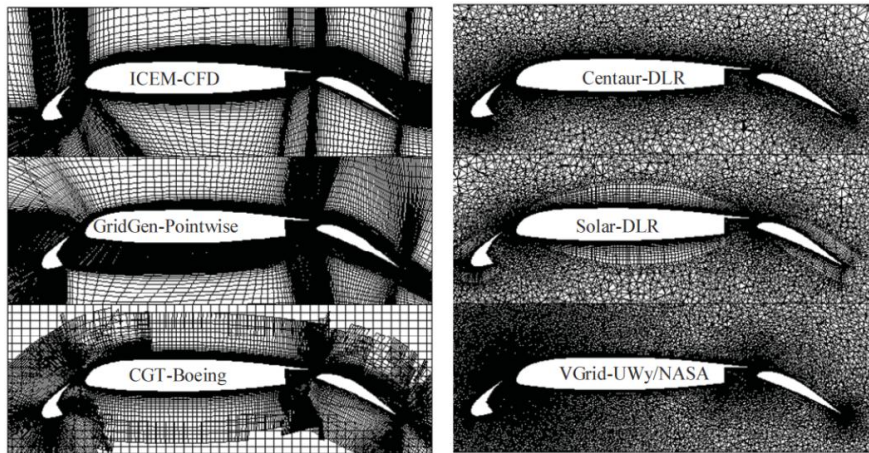


Fig. 5.15 HILPW-1 Trap Wing grids topologies. (Rumsey, 2011).

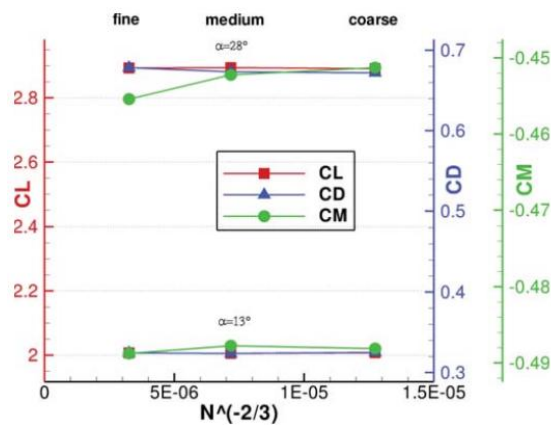


Fig. 5.16 CL, CD and CM grid convergence study for a structured mesh. (Wiar, 2011).

As an additional work, it was suggested to look at the flap/slat support (brackets) effects. Only seven sets of results were presented and further work is to be carried out in the next workshops. The general trend is a reduction of lift coefficient by about 0.01-0.02 at an angle of attack of 13°, and 0.06-0.09 at an angle of attack of 28°. An example of lift polar with the bracket effects can be found in figure 5.19 (Sclafani, 2011). This behaviour suggests that the lift at brackets-off condition is over-predicted. Sclafani (2011) suggests that given the flow is assumed fully turbulent, the thickness of the boundary layer will increase, causing a drop of lift.

This drop of lift will be counterbalanced by the increase of lift due to the bracket-off condition, bringing the results in line with the experiments. However, in the bracket-on condition the effect could still be in opposite value but with different magnitude. Future work is necessary to investigate this effect.

From the current pattern, even if the current CFD methods are able to predict the main high-lift flow features, it is clear that further research is necessary and although comprehensive high lift research activities have been carried out in the past, novel configurations and high lift systems may allow only a limited transfer of existing knowledge and require new design studies.

This is even more valid for the HPSI, where specific research activities are yet to be undertaken. The benefits are obvious, therefore future research has to be planned in order to assess the capabilities of the current tools and develop new ones.

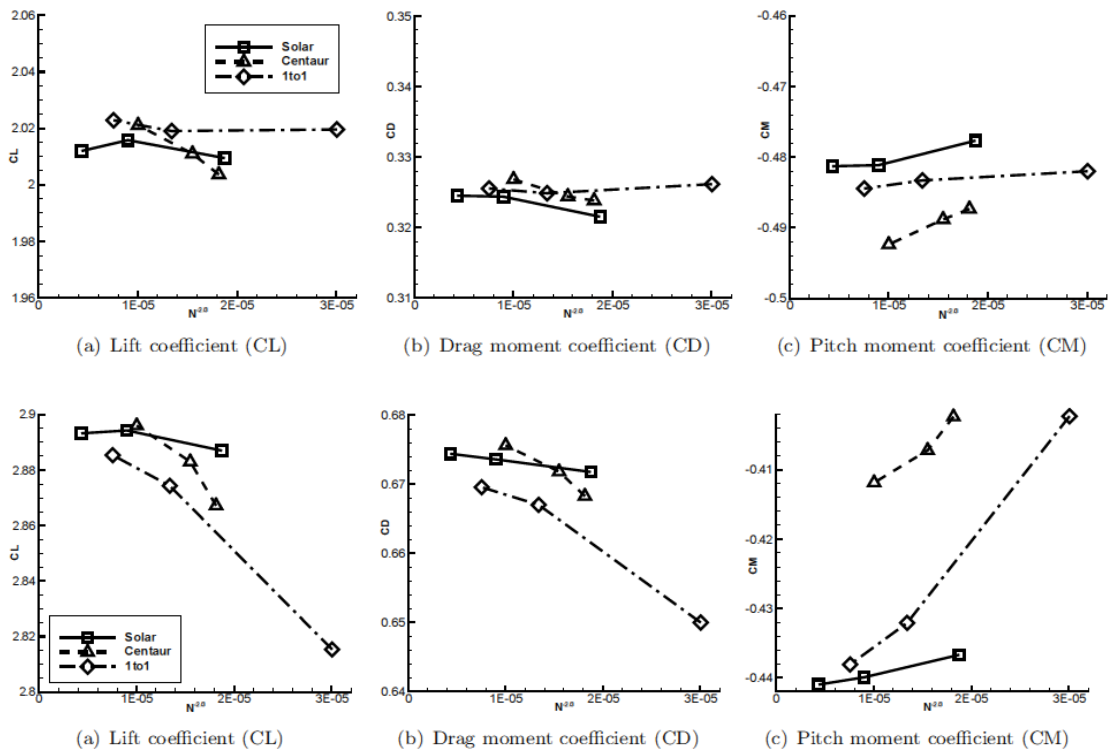


Fig. 5.17 CL, CD and CM grid convergence study for three unstructured meshes generated with different software: Solar, Centaur and 1to1 (Crippa, 2011). $\alpha = 15^\circ$ top, $\alpha = 28^\circ$ bottom

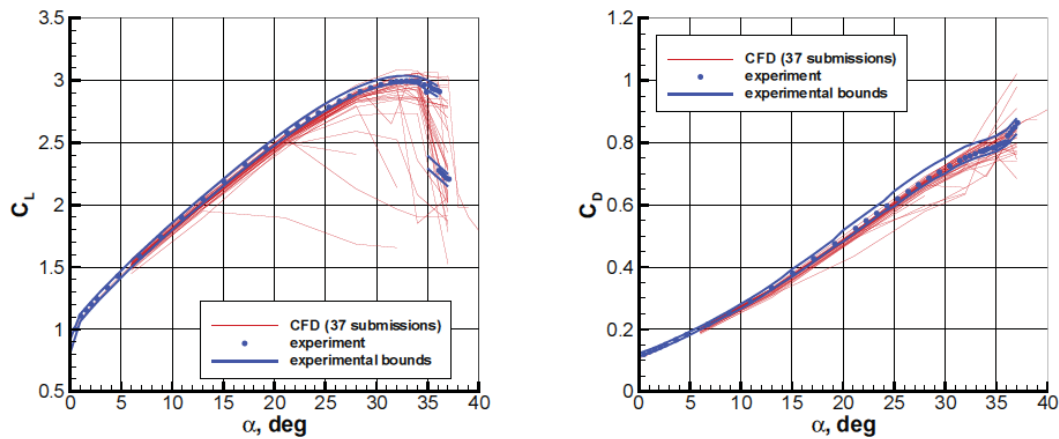


Fig. 5.18 HILPW-1 lift and drag coefficients of the 37 datasets. (Rumsey, 2011).

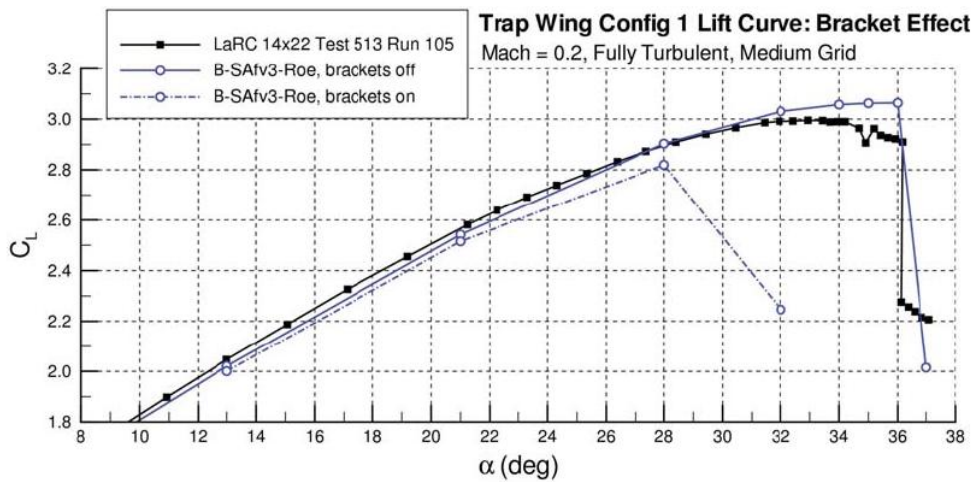


Fig. 5.19 Experimental (LaRC 14x22 Test 513 Run 105) and numerical lift polar for the configuration with flap/slat brackets (B-SAFv3-Roe, brackets on) and without (B-SAFv3-Roe, brackets on). (Slafani, 2011).

5.3 HIGH LIFT PROPULSION SYSTEM INTEGRATION

The installation of the engine in high-lift condition presents similar effects to the ones related to the cruise condition, increase of drag and a reduction of lift. However, at the high-lift conditions, the effect on lift is more relevant. The high angle of attack results in a more severe interaction of the engine nacelle and wing flow fields. As specified in the previous section, the maximum lift (C_{Lmax}) reduction is the driving factor in the design of high-lift configurations as well as one of the most limiting problems relating to HPSI.

It is therefore obvious that the $C_{L_{max}}$ is a key design parameter during the integration of the engine in landing and take-off configurations. The following sections present a closer look at the aerodynamics that affect the maximum lift.

First of all due to the physical installation of the engine the slat has to be cut to accommodate the pylon, therefore losing part of the lifting surface. This leads to a reduction of lift because of the missing slat portion and also because the adjacent part of the wing profile is now exposed to higher incidence flow and therefore subject to earlier flow separation.

The installation of the nacelle generates an up-wash flow (fig.5.20) shaped by the high angle of attack, the nacelle/pylon geometry and the flow features of the high-lift configuration. This up-wash flow is characterized by the presence of vortices, on both sides of the nacelle, given that the nacelle itself is producing a considerable amount of lift.

The up-wash flow interacts with the flow generated by the slat cut-out, and the low pressure field near the wing. If the engine is close enough, the vortices coming from the nacelle are captured and forced to attach to the surface of the wing by the low pressure zone at the leading edge (fig.5.21). This vortex boundary layer interaction is generally favourable, resulting in a *near-wall momentum addition*.

This *near-wall momentum addition* is a method of control of the flow separation, that consist in supplying additional energy to the particles which are being retarded in the boundary layer due to an adverse pressure gradient (Gad-el-Hak, 1991). The high-axial velocity of the vortex enhances the kinetic energy to the near-wall fluid particles, reducing the thickness of the boundary layer and making it able to withstand bigger adverse pressure gradients (Michael, 1987). However in a high angle of attack configuration the axial velocity of the vortex could not be enough to withstand the increased pressure field. If the axial core velocity will fall beyond a critical point, the vortex will disappear, also called vortex bursting (Leibovich, 1984), and without the momentum addition of the vortex, the boundary layer will separate.

Due to the forward position of the slat on the inboard side of the nacelle, compared to the outboard, the inboard vortex will be more exposed to increased pressure fields, therefore more prone to burst and cause separation. Consequently special attention should be addressed during the design of the inboard pylon/wing junction and the slat cut-out

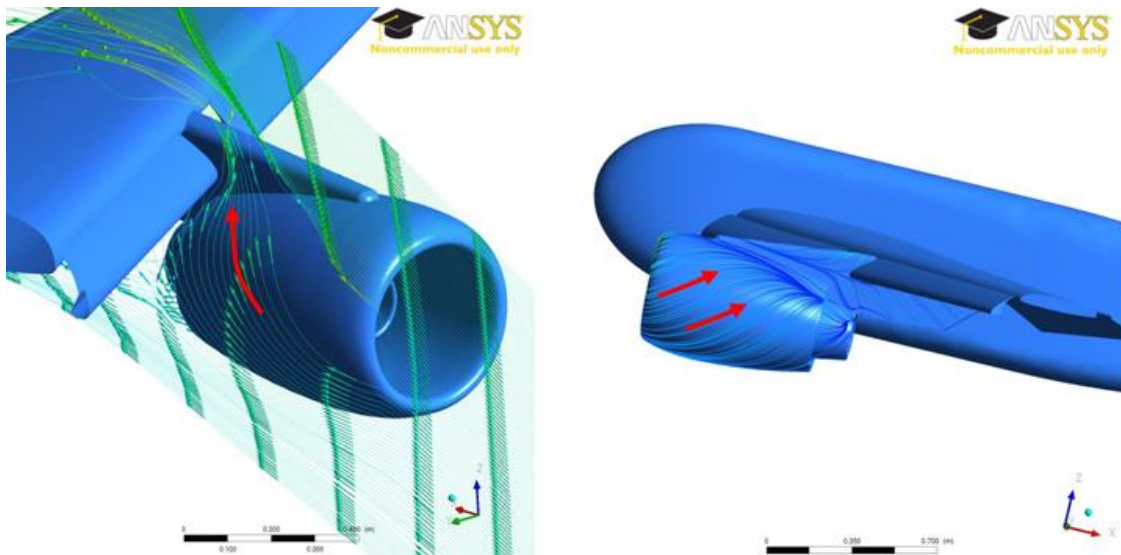


Fig. 5.20 HPSI aerodynamic effects: up-wash flow

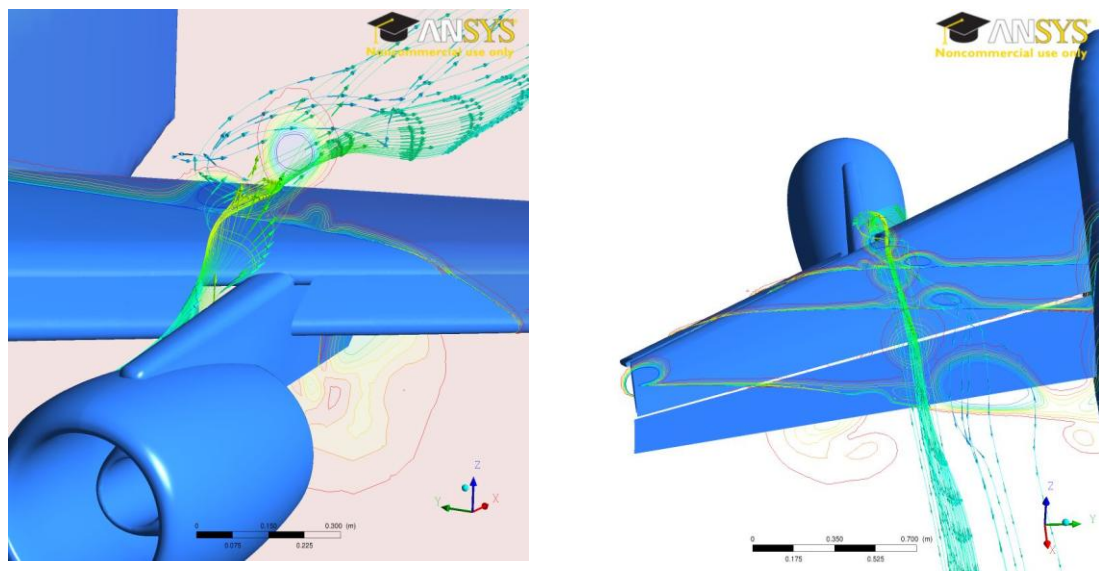


Fig. 5.21 HPSI aerodynamic effects: nacelle/pylon vortex

To overcome this problem, the McDonnell Douglas aircraft manufacturer (Richard, 1973) introduced the idea of mounting a pair of strakes on the nacelle to generate two additional vortices in order to control the wing flow separation (fig.5.22).

The nacelle strake, or chine, if correctly positioned, generates a vortex in a location where the boundary layer is relatively thin, with a flow characterized by higher axial velocity, compared to the low kinetic energy field of the pylon/wing junction.

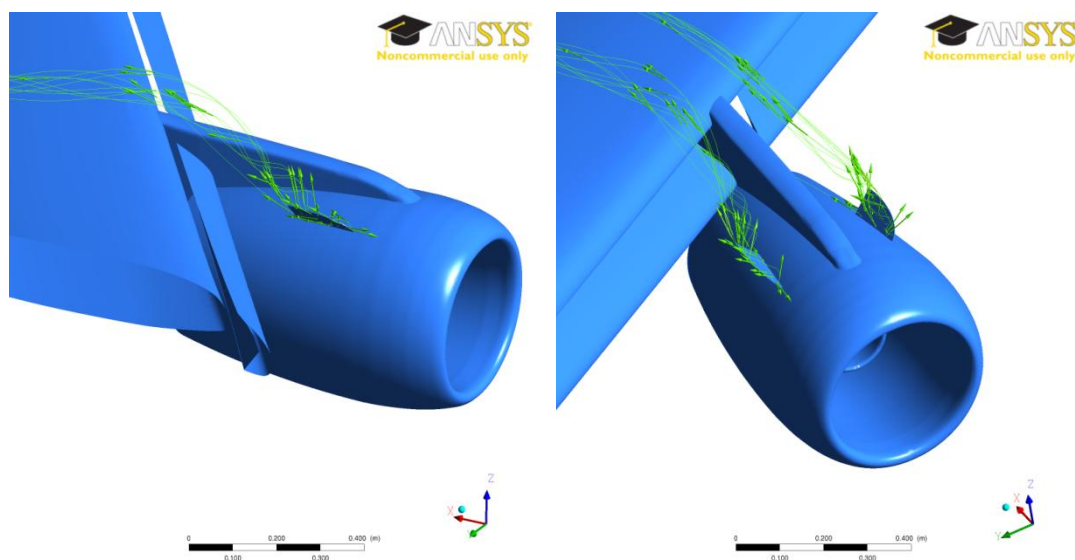


Fig. 5.22 Single and double nacelle strake vortices

This affects the axial velocity of the vortex, making it able to withstand greater adverse pressure gradients. Depending on the position of the strake and the nacelle/pylon/wing field, the strake can create a vortex with high axial velocity and avoid the generation of the slower nacelle vortex, or generate a vortex that interacts with the nacelle vortex, increasing its axial core speed.

As mentioned, for a swept wing, the inboard portion of the wing is more affected by the nacelle vortices, resulting in a local stall. Every so often, for a close-coupled engine, the interference can be so severe as to affect the outboard of the wing, causing a more dramatic flow separation. That is the reason why Douglas introduced a pair of nacelle strakes, one for each side.

The early work of Slotnick (2000) and Rogers (2000) on HPSI for WBNP and WBNP with a single chine (WBNPC) showed that the use of CFD to predict the magnitude of the chine lift increment was not yet appropriate with the computational resources of that time.

Therefore part of the EUROLIFT II project, previously discussed in paragraph 5.3, was dedicated to evaluate the capability of CFD to predict the engine integration and the use of the nacelle strake. Quix (2007) presented the results from the wind tunnel campaign for the KH3Y WB, WBNP and WBNP with a single chine (WBNPC). The KH3Y was representative for a commercial wide-body twin jet. The lift and drag polar are shown in figure 5.23, where configuration 1 stands for WB, configuration 2 stands for WBNP and configuration 3 stands for WBNPC. It can be seen that the integration of the engine causes a reduction of the maximum lift, but the installation of a strake on the inboard side of the nacelle leads to a 60-70% recovery of lost lift. The impact of the nacelle strake is so severe that in order to correctly evaluate the HPSI effects its influence can't be not taken in to account.

The CFD study of the same configurations is presented in reference (Von Geyr, 2007), where the effects of the nacelle stake and the stall mechanism are explained. Comparisons between Particle Image Velocimetry (PIV), infrared flow visualization (fig.5.24) and numerical results show that CFD is able to capture the main aerodynamic phenomena, vortex position and deformed streamlines due to the engine/pylon-wing interaction. Figure 5.24 shows that the wing flow separation starts in correspondence of the engine as explained in the previous paragraph. The conclusions outline that even if the nacelle and strake vortices interaction can be modelled with a satisfactory level, future work its necessary to increase the level of reliability.

In the Japan Aerospace Exploration Agency (JAXA), the equivalent of the American NASA, a research program regarding CFD of high-lift devices is currently undertaken (JAXA, 2012). The model used during the research is representative for a 100-passenger regional jet. Results are presented for WBNP and WBNPC configurations.

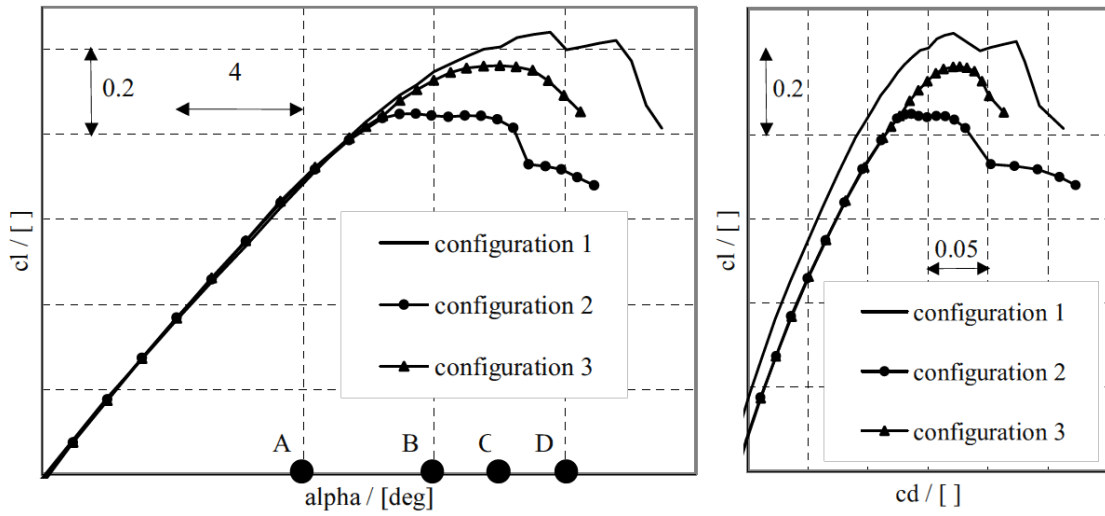


Fig. 5.23 Lift and drag polar for WB (conf.1), WBNP (conf.2) and WBNPC (conf.3). (Quix, 2007).

Details of the experimental campaign can be found in reference (Yokokawa, 2008). The results are similar to the ones presented in EUROLIFT II, showing the stall at the area adjacent to the nacelle/pylon (fig. 5.25). The PIV results confirm the interaction of the nacelle and nacelle-strake vortices are responsible for the increase of lift in the WBNPC configuration (fig.5.26).

A comparison of CFD and experimental results is presented in reference (Wild, 2009) showing reasonable agreement.

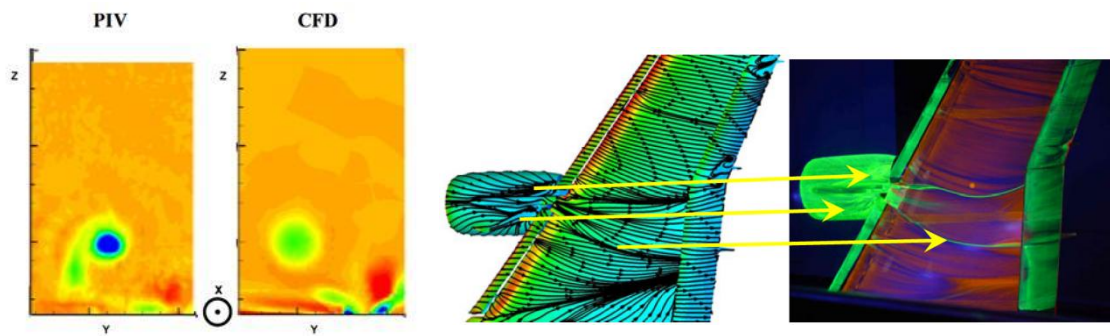


Fig. 5.24 PIV (left) and infra-Red flow visualization for WBNPC. (Von Geyr, 2009).

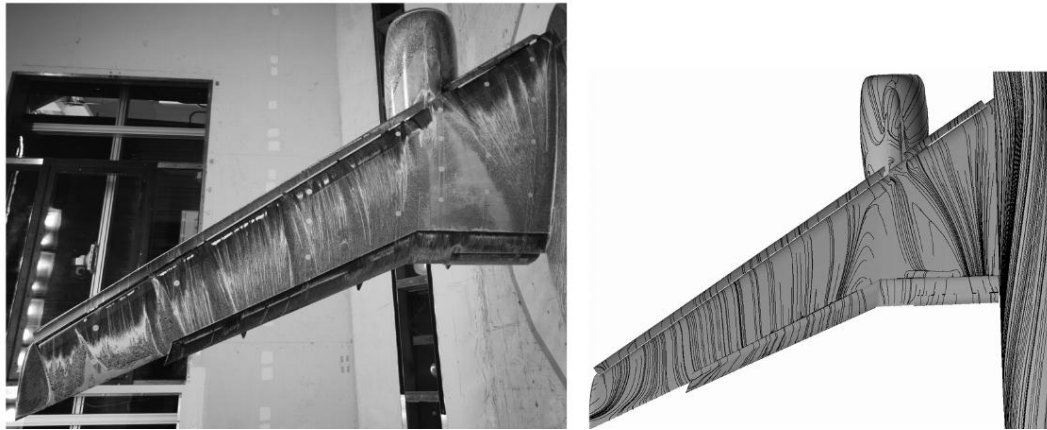


Fig. 5.25 Experimental (china clay) and numerical flow visualization for WBNP configuration (Yokokawa, 2008).

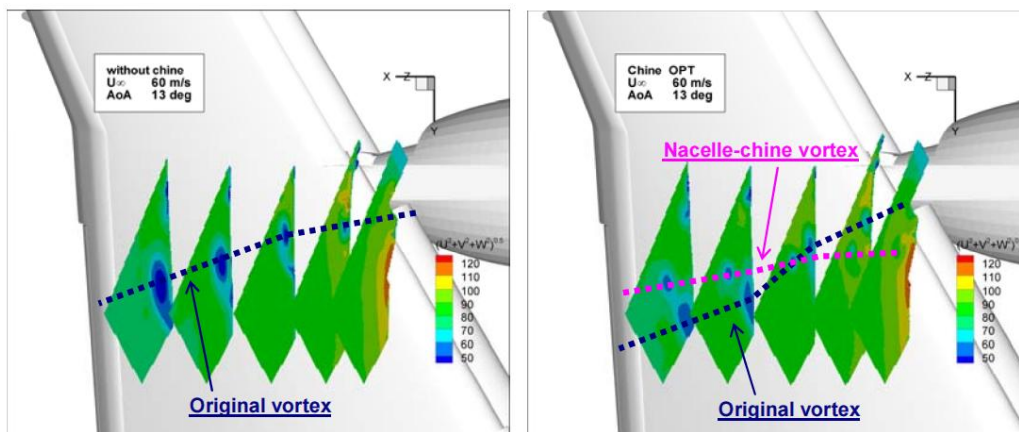


Fig. 5.26 PIV of nacelle/nacelle-strake vortices interaction (Yokokawa, 2008).

Even if the CFD is able of simulating the main aerodynamics of HPSI, it is clear that future work is necessary in order to increase the level of details and reliability of the simulations.

On another side a more detailed flow characterization for a HPSI with and without nacelle strakes is still not available in the open literature. The few previously presented projects did not present a description of flow around the nacelle, pylon, slat, wing and flap due the engine installation. A topological description of the installation vortices and their interaction with the wing flows is yet to be presented in open literature.

On a closer look to this project, it is necessary to understand the HPSI aerodynamics, driven by the interaction of the installation vortices, in order to be able to perform a CFD campaign similar to the one for the cruise condition. It is predicted that the position of the engine will significantly affect the HPSI aerodynamics. Consequently a topological description of the installation vortices is necessary to understand the effects of the engine positioning influence.

6 CFD HIGH LIFT PREDICTION WORKSHOP

6.1 GEOMETRY AND GRID GENERATION

Due to the availability of data and geometry, in order to evaluate the high lift aerodynamic it was decided to use the NASA Trap Wing geometry (NASA, 2012). The Trap Wing geometry is a three-element semi-span wing attached to a body pod (fig.6.1). The leading-edge slat is full span. The trailing-edge flap is available in both full-span and part-span configurations. Figure 6.2 illustrates the general Trap Wing layout and shows key geometric and reference parameters. For the purposes of the workshop, configuration 1 (slat at 30 degrees deflection, full-span flap at 25 degrees deflection) and configuration 8 (slat at 30 degrees deflection, full-span flap at 20 degrees deflection) were used in the CFD simulations. For both Trap Wing configurations, the nominal flap gap/chord (g/c) ratio was 0.015, and the nominal flap overlap/chord (o/c) ratio was 0.005.

For the purpose of this research it was decided to use configuration 1, due to the greater availability of experimental data. No significant difference on the PSI effects was expected using configuration 8.

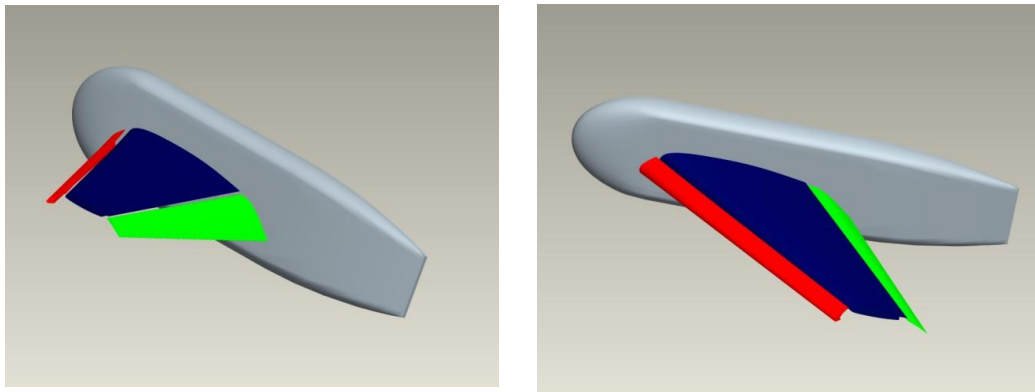


Fig. 6.1 Trap Wing geometry (configuration 1).

Trap Wing Geometry Cruise Wing Configuration

sources: coordinates - drawing AY9119
standoffs - DEI drawings 1080964, 1080967

J. Hannon
6-9-09

CFD Reference Parameters *

Reference area:	22.028 ft ²
mean aerodynamic chord:	39.634 in
semi-span:	85.054 in
aspect ratio:	4.561
LE sweep:	33.89 deg
1/4 c sweep:	29.97 deg
TE sweep:	16.24 deg
tip cruise chord:	21.116 in
root cruise chord:	53.473 in
moment reference:	x = 34.342 in y = -0.95 in z = 0 in

* based on model
without standoffs

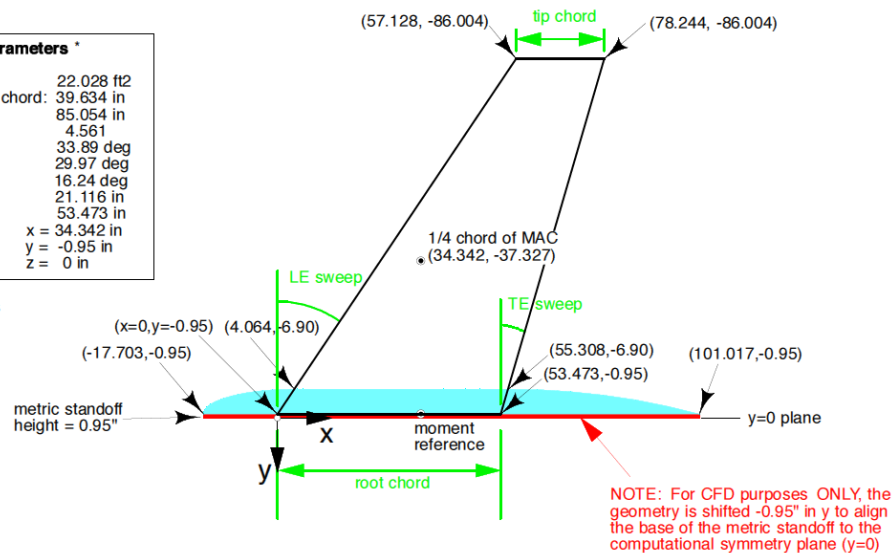


Fig. 6.2 Trap Wing layout and reference parameters (NASA, 2012).

The grids and domain were generated following the guidelines presented in chapter 5. It was decided to use a hybrid/unstructured approach to facilitate the generation of the grid even for the complicated geometry with the engine and pylon, maintaining a high level of solution accuracy even in the boundary layer. As pointed out by Eliasson (2011), the importance of correctly solving the boundary layer is fundamental to capture the high lift aerodynamics. The transition laminar/turbulent boundary layer is one of the key processes influencing separation.

Therefore special attention was given to the prism layer generation. The commercial grid generator was again ICEM-CFD. The software is able to generate prism layers in the boundary layer starting from surface mesh (ANSYS, 2012). Due to the configuration of the Trap Wing, multi-element wing with gaps between wing, slat and flap, particular attention was given to this process. In the ICEM-CFD prism-layer application, several parameters can be varied in order to generate the layers, adjusting the quality and generating the prearranged boundary layer thickness (ANSYS, 2012). Fig.6.3 shows the selected values for the whole Trap Wing. To find the correct parameter combinations it was decided to create a control volume around the wing/slat connection (fig.6.4).

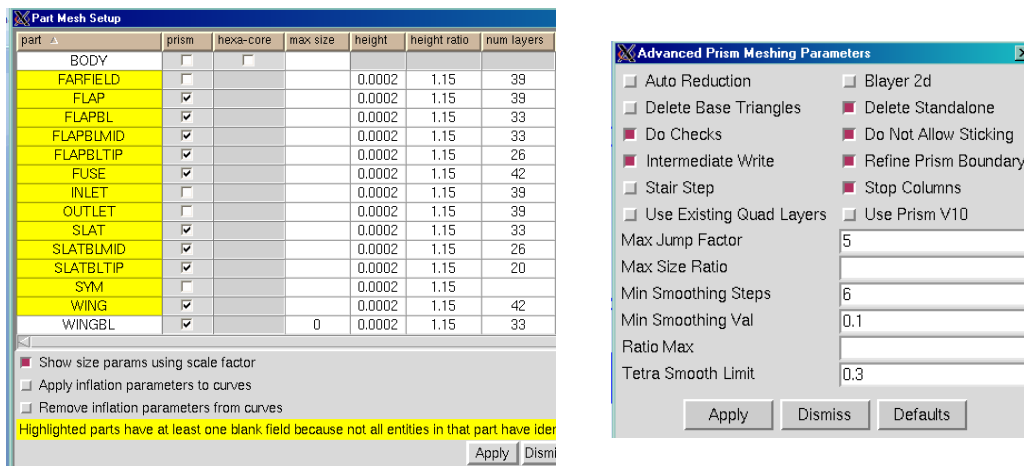


Fig. 6.3 ICEM-CFD prism layer parameters.

Given that the distance between the wing and the flap and slat changes from the root to the tip of the wing, special attention should be addressed on defining the number of layers and growth ratio and the height of the first layer. This will influence the requested level of accuracy ($Y^+ < 1$) and will avoid the crossing of the boundary layers of the different elements, causing a drop of mesh quality and in some cases the code will be unable to generate the mesh.

This was a bottle neck in the process given that the version of the code (ICEM-CFD 12.1) used to generate the mesh, presented stability problems on generating prism layers on multi-element geometries (ANSYS, 2012).

From the description of the latest version of the software, not available during this research project, it seems that this problem has been resolved.

The next figures (6.4 and 6.5) show the final mesh of the control volume and in particular, the zone between the wing and the slat. It is possible to see that the mesh was correctly constructed even on the junction between the wing and fuselage (right fig.6.5). These zones, as underlined by Murayama (2011), are particularly important in order to guarantee an adequate quality of the mesh. It is also possible to see that the total height of the prism layers on the slat increases going downstream to fulfil the high-lift gridding guide lines, in order to capture all the aerodynamic effects described in the previous section.

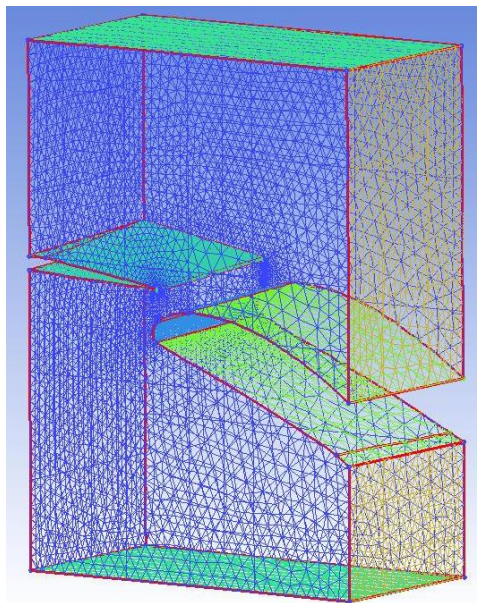


Fig. 6.4 Control volume at wing/slat connection.

The experience gained with the control volume allowed for the correct generation of the mesh for the whole Trap Wing (fig.6.6). The elements density around the wing and in the wake was controlled by density functions, to correctly capture the interaction of the wakes coming from the three elements and the generation of a single wake downstream of the profiles.

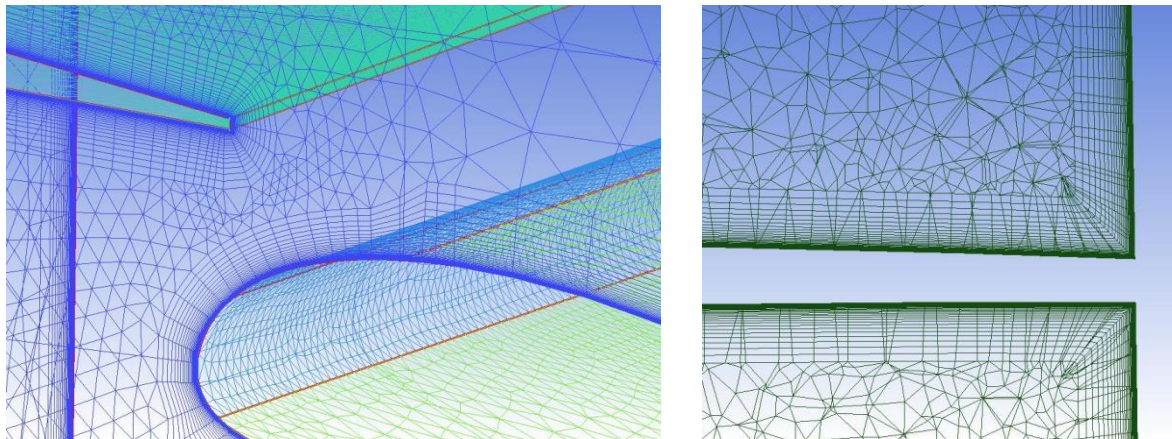


Fig. 6.5 Prism boundary layer at wing /flap (left) and wing/fuse (left).

A 2D cut of the volume mesh around the wing/flap/slat is represented in fig. 6.7, showing the increased mesh density around the profile, and the relatively thick prisms layer in order to capture the high-lift aerodynamics. Fig. 6.8 and 6.9 show the details of the slat/wing connection and the flap/wing connection respectively.

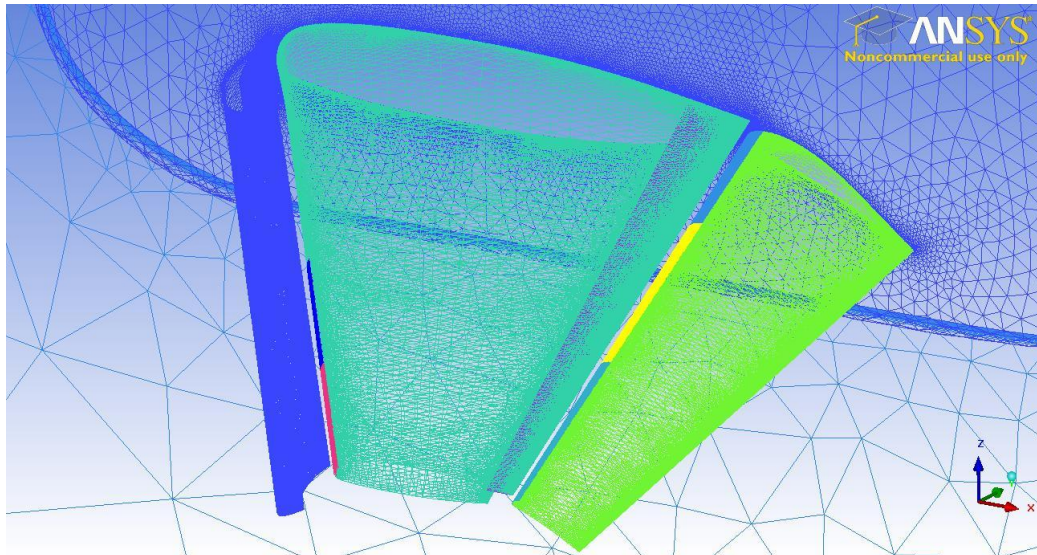


Fig. 6.6 Trap Wing Hybrid mesh

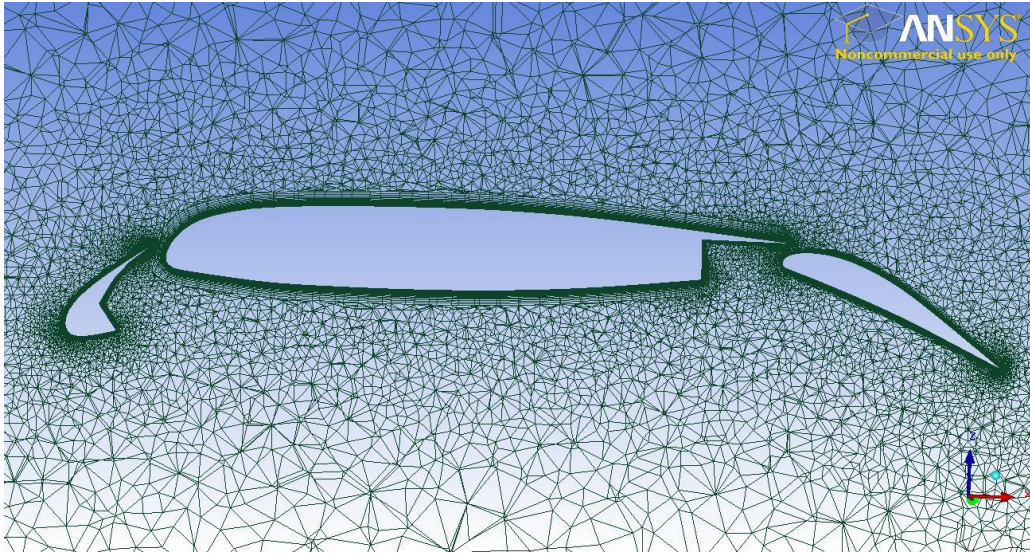


Fig. 6.7 2D cut of the volume mesh around the Trap Wing.

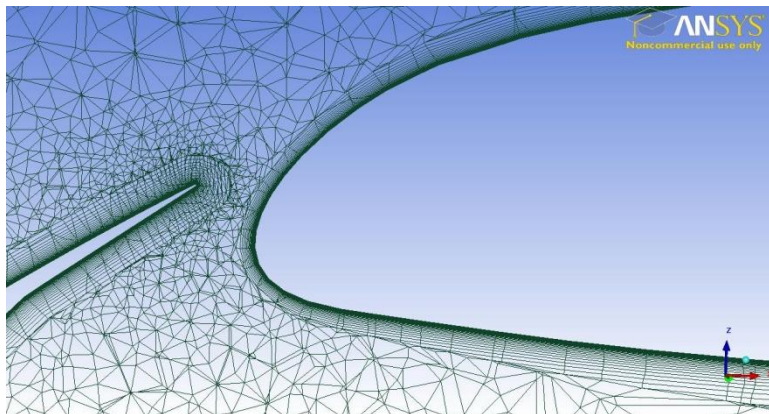


Fig. 6.8 Slat/Wing detail

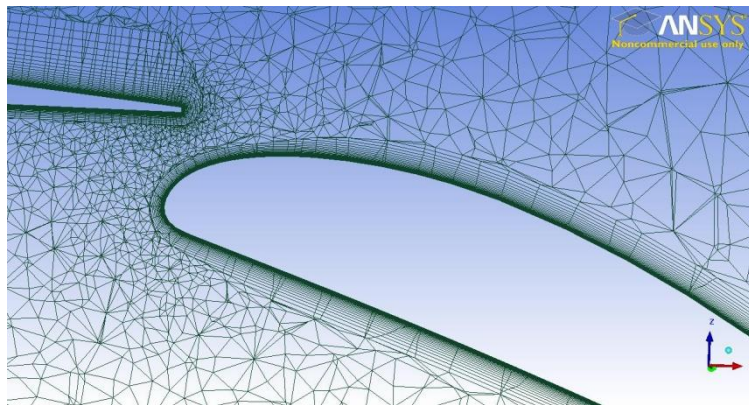


Fig. 6.9 Flap/Wing detail

A coarse, medium and fine hybrid meshes were generated in order to validate the mesh. A grid without the prisms the structure layer was also generated to evaluate the Wall Function method; this can be called unstructured mesh. The respective mesh sizes and wall distance parameter Y^+ , for the hybrid and unstructured grids, are presented in table 6.1.

Grid Type	Size	Nodes ($\times 10^6$)	Cells ($\times 10^6$)	Y^+
Hybrid	Coarse	26.5	9.5	<1
Hybrid	Medium	36	13	<1
Hybrid	Fine	45	19	<1
Unstructured	-	11	7	>10

Table 6.1 Hybrid grid sizes.

6.2 EXPERIMENTAL RESULTS

Experimental results were available (NASA, 2012), in order to validate the model. These results come from various experimental campaigns, using the same model. The initial Trap Wing tests occurred in 1998 and 1999 in the NASA Langley 14- by 22-Foot Subsonic Wind Tunnel (14x22) and the NASA Ames 12 Foot Pressure Wind Tunnel (PWT) facilities, respectively. These tests were part of the NASA Advanced Subsonic Technology (AST) program. The outcomes of the campaigns were basic force, moment, and surface pressure data for a variety of slat/flap deflection combinations at several different Reynolds numbers. Additional limited data, such as velocity profiles, boundary layer (BL) transition, and acoustic microphone array data were also obtained. However, the test data from the 12 Foot PWT indicated strong wall effects. In 2002 and 2003, additional testing was performed in the 14x22 Foot facility, to collect more flow physics data, and to reduce this wall dependency (McGinley, 2005). At the end of the campaign a repeatability study of the force and momentum were performed, in order to guarantee the highest quality of test results. Figure 6.10 show the lift polar for three different tests (T 478, T506 and T513), with the uncertainty bounds.

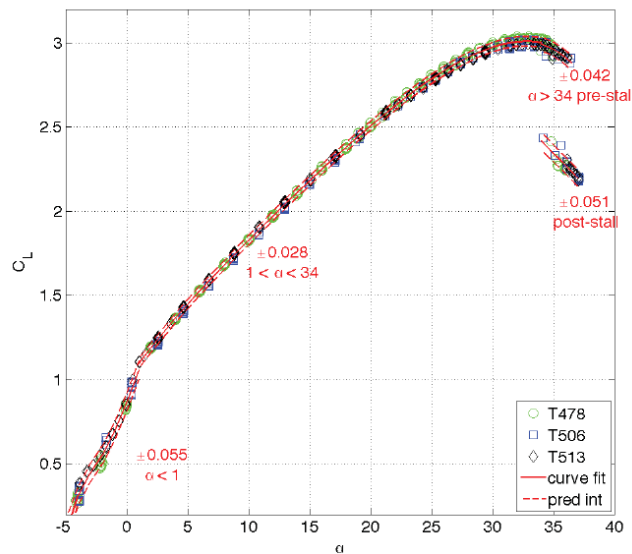


Fig. 6.10 CL polar repeatability. (NASA, 2012)

6.3 NUMERICAL METHOD AND RESULTS

The numerical method was again based on the Reynolds Averaged Navier-Stokes (RANS) equations, discretised using a vertex-based finite volume method. These were evaluated using a second-order advection scheme with a pressure-velocity coupling technique. The Reynolds stresses in the momentum equations, were computed using the Menter's zonal two equations κ - ω turbulence model. It was decided to use only one turbulence model for the wing alone configuration, given that a turbulence model sensitivity study was not the main objective of this research. The work done during the first HiLPW already presents the effects of different turbulence models, showing satisfactory results using the SST turbulence model (NASA, 2012). The assigned boundary conditions (NASA, 2012) are $Re = 4.3 \times 10^6$, $M = 0.2$ and $T = 288.17$ °K.

The lift and drag polar were calculated running simulations varying the angle of attack, more specifically the simulations were run at $\alpha = 6^\circ$, 13° , 21° , 28° , 32° , 34° and 37° . As pointed out in the previous chapter, the results presented at the HiLPW-1, showed a hysteresis effect. In order to avoid this non uniqueness of the solution, it was decided to initialize each computation with the results coming from the previous AOA.

A grid dependency study was performed in order to validate the mesh methodology presented in paragraph 6.2. Figure 6.11 shows the variation of drag coefficient with the number of mesh elements for a C_L of 2.5, and figure 6.12 shows the of lift coefficient with the number of mesh elements at an AOA of 28° . Both C_L and AOA values were selected at incipient flow separation to evaluate the mesh in high lift conditions. Increasing the number of elements, both predicted drag and lift coefficients, are more in line with the experimental values, however the mesh size increases from the 9.6M nodes of the coarse mesh to 19M nodes of the fine mesh, considerably increasing the computational cost.

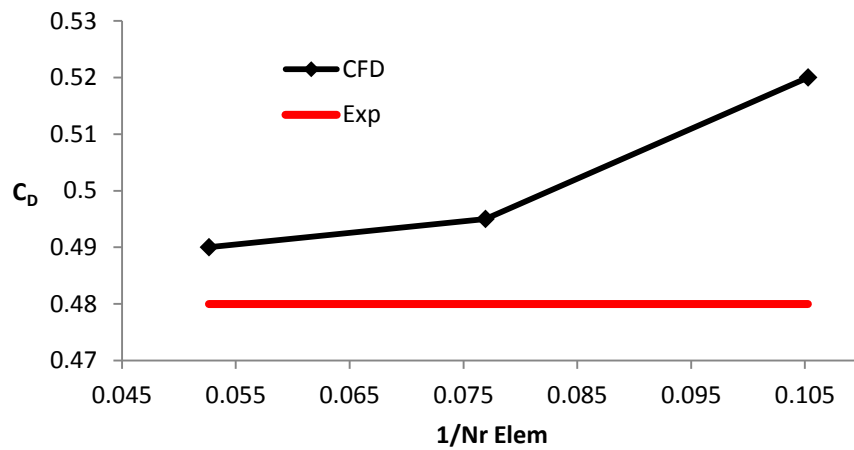


Fig. 6.11 C_D grid convergence study.

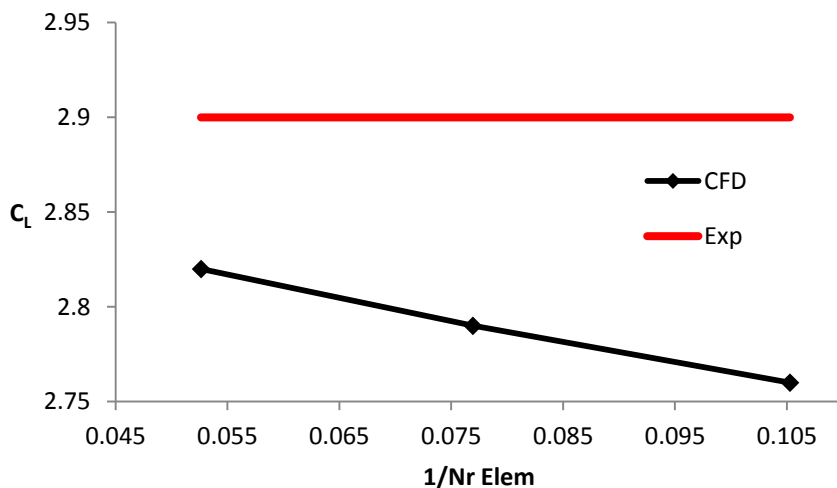


Fig. 6.12 C_L grid convergence study.

The lift polar for the unstructured grid, boundary layer calculated using wall functions, and hybrid grid, coarse and fine, are presented in figure 6.13.

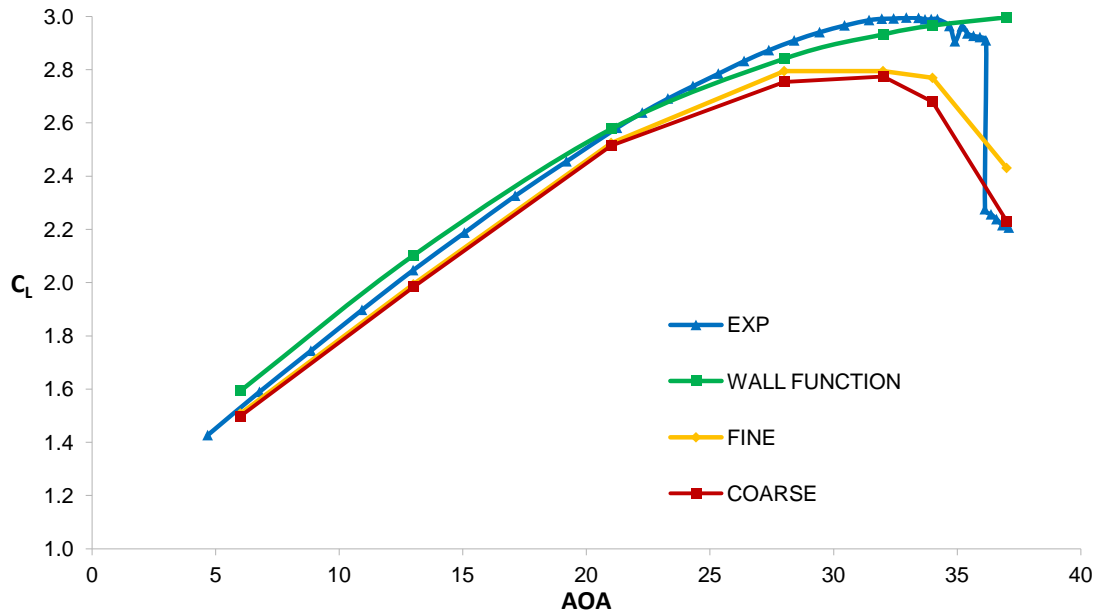


Fig. 6.13 Trap Wing numerical and experimental lift polar.

Looking at the wall function model results, the first impression is that the experimental data are matched with a higher degree of accuracy, especially for high angle of attack. However, with a closer look the flow detachment is postponed, and in this case not even detected at the maximum angle of attack, showing a similar behaviour to the results presented by Eliasson (2007). Therefore, as pointed out previously, the approximated boundary layer flow, using wall functions, led to an over prediction of the maximum lift.

As a result, in order to correctly capture all the aerodynamic features, it was decided to directly solve the boundary layer using a hybrid mesh with a $Y^+ \leq 1$. To reduce the computational cost, the coarse mesh was selected as a benchmark for the wing and body configuration. However a more refined mesh study should be performed and it will be one of the priorities in the continuation of this project.

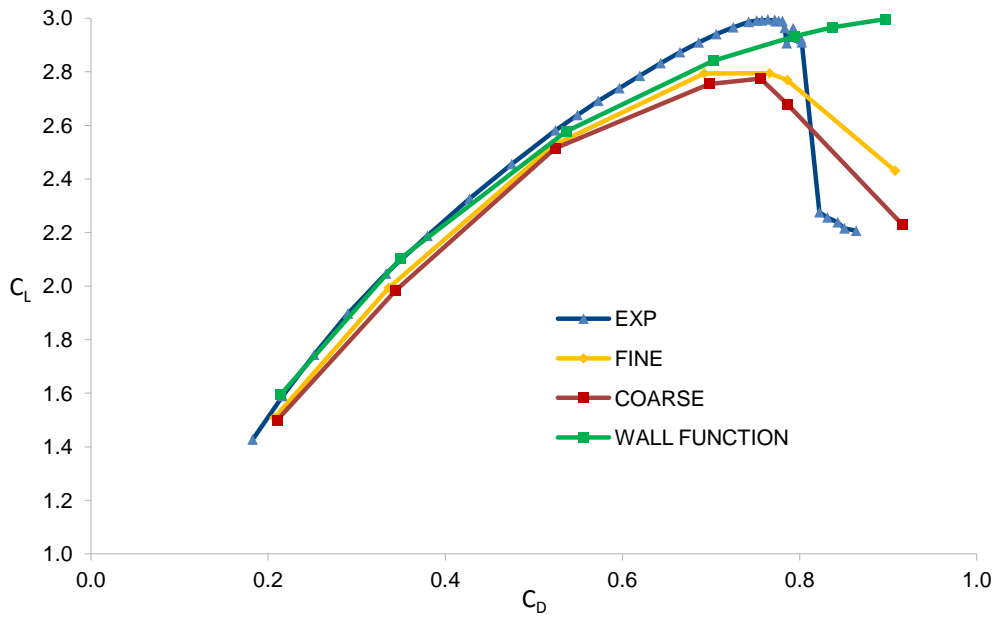


Fig. 6.14 Trap Wing numerical and experimental drag polar.

The next figures (6.17 to 6.35) present the comparison between the numerical, obtained with the coarse mesh, and experimental C_P at different wing/slat/flap positions defined in fig. 6.15. The selected pressure tap rows were at $\eta = 0.17, 0.5$ and 0.85 . Additionally, values were also extracted along the flap leading edge in the wing span direction (fig. 6.16). The pressure coefficients were extracted at different angles of attack, in particular at $\alpha = 6^\circ, 21^\circ$ and 32° .

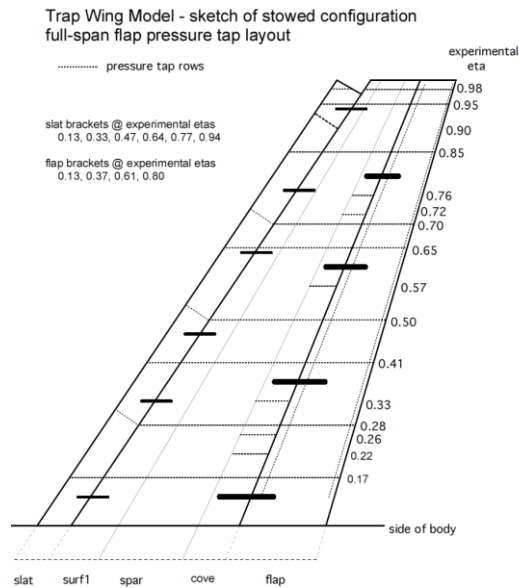


Fig. 6.15 Trap Wing pressure tap rows position. (NASA, 2012).

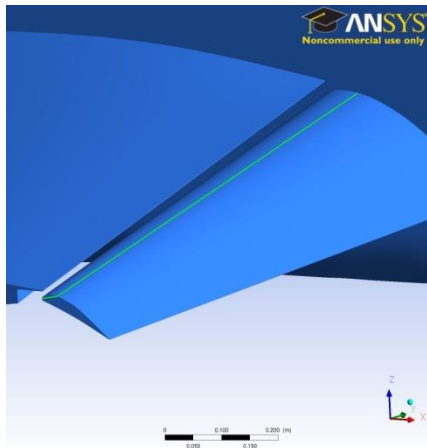


Fig. 6.16 Pressure taps around the flap trailing edge.

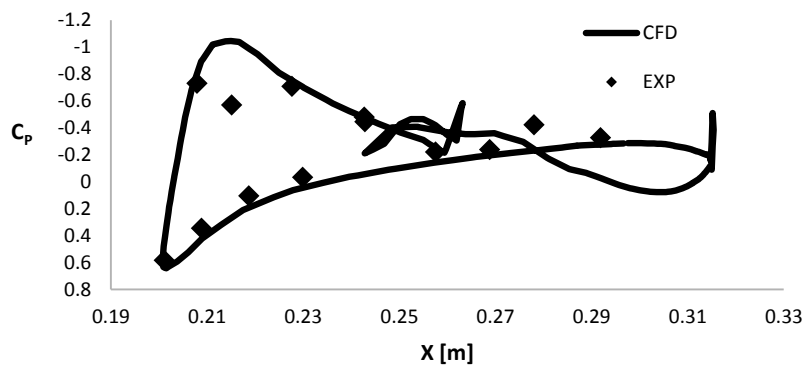


Fig. 6.17 Slat numerical and experimental slat C_p at $\eta = 0.17$, $\alpha = 6^\circ$.

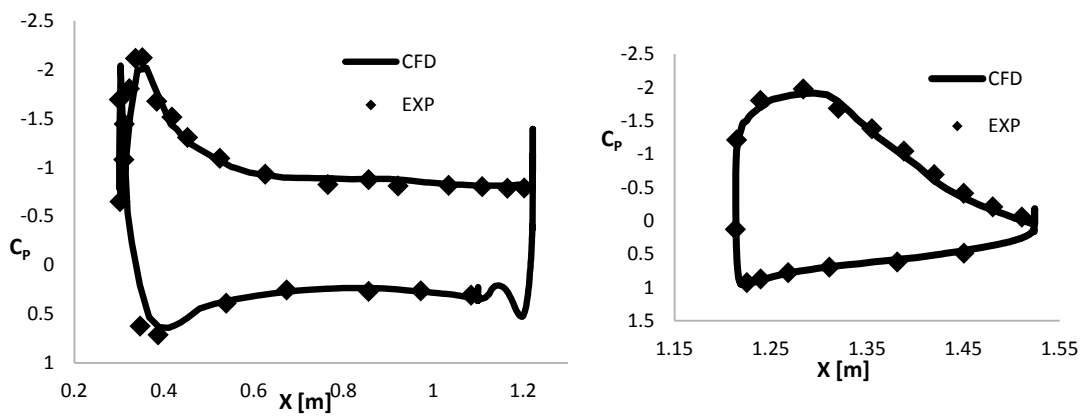


Fig. 6.18 Wing and flap numerical and experimental C_p at $\eta = 0.17$, $\alpha = 6^\circ$.



Fig. 6.19 Slat numerical and experimental slat C_p at $\eta = 0.50$, $\alpha = 6^\circ$.

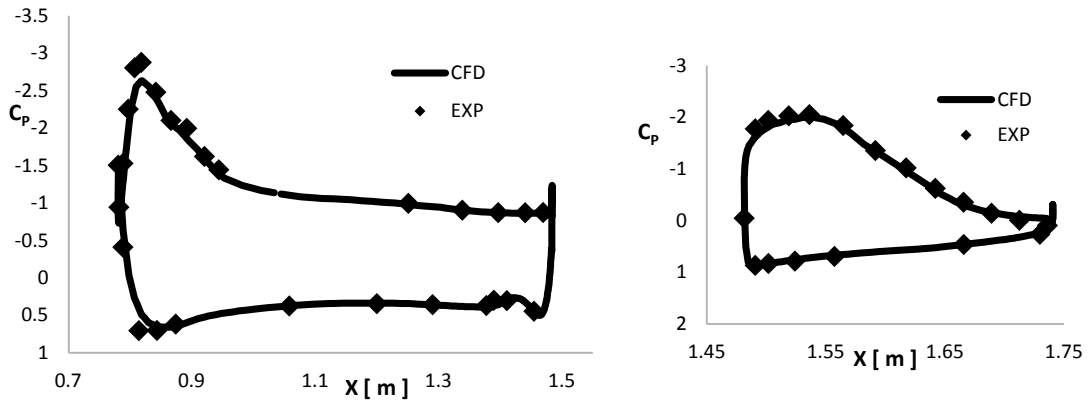


Fig. 6.20 Wing and flap numerical and experimental C_p at $\eta = 0.50$, $\alpha = 6^\circ$.

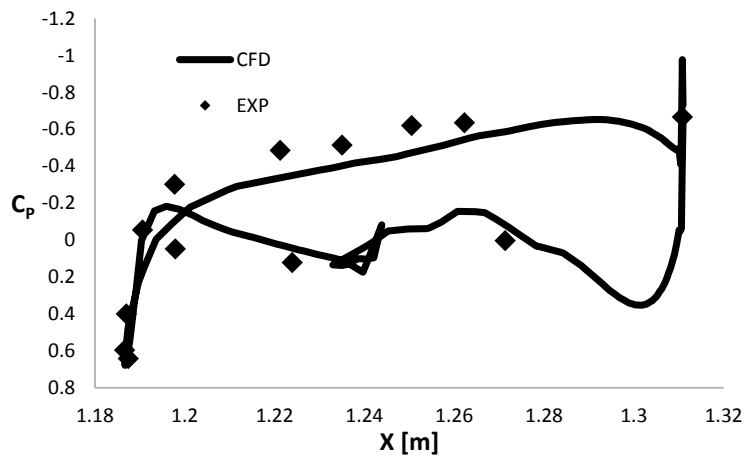


Fig. 6.21 Slat numerical and experimental slat C_p at $\eta = 0.85$, $\alpha = 6^\circ$.

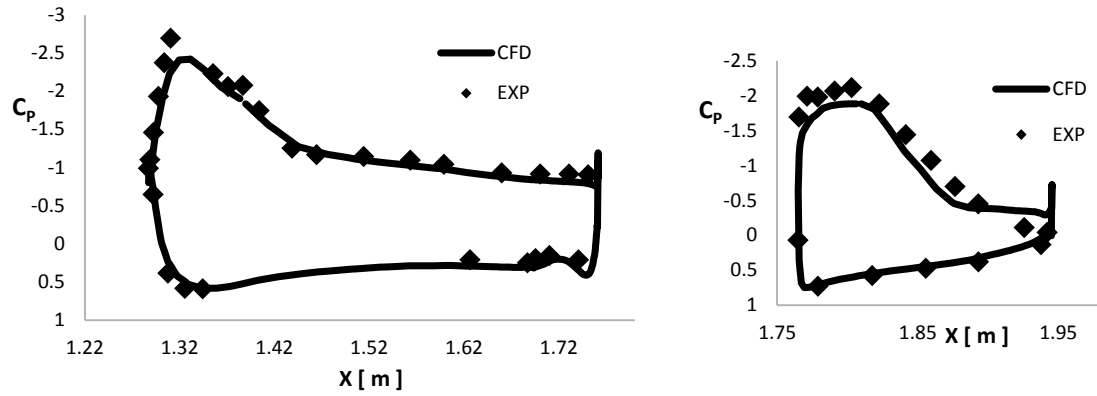


Fig. 6.22 Wing and flap numerical and experimental C_p at $\eta = 0.85$, $\alpha = 6^\circ$.

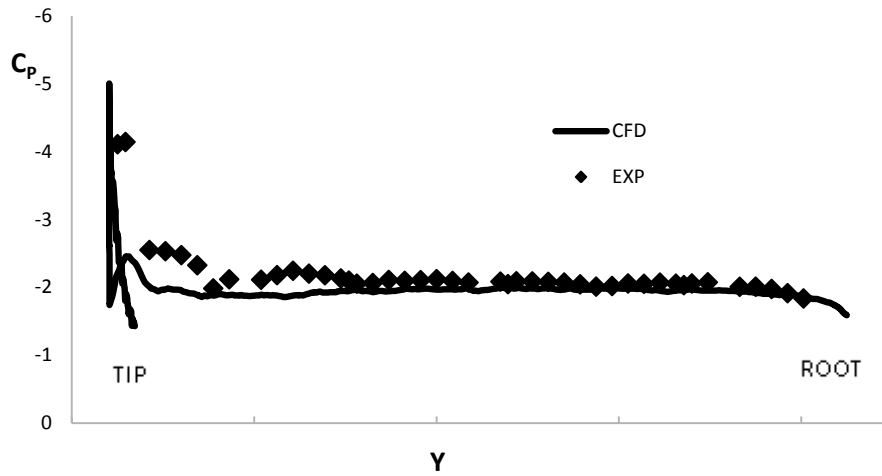


Fig. 6.23 Flap edge span numerical and experimental C_p , $\alpha = 6^\circ$.

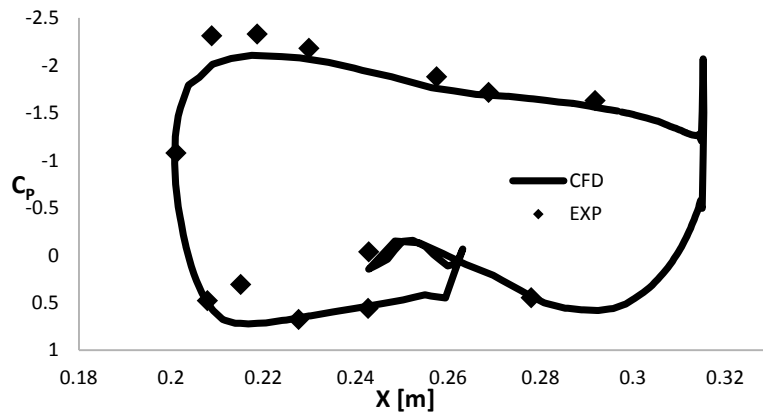


Fig. 6.24 Slat numerical and experimental slat C_p at $\eta = 0.17$, $\alpha = 21^\circ$.

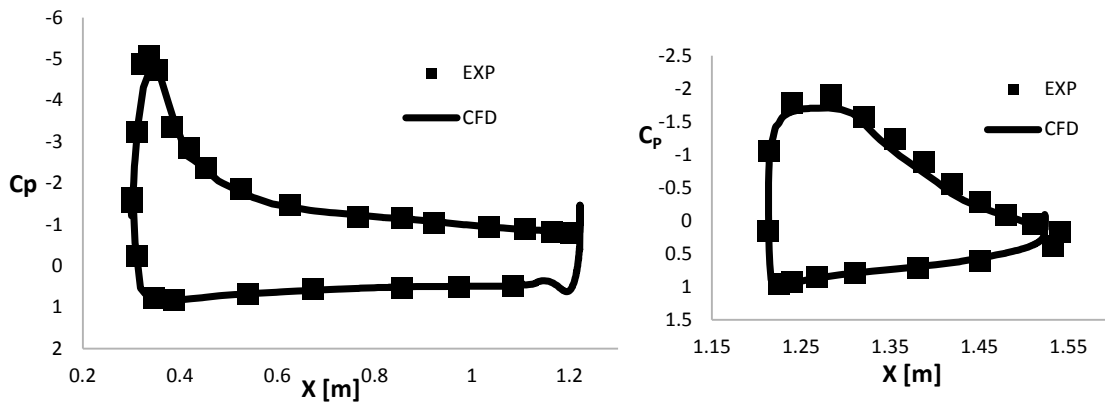


Fig. 6.25 Wing and flap numerical and experimental C_p at $\eta = 0.17$, $\alpha = 21^\circ$.

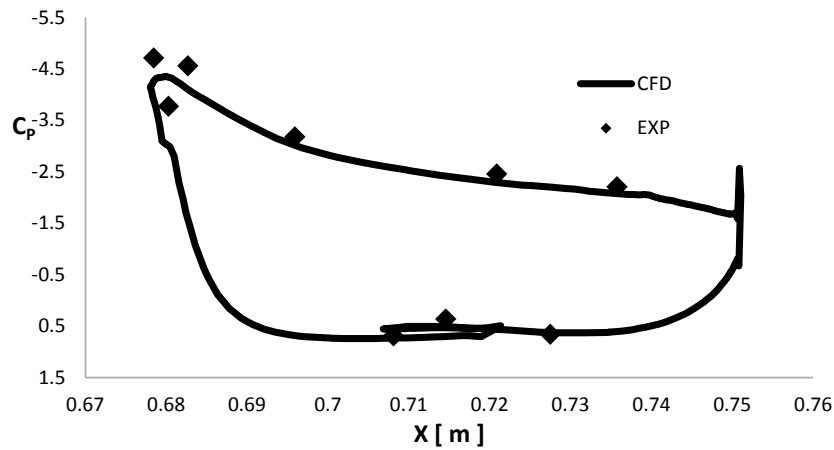


Fig. 6.26 Slat numerical and experimental slat C_p at $\eta = 0.50$, $\alpha = 21^\circ$.

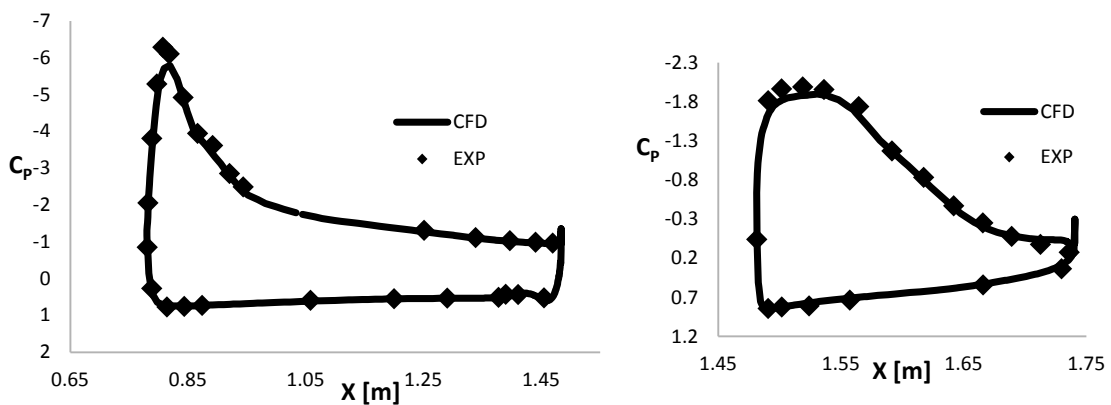


Fig. 6.27 Wing and flap numerical and experimental C_p at $\eta = 0.50$, $\alpha = 21^\circ$.

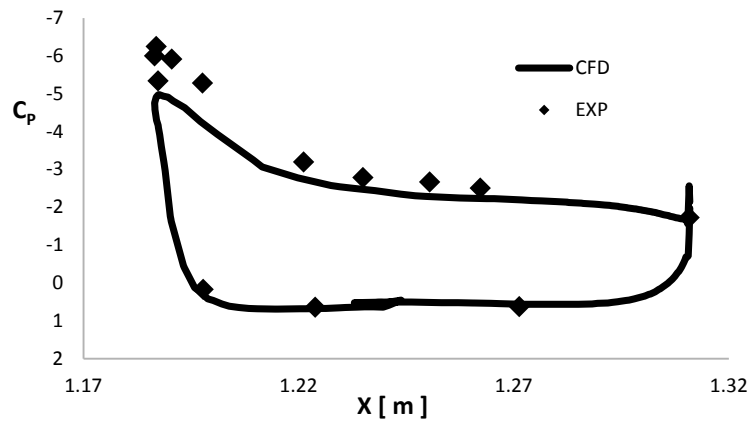


Fig. 6.28 Slat numerical and experimental slat C_p at $\eta = 0.85$, $\alpha = 21^\circ$.

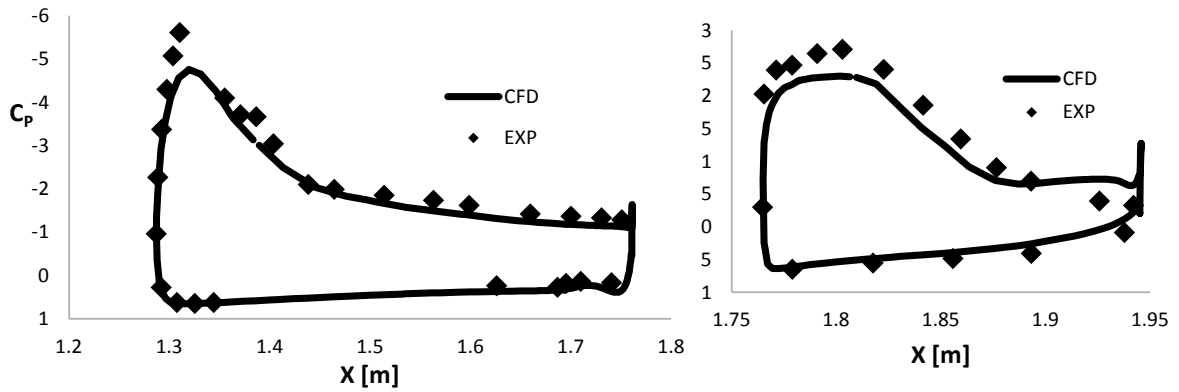


Fig. 6.29 Wing and flap numerical and experimental C_p at $\eta = 0.85$, $\alpha = 21^\circ$.

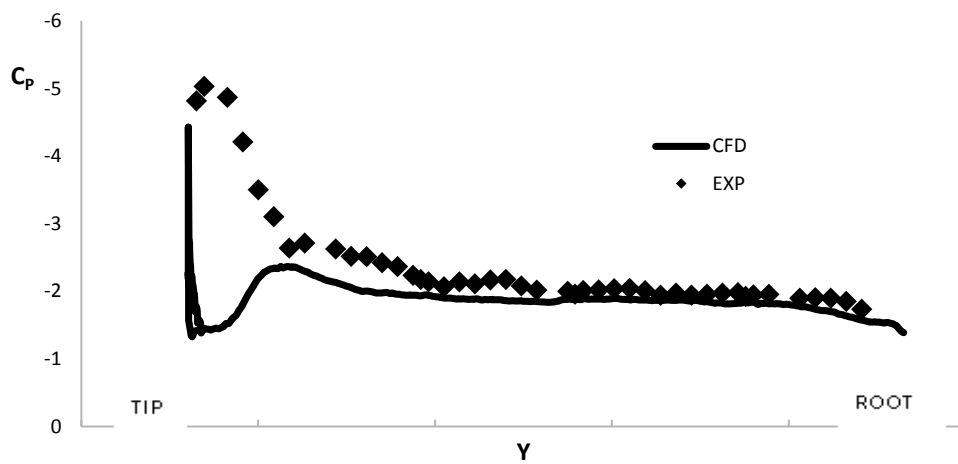


Fig. 6.30 Flap edge span numerical and experimental C_p , $\alpha = 21^\circ$.

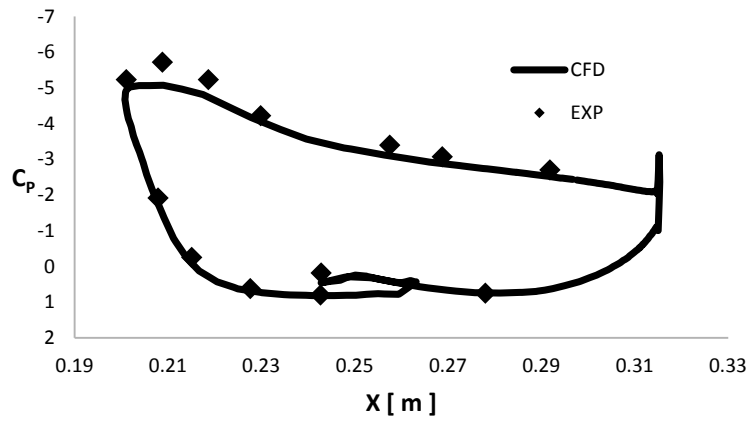


Fig. 6.31 Slat numerical and experimental slat C_p at $\eta = 0.17$, $\alpha = 32^\circ$.

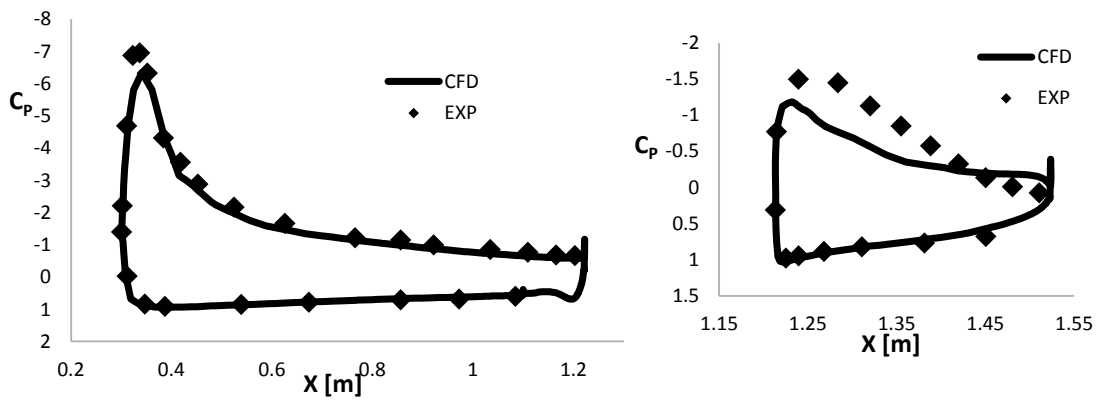


Fig. 6.32 Wing and flap numerical and experimental C_p at $\eta = 0.17$, $\alpha = 32^\circ$.

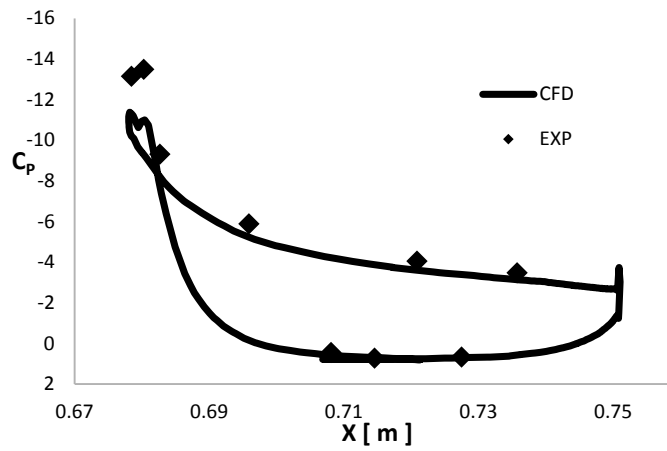


Fig. 6.33 Slat numerical and experimental slat C_p at $\eta = 0.50$, $\alpha = 32^\circ$.

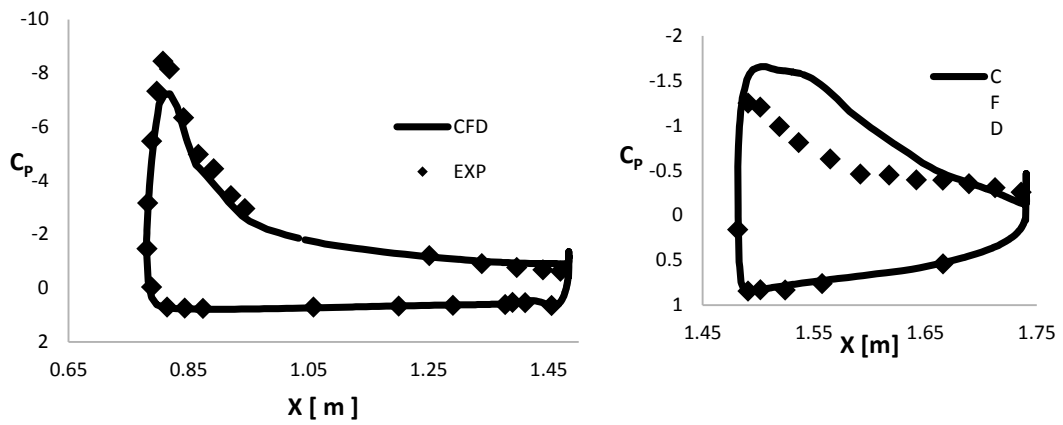


Fig. 6.34 Wing and flap numerical and experimental C_p at $\eta = 0.50$, $\alpha = 32^\circ$.

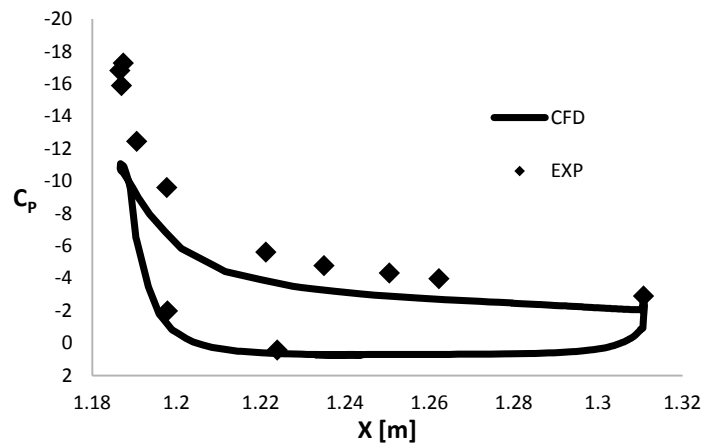


Fig. 6.35 Slat numerical and experimental slat C_p at $\eta = 0.85$, $\alpha = 32^\circ$.

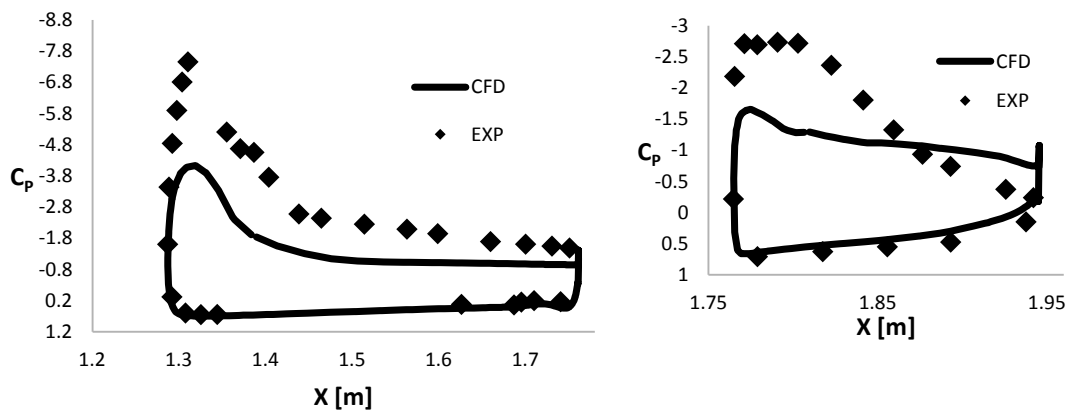


Fig. 6.36 Wing and flap numerical and experimental C_p at $\eta = 0.85$, $\alpha = 32^\circ$.

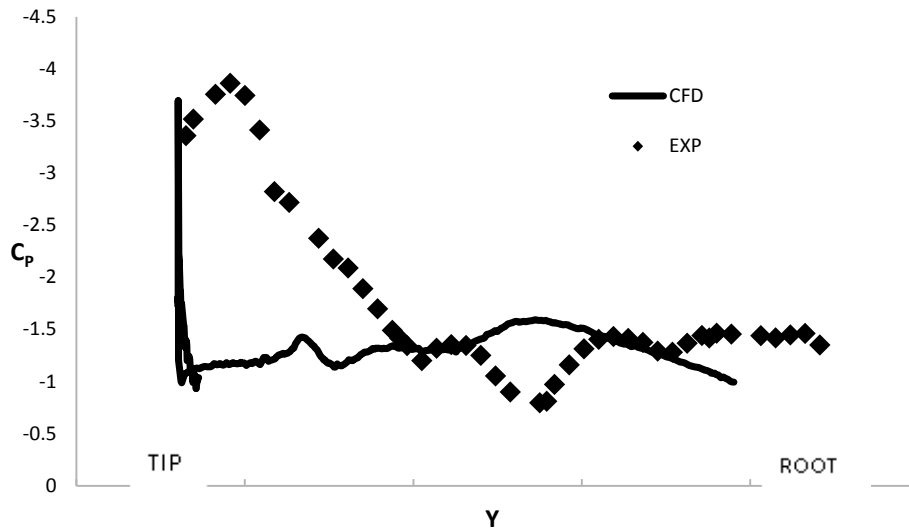


Fig. 6.37 Flap edge span numerical and experimental C_p , $\alpha = 32^\circ$.

From the first set of figures (fig.6.17 to 6.20), extracted at the wing root ($\eta = 0.17$) and wing mid span ($\eta = 0.5$) for an angle of attack of 6° , the numerical and experimental results are in good agreement. A relatively small difference can be seen on the slat pressure side (fig. 6.17 and fig. 6.19). In particular the pressure coefficient was overestimated at the slat root and underestimated at the slat mid span. Further mesh refinement could lead to closer agreement with experimental data. The wing pressure peak, at the mid span, is also underestimated. Note that in some positions, the CFD results present a region of overlapping plots, figure 6.19 for example; this is due to the intrinsic geometry approximation created by the mesh.

The differences between numerical end experimental technique increases moving towards the wing tip (fig. 6.21 to 6.22), $\eta = 0.85$. In particular the C_p on the pressure side of the flap (fig. 6.22 right) is underestimated. This trend is confirmed in fig 6.23, where moving from the root to the tip of the wing, the difference between the numerical and experimental pressure coefficient, considerably increase. Similar results were obtained by Wiart (2011).

At a higher incidence, $\alpha = 21^\circ$, (fig. 6.23 to 6.29) the differences increase further, and in this case even at the wing root. From fig. 6.30 it is possible to see that the C_p is considerably underestimated at the tip of the wing.

The results at 32° present the biggest deviance between numerical and experimental underlining the previously discussed difficulties on modelling the flow at a very high angle of attack.

The comparison of the three figures (6.23, 6.30 and 6.37) suggests that special care must be taken at the flap tip at all angles of attack, especially at high angle of attack. However, the results were considered satisfactory when compared to the other simulations performed during the HiLPW-1.

Further work could lead to an improvement of accuracy, but in the time frame of this project, and with the available resources it was decided to use this model to perform the calculations of the installed engine.

Figures 6.38 and 6.39 show the normalized turbulence intensity (eq. 6.1) at $\eta = 50$ at $\alpha = 21^\circ$. This quantity, (Steed, 2011), provides a more meaningful representation of the turbulent behaviour in wakes and boundary layer, making it possible to determine the boundary layer transition.

$$TU = \frac{\sqrt{\frac{2}{3} \text{Turbulence Kinetic Energy}}}{V} \quad (6.1)$$

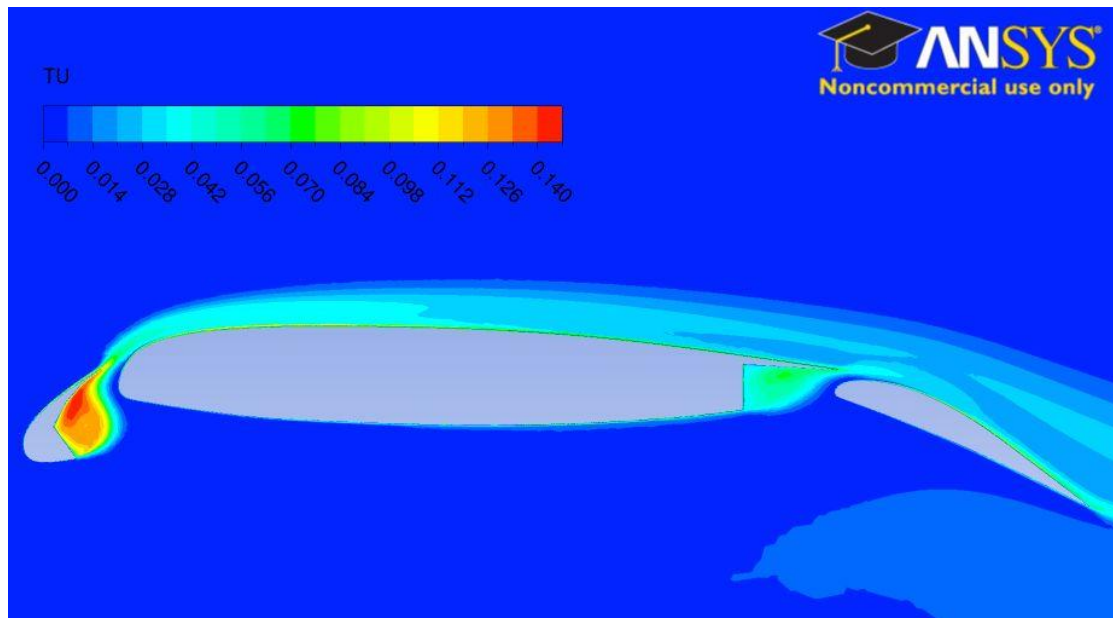


Fig. 6.38 Normalized turbulence intensity (TU) contours at $\eta = 50$, $\alpha = 21^\circ$.

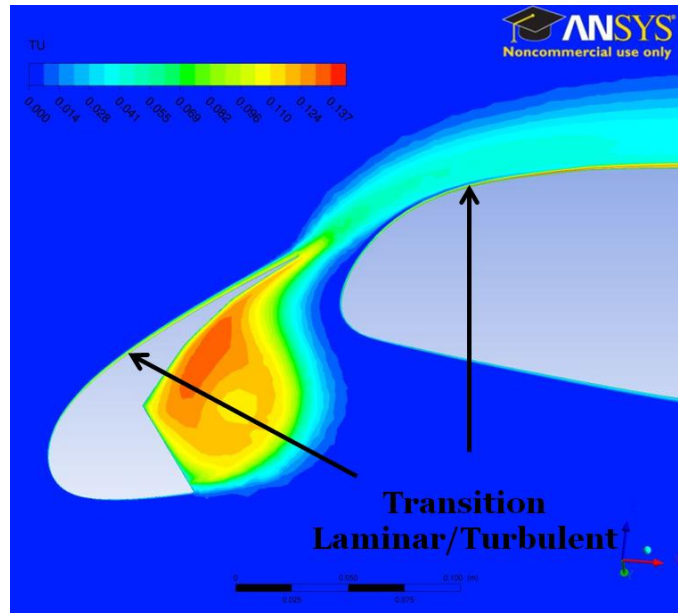


Fig. 6.39 Normalized turbulence intensity (TU) contours at $\eta = 50$, $\alpha = 21^\circ$. Note the high TU values at the transition location (Steed, 2011).

In the next three figures (fig.6.42, 6.45 and 6.45) the wall shear stresses and the surface stream lines show the flow behaviour at an angle of attack of 10° , 28° and 37° . It is possible to see that the flow separation starts at the wing tip, and it is therefore a critical location where the flow is more difficult to model.

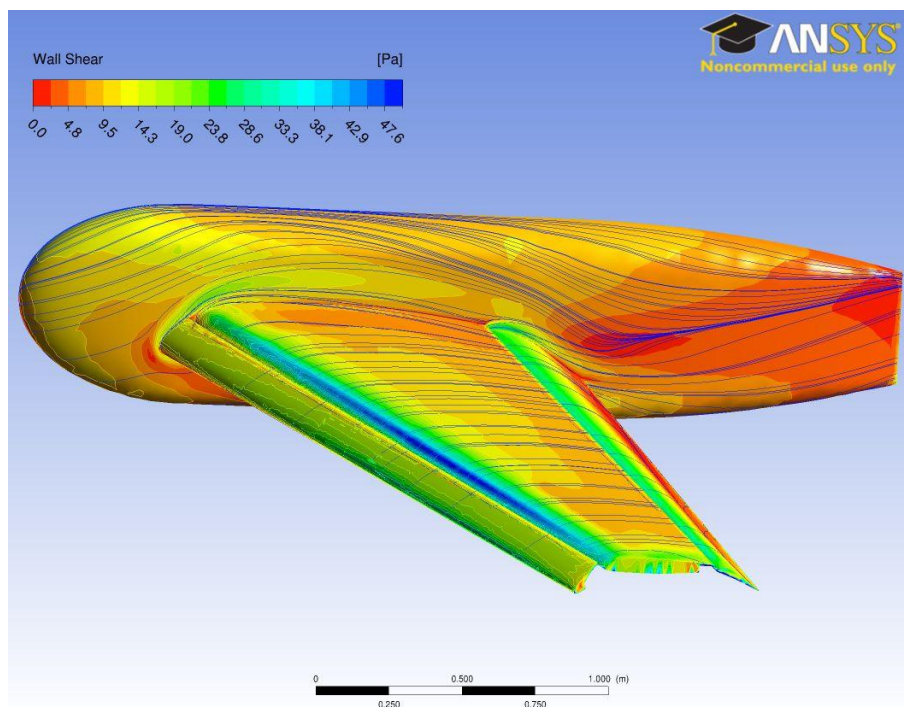


Fig. 6.40 Wall Shear contours and surface stream lines at $\alpha = 6^\circ$.

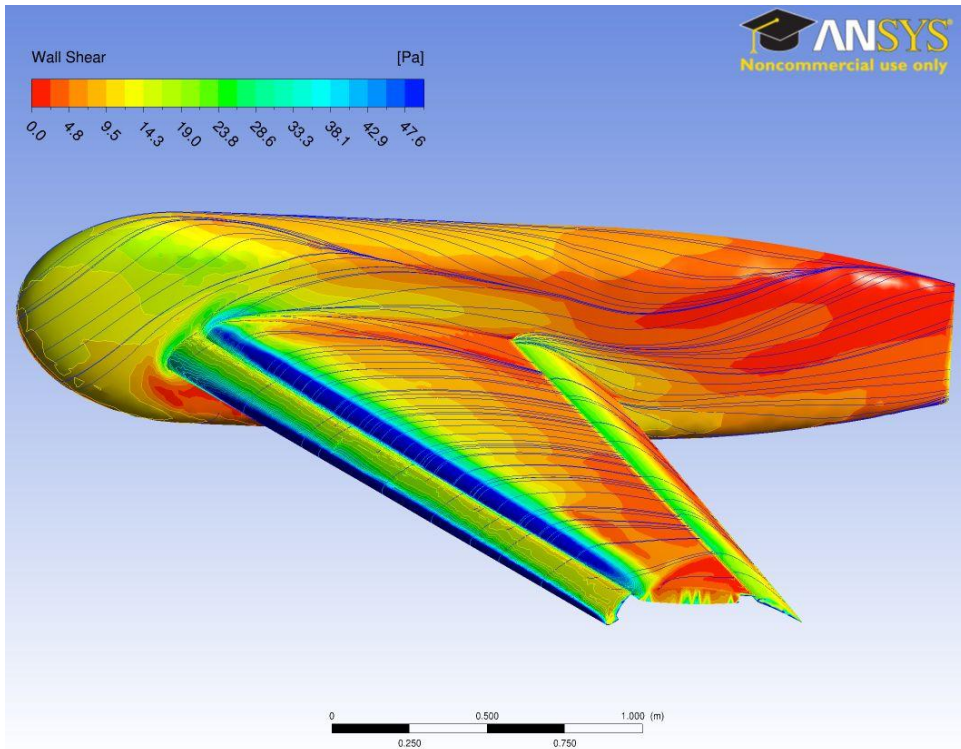


Fig. 6.41 Wall Shear contours and surface stream lines at $\alpha = 28^\circ$.

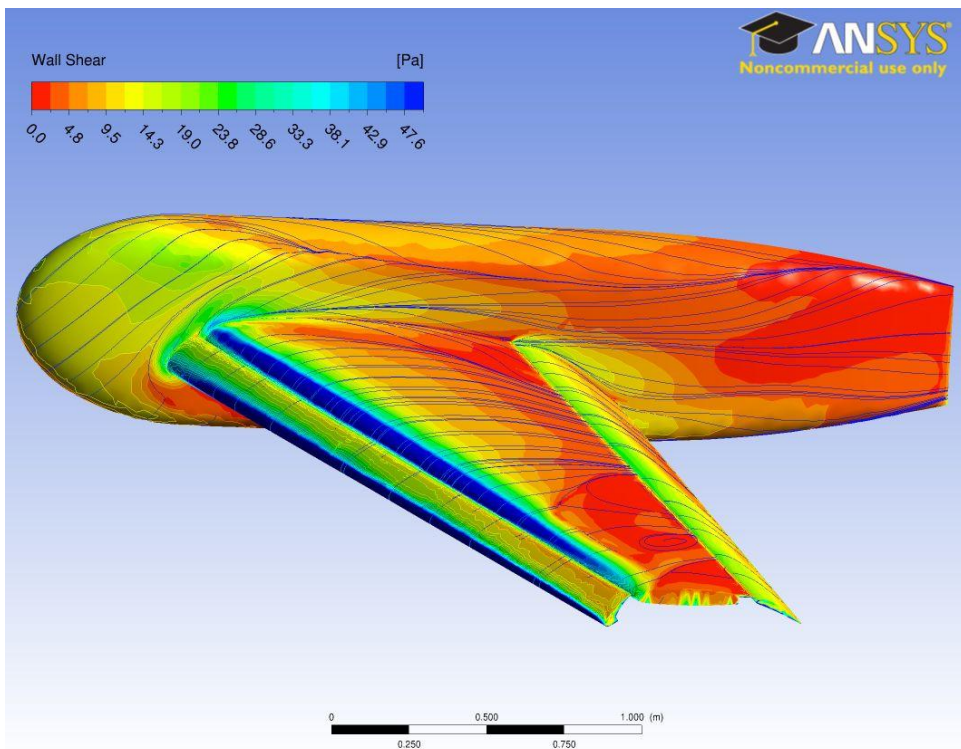


Fig. 6.42 Wall Shear contours and surface stream lines at $\alpha = 32^\circ$.

7 CFD PSI AT HIGH-LIFT CONDITION

7.1 NACELLE GEOMETRY GENERATION AND INSTALLATION

The flight conditions that involves large incidence of flow approaching (take-off, climb, approach, crosswind and engine failed), must be carefully examined because they typically result in a rapid acceleration and deceleration of the flow on the nacelle inlet lip, raising the possibility of flow separation. The parameter A_o/A_i , ratio of the far-field stream tube area to the inlet area, is a direct indication of the general incidence of the flow approaching the inlet (already presented in chapter 1). Referring to fig.7.1, a value of one means that the inlet is capturing its projection in the far-field at zero incidence. Values less than one indicates that the flow is pre-diffusing, and the flow is characterized by an outward incidence, this is generally the case at cruise condition. Contrarily A_o/A_i will exceed unity at low flow speed and at moderate to high-power settings, causing an inward flow incidence. The take-off and approach conditions, which fell in this category, are also characterized by a nonzero pitch attitude and a ground wind normal to the inlet axis (fig.7.1 right). This introduces the possibility of internal lip flow separation with a performance degradation and reduction of engine stability margin that may cause compressor surge and possibly engine flameout.

Schulze (2010) investigated the turbulent flow bubble generated at the nacelle lip at take-off conditions, underlining the importance of reducing the inlet flow separation. For these reasons in order to evaluate the effects of the engine installation at high-lift condition it was necessary to define an appropriate nacelle geometry. The methodology previously presented for the cruise condition was applied again, but in this case the nacelle was considered non axisymmetric, in order to closely represent the real nacelle aerodynamics at high-lift condition and to better control the nacelle flow separation (Seddon, 1993). The nacelle was generated using the boundary conditions applied for the Intercooled Core Engine presented in the chapter 4. Figure 7.2 shows the non-axisymmetric inlet geometry input file.

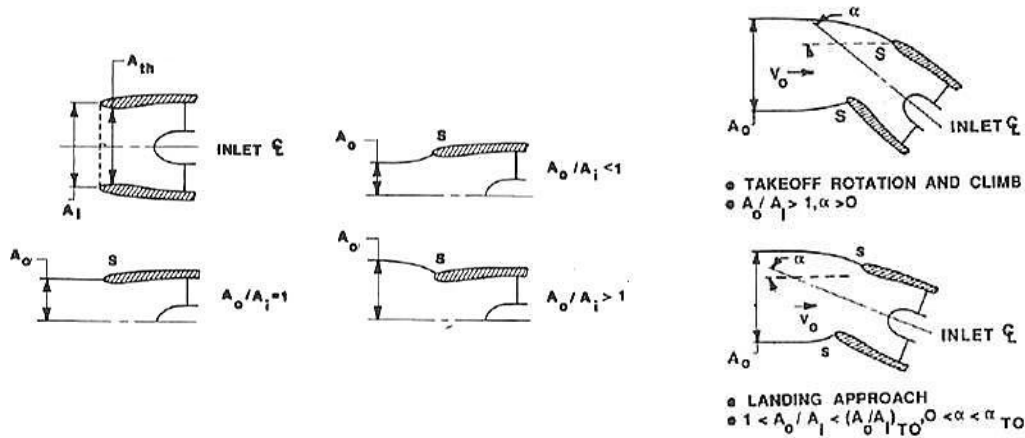


Fig. 7.1 Definition of the parameter A_o/A_i , and values at take-off and approach. (Seddon, 1993).

The inlet geometry was refined to reduce the flow separation at high incidence that particularly affects the inside of the keel lip (Seddon, 1993). Figure 7.3 shows the wall shear for the two different nacelle versions where the flow separation was reduced, extent of low wall shear contour reduced, varying the radius at the keel lip. The results are shown at an angle of attack of 21° . Further modifications could lead to an additional reduction but the geometry was considered satisfactory.

It was also decided to use a through-flow nacelle instead of powered nacelle to reduce the already high computational cost. It is important to remember that the main outcome of the project was to model the engine installation, and the

through-flow nacelle simulations represent an important step in understanding the HPSI aerodynamics. The TFN configuration is still able to represent the main PSI effects considerably reducing the computational cost compared to an engine on configuration (Rohlmann, 2012). A comparison of computed pressure coefficient for a through-flow nacelle and engine operative at high lift condition in the non-linear and next to the maximum lift segment is showed in figure 7.4. As explained in chapter 1 the main differences are due to the interaction of the jet with the wing. The through-flow nacelle is represented in figure 7.5, where the fan and core ducts are empty cavities. The exhaust area was defined to match the flight condition mass flow ratio (Berry, 1994 and Brodersen, 2002).

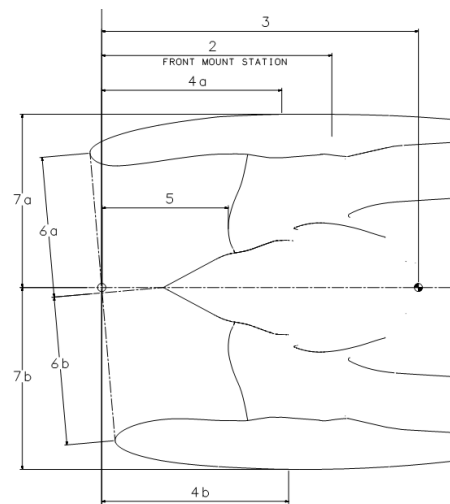


Fig. 7.2 Non-axisymmetric input inlet geometry. (Andreoletti, 2007).

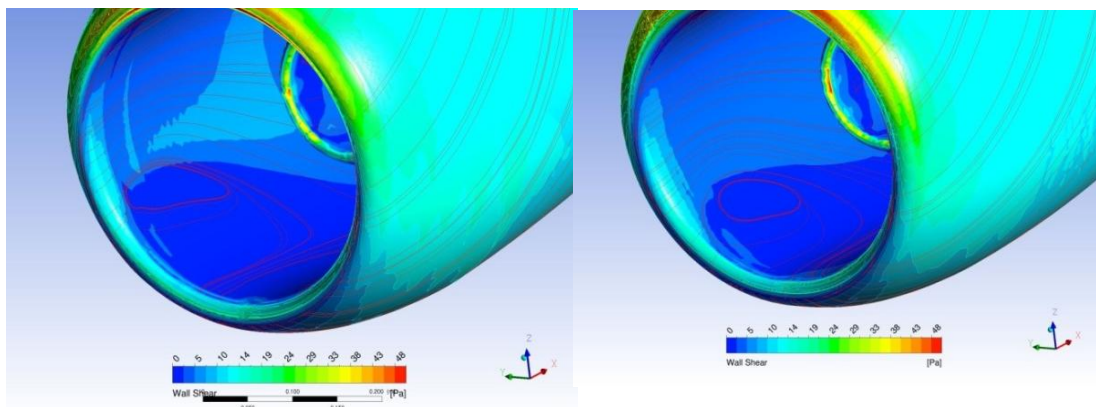


Fig. 7.3 Wall shear at the nacelle keel lip. Starting geometry(left), reduced separation geometry (right).

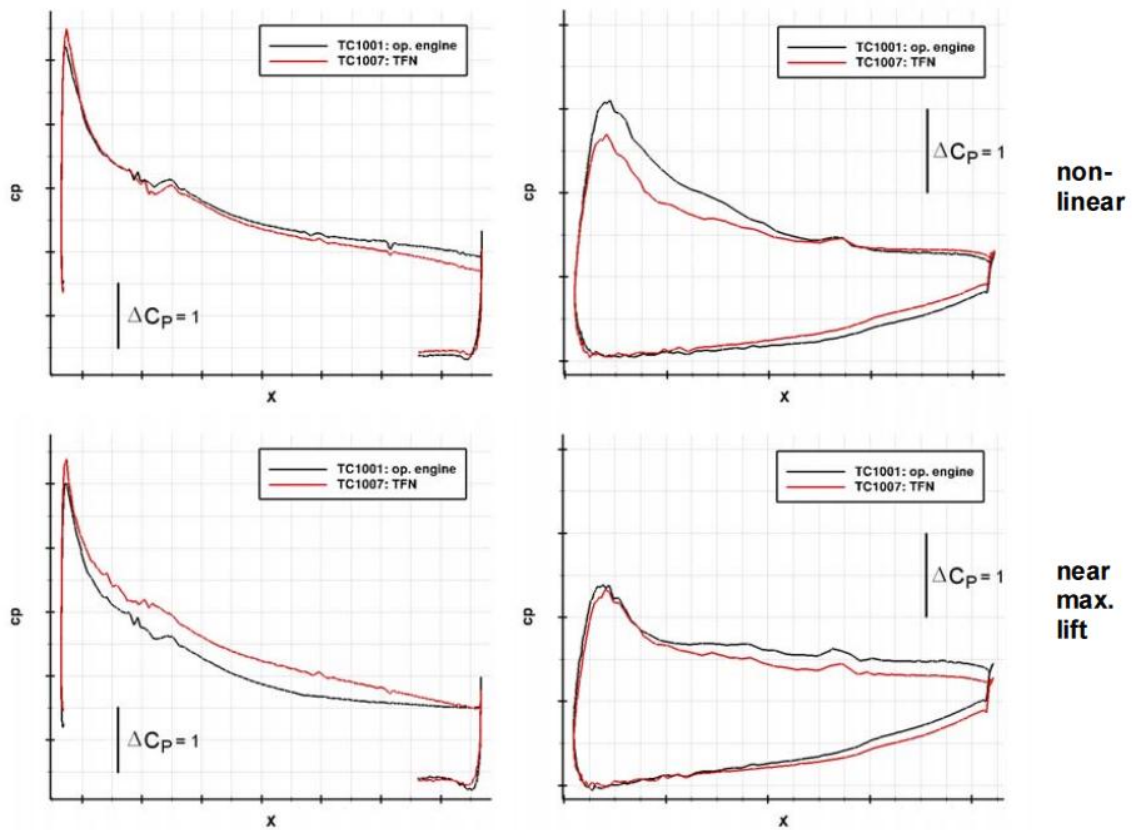


Fig. 7.4 Operational engine influence on the pressure distribution of the wing (left) and flap (right). (Rohlmann, 2012)

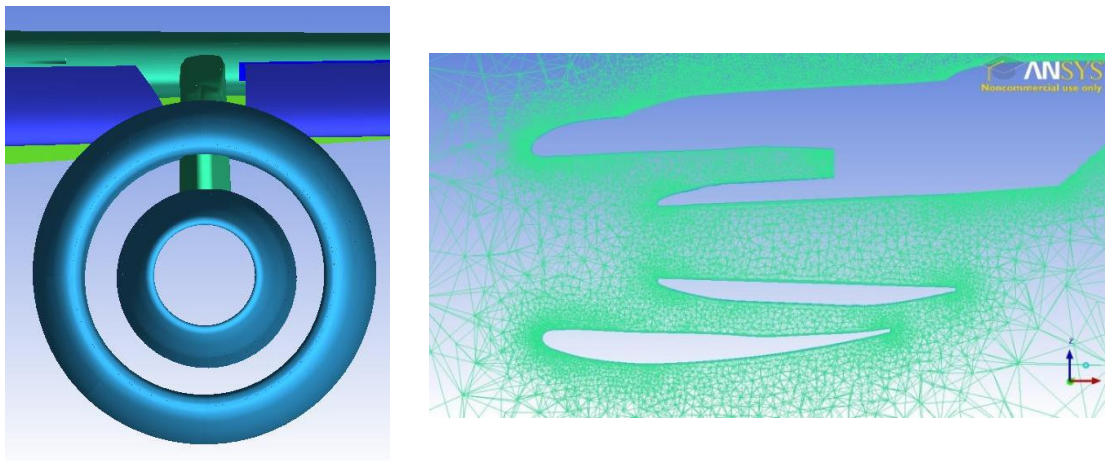


Fig. 7.5 Through-Flow Nacelle geometry (right) and mesh (left). Note the slat cut.

The final installed nacelle geometry is presented in figure 7.6, also shown in fig.7.5 (the cut on the slat due to the pylon). The geometry of the cut was defined in order to guarantee that at the not-extended portion of the wing trailing edge, the configuration was representative of a wing cruise profile.

Given that no guidelines were available, the author referred to real engine installation. The engine was positioned with a similar gap between the fuselage and the pylon, compared to the previous installation on the CRM model.

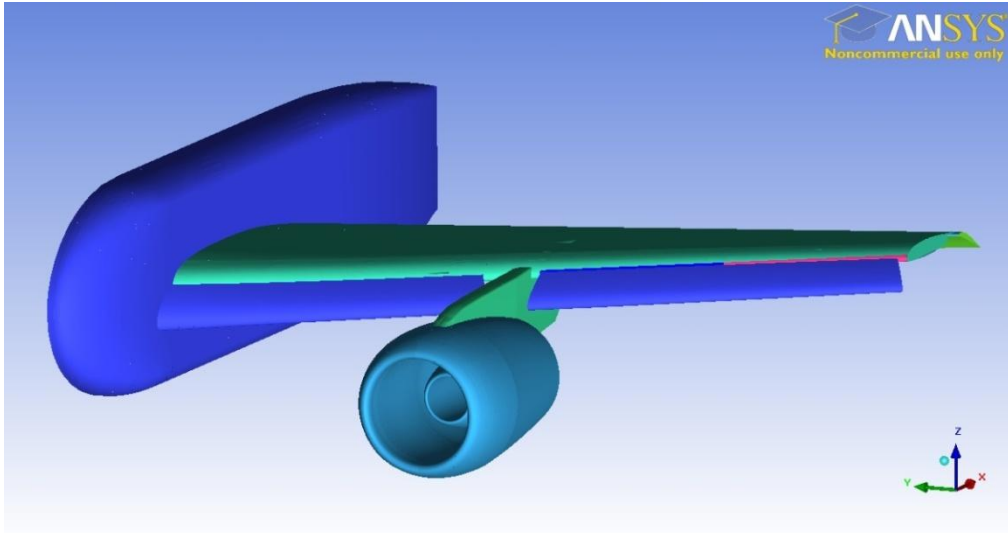


Fig. 7.6 High-lift engine-airframe geometry.

7.2 NUMERICAL METHOD AND RESULTS

The numerical method and the assigned boundary conditions were the same as the wing and body configuration: $Re = 4.3 \times 10^6$, $M = 0.2$ and $T = 288.73 \text{ }^\circ\text{K}$. The previously described mesh technique was applied to the nacelle and pylon, with the only difference that the coarse mesh was refined on the wing surface (fig.7.7) and in the nacelle/wing wakes.

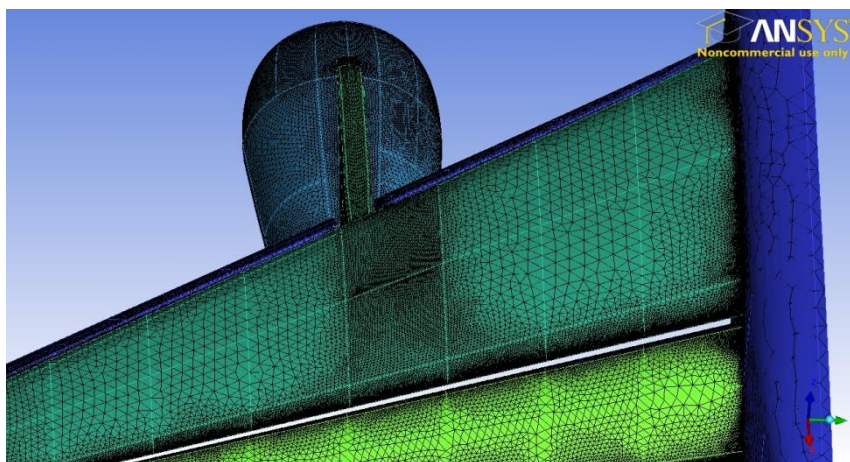


Fig. 7.7 Wing surface mesh refinement at the wing/pylon junction.

The resulted dimension of the mesh was: 39×10^6 elements and 16×10^6 nodes. Once again the lift and drag polar were calculated running simulations varying the angle of attack, in particular the simulations were run at $\alpha = 6^\circ, 10^\circ, 15^\circ, 17^\circ, 18^\circ, 19^\circ, 20^\circ, 21^\circ, 22^\circ$ and 24° . A relative small incidence increment between the calculations was used, due to the hysteresis effect. In order to avoid the non-uniqueness of the solution, each computation was initialized with the results coming from the previous AOA, and to capture the real flow separation the step was maintained as small as possible.

The comparison between the WB and WBNP lift and drag polar are presented in figure 7.8 and 7.9 respectively. It is possible to see that the maximum lift was considerably reduced due to the installation of the engine. For the WBNP configuration the maximum lift is reached at $\alpha = 21^\circ$ compared to an angle of attack of 32° for the WB configuration. The difference between the two values at $\alpha = 21^\circ$ is about 12%. The installation effects are also visible at low angle of attack (6°), where the lift is reduced by 2% due to the engine installation. Similar effects influence the drag polar (see fig 7.9) with a 4.6% drag reduction at $C_L = 1.54$ and a 24% reduction at the maximum WBNP $C_L = 2.25$.

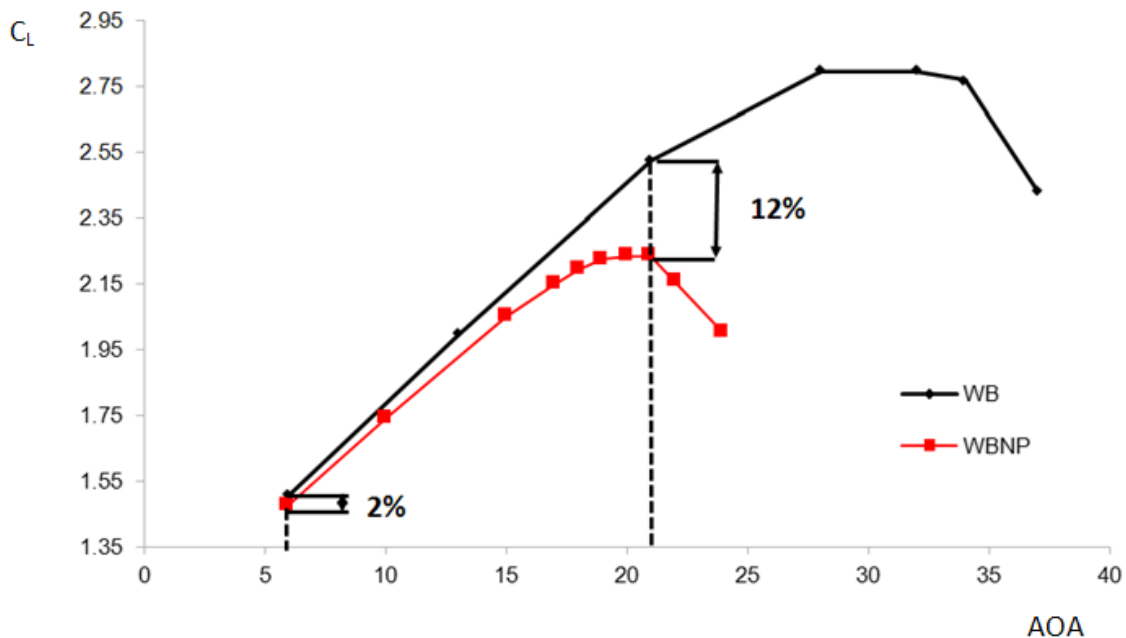


Fig. 7.8 Lift polar for the WB and WBNP configurations.

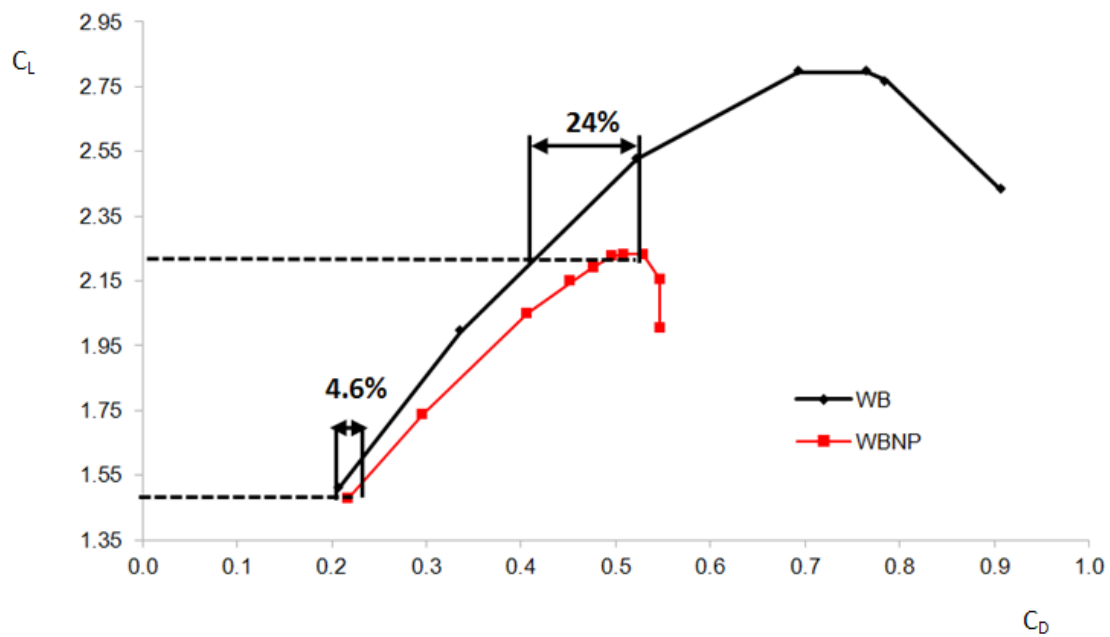


Fig. 7.9 Drag polar for the WB and WBNP configurations.

The reduction of lift can be explained looking at the physical installation of the engine given that in order to accommodate the pylon, the slat needs to be cut, interrupting the slat flow and losing part of the lifting surface. This leads to a reduction of lift because of the missing portion of the slat and also because the part of the wing profile adjacent to the cut is exposed to higher incidence flow and therefore subject to earlier flow separation.

The next figures (7.11 to 7.20) present the C_p comparison between the WB and WBNP configurations at different wing/slat/flap positions around the engine installation span position (figures 6.10). The selected pressure tap rows were at $\eta = 0.45, 0.5$ and 0.60 . The pressure coefficients were extracted at $\alpha = 6^\circ, 21^\circ$.

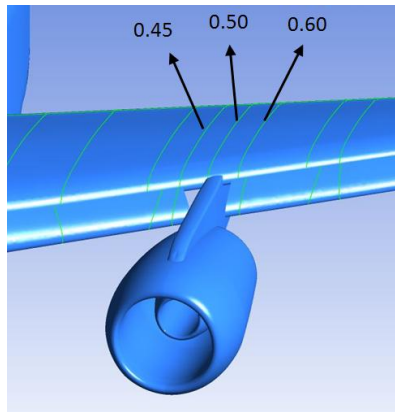


Fig. 7.10 Numerical pressure tap rows position WBNP and WB (values of eta).

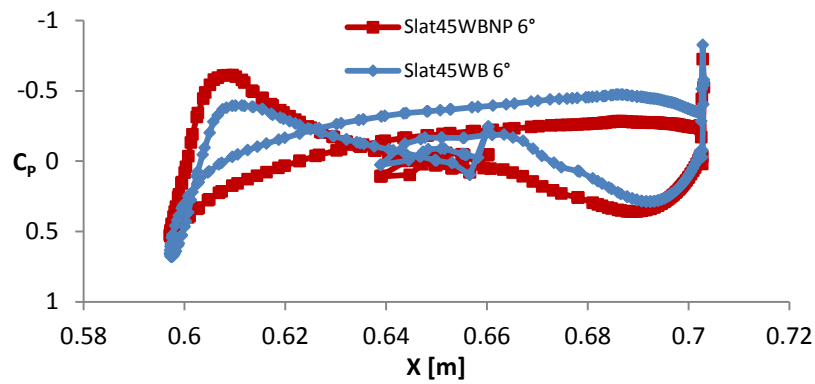


Fig. 7.11 WB and WBNP configurations slat pressure coefficient at eta = 0.45, $\alpha = 6^\circ$.

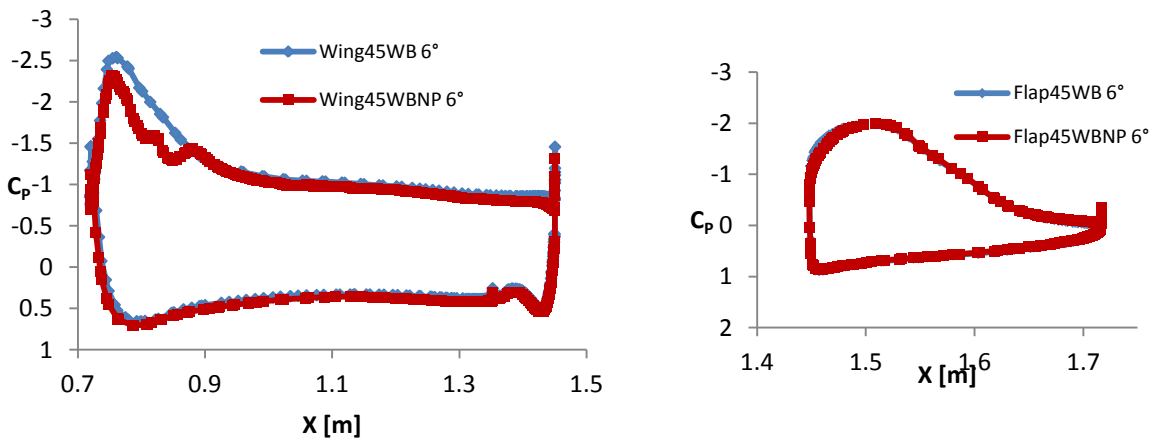


Fig. 7.12 Wing and flap WB and WBNP configurations pressure coefficient at eta = 0.45, $\alpha = 6^\circ$.

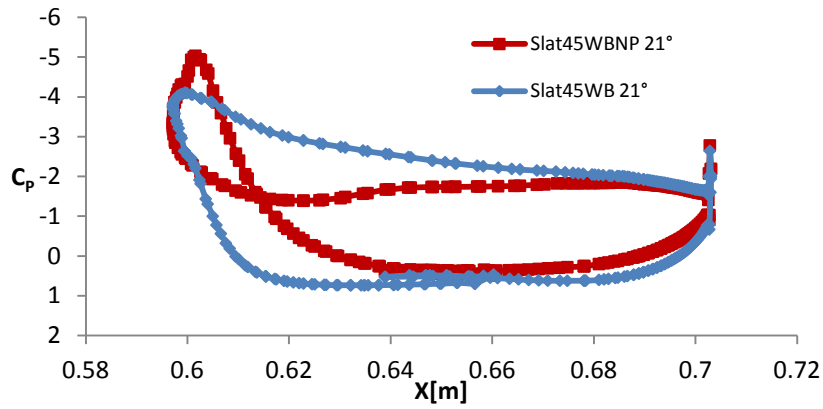


Fig. 7.13 WB and WBNP configurations slat pressure coefficient at $\eta = 0.45$, $\alpha = 21^\circ$.

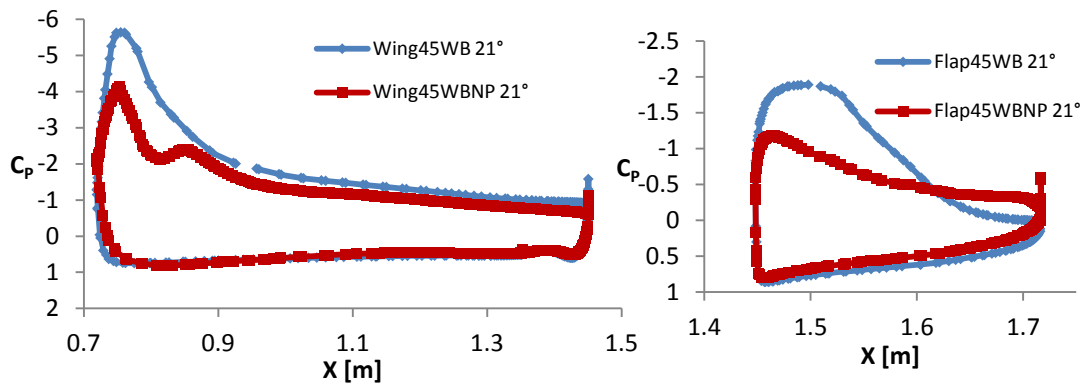


Fig. 7.14 Wing and flap WB and WBNP configurations pressure coefficient at $\eta = 0.45$, $\alpha = 21^\circ$.

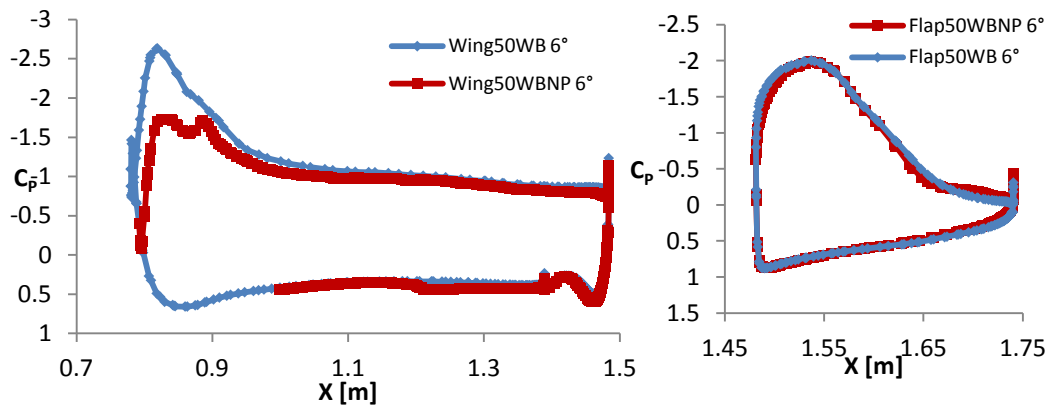


Fig. 7.15 Wing and flap WB and WBNP configurations pressure coefficient at $\eta = 0.50$, $\alpha = 6^\circ$.

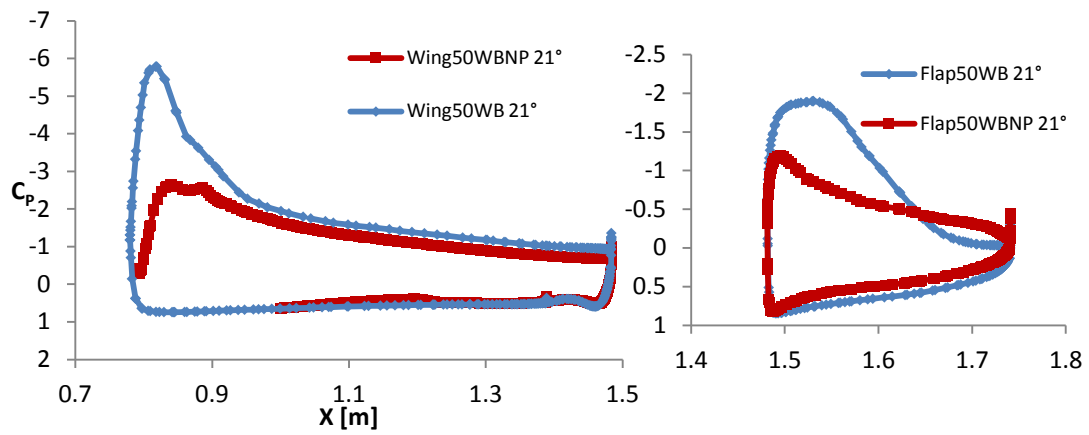


Fig. 7.16 Wing and flap WB and WBNP configurations pressure coefficient at $\eta = 0.50$, $\alpha = 21^\circ$.

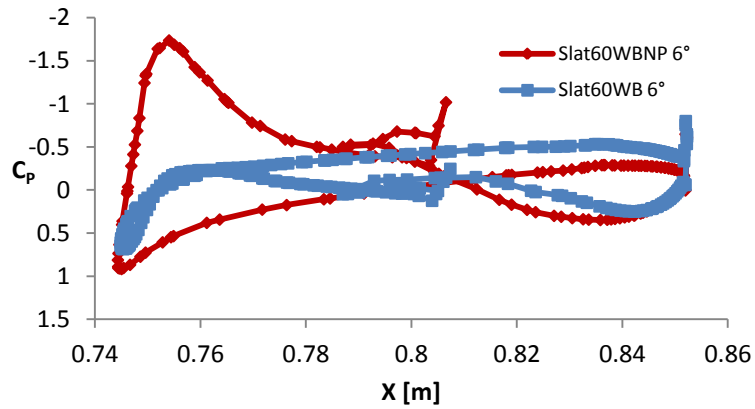


Fig. 7.17 WB and WBNP configurations slat pressure coefficient at $\eta = 0.60$, $\alpha = 6^\circ$.

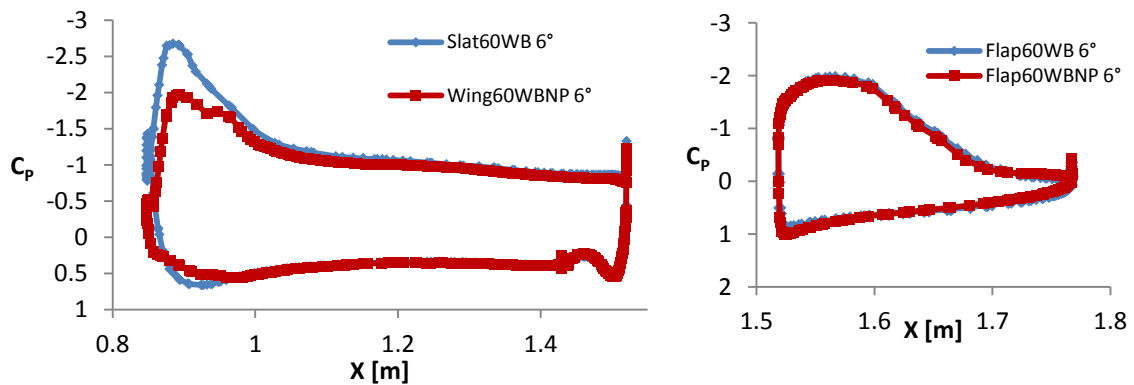


Fig. 7.18 Wing and flap WB and WBNP configurations pressure coefficient at $\eta = 0.60$, $\alpha = 6^\circ$.

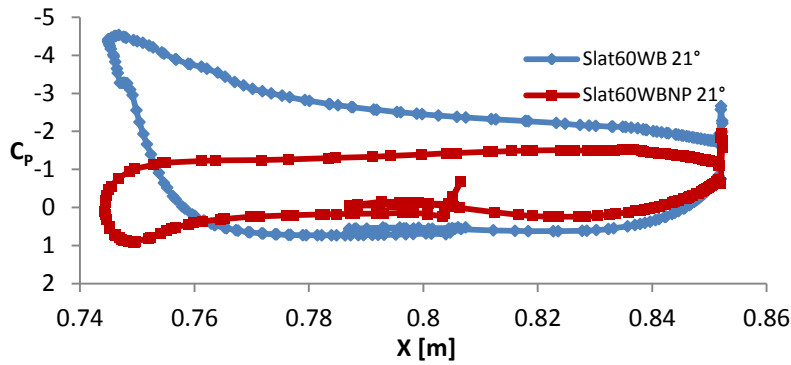


Fig. 7.19 WB and WBNP configurations slat

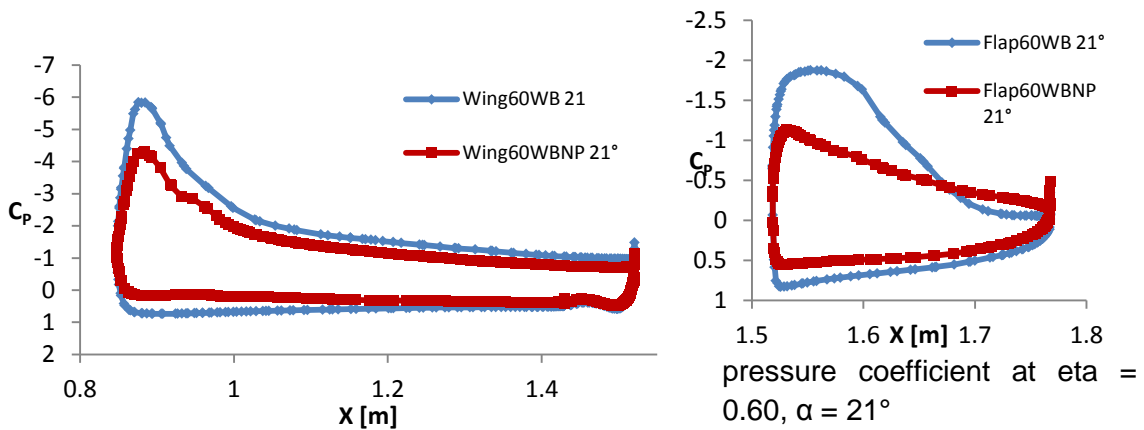


Fig. 7.20 Wing and flap WB and WBNP configurations pressure coefficient at eta = 0.60, $\alpha = 21^\circ$.

As expected it can be seen that generally the engine installation results in a reduction of the pressure coefficient. The plots presented in fig. 7.12 and 7.14 for the section at eta = 0.45, show that the engine installation reduces the pressure coefficient on the front side of upper wing surface, especially at the high angle of attack of 21° . Similar pressure reductions can be observed at the outboard section, eta = 0.6, fig. 7.17 and fig. 7.20. The mid-section, eta = 0.5, fig. 7.15 and fig. 7.16, presents higher pressure drops compared to both outboard and inboard sections, especially at higher angle of attack. This is due to the fact that the wing in this position is exposed directly to the high incidence flow, given that the slat is interrupted to accommodate the pylon.

As much as at high angle of attack all the sections present a similar reduction of the pressure coefficient at the upper flap surface (fig.7.14, fig.7.16 and 7.20), at low angle of attack the pressure coefficient is very similar for both WB and WBNP configuration (fig.7.12, fig.7.15 and fig.7.18).

This can be explained by the fact that the flap is mostly influenced by the flow coming from the wing trailing edge, and for all the sections at this part of the wing, the pressure coefficient seems unvaried at low angle of attack ($\alpha = 6^\circ$, fig.7.12, fig.7.15 and fig.7.18) or similarly reduced at high angle of attack ($\alpha = 21^\circ$, fig.7.14, fig.7.16 and fig.7.20).

Looking at the slat section at $\eta = 0.45$, 6° of incidence (fig.7.11), the WBNP configuration shows a higher pressure coefficient peak at the slat leading edge. This is also showed in fig.7.17 for the slat section at $\eta = 0.6$, 6° of incidence, where the increase is even bigger. These local increases of pressure can be the result of the vortices created by the engine installation that supply additional energy to the near-wall fluid particles. At higher angle of attack the pressure coefficient drops to lowest values, especially for the outboard section (fig.7.13 and fig. 7.19). Again this can be explained due to the reduction of axial velocity or disappearance of the installation vortices, with subsequent flow separation.

As stated in chapter 5, the up-wash flow due to the presence of the nacelle, interacts with the flow generated by the slat cut-out, and the low pressure field near the wing. If the engine is close enough, the vortices coming from the nacelle are captured and forced to attach to the surface of the wing by the low pressure zone at the leading edge. This vortex boundary layer interaction is generally favourable, given that the vortex supplies additional energy to the near-wall fluid particles that have been slowed down by the adverse pressure gradient. This exchange of kinetic energy reduces the thickness of the boundary layer, making it able to withstand bigger adverse pressure gradients (Michael, 1987). This phenomenon mitigates the installations effects decreasing the loss of lift due to the presence of the engine.

On a closer look to the objective of this project, it is necessary to understand the HPSI aerodynamics, driven by the interaction of the installation vortices, in order to be able to perform a CFD campaign similar to the one performed at cruise condition. It is predicted that the position of the engine will significantly affect the HPSI aerodynamics modifying the strength and position of the installation vortices,

It was therefore decided to present a topological description of these vortices and their interaction with the wing flows. No other similar studies were found in the open literature.

7.3 HIGH-LIFT ENGINE INSTALLATION VORTICES

At high incidence the up-wash effect deflects more flow to the upper surfaces strongly modifying the pressure patterns. This high incidence flow is responsible of generating six main vortices that actively interacts with each other: the nacelle vortex, the pylon vortex, two slat vortices and two leading edge-pylon vortices. These vortices play a key role in the HPSI, controlling the flow separation and strongly affecting the maximum lift achievable.

In order to detect and visualize the vortices from the computational dataset, it was decided to plot the iso-vorticity surfaces (Strawn, 1999) and due to its low computational cost, also to plot the velocity swirling normal on the plane perpendicular to the vortex (Garth, 2004, ANSYS, 2012). To evaluate the intensity and sense of rotation, the velocity curl in the stream direction (X) was plotted on the iso-vorticity surfaces (ANSYS, 2012). Additionally in few figures 3D streamlines and velocity vector fields were also presented.

Figures 7.21, 7.22 and 7.23 show the position of the installation vortices with a cut-off level of vorticity of 0.002 (resulting in iso-vorticity surfaces of 756 s^{-1}), at an AOA of 10° and 17° . The cut-off level parameter controls the selected volume around the vortex (ANSYS, 2012). There are not particular guidelines to how select this parameter, for this configuration a value of 0.002 s^{-1} presented reasonable results, allowing the visualization of the different vortices.

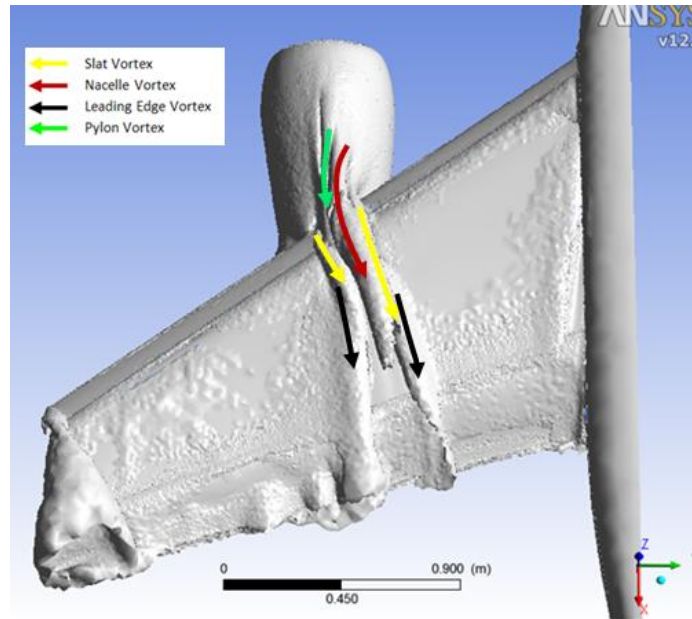


Fig. 7.21 Iso-vorticity surfaces (756 s^{-1}) with underlined high lift installation vortices at an AOA of 17° .

Due to the presence of the nacelle the flow that reaches the slat has a higher angle of attack compared to the WB configuration. The flow that goes over the slat suction side interacts with the nacelle up-wash flow, and in the proximity of the nacelle (black arrow fig. 7.24) the slat flow can be directed in the opposite direction compared to the nacelle flow.

This can result in a local velocity reduction that can lead to a flow separation, subsequently creating the nacelle vortex (fig. 7.25). This is mostly happening on the inboard side of the pylon, due to the proximity of the slat to the nacelle.

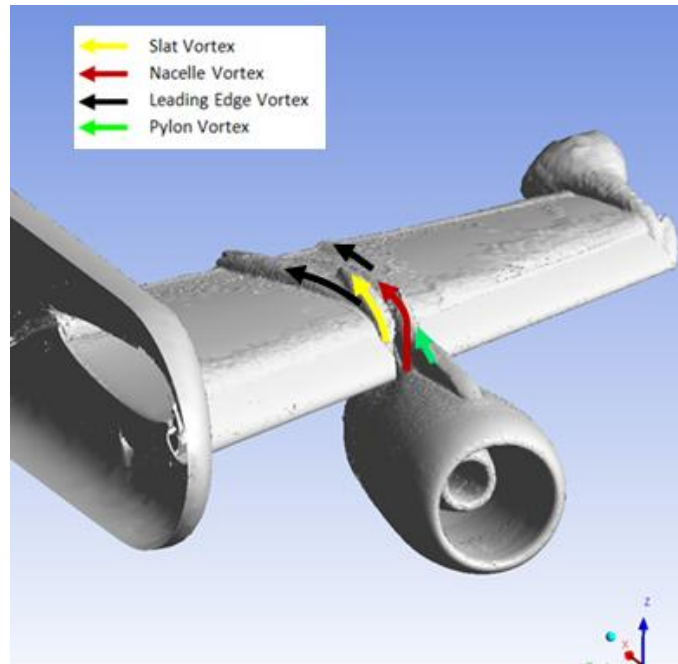


Fig. 7.22 Iso-vorticity surfaces (756 s^{-1}) with underlined high lift installation vortices at an AOA of 10° .

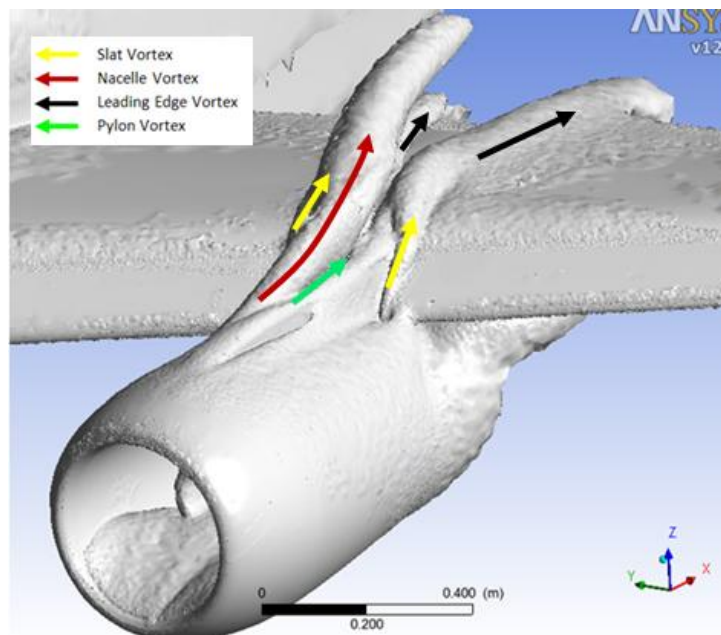


Fig. 7.23 Iso-vorticity surfaces (756 s^{-1}) with underlined high lift installation vortices at an AOA of 17° .

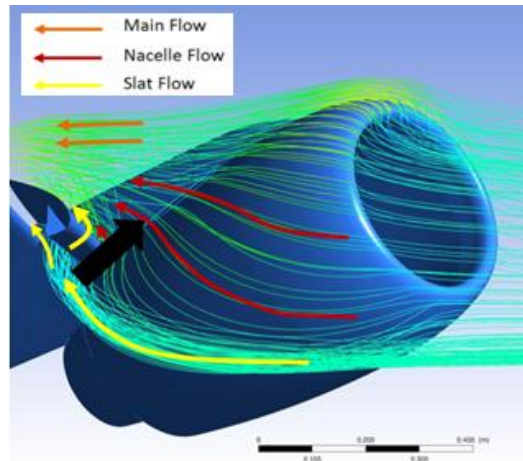


Fig. 7.24 High incidence effects on the nacelle, slat and wing flows. (3D streamlines at an AOA of 21°)

Similarly to the wing tip vortex, the slat gap generates two vortices, due to the pressure difference between the slat suction and pressure sides (fig.7.26).

The presence of the slat vortex, the nacelle vortex and the upstream position of the inboard slat, can create a pressure difference between the two sides of the pylon and subsequent flow displacement from one side to the other. This can lead to a flow recirculation on the upper surface of the pylon and a possible vortex generation. It is important to notice that the strength of the vortex can be reduced with an appropriate design of the pylon section.

The velocity swirling normal and the velocity vector field at a plane normal to the pylon are shown in figure 7.27, where is possible to notice a recirculation on the upper surface of the pylon and also an high velocity swirl zone, indicating the presence of a vortex.

Due to physical installation of the pylon a section of the slat is missing, hence the adjacent part of the wing profile will be now exposed to higher incidence flow and therefore subject to earlier flow separation. This flow separation can lead to the creation of vortices on the junction of the pylon and wing. One of the two leading edge vortices that characterize the WBNP configuration, used for project, is shown in fig. 7.28, plotting 3D streamlines and the swirling velocity normal. Again this can be mitigated re-profiling the wing leading edge and the pylon at their junction.

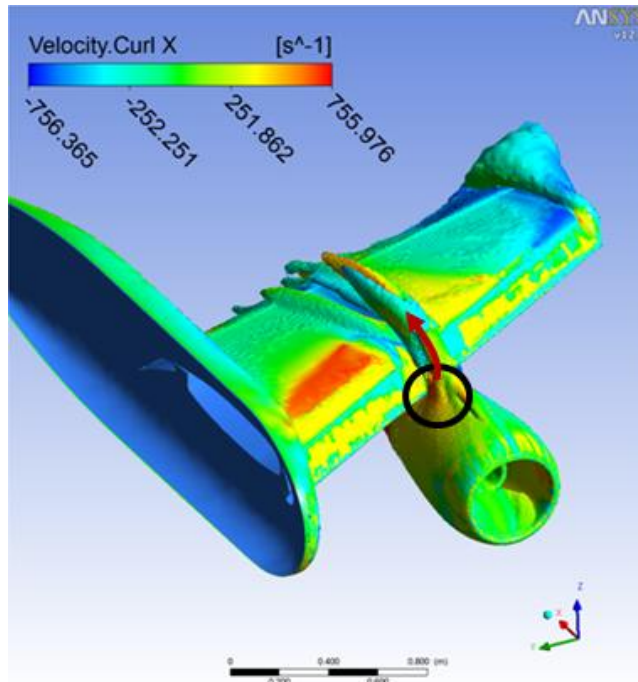


Fig. 7.25 Iso-vorticity surfaces (756 s^{-1}), velocity curl X contours and underlined nacelle vortex at an AOA of 10° .

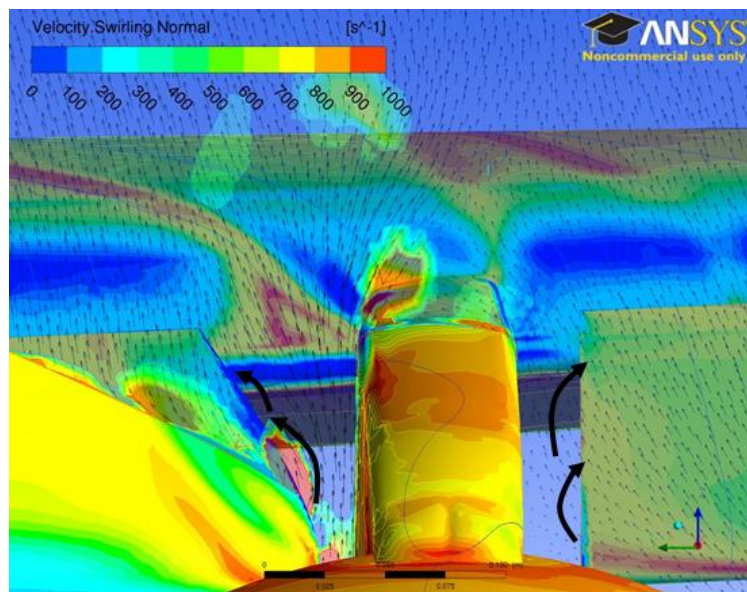


Fig. 7.26 Velocity swirling normal, velocity vortex field and underlined slat gap vortices at an AOA of 10° .

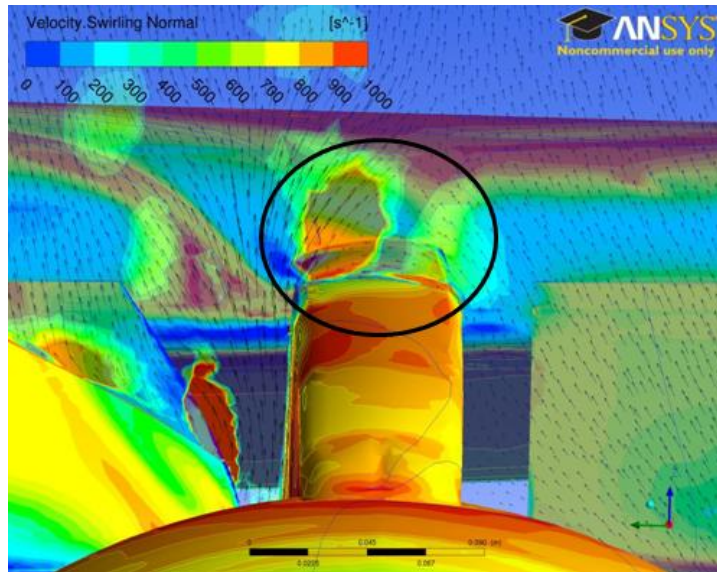


Fig. 7.27 Velocity swirling normal, velocity vortex field and underlined pylon vortex at an AOA of 17° .

It should be underlined that the amplitude and position of all the vortices is strictly related to the components configuration and installation. The nacelle/pylon/slat and wing geometries are normally optimized in order to reduce the installation penalties.

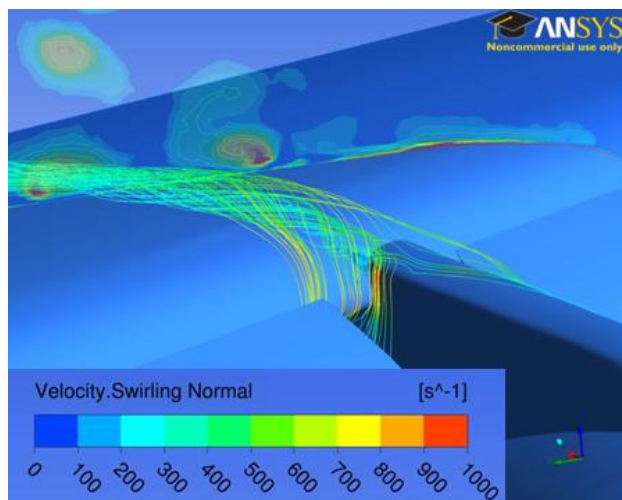


Fig. 7.28 Velocity swirling normal, 3D streamlines and underlined leading edge vortex at an AOA of 17° .

As previously stated the vortex boundary layer interaction is generally favourable, given that the high axial velocity of vortex reduces the thickness of the boundary layer, making it able to withstand bigger adverse pressure gradients.

However in a high angle of attack configuration the velocity of the vortices could not be enough to withstand the increased pressure field, given that when a vortex passes into an increasing pressure field, the axial velocity of its core is reduced. If this velocity falls beyond a critical point, the vortex will disappear, also called vortex bursting (Leibovich, 1984), and without the momentum addition of the vortex, the boundary layer will separate. Figure 7.29 shows the growth of vortices size increasing the angle of attack until the main vortex bursts and the wing is affected by a strong flow separation.

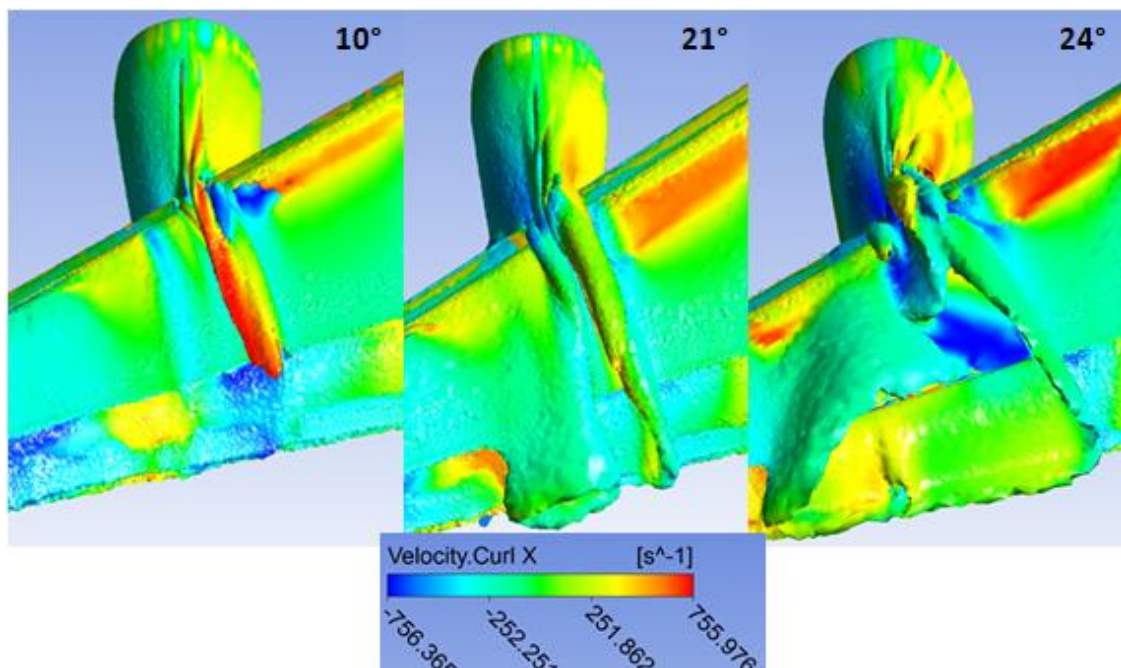


Fig. 7.29 Vortices size and intensity at different AOA (756 s^{-1} iso-vorticity surfaces and velocity curl X contours).

It is noticeable how the vortices strength, in this case represented by the velocity curl normal to the x direction, reduces with the increase of AOA, until the vortices disappear from the wing surface.

The wall shear stresses and the surface stream lines at an angle of attack of 10°, 21° and 24° are respectively presented in fig. 7.30, fig. 7.31 and fig. 7.32. It is possible to notice that the flow separates in correspondence of the engine span position (fig. 7.32, low shear stress area).

As mentioned before, the inboard side of the wing is normally more affected due to the forward position of the slat on the inboard side of nacelle compared to the outboard. The inboard vortices are more exposed to the increased pressure field, therefore more prone to burst and cause separation.

However for a close-coupled engine, the interference can be as severe as to affect the outboard of the wing, causing a more dramatic flow separation. It can be seen in the presented configuration that the flow is separating in both outboard and inboard sides (fig.7.32).

Figures 7.33 and 7.34 show similar vortices captured during two recent research projects. The two configurations present analogous flow characteristics and the vortices can be seen from the 3D visualizations, even if the studies available in open literature do not describe them in details.

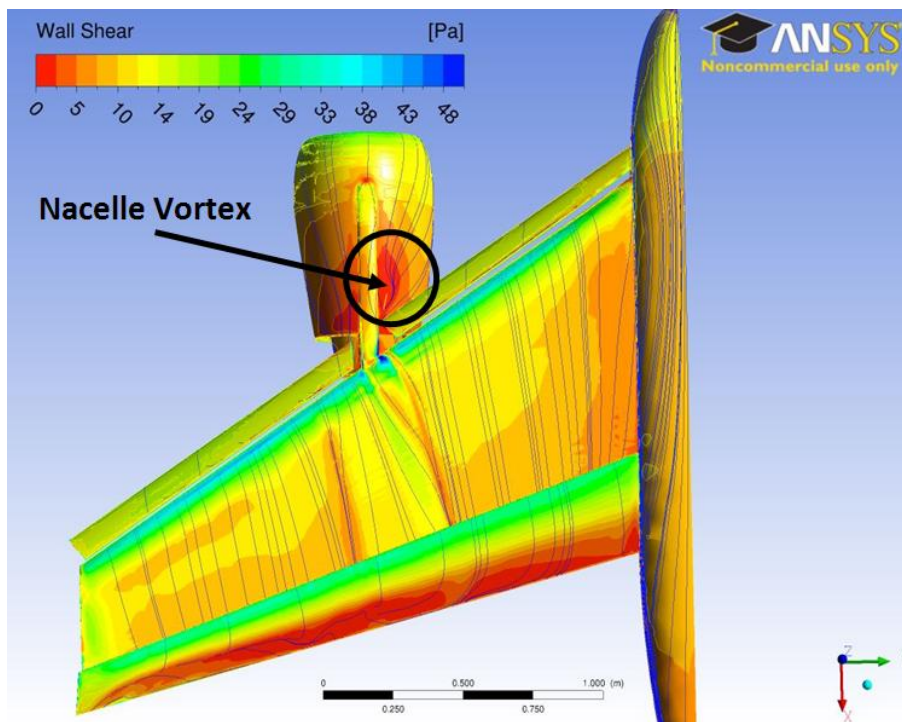


Fig. 7.30 WBNP wall shear and surface stream lines, $\alpha = 10^\circ$.

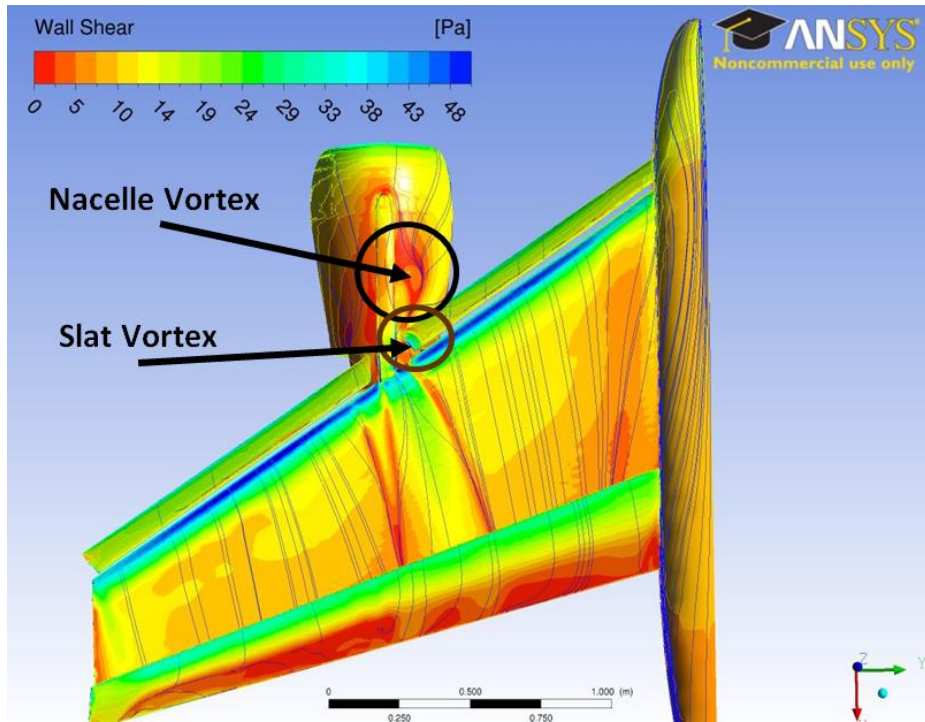


Fig. 7.31 WBNP wall shear and surface stream lines, $\alpha = 21^\circ$.

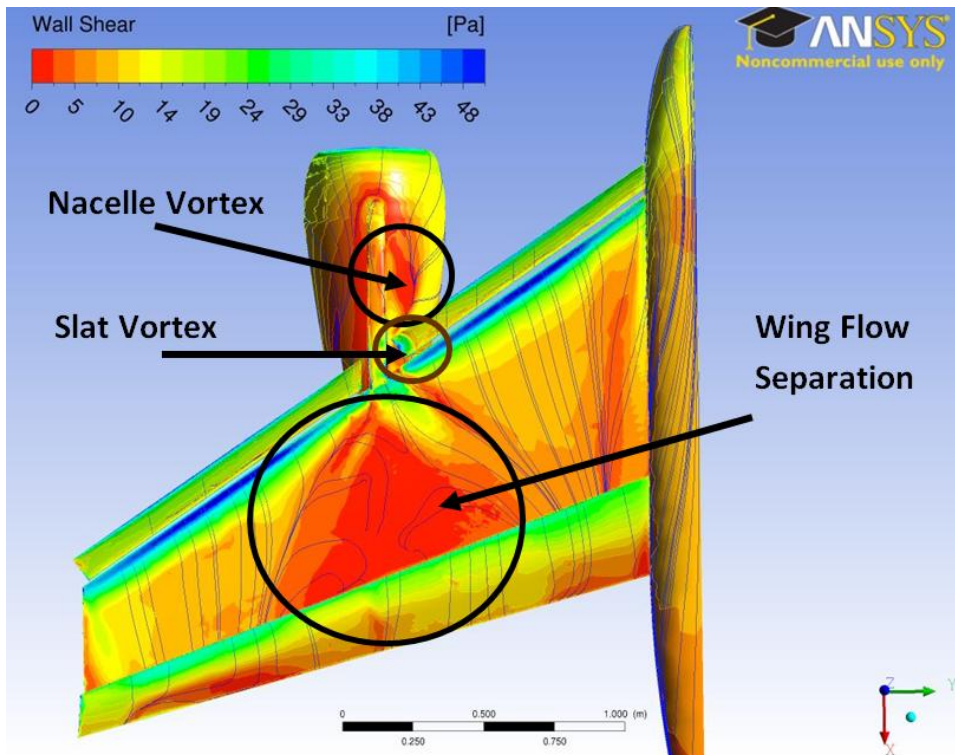


Fig. 7.32 WBNP wall shear and surface stream lines, $\alpha = 24^\circ$.

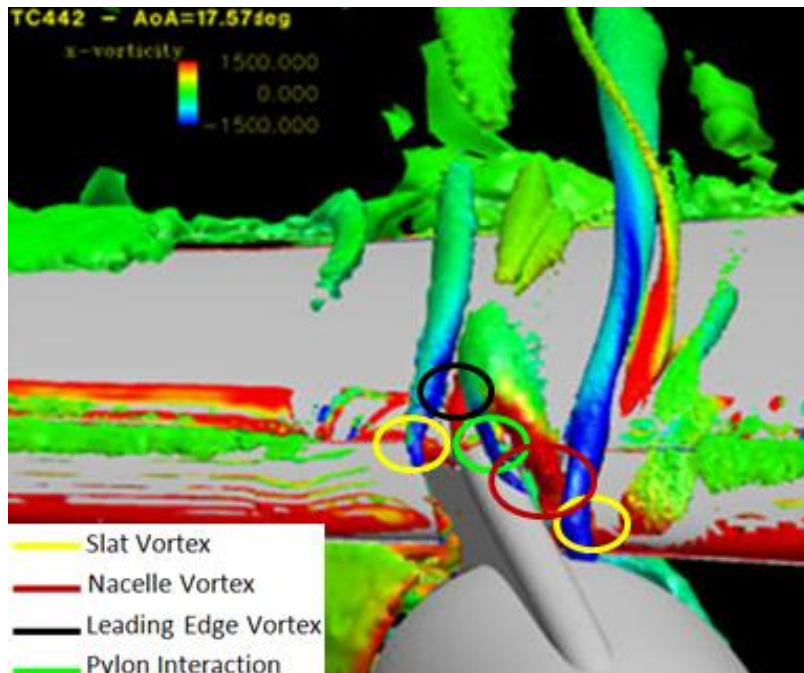


Fig. 7.33 Installation vortices (Von Geyr, 2007).



Fig. 7.34 Evaluation of vortex generation. (Rohlmann, 2012).

As previously stated in chapter 5 even if the installation vortices are generally favourable, they are originated in a zone of low kinetic energy, the wing/pylon junction. This gives to them an intrinsically low axial velocity compared to a vortex generated on the relatively clean flow, far from the nacelle/pylon connexion (Richard, 1973).

To overcome this problem, the aircraft manufacturer McDonnell Douglas, introduced the idea of mounting a pair of strakes on the nacelle to generate two vortices in order to control the wing flow separation. The nacelle strake, or chine, if correctly positioned, generates a vortex in a location where the boundary layer is relatively thin and the local velocity is higher compared to the low energy field of the pylon/wing junction. This is significantly affecting the position and strength of the installation vortices, increasing the maximum achievable lift. Therefore in order to correctly simulate the integration of the engine at high incidence it was decided to simulate its effects.

7.4 NACELLE CHINE

7.4.1 GEOMETRY DEFINITION AND INSTALLATION

The work presented by Quix (2007) shows that the installation of a strake on the inboard side of the nacelle leads to a 60-70% recovery of lost lift. The impact of the nacelle strake is so severe that in order to correctly evaluate the HPSI effects its influence can't be not taken in to account.

The installation of the nacelle chine represents the last step in the increase of the model complexity, starting with a wing and body configuration, then adding the propulsive system and finally including the nacelle vortex generator, to realistically evaluate the effects of the presence of the engine of the whole aircraft performance.

The chine geometry was defined following the patent US 2010/0176249 (Schwetzler, 2010) and other research projects (Von Geyr, 2007).

The chine is represented in figure 7.35 where the chine profile is defined by the eq.7.1 (Schwetzler, 2010):

$$y = HG \left[1 - \frac{(LG - x)^2}{LG^2} \right] \quad (7.1)$$

X is the longitudinal coordinate of the vortex generator with an overall length LG.

The length of the chine was defined keeping in mind that the typical ratio of length of the vortex generator/length of the nacelle is 10% to 15%. Y is the heights coordinate of the vortex generator with a maximum height HG . The selected values for these two parameters were: $LG = 0.152$ and $HG = 0.066\text{m}$.

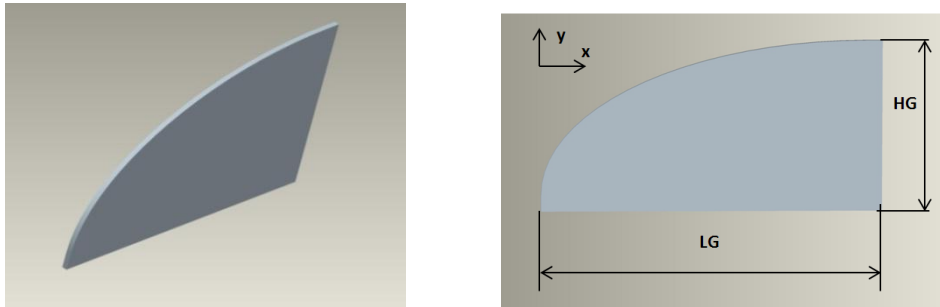


Fig. 7.35 Nacelle chine profile.

The nacelle chine was positioned following the results presented by Kanazaki (2008). The experimental design exploration suggested that the maximum lift increase, for this particular configuration, was achieved with the nacelle chine positioned in the vicinity of the pylon-nacelle junction (fig.7.36). In the absence of a predefined chine position, it was decided to adopt a similar positioning. In order to maximize the lift for this particular configuration, further CFD simulations are necessary; however this was not the main objective of this research project.

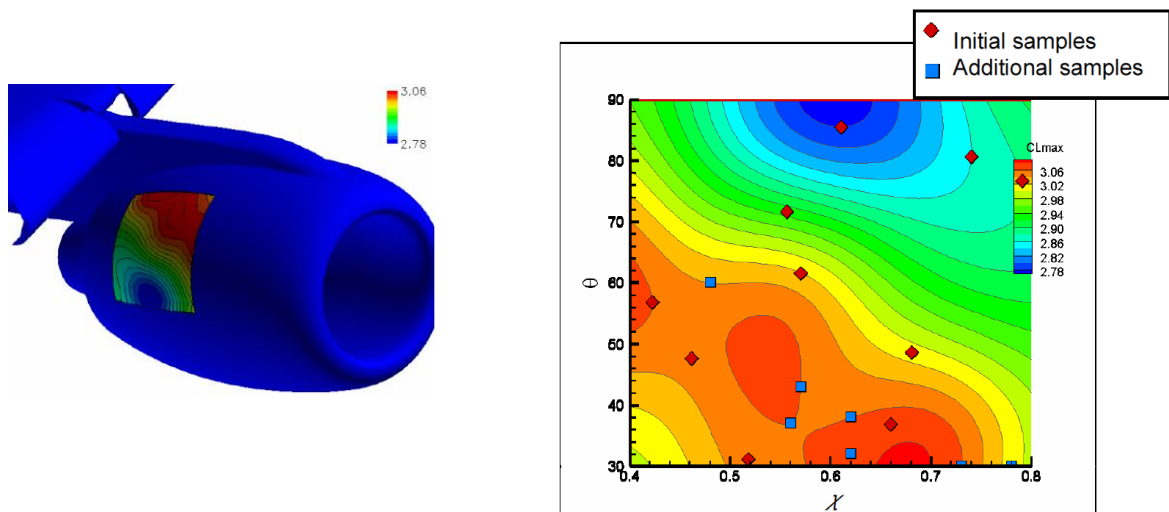


Fig. 7.36 Maximum lift chine positioning. θ and χ are the positioning parameters. (Kanazaki, 2008)

Another positioning parameter is the tilt angle relative to the longitudinal axis of the nacelle, $\Delta\theta$ (fig.7.37). As indicated by Schwetzler (2010), for standard applications, $\Delta\theta$ range between 0° and 10° . It was decided apply a $\Delta\theta$ of 5° . The installation of the nacelle chine is represented in fig. 7.38.

As stated before the interference between nacelle, pylon and slat can be so severe as to affect the outboard of the wing, causing a more dramatic flow separation. It can be seen that for the presented configuration, the flow is separating in both outboard and inboard sides (fig.7.32). Installing a second nacelle chine could control the flow separation on the outboard side considerably increasing the maximum lift.

Therefore in absence of a study similar the one presented by Kanazaki (2008) for the outboard, it was decided to evaluate two additional configurations: one with a second symmetric chine on the left side of the nacelle (WBNP2CS) and one with the chine positioned on the nacelle outboard and near the nacelle lip (WBNP2C2) (fig. 7.39). The profile of the chine and the longitudinal angle were kept the same for all the configurations.

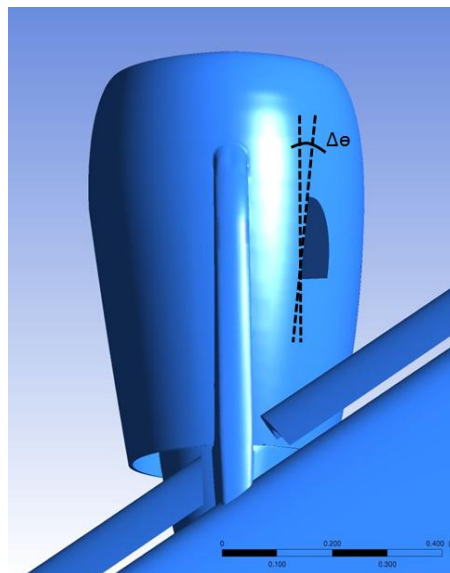


Fig. 7.37 Chine longitudinal angle.

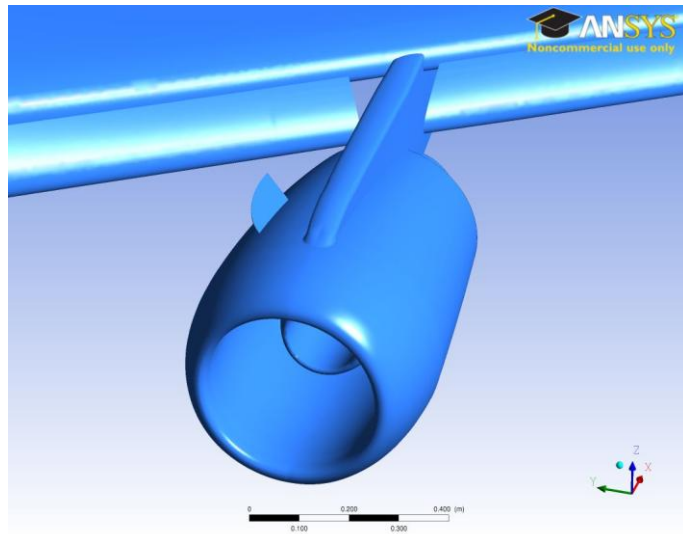


Fig. 7.38 Single nacelle chine installation.

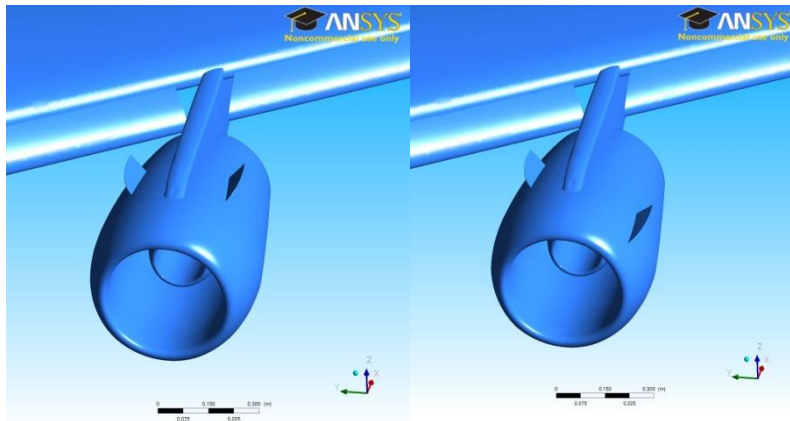


Fig. 7.39 Double chine installations. (Left WBNP2CS, Right WBNP2C2)

7.4.2 RESULTS

The numerical method and the assigned boundary conditions were the same as for the previous configurations: $Re = 4.3 \times 10^6$, $M = 0.2$ and $T = 288.88$ K. The mesh technique was also the same as applied to the WB and WBNP, starting from the WB coarse mesh, with the only difference being that the volume mesh was further refined in correspondence of the pylon-wing junction wingspan position and on the nacelle chine wake (fig. 7.40).

Once again the lift and drag polar were calculated running simulations varying the angle of attack, in particular the simulations were run at $\alpha = 10^\circ, 17^\circ, 19^\circ, 20^\circ, 21^\circ, 22^\circ, 23^\circ$ and 24° .

As for the WBNP, a relatively small incidence increment between the calculations was used, due to the hysteresis effect, and to capture the real flow separation the step was maintained as small as possible.

The comparison between the lift polar of the WB, WBNP, WBNPC, WBNP2CS and WBNP2C2 is presented in fig. 7.41. It can be seen that the chine increases the maximum lift and shifts the value at a higher AOA.

The single chine configuration separates at 23° compared to 22° for the WBNP configuration. However the maximum lift is nearly the same, $C_{LMAX} = 2.23$ for the WBNP and $C_{LMAX} = 2.26$ for the WBNPC.

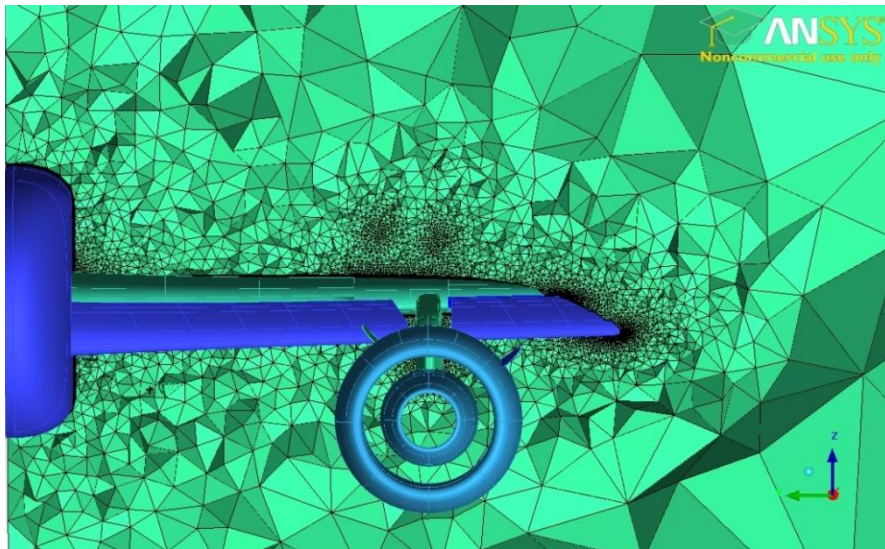


Fig. 7.40 Mesh refinement on the chine wake.

The second chine considerably increase the maximum lift, $C_{LMAX} = 2.3$, keeping 23° as the separated flow angle of attack. A further increase was reached with the chine installed on the nacelle lip. The C_{LMAX} was 2.34 and the flow separation appeared at 24° instead of 23° . The vortex generated from the chine positioned forward and far from the pylon (fig. 7.42), compared to the other two configurations (fig. 7.43 and 7.44) appeared to follow a path that goes over the main outboard separated flow wing region (figure 7.32), making the boundary layer able to withstand bigger adverse pressure gradients.

In addition it generates a vortex in a location of high kinetic energy. Therefore the vortex presents a high-axial velocity and when over the slat and the wing it will increase the kinetic energy of the near-wall fluid particles making their boundary layers able to withstand bigger adverse pressure gradients, and therefore increasing the maximum lift.

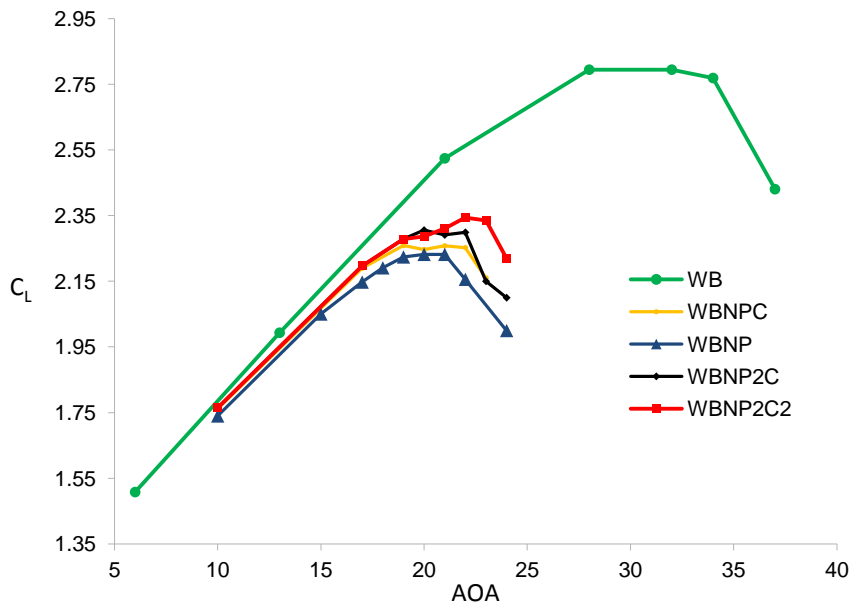


Fig. 7.41 Lift polar for the clean wing (WB), the engine installed (WBNP), the engine installed with one chine (WBNPC) and the two engine installed with two chines (WBNP2CS and WBNP2C2).

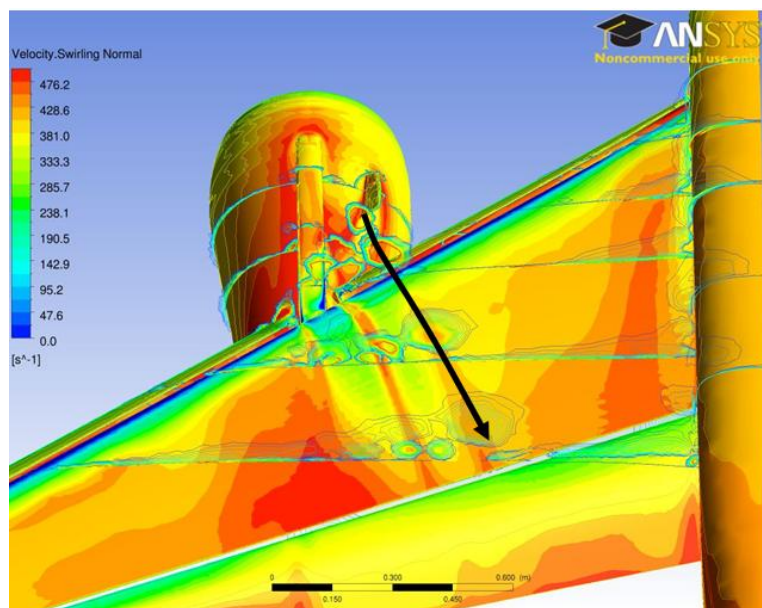


Fig. 7.42 Single chine configuration (WBNPC) vortex path (velocity swirl normal and shear stress at 21°).

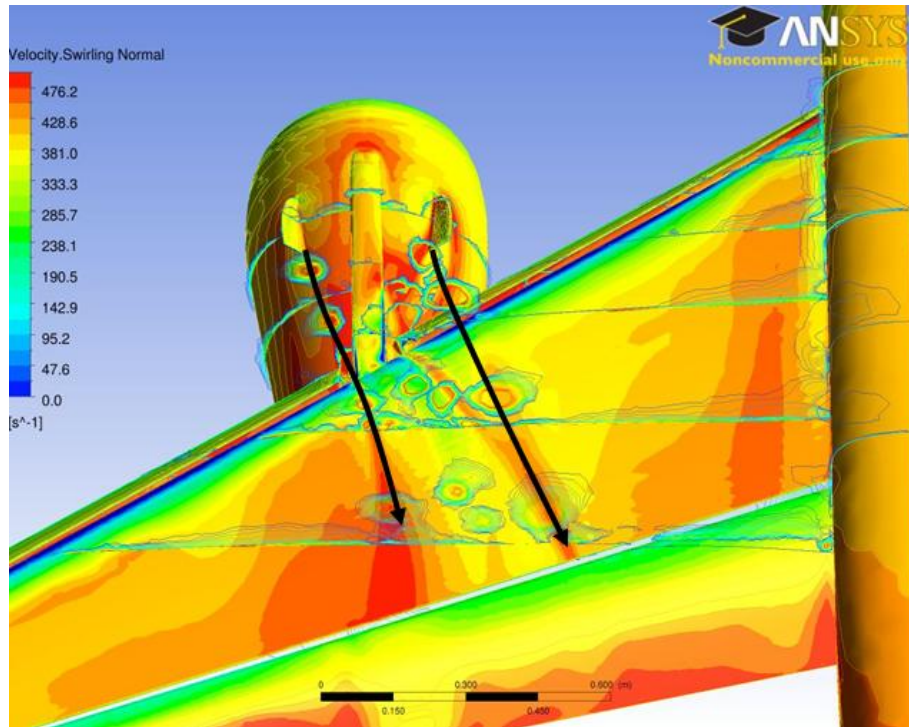


Fig. 7.43 Two-chines configuration (WBNP2CS) chines vortices paths (velocity swirl normal and shear stress at 22°)

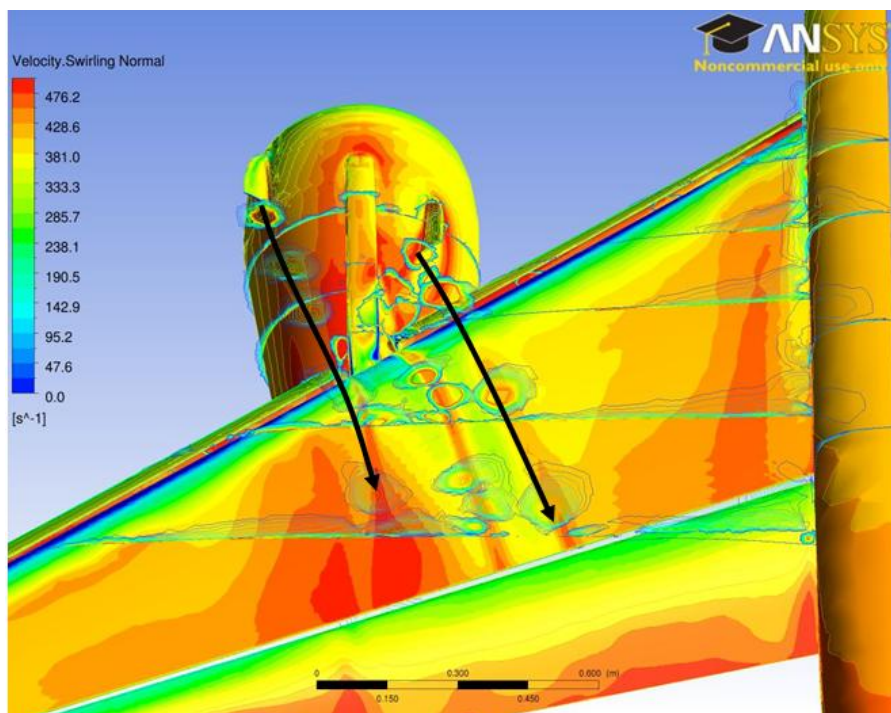


Fig. 7.44 Two-chines configuration (WBNP2C2) chines vortices paths (velocity swirl normal and shear stress at 22°).

Figure 7.45 shows the position of the installation vortices for the single and the double chine configurations. It is clear that the installation vortices are strongly affected by the presence of the chines. The addition of the second chine results in the extension of the pylon vortex to almost the entire wing and the inboard shift of the nacelle vortex. Due to the presence of the outboard chine vortex the slat vortex is characterized by a different path respect to the single chine installation.

Therefore it can be concluded that the chine vortex is not only affecting the boundary layer but also interacting with the installation vortices. Future work should be planned to better understand this vortices interaction.

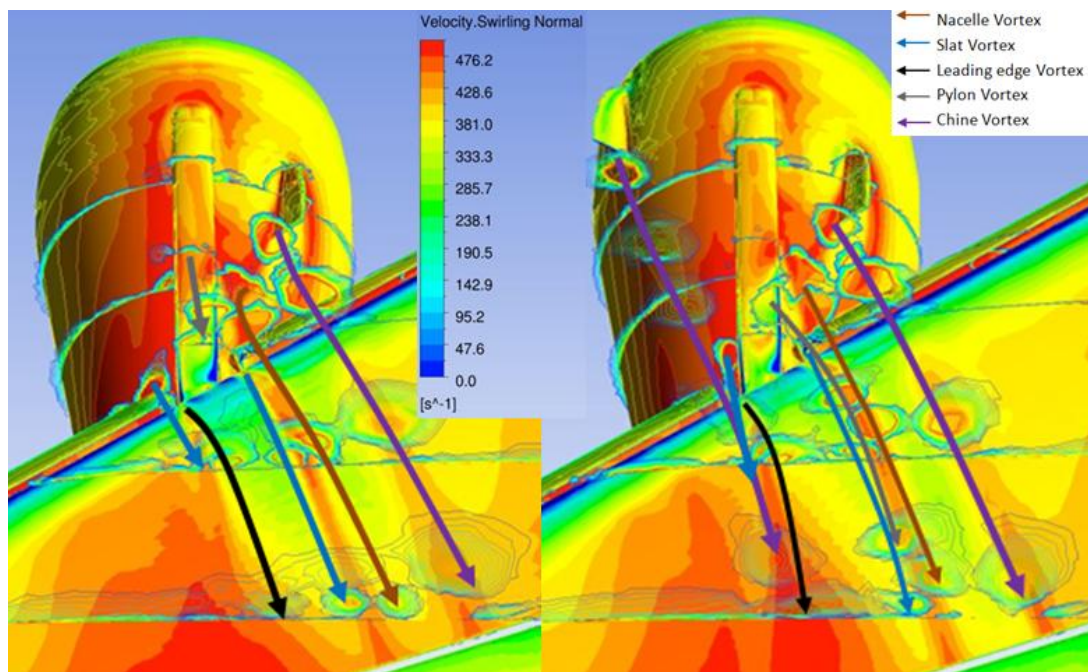


Fig. 7.45 Two-chines configurations (WBNP2CS and WBNP2C2) installation vortices (velocity swirl normal and shear stress).

The next figure (fig.7.46) shows the comparison of the shear stress contours and the surface streamlines for all the configurations at the critical angles of attack of 21°, 22° and 23°. It can clearly be seen that the flow separation is postponed at higher angle of attack using the nacelle chine, and in particular with the additional chine positioned on the nacelle lip.

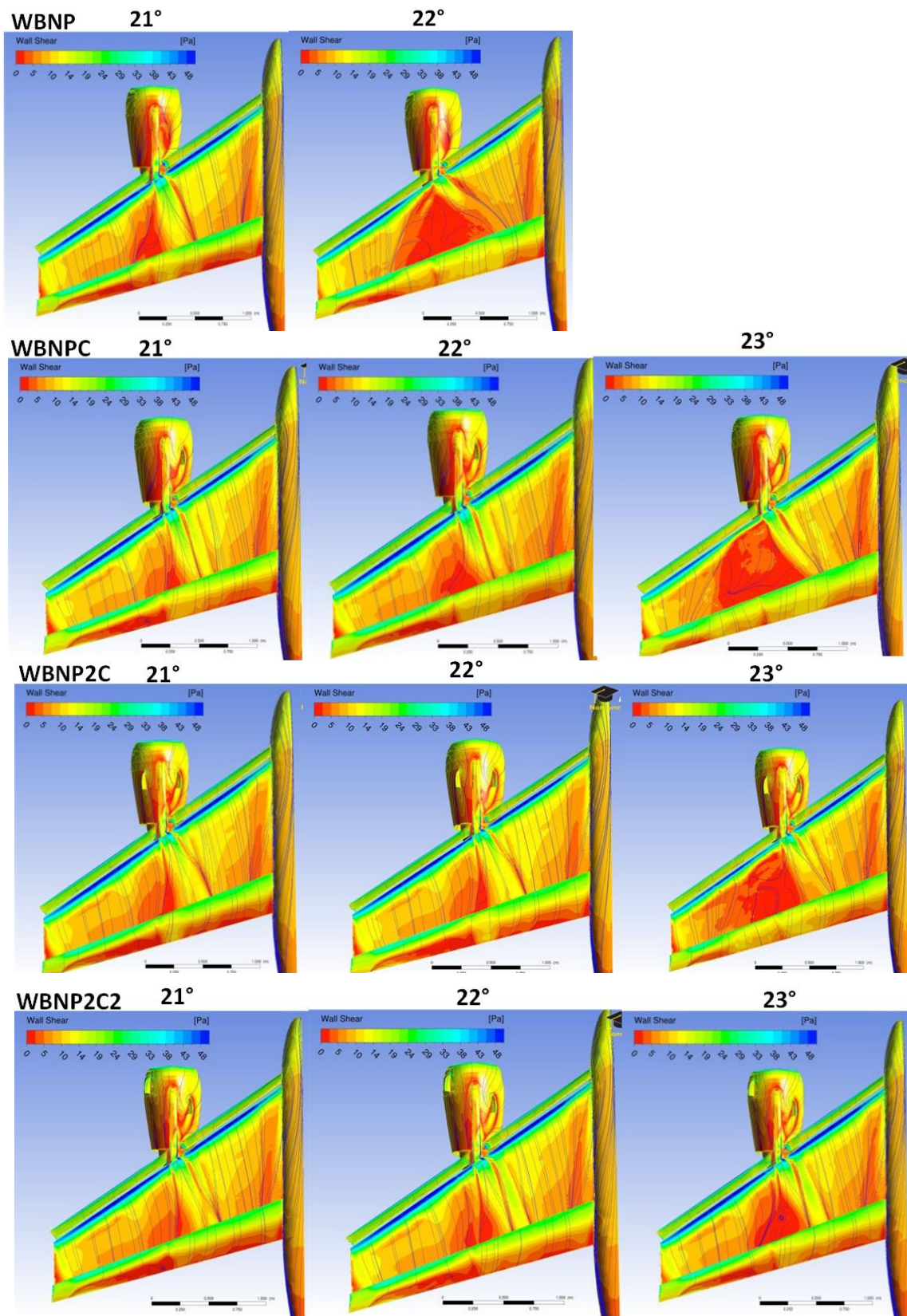


Fig. 7.46 Shear stress contours at 21°, 22° and 23° (streamlines/shear stress).

The last two figures, fig. 7.47 for the section at $\eta = 0.45$ and fig. 7.48 for the section at $\eta = 0.6$, present the pressure coefficient comparison between the WBNP and WBNP2C2 configuration at an AOA of 22° . Both plots show the considerable increase of pressure on the upper surface due to the presence of the nacelle vortices.

Furthermore the outboard section presents an even bigger difference in pressure coefficient on the upper surface of the wing. This can be explained by the fact that for the close coupled engine-airframe configuration used in this project, the flow starts to separate on the outboard side of the pylon (fig.7.46).

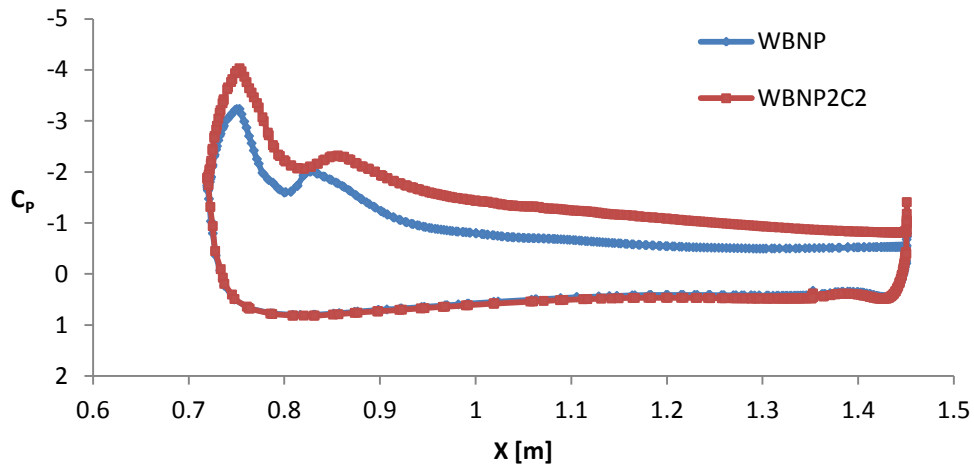


Fig. 7.47 WBNP and WBNP2C2 wing pressure coefficient at $\eta = 0.45$, $\alpha = 22^\circ$

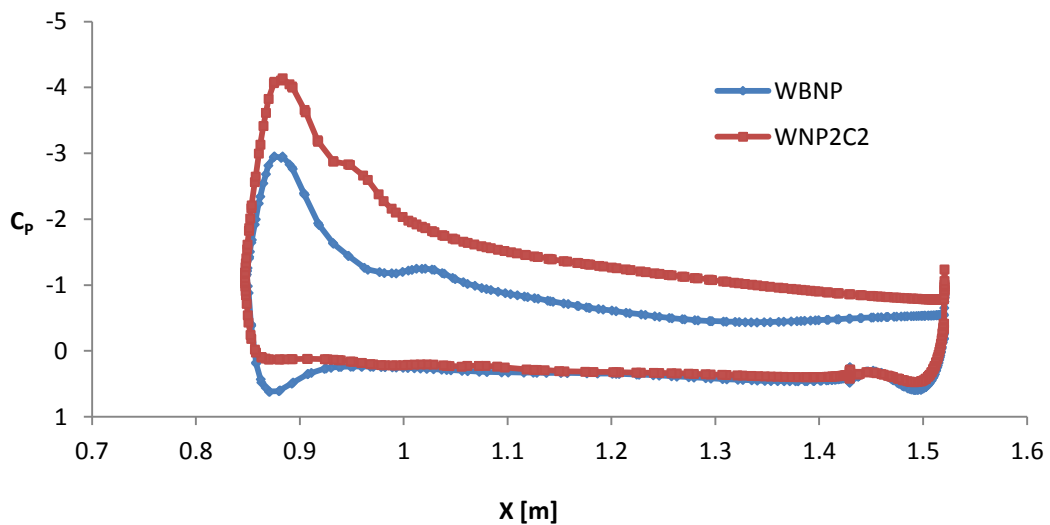


Fig. 7.48 WBNP and WBNP2C2 wing pressure coefficient at $\eta = 0.6$, $\alpha = 22^\circ$

7.5 CONCLUSIONS & FUTURE WORK

In an industrial process high lift performance is determined prior to the performance flight testing, by a complementary use of different wind tunnel facilities and numerical simulations. Numerical methods have reached a considerable degree of maturity in the demanding task of predicting high lift increments based on national and international research efforts. Very recent projects (Rudnik, 2012) demonstrate that the use of CFD can lead to an accurate prediction of the engine-airframe high-lift aerodynamic.

The main objective of modelling the high-lift PSI has been reached. The aerodynamic effects of integration of a large engine for an under the wing installation at high angle of attack have been evaluated. Even if no experimental data were available for the engine-airframe configuration, the model seems to correctly predict the main flow features, given that the results are similar to previous research projects (Rudnik, 2012, Von Geyr, 2007).

On another side a more detailed flow characterization for a HPSI with and without nacelle strakes was still not available in the open literature. A topological description of the installation vortices was yet to be presented in open literature.

Moreover, on a closer look to this project, it is necessary to understand the HPSI aerodynamics, driven by the interaction of the installation vortices, in order to be able to perform a CFD campaign similar to the one performed at cruise condition. It is predicted that the position of the engine will significantly affect the HPSI aerodynamics. A topological description of the installation vortices is necessary to understand the effects of the engine positioning influence.

The results and descriptions presented in this chapter can be considered the first open literature topological study of the high-lift installation vortices.

Additionally the nacelle chine installation was also evaluated due to its high impact on the HPSI aerodynamics. The results also showed its influence on the installation vortices.

The installation of the nacelle chine represents the last step in the increase of the model complexity, starting with a wing and body configuration, then adding the propulsive system and finally including the nacelle vortex generator, to realistically evaluate the effects of the presence of the engine of the whole aircraft performance. Future research will be based on this model to perform an aerodynamic optimization of the nacelle chine position, considerably reducing the time spent in the wind tunnel. The drag and other aerodynamic effects will also be taken in to account.

The presented results will be used as a starting point for a numerical campaign similar to the one performed for the cruise condition, in order to allow the PSI model to take into account the HPSI effects.

However further work is still necessary to rigorously evaluate all the flow features that characterize the high-lift engine airframe integration. The description of the generation and interaction of the vortices coming from the different components, even if can be regarded as the first in the open literature, can be improved with accurate measurements from the presented configuration and additional engine-airframe configurations. The intensity of the vortices and the interaction with the boundary layer (BL) should be evaluated following rigorous methodologies. In particular the axial velocity of the vortex should be measured along the entire extent of the vortex to determine the interaction with the BL. This should also be done given that it is well know that CFD is prone to vortex numerical diffusion, considerably reducing the vortex strength (Gad-el-Hak, M, 1991).

As stated, the interaction with the vortices coming from the nacelle and the boundary layer has a fundamental effect on the wing/slat/flap flow separation. Therefore the CFD methodology (mesh, turbulence model etc.) should be evaluated to verify if BL evolution, due to the interaction with vortices, wakes and the blend of the BLs of slat, wing and flap, is correctly captured.

Experimental velocities profiles for the WB configuration are now available (AIAA, 2012) (not available during the numerical campaign), and therefore they can be compared with numerical results. As pointed out by Eliasson (2011), correctly solving the boundary layer is fundamental to capture the high lift aerodynamics.

Accordingly a mesh refinement study that increases the level of accuracy along the vortices path should be performed. This will involve the creation of control volumes with refined mesh in correspondence of the vortices path, adjusted iteratively with feedbacks from the relative CFD results. An alternative could be using the mesh refinement tools inbuilt in the code (ANSYS, 2012).

Due to the intrinsic unstable behaviour of separated or incipient separated flows, non-steady state calculations should be performed. This will give a better picture of the high-lift flow, and will allow evaluating the inherent steady state simplifications.

8 MAIN CONCLUSIONS & FUTURE WORK

During this research project, studies of the installation penalties of novel Ultra High Bypass Ratio (UHBR) engines have been carried out, resulting in the development of a new coupled aircraft/engine performance modelling tool which is able to take in to account the variation of Net Propulsive Force (NPF) as a function of engine position and attitude.

The project was divided in two parts due to the peculiar characteristics of Propulsive System Integration (PSI) at different sections of the flight envelope. The first part relative to the cruise condition and the second focused on the PSI at high-lift conditions, characteristic of approach, take-off and landing.

In the first part of the project Computational Fluid Dynamic (CFD) has been used to determine the aerodynamic effects due to the engine installation. Correlations were extracted from the resulting numerical data defining the Net Propulsive Force as a function of horizontal and vertical engine position. The selected engines were two novel configurations presented in the NEWAC project. The results showed similarities with previous studies (Oliveira, 2003; Rossow, 1992), giving to the horizontal engine position (X) more influence on the NPF variance than the vertical (Y) engine position. Using these correlations the new tool was able to determine the variation of consumed fuel during the cruise as a function of the engine position, indicating increases of up to 6.4% when placing the engine near the wing.

According to the extensive literature review performed, this study can be regarded as the first open literature engine position-NPF parametric study using CFD.

In the second part of the project the effects of integrating a large engine for an under the wing installation at high angle of attack were modelled using CFD. No experimental data were available for the engine-airframe configuration, but the model seems to correctly predict the main flow features, given that the

results are similar to previous research findings (Rudnik, 2012, Von Geyr, 2007).

However a detailed flow characterization for a HPSI with and without nacelle chine was still not available in the open literature. A topological description of the installation vortices was yet to be presented. Moreover, on a closer look to this project, it was necessary to understand the HPSI aerodynamics, driven by the interaction of the installation vortices, in order to be able to perform a CFD campaign similar to the one performed at cruise condition. It is predicted that the position of the engine will significantly affect the HPSI aerodynamics. Therefore it was decided to perform a topological study of the high-lift installation vortices, and it can be considered the first in the open literature.

However due to the timeframe of this project and the considerable time spent on this task, it was not possible to perform a CFD campaign similar to one for the cruise condition in order to feed the PSI module. This remains a priority for future work.

Regarding the future work it can be noticed that the studies at cruise condition, were carried out looking only at vertical and horizontal position; other position variables, like engine orientation angles, could be used as parameters. The current study has also assumed fixed wing geometry and has not allowed for any reprofiling of the wing to minimise interference effects for particular powerplant locations. It is probable that the reported installation penalties could, in practice, be reduced by detailed wing design iterations. Future work should be addressed, performing sensitivity studies. Another important factor is that due to the lack of available data to generate detailed nacelle and pylon geometry, these are still not totally representative of a “standard” configuration. Further CFD calculations could refine the geometries and improve the quality of the results.

Regarding the HPSI study, further work is still necessary to rigorously evaluate all the flow features that characterize the high-lift engine airframe integration. The description of the generation and interaction of the vortices coming from the different components, even if can be regarded as the first in the open literature, can be improved with accurate measurements from the presented configuration and additional engine-airframe configurations. The intensity of the vortices and the interaction with the boundary layer (BL) should be evaluated following rigorous methodologies. In particular the axial velocity of the vortex should be measured along the entire extent of the vortex to determine the interaction with the BL. This should also be done given that it is well known that CFD is prone to vortex numerical diffusion, considerably reducing the vortex strength (Gad-el-Hak, M, 1991).

As stated, the interaction with the vortices coming from the nacelle and the boundary layer has a fundamental effect on the wing/slat/flap flow separation. Therefore the CFD methodology (mesh, turbulence model etc.) should be evaluated to verify if BL evolution, due to the interaction with vortices, wakes and the blend of the BLs of slat, wing and flap, is correctly captured. Experimental velocities profiles for the WB configuration are now available (AIAA, 2012) (not available during the numerical campaign), and therefore they can be compared with numerical results. As pointed out by Eliasson (2011), correctly solving the boundary layer is fundamental to capture the high lift aerodynamics.

Accordingly a mesh refinement study that increases the level of accuracy along the vortices path should be performed. This will involve the creation of control volumes with refined mesh in correspondence of the vortices path, adjusted iteratively with feedbacks from the relative CFD results. An alternative could be using the mesh refinement tools inbuilt in the code (ANSYS, 2012).

Due to the intrinsic unstable behaviour of separated or incipient separated flows, non-steady state calculations should be performed. This will give a better picture of the high-lift flow, and will allow evaluating the inherent steady state simplifications.

Due to the already complex flow at high angle of attack, the evaluation of PSI effects requires state-of-art CFD simulations. Major research projects (NASA, 2012, Rudnik, 2012) are currently underway to increase the capabilities of numerical codes to correctly simulate such high-lift aerodynamics. The correct simulation of the high-lift PSI still represents a challenge for the actual numerical methods/resources.

REFERENCES

(A)

AIAA (2012), *Drag Prediction Workshop*, available at:
<http://aaac.larc.nasa.gov/tsab/cfdlarc/aiaa-dpw/>.

Andreoletti, M. (2007), *Summary of NEWAC engine geometry specifications*, D1.1.1B, NEWAC.

ANSYS (2012), *ANSYS CFD Manual*, available at: www1.ansys.com.

Atkins, H. L. (1991), "A multi-block multigrid method for the solution of the Euler and Navier-Stokes equations for three-dimensional flows", *Aerospace Sciences Meeting, 29th*, AIAA-1991-101, Jan 7-10, 1991, Reno, NV, USA, AIAA.

(B)

Berry, D. L. (1994), "The Boeing 777 engine/aircraft integration aerodynamic design process", *ICAS, Congress, 19th, Anaheim, CA, Proceedings*. Vol. 2; UNITED STATES; 18-23 Sept. 1994; ICAS, pp. 1305.

Biber, K. and Zumwalt, G. W. (1993), "Hysteresis Effects on Wind Tunnel Measurements of a Two-Element Airfoil", *AIAA Journal*, vol. 2, no. 1993, pp. 326.

Bretschneider, S., Arago, O. and Staudacher, S. (2007), "Architecture of a Techno and Environmental Risk Assessment Tool Using a Multi-Modular Build Approach", *ISABE 2007*, ISABE-2007-1103, 2007, ISABE.

Brodersen, O. and Rossow, C. (1993), "Calculation of interference phenomena for a transport aircraft configuration considering viscous effects", *Recent developments and applications in aeronautical CFD; Proceedings of the 1993 European Forum*, 1993, London, UK, Royal Aeronautical Society, pp. 61.

Brodersen, O. (2002), "Drag prediction of engine-airframe interference effects using unstructured Navier-Stokes calculations", *Journal of Aircraft*, vol. 39, no. 6, pp. 927-935.

Brodersen, O., Eisfeld, B., Raddatz, J. and Frohnafel, P. (2008), "DLR results from the Third AIAA Computational Fluid Dynamics Drag Prediction Workshop", *Journal of Aircraft*, vol. 45, no. 3, pp. 823-836.

Brodersen, O., Rakowitz, M., Amant, S., Larrieu, P., Destarac, D. and Sutcliffe, M. (2005), "Airbus, ONERA, and DLR results from the second AIAA drag prediction workshop", *Journal of Aircraft*, vol. 42, no. 4, pp. 932-940.

Burgsmueller, W., Hoheisel, H. and Kooi, J. W. (1994), "Engine/airframe interference on transport aircraft with ducted propfans - The European research program DUPRIN", *19th ICAS Congress*, ICAS-94-3.7.1, 18-23 Sept. 1994, Anaheim CA US, ICAS, pp. 2383.

Burgsmueller, W. and Szodruch, J. (1985), "Benefits and costs of powered engine simulation at low speeds", *Aerospace Sciences Meeting, 23rd*, AIAA-1985-381, Jan 14-17, 1985., Reno, NV, USA, AIAA, pp. 7.

Burgsmüller, W., Hoheisel, H. (2000), "ENIFAIR — EU research into engine integration on future transport aircraft", *Air & Space Europe*, vol. 2, no. 2, pp. 81-85.

(C)

Clark, D. R., Maskew, B. and Dvorak, F. A. (1984), "The application of a second generation low-order panel method - program 'Vsaero' - to powerplant installation studies", *Aerospace Sciences Meeting, 22nd*, AIAA-1984-122, Jan 9-12, 1984, Reno, NV, USA, AIAA.

Cranfield University (2007), "The Turbomatch Code", *Lecture notes*, Cranfield University.

Crippa, S., Melber-Wilkending, S. and Rudnik, R. (2011), "DLR contribution to the first high lift prediction workshop", *49th AIAA Aerospace Sciences Meeting Including the New Horizons Forum and Aerospace Exposition*.

(D)

De Souza, A. M., Da Silveira Neto, A., De Souza, F. J., De Jesus, A. B., Oliveira, G. L. and Azevedo, J. L. F. (2008), "Parametric analysis of different nacelle positions in the DLR-F6 model by means of the CFD++ code", *Collection of Technical Papers - AIAA Applied Aerodynamics Conference*.

Devine, R., Cooper, R. K., Gault, R., Watterson, J. K. and Benard, E. (2009), "Comparison of conventional and compression pylon designs for an under wing nacelle", *Journal of Aircraft*, vol. 46, no. 1, pp. 325-328.

Dinesh, A.N., Ingraldi, A.M., (1992), "Experimental Study of Pylon Geometries for Transport Aircraft". AIAA Paper, AIAA-1992-0153.

Doulgeris, G. (Sep.2009), "Hermes V5 & TmatchCalls V3", Cranfield University.

(E)

Eliasson, P. (2003), "Improved CFD predictions for high lift flows in the European project EUROLIFT ", *Collection of Technical Papers – 21st AIAA Applied Aerodynamics Conference. AIAA-2003-3795, Jun. 23-26, 2003, Orlando, Florida, USA,AIAA.*

Eliasson, P., Catalano, P., Pape, M. - L., Ortmann, J., Pelizzari, E. and Ponsin, J. (2007), "Improved CFD predictions for high lift flows in the European project EUROLIFT II", *Collection of Technical Papers - AIAA Applied Aerodynamics Conference, Vol. 3, pp. 1614.*

Eliasson, P., Peng, S. and Hanifi, A. (2011), "Improving the Prediction for the NASA High-Lift Trap Wing Model", *49th AIAA Aerospace Sciences Meeting including the New Horizons Forum, AIAA-2011-867, Jan. 4-7, 2011, Orlando, Florida, USA, AIAA.*

ESDU (1994), "NACA 1-SERIES Geometry Representation for Computational Fluid Dynamics", ESDU-94013, no. June 1994.

(G)

Gacherieu, C., Collercandy, R., Larrieu, P., Soumillon, P., Tourrette, L. and Viala, S. (2000), "Navie -Stokes Calculations at Aerospatiale-Airbus for Aircraft Design", *22nd Congress of International Council of the Aeronautical Sciences, ICAS 200-2.6.1, 28 August - 1st September, 2000, Harrogate, UK, ICAS.*

Gad-el-Hak, M. and Bushnell, D. M. (1991), "Separation control: review", *Journal of Fluids Engineering, Transactions of the ASME*, vol. 113, no. 1, pp. 5-30.

Garth, C., Tricoche, X., Salzbrunn, T., Scheuermann, G., (2004), "Surface Techniques for Vortex Visualization", Joint EUROGRAPHICS - IEEE TCVG Symposium on Visualization, IEEE, 2004.

Gea, L. M., Halsey, N. D. and Intemann, G. A. (1994), "Application of the 3D Navier-Stokes code OVERFLOW for analyzing propulsion-airframe integration related issues on subsonic transport", *19th ICAS Congress*, Vol. ICAS-94-3.7.4, 18-23 Sept. 1994, Anaheim, CA USA, ICAS, pp. 2420.

(H)

Haines, A. B., (1999), "Scale Effects at High Lift and Low Speed", *AGARD-AG-323 Scale Effects on Aircraft and Weapon Aerodynamics*, AGARD July 1999, pp. 27-65.

Hansen, H., Thiede, P., Moens, F., Rudnik, R. and Quest, J. (2004), "Overview about the European high lift research programme EUROLIFT", *42nd AIAA Aerospace Sciences Meeting and Exhibit*, AIAA-2004-767 Jan. 5-8, 2004, Reno, Nevada.

Harris, A., Kutney, J.T. and Ogilvie, F.B. (1995), "25 years of turbine powered simulation success", *Proceeding of the International Forum on Turbine Powered Simulation*, May 16-17, 1995.

Hoheisel, H. (1997), "Aerodynamic Aspects of Engine-Aircraft Integration of Transport Aircraft", *Aerospace Science and Technology*, vol. 1, no. 7, pp. 475-487, 1997.

(J)

JAXA (2012), "*High Lift Research*", available at:
<http://www.apg.jaxa.jp/eng/research/ctt/ctt-index.html>.

(K)

Kanazaki, M., Yokokawa, Y., Murayama, M., Ito, T., Jeong, S. and Yamamoto, K. (2008), "Efficient design exploration of nacelle chine installation in wind tunnel testing", *46th AIAA Aerospace Sciences Meeting and Exhibit*, Jan 7-10 2008, Reno, Nevada.

Kumano, T., Jeong, S., Obayashi, S., Ito, Y., Hatanaka, K. and Morino, H. (2006), "Multidispinary design optimization of wing shape with nacelle and pylon", *European Conference on Computational Fluid Dynamics ECCOMAS CFD 2006*, Vol. 1, Netherlands, Delf.

(L)

Lednicer, D., Tidd, D. and Nigel, B. (1994), "Analysis of Close Coupled Nacelle Installation Using a Panel Method (VSAERO) and a multigrid euler method (MGAERO)", *19th ICAS Congress*, Vol. ICAS-94-3.7.3, 18-23 Sept. 1994, Anaheim CA USA, ICAS, pp. 2409.

Leibovich, S., (1984), "Vortex Stability and Breakdown: Survey and Extension", *AIAA Journal*, Vol.22, No.9, Sept. 1984, pp.1192-1206.

Li, J., Qin, E., Li, F. and Chen, H. C. (1998), "3-D flow simulations for general powered engine nacelles using Euler equations" AIAA-1998-929 ,*Aerospace Sciences Meeting and Exhibit, 36th*, Reno, NV, Jan. 12-15, 1998", *Aerospace Sciences Meeting and Exhibit, 36th*, Vol. AIAA-1998-929, Jan. 12-15, 1998, Reno, NV, USA, AIAA.

Longeville, O. (2007), "Summary of NEWAC engine performance specifications", D1.1.1A NEWAC deliverable.

Lynch, F. T. and Intermann, G. A. (1994), "The Modern Role of CFD in Addressing Airframe/Engine Integration Issues for Subsonic Transports ", *ICAS Congress, 19th*, Vol. ICAS-94-6.4.3, 18-23 Sept. 1994, Anaheim, CA, USA, ICAS.

(M)

Maskew, B. (1981), "Prediction of subsonic aerodynamic characteristics - A case for low order panel methods", *Aerospace Sciences Meeting, 19th*, Vol. AIAA-1981-252, Jan 12-15, 1981, St. Louis, Mo, USA, AIAA.

Mavriplis, D. J., Vassberg, J. C., Tinoco, E. N., Mani, M., Brodersen, O. P., Einfeld, B., Wahls, R. A., Morrison, J. H., Zickuhr, T., Levy, D. and Murayama, M. (2009), "Grid Quality and Resolution Issues from the Drag Prediction Workshop Series", *Journal of Aircraft*, vol. 46, no. 3, pp. 935-950.

McGinley, C., Jenkins, L., Watson, R. and Bertelrud, A. (2005), "3-D High-Lift Flow-Physics Experiment – Transition Measurements", *35th AIAA Fluid Dynamics Conference and Exhibit*, Vol. AIAA-2005-5148, June 6-9, 2005, Toronto, Ontario, Canada, AIAA.

Menter, F. R. (1994), "Two-equation eddy-viscosity turbulence models for engineering applications", *AIAA Journal*, vol. 32, no. 8, pp. 1598-1605.

Meredith, P. (1993), "Viscous Phenomena Affecting High-Lift Systems and Suggestions for the Future CFD Development ", *High-Lift System Aerodynamics*, Vol.3, AGARD-CP-515, Sept. 1993, AGARD.

Michael L. and Henderson, R.B.O (1987) "Nacelle/wing assembly with vortex control device". Patent no. US 4685643.
Available at: www.google.com/patents/US4685643.pdf.

MIDAP, (1979), "*Guide to In-Flight Thrust Measurement of Turbojets and Fan Engines*", 237th ed., AGARD AG-237, France.

Mitsuhiro, M., Yuzuru, Y., Hiroyuki, K., Kanazaki, M., Kazuomi, Y. and Takeshi, I. (2008), "Computational Study for High-Lift Aerodynamics in Jaxa", *26th International Congress of the Aeronautical Sciences, ICAS-98-2.2.1*. Sept. 14-19, 2008, Anchorage, Alaska, USA. ICAS.

Mogilka, P., Colin, P. and Esteve, P. (1994), "Aerodynamic study of new engine/airframe integration concepts", *19th ICAS Congress*, ICAS-94-6.4.2, 18-23 Sept. 1994, Anaheim CA USA, ICAS.

Murayama, M., Yamamoto, K. and Tanaka, K. (2011), "CFD comparison study for trapezoidal high-lift wing configurations by structured and unstructured mesh method", *49th AIAA Aerospace Sciences Meeting Including the New Horizons Forum and Aerospace Exposition*. AIAA 2011-937, Jan 4-7 2011, Orlando, Florida, USA. AIAA.

(N)

Naik, D. A., Anthony, M. and Pendergraft, O. C. J. (1992), "Experimental study of pylon geometries for transport aircraft", *Aerospace Sciences Meeting and Exhibit*, Vol. AIAA 1992-153, Jan 6-9, 1992, Reno, NV, USA, AIAA.

Naik, D. A., Chen, H. C., Su, T. Y. and Kao, T. J. (1992), "Euler Analysis of Turbofan/Superfan Integration for a Transport Aircraft ", *AGARD-CP-498 - Aerodynamic Engine/Airframe Integration for High Performance Aircraft and Missiles* , 7-10 October 1991, Fort Worth, Texas,USA, AGARD,

NASA (2012), *High Lift Prediction Workshop*, available at:
<http://hiliftpw.larc.nasa.gov/>.

Nicholson, L. F. (1957)," Engine-Airframe Integration", *RAeS Journal*, vol. 61, no. 3. April 1957.

(O)

Obert, E. (1993), "Forty Years of High-Lift R&D-an Aircraft Manufacturer's Experience ", *High Lift System Aerodynamics Vol.2*, AGARD-CP-515, Sept.1993, AGARD.

Oliveira, G. L., Puppim-Macedo, A. and Trapp, L. G. (2003), " Integration methodology for regional jet aircraft with underwing engines", *41st Aerospace Sciences Meeting and Exhibit*, AIAA 2003-0934, Jan. 6-9, 2003, Reno, Nevada USA, AIAA.

(P)

Pate, L., Lecordix, J. L. and Dessale, B. (1995), "CFD tools for designing isolated and installed nacelles", *ASME, SAE, and ASEE, Joint Propulsion Conference and Exhibit, 31st*, AIAA-1995-2625, July 10-12 1995, San Diego CA, AIAA.

(Q)

Quix, H., Schulz, M., Quest, J., Rudnik, R. and Schröder, A. (2007), "Low speed high lift validation tests within the European project EUROLIFT II", *Collection of Technical Papers - AIAA Applied Aerodynamics Conference*, Vol. 2, pp. 1545.

(R)

Raw, M. (1996), "Robustness of coupled Algebraic Multigrid for the Navier-Stokes equations", *Aerospace Sciences Meeting and Exhibit*, Vol. AIAA-1996-297, Jan. 15-18, 1996, Reno, NV,USA, AIAA.

- Richard, K.** (1973) "Lift vanes". Patent no. US 3744745.
Available at: www.google.com/patents/US3744745.
- Rivoire, V.** (2007), "Propulsion Integration Challenges", Lecture to DGLR, Hamburg, 5th July 2007.
- Rogers, S. E.,** Roth, K., Cao, H. V., Slotnick, J. P., Whitlock, M., Nash, S. M. and Baker, M. D. (2000), "Computation of viscous flow for a Boeing 777 aircraft in landing configuration", *Journal of Aircraft*, vol. 38, no. 6, pp. 1060-1068.
- Rohlmann, D.** and Rudnik, R. (2012), "Numerical Maximum Lift Predictions of a Realistic Commercial Aircraft in Landing Configuration", *50th AIAA Aerospace Sciences Meeting including the New Horizons Forum*, AIAA-2012-279, Jan. 9-12, 2012, Nashville, Tennessee, USA, AIAA.
- Rossow, C.,C.** and Ronzheimer, A. (1992), "Investigation of interference phenomena of modern wing-mounted high-bypass ratio engines by the solution of the Euler-equations", *AGARD-CP-498-Aerodynamic Engine/Airframe Integration for High Performance Aircraft and Missiles*, September 1992, AGARD, pp. 51.
- Rossow, C.** and Hoheisel, H. (1994), "Numerical study of interference effects of wing-mounted advanced engine concepts", *19th ICAS, Congress*, ICAS-94-6.4.1, 18-23 Sept. 1994, Anaheim, CA USA, ICAS, pp. 1272.
- Rossow, C.,** Godard, J., Hoheisel, H. and Schmitt, V. (1994), "Investigations of propulsion integration interference effects on a transport aircraft configuration", *Journal of Aircraft*, vol. 31, no. 5, pp. 1022-1030.
- Rubbert, P. E.** and Tinoco, E. N. (1983), "The impact of computational aerodynamics on aircraft design", *Atmospheric Flight Mechanics Conference*, AIAA-1983-2060, Aug 15-17, 1983, Gatlinburg, TN, AIAA.
- Rudnik, R.** (2003), "CFD Assessment for 3D High Lift Flows in the European Project EUROLIFT", *21st AIAA Applied Aerodynamics Conference*, Vol. AIAA-2003-3794, June 23-26, 2003, Orlando, Florida, USA, AIAA.
- Rudnik, R.** and Frhr. v. Geyr, H. (2007), "The European high lift project EUROLIFT II - Objectives, approach, and structure", *Collection of Technical Papers - AIAA Applied Aerodynamics Conference*, Vol. 2, pp. 1517.

Rudnik, R. and Germain, E. (2007), "Re-No. Scaling effects on the EUROLIFT high lift configurations", *Collection of Technical Papers - 45th AIAA Aerospace Sciences Meeting*, Vol. 13, pp. 9316.

Rudnik, R. and Reckzeh, D. (2012), "HINVA - High lift INflight VALidation - Project Overview and Status", *50th AIAA Aerospace Sciences Meeting including the New Horizons Forum*, AIAA-2012-106, Jan. 9-12, 2012, Nashville, Tennessee, USA, AIAA.

Rudnik, R., Rossow, C. and Frhr. v. Geyr, H. (2002), "Numerical simulation of engine/airframe integration for high-bypass engines", *Aerospace Science and Technology*, vol. 6, no. 1, pp. 31-42.

Rudolph, P. K. C. (1996), *High-lift Systems on Commercial Subsonic Airliner* NASA CR 4746, NASA.

Rumsey, C. L. and Ying, S. X. (2002), "Prediction of high lift: Review of present CFD capability", *Progress in Aerospace Sciences*, vol. 38, no. 2, pp. 145-180.

Rumsey, C. L., Long, M., Stuever, R. A. and Wayman, T. R. (2011), "Summary of the first AIAA CFD high lift prediction workshop (invited)", *49th AIAA Aerospace Sciences Meeting Including the New Horizons Forum and Aerospace Exposition*. AIAA 2011-939, Jan 4-7, 2011, Orlando, Florida, USA. AIAA.

(S)

Schulze, S. and Kahler, C. J. (2010), "Analysis of the Flow in Stalling Engine Inlet Models with Different Visualization and Measurement Techniques", June 22nd - 23rd, 2010, Braunschweig, Germany.

Schwetzler, D. (2010) "Engine Nacelle on a Aircraft Comprising a Vortex Generator Arrangement" Patent no. US 20100176249.
Available at: www.google.com/patents/US20100176249.pdf.

Sclafani, A. J., Slotnick, J. P., Vassberg, J. C., Pulliam, T. H. and Lee, H. C. (2011), "OVERFLOW analysis of the NASA trap wing model from the first high lift prediction workshop", *49th AIAA Aerospace Sciences Meeting Including the New Horizons Forum and Aerospace Exposition*, AIAA 2011-866, Jan 4-7, 2011, Orlando, Florida, USA. AIAA.

Seddon, J. (1993), "Practical Intake Aerodynamic Design", AIAA Education. AIAA.

Slotnick, J. P., Michael, Y., Mysko, S. J., Yeh, D. T., Roth, K., Rogers, S. E. and Baker, M. D., (2000), "Navier-Stokes analysis of a High Wing Transport high-lift configuration with externally blown flaps", *AIAA Applied Aerodynamics Conference, 18th*, AIAA-2000-4219, Aug. 14-17, 2000, Denver, CO,USA, AIAA.

Smith, A. M. O. (1975), "High-Lift Aerodynamics", *Journal of Aircraft*, vol. 12, no. 6, pp. 501-530.

Steed, S. (2011), "High Lift CFD Simulations with an SST-Based Predictive Laminar to Turbulent Transition Model", *49th AIAA Aerospace Sciences Meeting including the New Horizons Forum*, AIAA-2011-864, Jan. 4-7, 2011, Orlando, Florida, AIAA.

Strawn, R., Kenwright, D. N., and Ahmad, J, (1999), "Computer Visualization of Vortex Wake Systems", *AIAA Journal*, vol.37, no.4, pp. 511-512, April 1999, AIAA.

(T)

Tinoco, E. N. (2001), "An assessment of CFD prediction of drag and other longitudinal characteristics", *Aerospace Sciences Meeting and Exhibit, 39th*, AIAA-2001-1002, Jan. 8-11, 2001, Reno, NV, USA, AIAA.

(V)

Van Dam, C. P. (2002), "The aerodynamic design of multi-element high-lift systems for transport airplanes", *Progress in Aerospace Sciences*, vol. 38, no. 2, pp. 101-144.

Vassberg, J. C., DeHaan, M. A., Rivers, S. M. and Wahls, R. A. (2008), "Development of a common research model for applied CFD validation studies", *Collection of Technical Papers - AIAA Applied Aerodynamics Conference*.

VITAL (2005) "Data for the PDE4089 R&R Vital, VITAL project", VITAL.

Von Geyr, H. F. and Rossow, C. (2005), "A Correct Thrust Determination Method for Turbine Powered Simulators in Wind Tunnel Testing", *41st*

AIAA/ASME/SAE/ASEE Joint Propulsion Conference and Exhibit. AIAA-2005-3707, July 10-13, 2005, Tucson, Arizona, USA, AIAA.

Von Geyr, H. F., Schade, N., Burg, J. W. V. D., Eliasson, P. and Esquieu, S. (2007), "CFD prediction of maximum lift effects on realistic high-lift-commercial- aircraft-configurations within the European project EUROLIFT II", *Collection of Technical Papers - AIAA Applied Aerodynamics Conference*, Vol. 2, pp. 1560.

(W)

Wallin, S. and Johansson, A. V. (2000), "An explicit algebraic Reynolds stress model for incompressible and compressible turbulent flows", *Journal of Fluid Mechanics*, vol. 403, pp. 89-132.

Wiert, L. and Meunier, M. (2011), "Computational Assessment of the HiLiftPW-1Trap-Wing Model Using the elsA CFD Software", *49th AIAA Aerospace Sciences Meeting including the New Horizons Forum and Aerospace Exposition*, AIAA-2011-865, Jan. 4-7, 2011, Orlando, Florida, USA, AIAA.

Wilcox, D.C., (1988), "Reassessment of the scale determining equation for advanced turbulence models", *AIAA Journal*, Vol. 26, pp.1299-1310. AIAA.

Wild, J., Brezillon, J., Amoignon, O., Quest, J., Moens, F. and Quagliarella, D. (2009), "Advanced design by numerical methods and wind-tunnel verification within European High-Lift Program", *Journal of Aircraft*, vol. 46, no. 1, pp. 157-167.

Wilfert, G., Sieber, J., Rolt, A., Baker, N., Touyeras, A. and Colantuoni, S. (2007), "New Environmental Friendly Aero Engine Core Concepts", *ISABE 2007*, Vol. ISABE-2007-1120., ISABE.

Williams, D. (2009), *Propulsion Systems Performance and Integration. Airframe Engine Integration*, Lecture Notes, Cranfield University.

(Y)

Yip, P. L., Vijegen, P. M. H. W., Hardin, J. D. and Van Dam, C. P. (1993), "In Flight Pressure Distribution and Skin-Friction Measurements on a Subsonic High-Lift Section ", *High-Lift System Aerodynamics*. AGARD-CP-515, Sept.1993, AGARD.

Yokokawa, Y., Murayama, M., Kanazaki, M., Murota, K., Ito, T. and Yamamoto, K. (2008), "Investigation and improvement of high-lift aerodynamic performances in lowspeed wind tunnel testing", *46th AIAA Aerospace Sciences Meeting and Exhibit*. AIAA 2008-350, Jan, 7-10, Reno, Nevada, USA, AIAA.

APPENDICE

ADDITIONAL WORK

ABSTRACT

An additional work was undertaken at the beginning of the project in order to reduce the computational effort requested to evaluate the Propulsive System Integration (PSI) effects. The prediction and decomposition of drag associated to PSI was investigated applying a methodology based on entropy variations in the flow and the momentum conservation theorem. This advanced prediction method can decompose the total drag in to viscous, wave, induced and spurious drag, allowing a better understanding of the flow. The spurious drag, due to numerical errors, can be eliminated reducing the dependency of the solution on the grid quality. Four applications are presented: two wing-body configurations, a wing-body-nacelle-pylon with trough-flow-nacelle, and a wing-body-nacelle-pylon with a very-high-bypass-ratio engine in power-on condition. One objective was to minimize grid resolution to enable design optimization.

Even if the results were encouraging, it was decided to focus the research on the main project objective. The method still needs to be refined and generalised, reducing the sensitivity of the results to the cut-off parameters. Future research is planned. The results of this work were presented at the ASME Turbo Expo 2011 and published in the conference proceedings.

INTRODUCTION

The prediction of drag in CFD is still a big challenge and in spite of the rapid development of numerical schemes and computing power the challenge is still open (Mavriplis, 2009). One of the major issues responsible for this remains computational mesh dependency; reliable results need fine meshes.

The quality of the grid is directly related to the numerical dissipation and discretization errors that generate spurious drag, increasing the difference between the numerical solution and the real flow.

To overcome this problem, different approaches were proposed (Kusunose, 1998; Van Dam, 1999; Desterac, 2003), and in particular one of them has recently gained interest: the *mid-field method*.

This method is intended to offer a substitute to the traditional *near-field method* that computes the drag by performing a surface integration of pressure and stress tensor, integrating entropy drag and related quantity on defined volumes and planes around the body (Paparone, 2003). The approach is based on the *far-field method* in which the drag is calculated by applying a momentum balance evaluated on a surface far from the body (Kusunose, 1998). The application of Gauss's theorem, to obtain a volume integral formulation, allows one to limit the integration in parts of the control volume where the entropy drag has physical sources: boundary layers and shocks, and therefore to identify and eliminate the spurious drag. This method substantially reduces the numerical error associated with poor quality meshes compared to the *near-field method*. Another intrinsic advantage of this technique is the drag breakdown capability which allows a better understanding of the flow around the body.

This appendice gives a brief introduction to this methodology showing its suitability for PSI, and ends with four numerical applications: two wing-body configurations (WB), a wing-body-nacelle-pylon with trough-flow-nacelle (WBNP-TF), and a wing-body-nacelle-pylon with a VHBPR engine in power-on condition (WBNP-PO). The object of this work was to assess the capability of the *mid-field method* for PSI, that potentially increases the accuracy of the drag evaluation and simplify the way to do it at the same time (Tognaccini, 2005; Van der Vooren 2004).

DRAG ESTIMATION

Applying the momentum balance for a steady flow with free stream velocity V_∞ , on a volume that surrounds an unpowered aircraft, we can define the aerodynamic force as:

$$\begin{aligned} F &= \int_{S_{body}} [(p - p_\infty) - (\boldsymbol{\tau}_w \cdot \mathbf{n})] dS = & \text{(A.1)} \\ &= - \int_{S_{far}} [\rho V \mathbf{V} + (p - p_\infty) \mathbf{V} - \boldsymbol{\tau}_w] \cdot \mathbf{n} dS \end{aligned}$$

Showing that we can evaluate the force in two different ways: integration the pressure and stress tensor on the body surface of aircraft (left equation), or evaluation the net momentum flux across the surface S_{far} (right equation), located far from the body. The first integral is used by the well know *near-field method* and the second one to derive the *far-field method*.

Expanding the second integral in Taylor's series with respect to the pressure, entropy and total enthalpy, it is possible to obtain the so called entropy drag (Paparone, 2003) (eq. A.2), the first term of the expansion that only for a two-dimensional adiabatic flow, represent the total drag. The second term, related to enthalpy variations, is negligible on power-off conditions.

$$D_{\Delta s} = -V_\infty \int_{S_{far}} \rho g(\Delta s/R) (\mathbf{V} \cdot \mathbf{n}) dS \quad \text{(A.2)}$$

With:

$$g = cs1 \left(\frac{\Delta s}{R} \right) \quad \text{(A.3)}$$

Where Δs is the entropy variation respect to the free-stream condition and the $cs1$ coefficient, coming from the Taylor's expansion, is:

$$c_{s1} = - \frac{1}{\gamma M_\infty^2} \quad \text{(A.4)}$$

Applying the Gauss's divergence theorem to the vector field $\rho g\mathbf{V}$ in the finite flow domain Ω , eq. A.2 becomes:

$$D_{\Delta s} = -V_{\infty} \int_{\Omega} \nabla \cdot (\rho g\mathbf{V}) d\Omega \quad (\text{A.5})$$

It is convenient to express the vector $\rho g\mathbf{V}$ as:

$$\mathbf{f}_{vw} = -\rho g\mathbf{V} \quad (\text{A.6})$$

Decomposing the domain Ω in shock waves volume Ω_w , viscous volume Ω_v , and spurious volume Ω_{sp} , the entropy drag can be defined as:

$$D_{\Delta s} = D_v + D_w + D_{sp} \quad (\text{A.7})$$

Where:

$$D_v = V_{\infty} \int_{\Omega_v} \nabla \cdot \mathbf{f}_{vw} d\Omega, \quad D_w = V_{\infty} \int_{\Omega_w} \nabla \cdot \mathbf{f}_{vw} d\Omega \quad (\text{A.8})$$

$$D_{sp} = V_{\infty} \int_{\Omega_{sp}} \nabla \cdot \mathbf{f}_{vw} d\Omega$$

The drag can therefore be evaluated separately for each component. The selection of the respective volumes is computed using selectors proposed by Tognaccini (2005). The shock wave zone is based on the non dimensional function:

$$F_{shock} = \frac{V \cdot \nabla p}{a|\nabla p|} > 0 \quad (\text{A.9})$$

Where a is the sound speed. We can notice that sensor will be negative in expansion zones and positive in compression zones. Hence cells with negative F_{shock} can be excluded from the wake region.

The boundary-layer and wake region is selected using a sensor based on the eddy viscosity:

$$F_{visc} = \frac{\mu_t}{\mu_l} + 1 \quad (\text{A.10})$$

Where μ_l and μ_t are respectively the laminar and eddy viscosities. The value of F_{visc} will be very high in the viscous zone and ≈ 1 in the other zones. Hence the selection can be done applying:

$$F_{visc} > K_{visc} \cdot F_\infty \quad (\text{A.11})$$

Where F_∞ is the value of eq. A.10 in the freestream condition, and K_{visc} is a cut-off parameter.

As pointed out the entropy drag, equal to the well-know Oswatitsch (1956) expression, is different from the total drag for a three-dimensional adiabatic flow, due to the Taylor's first order approximation, being only related to the irreversible processes.

To get the exact *near-field/mid-field* drag balance, the fourth drag component, the induced drag D_i , related to reversible processes, can be computed using the Van der Vooren's formulation (Van der Vooren, 2004):

$$D_i = \int_{\Omega_v + \Omega_w} \nabla \cdot \mathbf{f}_i d\Omega - \int_{S_D} (\mathbf{f}_i \cdot \mathbf{n}) dS \quad (\text{A.12})$$

Where S_D is a downstream surface and \mathbf{f}_i defined by:

$$\mathbf{f}_i = -\rho(u - u_\infty - g)\mathbf{V} - (p - p_\infty)\mathbf{n} + \tau_x \quad (\text{A.13})$$

The total drag can now be computed as:

$$D = D_v + D_w + D_i + D_{sp} \quad (\text{A.14})$$

Defining the vector \mathbf{f} as:

$$\mathbf{f} = \rho V \mathbf{V} + (p - p_\infty) \mathbf{V} - \boldsymbol{\tau}_w \quad (\text{A.15})$$

From eq. (1) and (2):

$$\mathbf{f} = \mathbf{f}_{vw} + \mathbf{f}_i \quad (\text{A.16})$$

Assuring the exact drag balance from the two different methods and given that $\nabla \cdot \mathbf{f} = 0$, eq. A.12 can be rewritten in a easier implementation formula:

$$D_i = - \int_{\Omega_v + \Omega_v} \nabla \cdot \mathbf{f}_{vw} d\Omega - \int_{S_{skin}} (\mathbf{f}_i \cdot \mathbf{n}) dS \quad (\text{A.17})$$

The assumptions may be violated in jet or propeller configurations therefore Van der Vooren (2004) proposed an alternative formulation for power-on configurations:

$$\begin{aligned} D_i = & - \int_{\Omega_v + \Omega_w} \nabla \cdot \mathbf{f}_{vw} d\Omega - \int_{S_{airframe+engine}} (\mathbf{f}_i \cdot \mathbf{n}) dS \\ & + \frac{1}{2} \int_{S_{engine}} \rho (v^2 + w^2) n_x dS \end{aligned} \quad (\text{A.18})$$

The correct drag-thrust bookkeeping is assured defining the engine, S_{engine} and airframe $S_{airframe}$ domains (Tognaccini, 2005; Van der Vooren, 2004; Oswatitsch, 1956). The second set of calculations, showed at the end of this paper, is performed on a power-on condition, where the approximation of negligible enthalpy variations doesn't stand. However Tognaccini (2005) and Van der Vooren (2004) pointed out that the entropy drag related to the external flow for power on condition (eq. A.18) is the same as eq. A.2, but with a different volume of integration.

Note that the force associated to the total enthalpy variations is negligible outside the fan and core jets, therefore in the entropy drag can be written as:

$$D_{\Delta s} = V_{\infty} \int_{\Omega'} \nabla \cdot (\rho g \mathbf{V}) d\Omega \quad (\text{A.19})$$

Where Ω' is the domain volume minus the inlet/jet flows volumes.

$$\Omega' = \Omega - \Omega_{pre} - \Omega_{jet} \quad (\text{A.20})$$

Like the power-off condition the entropy drag can be decomposed in viscous, shock and spurious components. Once again to compute the total drag, the induced drag (eq. A.18) is added to the other components.

TEST CASES

The selected geometries are, already used in chapters 2 and 4: for the first set of results, the DLR-F6 (AIAA, 2012) WB and WBNP-TF, and for the second set the CRM (AIAA, 2012) and WBNP-PO, with a VHBPR engine. For the DLR-F6 the design Mach number is 0.75, with a Reynolds number, based on the mean aerodynamic cord, of $Re = 3 \times 10^6$. The CRM is characterized by a design Mach number of 0.85, and a Reynolds number, based on the mean aerodynamic cord, of $Re = 5 \times 10^6$.

NUMERICAL METHOD

The Reynolds Averaged Navier-Stokes (RANS) equations are discretized using a vertex-based finite volume method, and evaluated using a second-order advection scheme with a pressure-velocity coupling technique. The Reynolds stresses in the momentum equations, are computed using the Menter's Zonal two equations κ - ω turbulence model (Menter, 1994).

The grids are hybrid type and have been constructed following the basic gridding guidelines proposed after the experience gained within drag prediction workshops (AIAA, 2012).

Two grid levels are used for the DLR-F6: coarse grids with approximately 2×10^6 nodes for the WB and 3×10^6 nodes for the WBNP, and a medium grid with approximately 5×10^6 nodes for the WB and 5.5×10^6 nodes for the WBNP.

The results for the CRM case are computed using meshes of the order of 8×10^6 nodes for the WB, and 12×10^6 nodes for the WBNP-PO.

The selected meshes for the DLR-F6 cases are very coarse in order to allow a correct evaluation of the *mid-field* method potential. One objective of this study is to minimize grid resolution to enable automated PSI design optimization for future work.

DLR-F6 RESULTS

Using the selectors, (eq. A.9-10), the viscous and shock volumes can be visualized as show in figs. A.1 and A.2. Note the inboard pylon shock on fig. A.1, revealing good agreement with the experimental results.

In fig.A3, A4, and A5 the *mid-field* drag decomposition results are shown, revealing that the methodology can predict viscous, shock and induced drag, isolating the spurious drag. The different components are plotted for the coarse and medium meshes, revealing that they are almost independent of the mesh size.

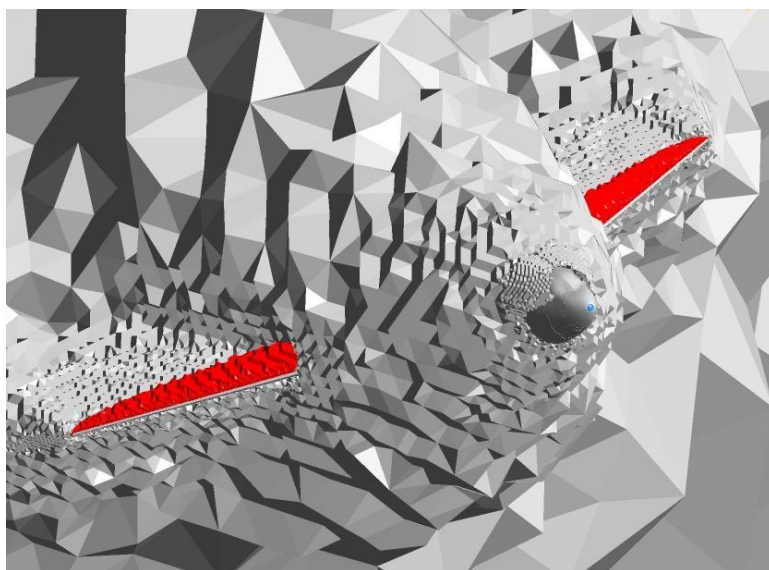


Fig.A.1 Shock (red) and viscous (grey) volume selection for DLR-F6 WB

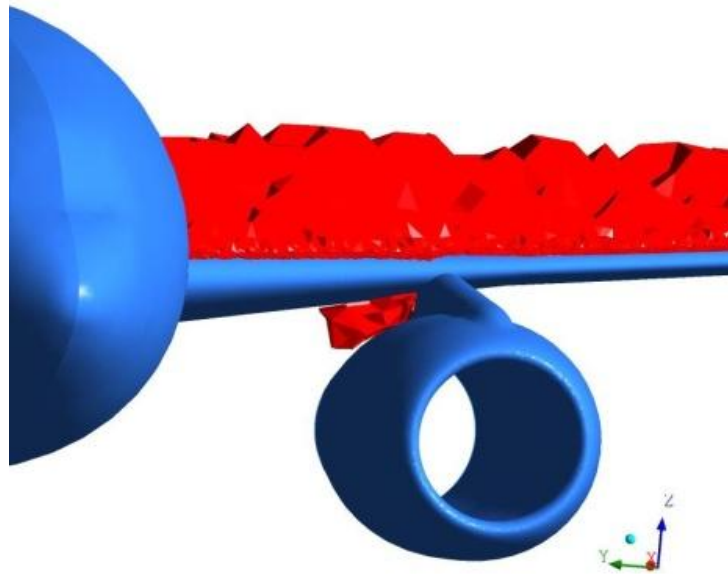


Fig.A.2 Shock volume selection for DLR-F6 WBNP-TF configuration

This is confirmed in fig. A6 and A7, showing lower uncertainty bands for the *mid-field* method respect to the *near-field* ($h = 1$ specify the finest grid size). From fig. A3, A4 and A5 can be pointed out that the total *mid-field* drag estimation and the experimental results are in better agreement compared with the results extracted using the *near-field* method, in both WB and WBNP-TF configurations.

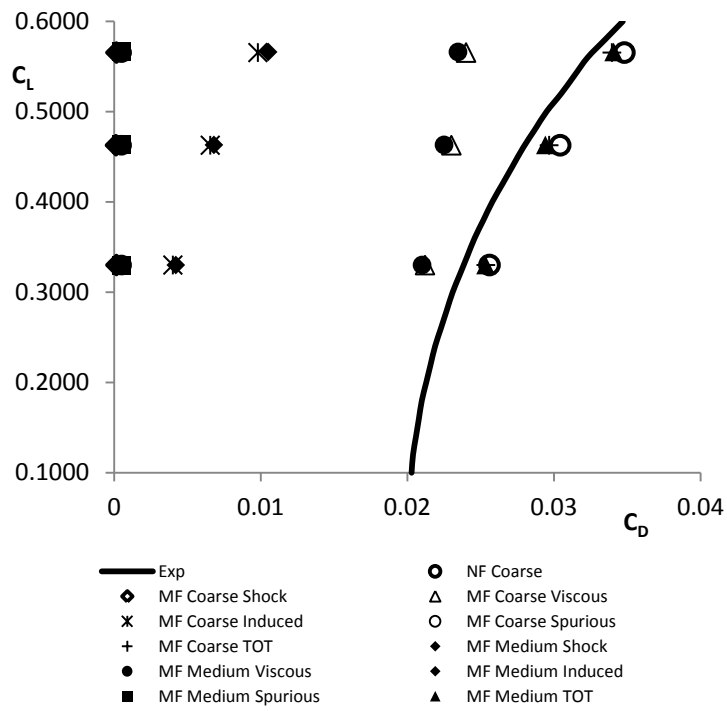


Fig.A.3 Mid-field results for DLR-F6 WB configuration

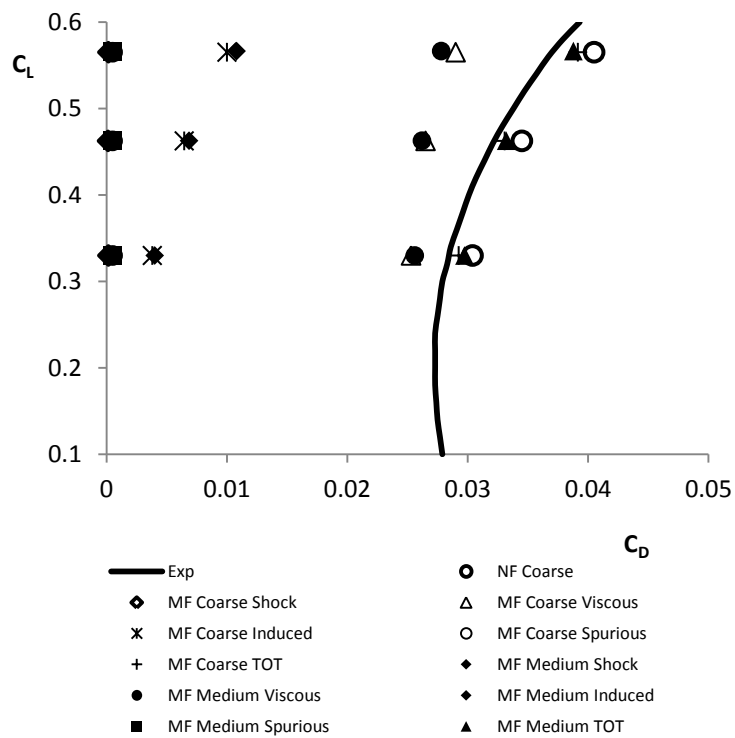


Fig.A.4 Mid-field results for DLR-F6 WBNP configuration

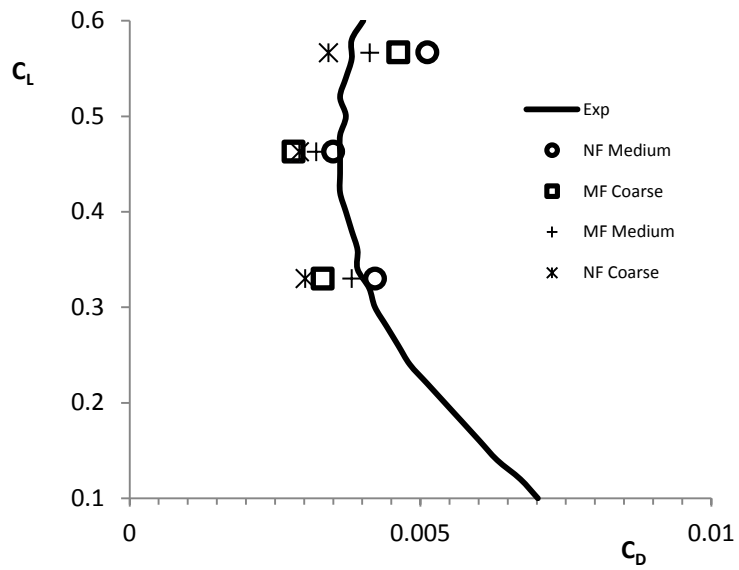


Fig.A.5 Mid-field installation Drag polar DLR-F6 configuration

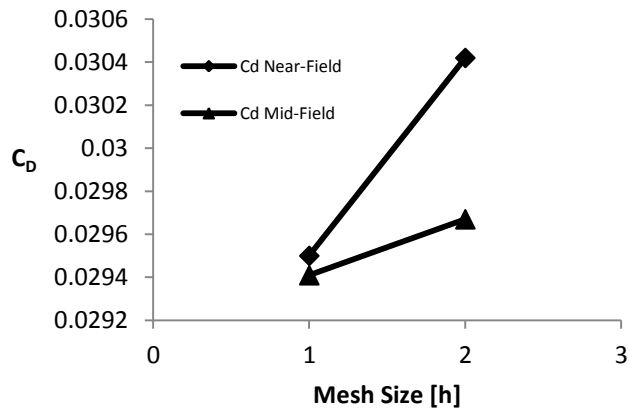


Fig.A.6 Mid-field/Near-Field mesh size sensibility for DLR-F6 WB configuration

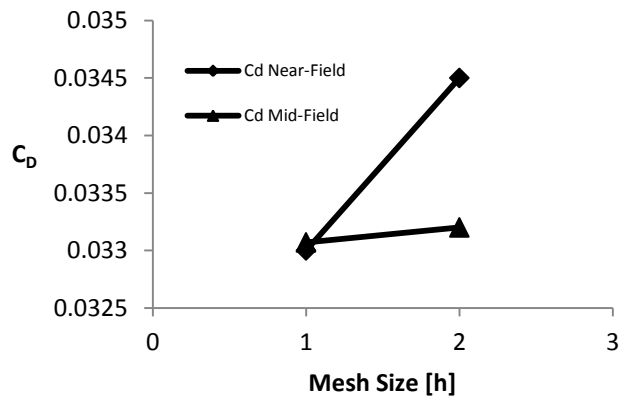


Fig.A.7 Mid-field/Near-Field mesh size sensibility for DLR-F6 WBNP configuration

CRM RESULTS

The CRM PSI aerodynamics is characterized by a strong shock on the inboard side of the pylon, and a separation zone. This because the pylon and nacelle geometries still need to be refined in order to represent a standard PSI case. The nacelle is asymmetric to reduce the complexity of the geometry and because of the lack of information at this state of the project. All of this assumption and simplification don't influence the assessment of the potential capability of the *mid-field* method on PSI applications.

To correctly evaluate the PSI installation drag and avoid double accounting, a proper thrust-and-drag bookkeeping is crucial, especially in a power-on configuration. In order to fulfil this requirement, the integration domain was divided as suggested by Tognaccini (2005) and Van der Vooren (2004). The shock volume selection for the WBNP-PO configuration is showed in fig.8 confirming the presence of the strong shock on the inboard side.

Table A.1-2 and A.3 summarize the results for the CRM WB and WBNP-PO configurations. The results look encouraging, allowing, again, to decompose and evaluate, the spurious drag, increasing the reliability of the CFD results. Form table A.1 and A.2 we can see that the spurious drag is higher on the WBNP-PO configuration due to the lower mesh quality associated to the more complicated geometry.

CL	CD _{NF}
0.485	0.0315

CL	CD _v	CD _w	CD _i	CD _{sp}	CD _{TOTMF}
0.485	0.0185	0.0011	0.0113	0.0006	0.0309

Table A.1 *Mid-field/Near-Field* Drag CRM WB configuration

CL	CD _{NF}
0.495	0.0385

CL	CD _v	CD _w	CD _i	CD _{sp}	CD _{TOTMF}
0.495	0.0215	0.0025	0.0134	0.0009	0.0374

Table A.2 *Mid-field/Near-Field* Drag CRM WBNP-PO configuration

CL	CD_{NFinst}	CD_{MFinst}
0.495	0.007	0.0065

Table A.3 *Mid-field/Near-Field* Installation Drag CRM configuration.

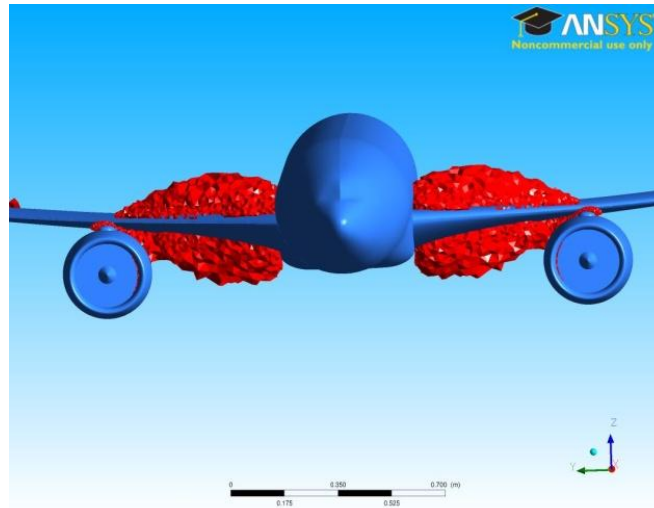


Fig.A.8 Shock volume selection for CRM WBNP-PO configuration.

CONCLUSIONS AND FUTURE WORK

The prediction and decomposition of drag associated to Propulsive System Integration (PSI) has been investigated applying a new methodology based on entropy variations in the flow and the momentum conservation theorem. The installation drag of two different aircrafts for a conventional and a VHBR nacelle in through flow and power on condition, respectively, has been evaluated showing better agreement with the experimental results than the classic *near-field* method. This because the spurious drag, due to numerical errors, can be eliminated reducing the dependency of the solution on the grid quality.

The objective of this work is to minimize grid resolution to enable PSI design optimization, given that the computational effort on PSI application is very high, due to the complexity of the problem.

However the methodology needs to be refined given that the sensibility to the viscous and shock sensors is still very high. This is not tolerable especially if the method will be used to run an optimization.

One objective for the future work will be to reduce this cut-off sensibility passing from an external volume surface integration, in order to resolve eq. A.12, to an actual integration over the surface of each element.

APPENDICE REFERENCES

Oliveira, G.L., Puppim-Macedo, A. and Trapp, L.G., (2003), "Integration Methodology for Regional Jet Aircraft With Underwing Engines". AIAA Paper 2003-0934.

Rossow, C. Godard, J. -, Hoheisel, H. and Schmitt, V. (1992), "Investigations of Propulsion Integration Interference Effects on a Transport Aircraft Configuration", *AIAA, SAE, ASME, and ASEE, Joint Propulsion Conference and Exhibit*, 28th, Nashville, TN; UNITED STATES; 6-8 July 1992, AIAA-92-3097.

Mavriplis, D. J., Vassberg, J. C., Tinoco, E. N., Mani, M., Brodersen, O. P., Einfeld, B., Wahls, R. A., Morrison, J. H., Zickuhr, T., Levy, D. and Murayama, M. (2009), "Grid quality and resolution issues from the drag prediction workshop series", *Journal of Aircraft*, vol. 46, no. 3, pp. 935-950.

Kusunose K. (1998) "Drag Prediction Based on Wake Integral Method", AIAA Paper, Applied Aerodynamics Conference, 16th, Albuquerque, NM, June 15-18, 1998, AIAA-98-2723.

Van Dam, C.P., "Recent Experience with Different Methods of Drag Prediction", *Progress in Aerospace Sciences*, vol.35, No.8, 1999, pp-751-798.

Desterac, D. (2003) "Far-Field/Near-Field drag balance an applications of drag extraction in CFD", *CFD-Based Aircraft Drag Prediction and Reduction*", LS 2003-02, von Karman Inst. For Fluid Dynamics Lecture Series, von Karman Inst. for Fluid Dynamics, Rhode St-Genese, Belgium.

- Paparone, L.** and Tognaccini, R. (2003), "Computational fluid dynamics-based drag prediction and decomposition", *AIAA Journal*, vol. 41, no. 9, pp. 1647-1657.
- Tognaccini, R.** (2005), "Drag Computation and Breakdown in Power-on Conditions", *Journal of Aircraft*, vol. 42, no. 1, pp. 245-252.
- Van Der Vooren,** and Destarac D., (2004), "Drag/thrust analysis of jet-propelled transonic transport aircraft - Definition of physical drag components", *Aerospace Science and Technology*, vol. 8, no. 6, pp. 545-556.
- Oswatitsch, K.**, "Gas Dynamics", *Academic Press*, New York, 1956, pp.177-210.
- MIDAP,** (1979) "Guide to In-Flight Thrust Measurement of Turbojets and Fan Engines", AGARD-AG-273, Jan.1979.
- AIAA** (2012), *Drag Prediction Workshop* , available at:
<http://aaac.larc.nasa.gov/tsab/cfdlarc/aiaa-dpw/>.
- Brodersen, O.** and Stuermer, A. (2001), "Drag prediction of engine-airframe interference effects using unstructured Navier-Stokes calculations", *AIAA Applied Aerodynamics Conference, 19th, Anaheim, CA; UNITED STATES; 11-14 June 2001, AIAA-2001-2414*.
- Menter, F.R.**, (1994) "Two-equation Eddy-Viscosity Turbulance Models for Engineering Applications". *AIAA Journal* Vol.32, No.8, August 1994, pp 1598-1605.